Entwicklung neuartiger Metall-organischer Gerüstverbindungen auf der Basis von Carboxylat- und bifunktionellen Monoalkylphosphonat-Carboxylat-Liganden

Dissertation

Zur Erlangung des Doktorgrades
der Mathematisch-Naturwissenschaftlichen Fakultät
der Heinrich-Heine-Universität Düsseldorf

vorgelegt von

Anna Goldman
aus Tallinn, Estland

Düsseldorf, Juni 2020

aus dem Institut für Anorganische Chemie und Strukturchemie I
der Heinrich-Heine-Universität Düsseldorf

Gedruckt mit der Genehmigung der
Mathematisch-Naturwissenschaftlichen Fakultät der
Heinrich-Heine-Universität Düsseldorf

Berichterstatter:

1. Prof. Dr. Christoph Janiak

2. Prof. Dr. Christian Ganter

Tag der mündlichen Prüfung: 16.07.2020

Eidesstattliche Erklärung

Ich versichere an Eides statt, dass die Dissertation von mir selbstständig und ohne unzulässige fremde Hilfe unter Beachtung der „Grundsätze zur Sicherung guter wissenschaftlicher Praxis“ an der Heinrich-Heine-Universität Düsseldorf erstellt worden ist. Die aus fremden Quellen direkt oder indirekt übernommenen Gedanken sind als solche kenntlich gemacht. Die Arbeit wurde bisher weder im Inland noch im Ausland in gleicher oder ähnlicher Form einer anderen Prüfungsbehörde vorgelegt. Es wurden keine früheren erfolglosen Promotionsversuche unternommen.

………………………………….................. ……………………………………......................

Ort, Datum Unterschrift

Danksagung

An dieser Stelle möchte ich mich bei all denjenigen bedanken, die mich während der Anfertigung dieser Dissertation unterstützt und motiviert haben.

Zuerst gebührt mein Dank Herrn Prof. Dr. *Christoph Janiak*, für die Möglichkeit meine Dissertation in seinem Arbeitskreis anzufertigen. Ich bedanke mich für die hilfreichen Anregungen und die konstruktive Kritik sowie die mir gewährten Freiräume und das Stellen von neuen Herausforderungen, an denen ich lernen und wachsen konnte.

Herrn Prof. Dr. *Christian Ganter* möchte ich herzlich für die freundliche Übernahme des Co-Referates sowie für die interessanten wissenschaftlichen Anregungen und die angenehme Atmosphäre im gemeinsamen Seminar danken. Weiterhin bedanke ich mich für die stete Ansprechbarkeit und Hilfsbereitschaft sowohl während des Studiums als auch während der Promotion.

Des Weiteren danke ich Herrn Dr. *Ishtvan Boldog* für seine große Hilfsbereitschaft und Unterstützung sowie die anregenden wissenschaftlichen Diskussionen in den letzten Zügen dieser Arbeit.

Herzlich danke ich allen Mitarbeitern der beiden Arbeitsgruppen des Instituts Anorganische Chemie I für die tolle Arbeitsatmosphäre und Unterstützung in fachlichen Fragen.

Für die organisatorische Hilfe danke ich *Claudia Schäfer* und *Jutta Bourgeois*.

Birgit Tommes, *Annette Ricken* und *Marcell Demandt*, danke ich für die stete Ansprechbarkeit und Hilfestellungen bei technischen Fragen. *Birgit Tommes* danke ich weiterhin für die IR-Messungen und die netten Gespräche.

Ein ganz besonderer Dank gilt Dr. *Simon Millan* und Prof. Dr. *Beatriz Gil-Hernández* für die Unterstützung und die anregenden Diskussionen, die in den verschiedensten Aspekten meiner Arbeit eingeflossen sind. Danke für die Motivation und das schöne Zusammensein in jeder Phase der Promotion sowohl fachlich als auch privat. In gleicher Weise danke ich Dr. *Janina Dechnik*, *Alexander Nuhnen*, *Stefanie Büge*l, *Ülkü Kökçam-Demir*, *Yangyang Sun*, Dr. *Gamall Makhloufi*, Dr. *Serkan Gökpinar*, *Moritz Steinert*, Dr. *Emrah Hastürk*, Dr. *Biju Francis*, *Anna Kautz*, Dr. *Christian Heering*, Dr. *Marvin Siebels*, Dr. *Tobie Matemb Ma Ntep*, Dr. *Jun Liang*, *Alexa Schmitz*, *Vasily Gvilava*, Dr. *Sandra Nießing*, *Carsten Schlüsener*, *Secil Öztürk*, *Alex Spieß*, C*hristian Jansen*, *Philipp Brandt*, *Bastian Moll*, *Saskia Menzel*, *Simon-Patrick Höfert* und Dr. *Shang Hua Xing* für die schöne Arbeitsatmosphäre und unvergessliche Zeit.

Ich danke den M.Sc. Absolventen *Tobias Amrehm* und M.Sc *Katharina Nardin* für die engagierte Zusammenarbeit und den Beiträgen zu dieser Arbeit

Von ganzem Herzen danke ich meiner Famile für Ihre Liebe und den immerwährenden bedingungslosen Rückhalt. Ich danke meiner Mutter *Faina Goldman*, die immer in meinem Herzen weiterlebt und mir Kraft gibt. Meinem Vater *Rafail Goldman* danke ich für seine Herzlichkeit, sein Vertrauen und die weisen Ratschläge in jeder Lebensphase. Ich danke meiner Schwester *Julia Goldman*, dafür dass Sie immer für mich da ist und mir zeigt, dass nichts unmöglich ist. Dem bezaubernsten Menschen den ich kenne, meiner Nichte *Rafaela Goldman* danke ich für die Motivation und Unterstützung. Du bist für mich ein Ruhepol. Ich muss immer lächeln, wenn ich an dich denke. Abschließend danke ich meinem Lebensgefährten *Sadedin Rufat*. Du bist für mich im wahrsten Sinne des Wortes der stärkste Mann der Welt. Ich danke dir für deine fortwährende Unterstützung in allen Situationen und dass du immer an mich geglaubt hast. Ohne Euren Halt wäre nichts möglich. Ich liebe Euch.

Für meine Familie

Kurzzusammenfassung

Metall-organische Gerüstverbindungen (MOFs) sind poröse Materialien, die als vielversprechende Kandidaten für eine Vielfalt von möglichen Anwendungen, wie z.B. Gasspeicherung und -trennung, Katalyse und Sensorik angesehen werden. Aufgrund ihrer strukturellen Vielseitigkeit und funktionalen Abstimmbarkeit, haben sie sich zu einem Themengebiet von erheblichem Interesse für die Wissenschaft und Forschung entwickelt. Bislang konnte die Leistungsfähigkeit vor allem von MOFs basierend auf Carboxylat-Liganden durch vielfältige Funktionalisierungsstrategien wie beispielsweise die Generierung von offenen Metallstellen, Einführung von funktionellen Gruppen oder die isoretikulare Chemie angepasst und gesteigert werden. Ein aussichtsreiches Forschungsfeld ist weiterhin die Entwicklung von neuartigen MOFs auf der Basis von Organophosphonat-Liganden, welches einen Zugang zu chemisch und thermisch stabilen Materialien ermöglicht. Die Verwendung von tridentaten Phosphonsäuren ($–PO_3H_2$) für die Synthese von MOFs äußerst interessant, da diese starken Bindungen und vielfältige Koordinationsmodi mit Metallen ausbilden können. Allerdings sind Metallphosphonate im Vergleich zu den herkömmlichen (Carboxylat-basierenden) hochkristallinen MOFs meist schwach kristallin, was deren strukturelle Aufklärung erschwert. Außerdem führt die hohe Bindungsaffinität von Organophosphonsäuren typischerweise zur Ausbildung von Schichtstrukturen, die keine oder geringe Porosität aufzeigen.

Die Verwendung von bidentaten Monoalkylphosphonat-Liganden für eine gezielte Synthese von kristallinen Netzwerkstrukturen ist der Schwerpunkt dieser Arbeit und beschäftigt sich mit der Charakterisierung und dem Anwendungspotential dieser Materialien. Die Forschung wurde von Strategien, wie die Verwendung von bifunktionellen Monoalkylphosphonaten, deren Potential zur synergistischen Kombination mit der Carboxylatunktionalität in einem Liganden und die Verwendung von N-Donor-Co-Liganden, inspiriert. Im Rahmen dieser Arbeit wurden zwei kristalline isostrukturelle Monoethylphosphonat-Carboxylat MOFs $[Zn_2(EtBCP)_2(DABCO)_{0.5}]\cdot 2DMA$, **2** und $[Co_2(EtBCP)_2(DABCO)_{0.5}]\cdot 2DMA$, **3** ($H_2EtBCP$ = *O*-Ethyl-P-(4-carboxyphenyl)phosphonsäure, DABCO = Diazabicyclo[2.2.2]octan) synthetisiert. Die Strukturen sind basieren auf kettenförmigen Monoethylphosphonat-$\{M_2(PO_2(OEt))_2\}_n$ SBUs und auf DABCO-expandierten archetypischen Schaufelrad-Carboxylat-$\{M_2(COO)_4(DABCO)\}$ Einheiten. Das resultierende Netzwerk kann als ein kubisch primitives Netz, **pcu** interpretiert werden, in dem die Phosphonat-Monoester- und die Carboxylat-SBU-Fragmente 6-c Knoten bilden. Diese strukturelle Organisation bedingt, gegenüber der DABCO-freien Vorläuferverbindung $[Zn_2(EtBCP)_2(Solv)]\cdot(Solv')$, **1**, eine hohe thermische Belastbarkeit sowie eine Stabilität gegen Luftfeuchtigkeit, Wasserdampf und Lösungsmitteln wie Chloroform, Ethanol und Aceton. Darüber hinaus, weisen die aktivierten MOFs signifikante CO_2-Aufnahmen von 115 $cm^3\ g^{-1}$ für **2'** und 128 $cm^3\ g^{-1}$ für **3'** bei 1 bar und 195 K auf (**'** steht für die aktivierte Probe), was eine Schätzung der Langmuir Oberfläche auf

330 m^2 g^{-1} für **2'** und 327 m^2 g^{-1} für **3'** ermöglichte. Die Verbindungen zeigen interessanterweise einen zweistufigen Adsorptionsprofil vom Typ-FI für CO_2 bei 195 K, welches auf eine strukturelle Flexibilität zurückzuführen ist.

Short Summary

Metal-organic frameworks (MOFs) are porous materials, which have been considered to be promising candidates for a diversity of potential applications such as gas storage and separation, catalysis and sensor technology. Because of their structural versatility and functional adaptability, they have turned into a field of considerable interest in science and research. So far, the performance of MOFs, which are particularly based on carboxylate ligands, has been adapted and increased using various functionalization strategies such as the synthesis of open metal sites, the introduction of functional groups or isoreticular chemistry. A promising research field is the development of new MOFs based on organophosphonate ligands, which enables access to chemically and thermally stable materials. The use of tridentate phosphonic acids ($–PO_3H_2$) is extremely interesting for the synthesis of MOFs, as they can form strong bonds and diverse coordination modes with metals. However, metalphosphonates are usually weakly crystalline compared to the conventional (carboxylate derived) highly crystalline MOFs, which complicates their structural characterization. Moreover, the high binding affinity of organophosphonic acids typically leads to the formation of layered structures, with low or no porosity.

The use of bidentate monoalkylphosphonate ligands for the targeted synthesis of crystalline network structures is the focus of this work and deals with the characterization and application potential of these materials. The research was inspired by strategies such as the use of bifunctional monoalkylphosphonates, their possible synergistic combination with the carboxylate functions in one ligand and the use of N-donor-co-ligands. This work focuses on the synthesis of two isostructural monoethylphosphonate-carboxylate MOFs: $[Zn_2(EtBCP)_2(DABCO)_{0.5}]\cdot 2DMA$, **2** and $[Co_2(EtBCP)_2(DABCO)_{0.5}]\cdot 2DMA$, **3** ($H_2EtBCP$ = *O*-ethyl-P-(4-carboxyphenyl)phosphonic acid, DABCO = diazabicyclo[2.2.2]octane). The structures are based on the chain-shaped monoethylphosphonate-$\{M_2(PO_2(OEt))_2\}_n$ SBUs, and on DABCO-expanded archetypal paddle-wheel carboxylate units $\{M_2(COO)_4(DABCO)\}$. The resulting network can be interpreted as a primitive cubic network, **pcu**, in which the phosphonate monoester and carboxylate SBU fragments form 6-c nodes. This structural organization requires (compared to the DABCO-free precursor compound $[Zn_2(EtBCP)_2(Solv)]\cdot(Solv')$, **1**) high thermal resistance and stability against air humidity, water vapor and solvents such as chloroform, ethanol and acetone. In addition, both activated MOFs display significant CO_2 uptakes of 115 $cm^3\ g^{-1}$ for **2'** and 128 $cm^3\ g^{-1}$ for **3'** at 1 bar and 195 K (**'** stands for the activated sample), which gives an estimate of the Langmuir surface area of 330 $m^2\ g^{-1}$ for **2'** and 327 $m^2\ g^{-1}$ for **3'**. Interestingly, the compounds show a two-step type F-I adsorption profile for CO_2 at 195 K, which is attributed to the structural flexibility.

Publikationsliste

Anna Goldman, Katharina Nardin, Simon-Patrick Höfert, Simon Millan and Christoph Janiak: „*Two-dimensional Cobalt-Carboxylate Framework with Hourglass Trinuclear* $Co_3(COO)_6(DMA)_3$ *Secondary Building Unit*"
Z. Anorg. Allg. Chem., 2018, **644**, 1387–1392. DOI: 10.1002/zaac.201800330.

Anna Goldman, Beatriz Gil-Hernández, Simon Millan, Serkan Gökpinar, Christian Heering, Ishtvan Boldog and Christoph Janiak: „*Flexible bifunctional monoethylphosphonate/ carboxylates of Zn(II) and Co(II) reinforced with DABCO co-ligand: paradigmatic structural organization with* ***pcu*** *topology*"
CrystEngComm, 2020, **22**, 2933–2944. DOI: 10.1039/D0CE00275E

Ülkü Kökçam-Demir,[‡] Anna Goldman,[‡] Leili Esrafili, Maniya Gharib, Ali Morsali,[‡] Oliver Weingartc and Christoph Janiak[‡]: „*Coordinatively unsaturated metal sites (open metal sites) in metal–organic frameworks: design and applications*"
Chem. Soc. Rev., 2020, **49**, 2751–2798. DOI: 10.1039/C9CS00609E

Abkürzungsverzeichnis

CALF	Calgary Framework
HKUST	Hong Kong University of Science and Technology
ip	intermediate pore
IRMOFs	Isoreticular MOFs
lp	large pore
MIL	Material of Institute Lavoisier
MOFs	Metal-organic frameworks
np	narrow pore
OMS	open metal sites
RCSR	Reticular Chemistry Structure Resource
SBU	Secondary Building Unit
SPCs	Soft porous crystals

Liganden

ADI	Adiponitril
BIPY	4,4‘-Bipyridin
BME-BDC^{2-}	2,5-Bis(2-Methoxyethoxy)-1,4-benzoldicarboxylat
DABCO	Diazabicyclo[2.2.2]octan
H_4ATC	Adamantan-1,3,5,7-tetracarbonsäure
H_2BDC	Benzol-1,4-dicarbonsäure
BIM	Bis(1*H*-imidazol-1-yl)methan
H_4BPBMP	*N,N'*-Bipiperidinbis(methylenephosphonsäure)
H_2BPDP	4'-Biphenyldiphosphonatbis(monoethylester)
H_3Isa-az-dmpz	5-(4-(3,5-Dimethyl-1*H*-pyrazolyl)azo)isophthalsäure
H_4PBM	*N,N'*-Piperazindi(methylenphosphonsäure)
$H_3{}^i$PrBTP	1,3,5-Benzoltriphosphonatmonoisopropylester
Me_2/Et_2BDP^{2-}	1,4-Benzoldiphosphonatbis(mono(methyl/ethyl)ester)
TCTPM	4,4',4",4"'-Tetracyanotetraphenylmethan
TIB	1,3,5-Tri(1*H*-imidazol-1-yl)benzol

Topologien

dia	Diamant (engl. diamond)
pcu	primitives kubisches Netz (engl. primitive cubic net)
pts	Platin(II)-sulfid (engl. platinum(II) sulfide)
rtl	Rutil (engl. rutile)

sql	quadratisches Gitter (engl. square lattice)
tbo	verdrehtes Boracit (engl. twisted boracite)

Inhaltsverzeichnis

Kurzzusammenfassung I

Short Summary III

Publikationsliste IV

Abkürzungsverzeichnis V

1 Einleitung 1

1.1 Metall-organische Gerüstverbindungen 1

1.2 Koordinationspolymere und Metall-organische Gerüstverbindungen auf der Basis von Phosphonat- und Phosphonatemonoester-Liganden 14

2 Zielsetzung und Motivation 20

3 Kumulativer Teil 22

3.1 Flexible bifunctional monoethylphosphonate/ carboxylates of Zn(II) and Co(II) reinforced with DABCO co-ligand: paradigmatic structural organization with pcu topology 23

3.1. Coordinatively unsaturated metal sites (open metal sites) in metal–organic frameworks: design and applications 86

3.2. Two-dimensional Cobalt-Carboxylate Framework with Hourglass Trinuclear $Co_3(COO)_6(DMA)_3$ Secondary Building Unit 198

4 Zusammenfassung und Ausblick 216

5 Literaturverzeichnis 220

1 Einleitung

1.1 Metall-organische Gerüstverbindungen

Metall-organische Gerüstverbindungen (engl. metal-organic frameworks, MOFs) haben in den letzten zwei Jahrzehnten ein hohes wissenschaftliches Interesse geweckt und es wurden große Erwartungen in die Optimierung sowie Weiterentwicklung dieser Materialien gesetzt. Der Begriff MOF wurde 1995 von Yaghi[1] eingeführt und definiert die Verknüpfung von anorganischen (mehrkernige Cluster, unendliche Ketten) und organischen Bausteinen (Liganden, Linker) zu kristallinen Netzwerkstrukturen. Nach der IUPAC werden MOFs als zwei- und dreidimensionale (2D und 3D) Koordinationsnetzwerke mit potentieller Porosität definiert.[2,3] Das Gebiet der synthetischen Metall-organischen Gerüstverbindungen findet ihren Ursprung in der klassischen Koordinationschemie und reicht bis in das 18. Jahrhundert zurück. Den Grundstein setzte Alfred Werner in seinen Arbeiten zum Verständnis der Konstruktion von Übergangsmetallkomplexen der Zusammensetzung $[Co(NH_3)_6]Cl_3$, $[Co(NH_3)_5Cl]Cl_2$ und $[Co(NH_3)_4Cl_2]Cl$.[4] Spätere Arbeiten zeigten, dass Werner-Komplexe der Zusammensetzung $[M(4\text{-Methylpyridin})_4(SCN)_2]$ ($M = Co^{2+}$, Ni^{2+} und Mn^{2+}) (Abbildung 1), eine Zugänglichkeit für Gase in den winzigen Spalten innerhalb ihrer Kristallstruktur aufweisen, jedoch infolge von wiederholten Sorptionszyklen, eine nicht poröse Anordnung annehmen.[5] Frühe bekannte Vertreter, die später als anorganische Koordinationspolymere mit offenen Hohlräumen verstanden wurden, sind die Metall-Cyanid Netzwerke Berliner Blau und die Hofmann Clathrate (Abbildung 1 b, c).[6,7,8]

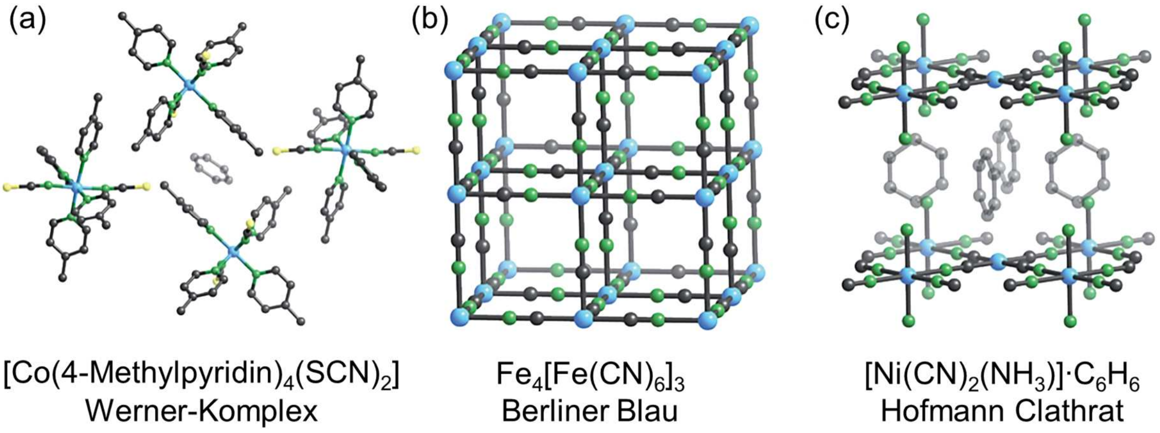

Abbildung 1 Darstellung der Kristallstrukturen eines porösen Werner-Komplexes (a) sowie der Metall-Cyanid-Koordinationsverbindungen Berliner Blau (b) und Hofmann Clathrat (c). Abbildung wurde reproduziert aus der Literatur 9 mit Genehmigung von the Royal Society of Chemistry 2017.

Das Hofmann Clathrat mit der Zusammensetzung $[Ni(CN)_2(NH_3)]\cdot C_6H_6$ wurde erstmals im Jahre 1897 literaturbekannt, während dessen Kristallstruktur von Rayner und Powell im Jahre 1952 mittels Einkristall-Röntgenstrukturanalyse aufgeklärt wurde.[6,10] Die Struktur basiert auf 2D-Schichten aus alternierenden oktaedrischen und quadratisch planaren Ni^{2+}-Ionen, die über CN^--Ionen miteinander verbunden sind (Abbildung 1 c). Terminale Ammoniakliganden ragen in Richtung der benachbarten Schichten, wodurch Hohlräume entstehen, die mit dem Syntheselösungsmittel z.B. Benzol gefüllt sind. Spätere Arbeiten zeigten, dass die 2D-Schichten durch Diaminoalkane zu 3D erweiterten Netzwerken verknüpft werden können.[11,12,13] Die ersten Koordinationsnetzwerke, wurden durch die Koordination von ditopischen Alkylnitril-Liganden an Cu^+ Ionen erhalten.[14,15,16] Hierzu gehört das von Saito synthetisierte $[Cu(ADI)_2](NO_3)]$ (ADI = Adiponitril) dessen 3D-Struktur auf dem Diamant Netzwerk (**dia**) basiert (Abbildung 2).[16]

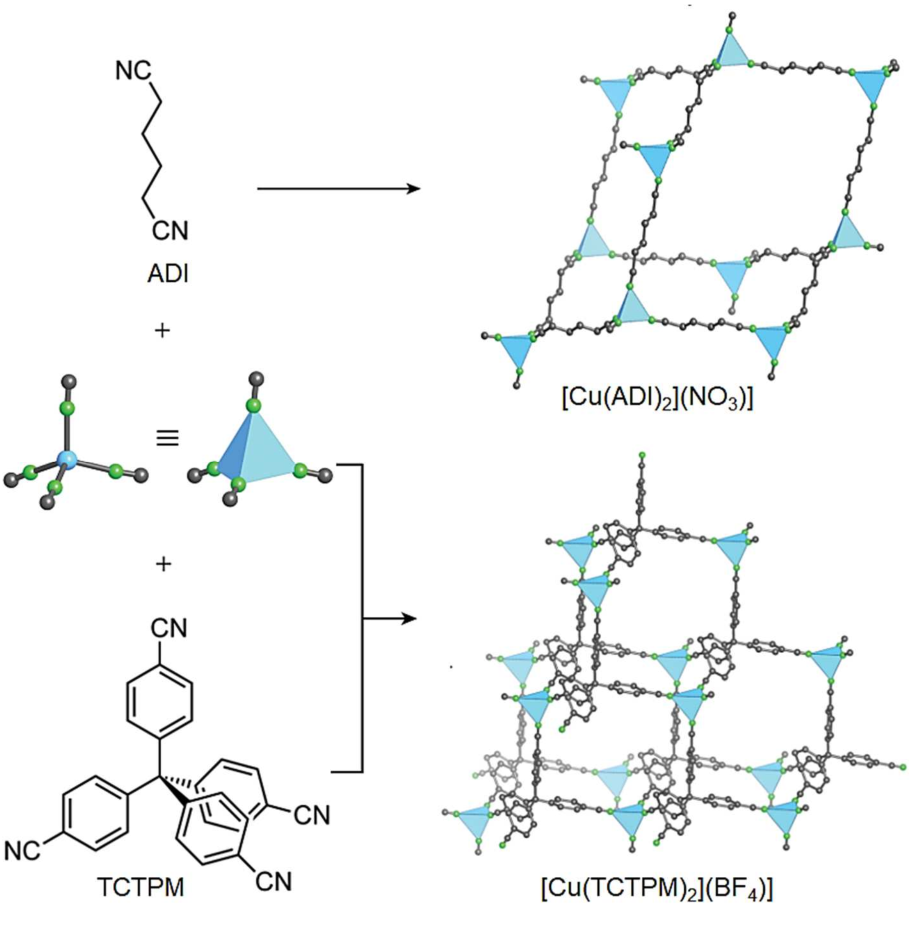

Abbildung 2 Kristallstrukturen der kationischen Koordinationsnetzwerke mit **dia**-Topologie: $[Cu(ADI)_2](NO_3)]$, basierend auf Cu^+ Ionen mit einer tetraedrischen Koordinationsumgebung und dem linearen ADI-Linker; und $[Cu(TCTPM)](BF_4)]$, Cu^+ Ionen mit einer tetraedrischen Koordinationsumgebung und dem tetraedrischen TCTPM-Linker. Abbildung wurde reproduziert aus der Literatur 17 mit Genehmigung von John Wiley and Sons 2019.

Theoretisch könnte gemäß der üblichen Koordinationszahlen eines gegebenen Metallions und der Ligand-Stöchiometrie eine bestimmte Geometrie des resultierenden Netzwerks auf die bevorzugte Koordinationszahl und -umgebung des Metalls abgestimmt werden. Die Vorhersagbarkeit der Struktur eines bestimmten Netzwerks wird jedoch aufgrund der unterschiedlichen strukturellen und geometrischen Aspekte der primären Bausteine (Metallsalze und organische Liganden) und der Vielzahl an möglichen Kombinationen, erschwert. Die topologische Klassifikation von Koordinationsnetzwerken mit dem „Knoten-Verbindungs“-Ansatz („node and pacer“) geht auf die Arbeiten von A. F. Wells zur Interpretation anorganischer Festkörper als Netzwerkstrukturen zurück und beruht auf Geometrieprinzipien der Komplexchemie.[18,19] Kristallstrukturen werden hier vereinfacht in Form von Netzen, aus Metallionen (Knoten) und linearen Linkern (spacer) beschrieben.[20] Für die Nomenklatur der Netz-Topologien verwendet man Buchstabencodes, welche häufig im Zusammenhang mit der spezifischen Topologie für natürlich vorkommende Mineralien stehen (z. B. Diamant, **dia**; Platin(II)-sulfid**, pts**; Rutil, **rtl**) oder willkürlich vergeben werden können. In der von O’Keeffe und Yaghi zusammengestellten Reticular Chemistry Structure Resource (RCSR) Datenbank, sind Netz-Topologien hinterlegt.[21] Die Ableitung der Netzwerktopologie erfolgt durch die Zerlegung des Netzes in Eckpunkte und Kanten (Knoten und Linker), die anhand der Anzahl ihrer Ausdehnungspunkte unterschieden werden. Das archetypische **dia**-Netz in $[Cu(ADI)_2](NO_3)]$ resultiert aus der Verknüpfung der tetraedrischen Kupferatomen als 4-fach verknüpfende Knotenpunkte durch die linearen ditopen ADI Linker (Abbildung 2). In den frühen neunziger Jahren wurde der „Knoten-Verbindungs“-Ansatz durch Robson *et al*. zur gezielten Erzeugung bzw. Beschreibung von Koordinationspolymeren entwickelt.[22,23,24,25,26] Robson und Hoskins zeigten beispielsweise, dass die Verknüpfung von tetraedrischen Kupferatomen mit dem tetraedrischen Linker 4,4',4'',4'''-Tetracyanotetraphenylmethan (TCTPM) ein Koordinationsnetzwerk der Zusammensetzung $[Cu(TCTPM)](BF_4)]$ ergibt, welches auf einem **dia**-Netz basiert (Abbildung 2). Ist die stabilste Koordinationsumgebung eines Metalls ein Oktaeder, so ist die Ausbildung eines Gitters mit quadratischen oder oktaedrischen Knoten wahrscheinlich. Hierzu gehören die frühen Koordinationsnetzwerke mit 4,4‘-Bipyridin (BIPY) wie $[Cd(BIPY)_2(NO_3)_2]$[27] mit einem 2D quadratischen **sql**-Netz (**sql** = square lattice) und $[Zn(BIPY)_2(SiF_6)]$,[28] welches auf einem 3D **pcu**-Netz (**pcu** = primitive cubic net) basiert.

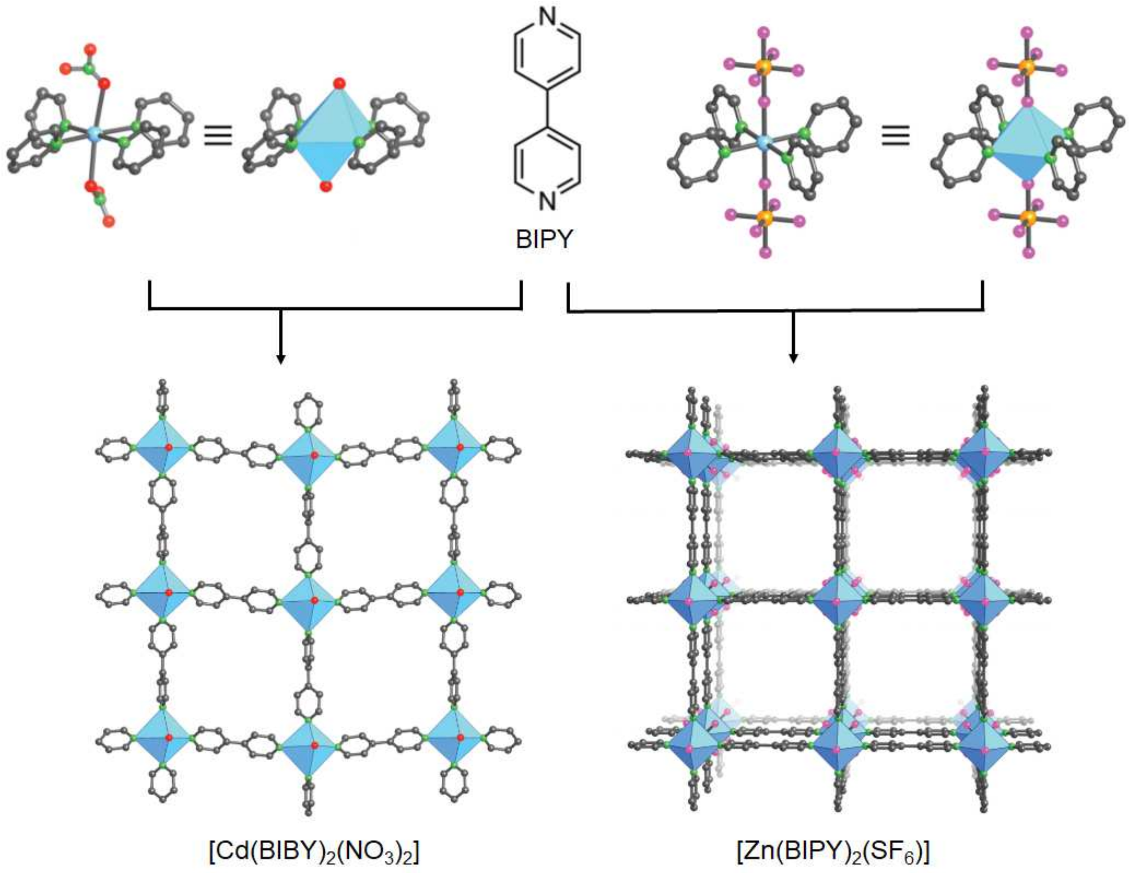

Abbildung 3 Kristallstrukturen der Koordinationsnetzwerke [Cd(BIPY)$_2$(NO$_3$)] mit **sql**-Topologie und [[Zn(BIPY)$_2$(SiF$_6$)], mit **pcu**-Topologie. Die Umsetzung von Cd^{2+}-Ionen mit BIBY resultiert in einer erweiterten quadratischen Gitterstruktur (**sql**) der Formel [Cd(BIPY)$_2$(NO$_3$)]. In SIF-6 werden die oktaedrisch koordinierten Zn^{2+}-Ionen mit BIPY zu 2D-**sql**-Schichten verbunden. Diese Schichten werden mit SiF$_6$ zu einem ladungsneutralen 3D-**pcu**-Netzwerk verknüpft. Abbildung wurde reproduziert aus der Literatur 17 mit Genehmigung von John Wiley and Sons 2019.

Darauf anschließend wurde von O'Keefe und Yaghi ein neues Teilgebiet der Chemie, die sogenannte retikuläre Chemie (reticular chemistry) eingeführt.[29,30] Der Begriff "retikulär" leitet sich vom lateinischen "reticulum" ab und bedeutet "die Form eines Netzes haben" oder "netzartig". Grundlage der retikulären Chemie ist die Untersuchung der Verknüpfung diskreter chemischer Baueinheiten (organische Liganden und Metall-Cluster), die durch relativ starke Bindungen ausgedehnte Strukturen ausbilden.[31]

Das Fortschreiten der MOF-Chemie führte zu Materialien höherer Komplexität und Funktionalität. Die Zusammensetzung von MOFs steht im Zusammenhang mit hochsymmetrischen sekundären Baueinheiten (Secondary Building Units, SBUs) in Form von Metallclustern, welche infolge ihrer Ausdehnungspunkte durch die Verknüpfung mit organischen Liganden ausgedehnte Netzwerke ausbilden. Die SBU-Geometrie und Konnektivität ihrer Ausdehnungspunkte setzt die Basis für die Beschreibung des resultierenden Netzwerks.[32,33,34,35] Für die Beschreibung der Gerüsttopologie wird das Netz in seine molekularen Bausteine zerlegt. Die Zusammensetzung eines bestimmten Bausteins kann in Form von Metallclustern, -komplexen oder rigiden Liganden auftreten, wobei die SBU eine aus diesen Bausteinen resultierende Geometrie und Konnektivität ihrer Ausdehnungspunkte reflektiert. Die gängigsten MOFs basieren auf Metall-Carboxylat-Clustern. Eine große Vielfalt an MOF-Netzwerken beruht auf der zweikernigen $\{M_2(CO_2)_4\}$ paddle-wheel-SBU, die vier Ausdehnungspunkte (4-c; Bezeichnung -c = Koordination des jeweiligen Clusters) enthält und mit einer Vielzahl von multiplen Linkern unterschiedlicher Länge und Geometrie verknüpft werden kann (Abbildung 4).[36]

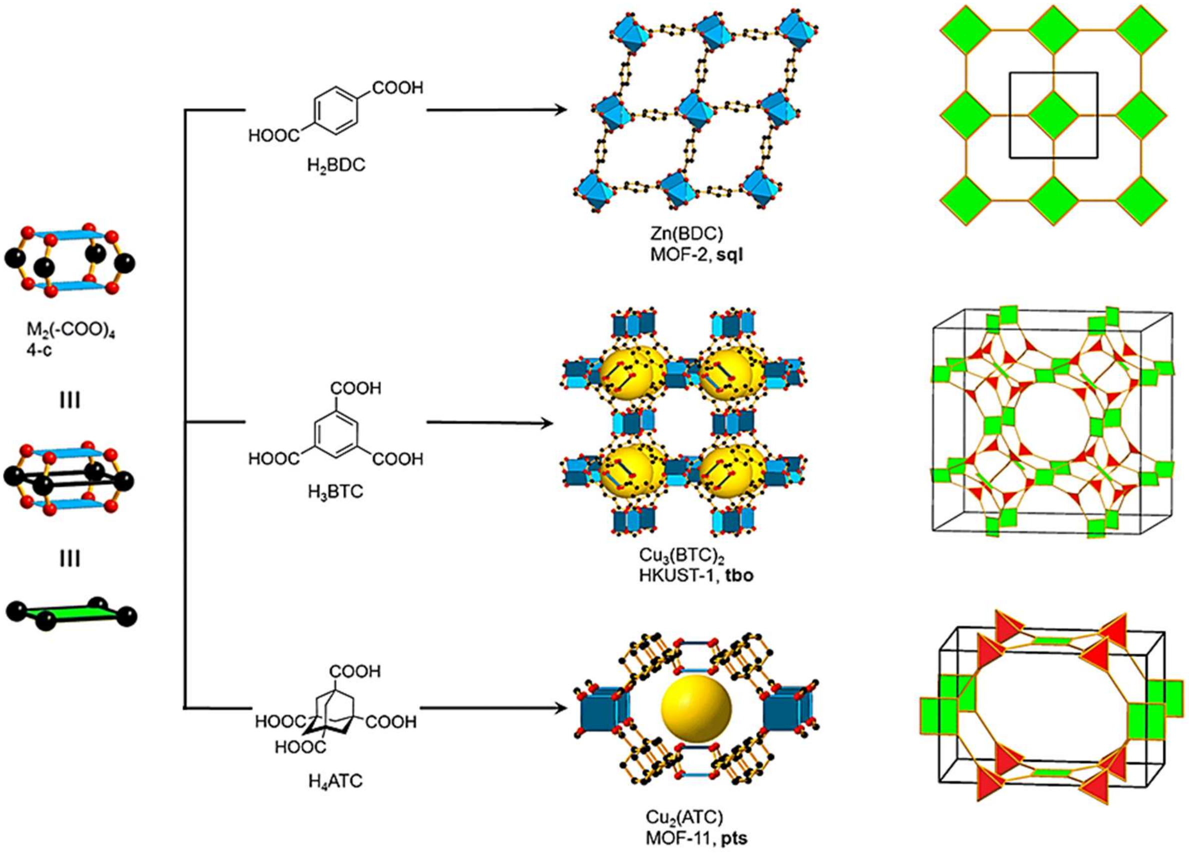

Abbildung 4 MOFs auf Basis von quadratischen paddle-wheel-SBUs. Abbildung wurde reproduziert aus der Literaturquelle 36 mit Genehmigung von Springer Nature Switzerland AG 2020.

MOF-2, Zn(BDC)(H_2O) (H_2BDC = Benzol-1,4-dicarbonsäure) besteht aus $\{M_2(CO_2)_4\}$ paddle-wheel-SBUs die in Verbindung mit linearen, ditopischen BDC^{2-}-Linkern ein 2D quadratisches Gitter mit der 4-c **sql**-Topologie ausbilden.[37] HKUST-1 (HKUST = Hong Kong University of Science and Technology), $[Cu_3(btc)_2(L^A)_2]$ (L^A = apikaler Ligand, (H_2O, DMA, etc.)) basiert auf einem 3D kubischen Netz mit der (3,4)-c **tbo**-Topologie (**tbo** = twisted boracite). Der 3-c Knoten entspricht der trigonalen Geometrie der BTC-Einheit (Abbildung 5).

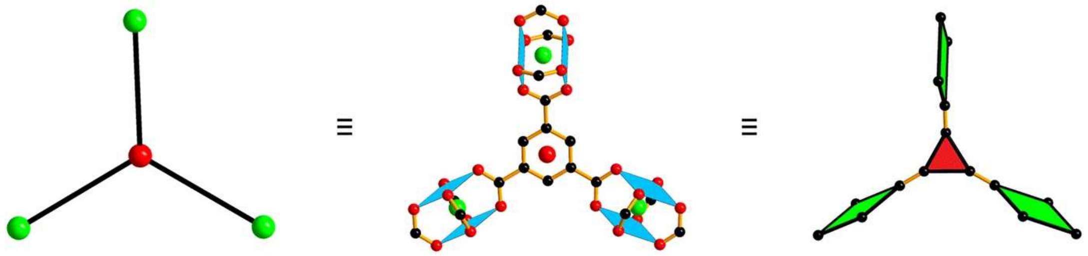

Abbildung 5 Dekonstruktionsansatz von HKUST-1. $Cu_2(\text{-}COO)_4$-Cluster repräsentieren quadratische planare SBUs und BTC Linker repräsentieren dreieckige SBUs. Abbildung wurde reproduziert aus der Literaturquelle 36 mit Genehmigung von Springer Nature Switzerland AG 2020.

$Cu_2(ATC)$, MOF-11 (H_4ATC = Adamantan-1,3,5,7-tetracarbonsäure) kristallisiert in einer binodalen 4-c **pts**-Topologie. Die binodale **pts**-Topologie basiert auf der Verknüpfung von quadratischen $\{M_2(CO_2)_4\}$ und tetraedrischen ATC^{4-} 4-c sekundären Baueinheiten.[38] Die oktaedrische Geometrie und Struktur von basischem Zinkacetat findet sich in der 6-c $\{Zn_4O(CO_2)_6\}$ SBU des prototypischen $Zn_4O(BDC)_3$, MOF-5, wieder. Die SBU basiert auf Zn_4O-Tetraedern, deren Kanten über sechs Carboxylat-Linker verbunden sind. Die Verknüpfung dieser oktaedrischen SBU mit BDC^{2-} ergibt die 6-c **pcu**-Topologie (Abbildung 6).

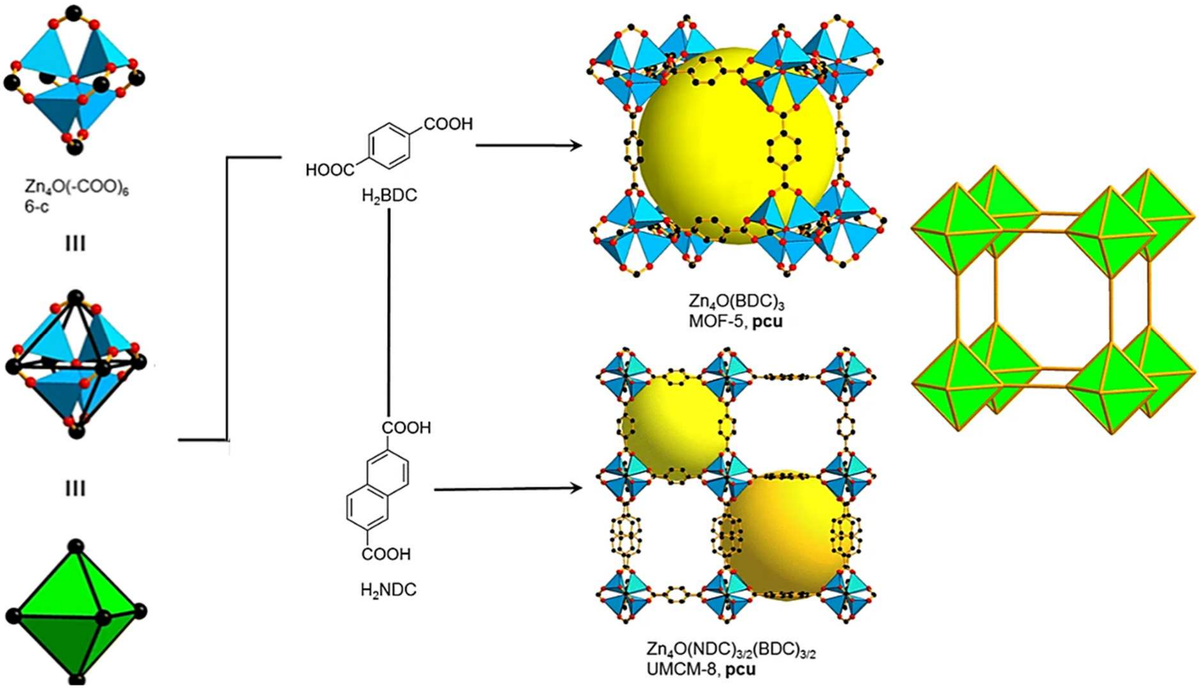

Abbildung 6 Beispiele für MOFs auf der Basis von MOFs, konstruiert aus 6-c $Zn_4O(CO_2)_6$ SBUs. Abbildung wurde reproduziert aus der Literaturquelle 36 mit Genehmigung von Springer Nature Switzerland AG 2020.

Das Konzept der retikulären Chemie wurde auf die Struktur von MOF-5 zur Synthese von einer Serie von isoretikulären (gleiche Netz-Topologie) Verbindungen den sogenannten IRMOFs (isoreticular MOFs) angewandt.[39,40,41] So konnte beispielsweise durch Verlängerung des Linkers die Porengröße unter Erhalt der **pcu**-Netzwerktopologie systematisch variiert und auf spezifische Eigenschaften angepasst werden oder durch die Einführung von funktionellen Gruppen höhere Selektivitäten für CO_2 erzielt werden.[30,39,42] Des Weiteren wurde gezeigt, dass gemischt-Ligandensysteme unterschiedlicher Länge zur Herstellung neuer Verbindungen unter Beibehaltung der Netzwerktopologie eingesetzt werden können (Abbildung 6). Die strukturelle Vielseitigkeit und die funktionelle Abstimmbarkeit ist ein entscheidendes Merkmal von MOFs und zeichnet diese gegenüber anderen porösen Materialklassen, wie den Zeolithen und porösen kohlenstoffbasierten Materialien aus.[43,44,45] Die MOF-Kristallchemie bietet somit die Möglichkeit, durch eine Vorauswahl der molekularen Bausteine oder durch postsynthetische Modifikation gewünschte Eigenschaften gezielter abzustimmen. Daher gelten MOFs als vielversprechende Kandidaten, die spezifisch für eine Fülle potentieller Anwendungen unter anderem Gassorption[46], einschließlich Gastrennung[47] und -speicherung sowie Katalyse[48], Sensorik, optische Anwendungen und Wärmetransformation hergestellt und moduliert werden können.[9]

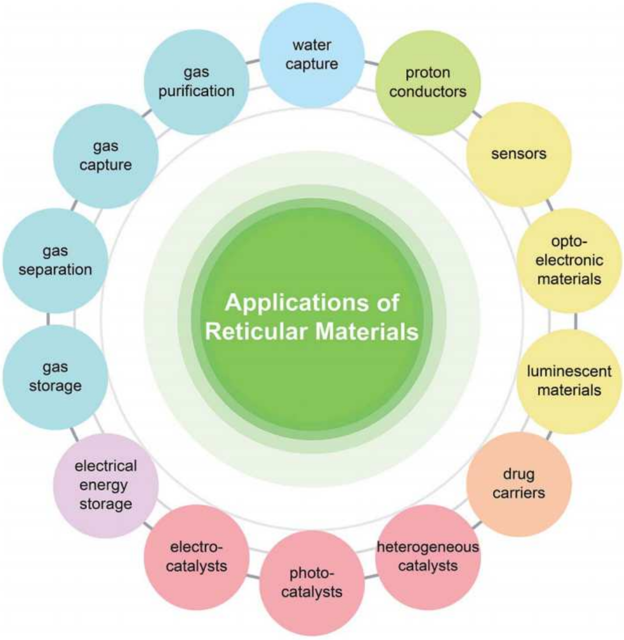

Abbildung 7 Übersicht über potentielle Anwendungen von Metall-organischen Gerüstverbindungen. Darstellung wurde entnommen aus Literatur 9 mit Genehmigung von Royal Society of Chemistry 2017.

Bei der Synthese von MOFs können neben den organischen Liganden auch insbesondere Lösungsmittelmoleküle die Koordinationsumgebung der Metallionen in den Clustern vervollständigen. Diese können durch ein geeignetes Aktivierungsprotokoll analog zu dem in den Poren eingelagerten Gastmolekülen häufig unter Erhaltung der Struktur entfernt werden und zur Generierung sogenannter offenen Metallstellen (open metal sites, OMS) dienen. Die

Erzeugung von OMS ist eine attraktive Strategie um die Affinität zu H_2, CO_2, CO, NO und C_2H_2 zu erhöhen. Das Vorhandensein von OMS in MOFs führt zu verstärkten Wechselwirkungen zwischen der OMS als freie Koordinationsstelle am Metall und den Gastmolekülen, wodurch sie als primäre Adsorptionsstelle fungiert und zu hohen Adsorptionswärmen (Q_{st}) führt. Dementsprechend gehören MOFs mit OMS zu den vielversprechenden Adsorbenzien zur selektiven Entfernung von CO_2 aus trockenen Gasgemischen und werden als hochaktive Lewis-Säure-Katalysatoren beschrieben.[49,50,51,52] Offene Metallstellen in MOFs können durch die Entfernung von labilen terminalen Liganden, typischerweise Lösungsmittelmolekülen, aus den gesättigten Metallzentren generiert werden. Die Ligandenentfernung kann durch thermische, chemische oder photothermische Aktivierung erfolgen. Voraussetzung für das Vorhandensein einer offenen Metallstelle ist, dass die MOF-Struktur nach der Aktivierung nicht kollabiert und ihre Kristallinität und Porosität beibehält. Beispielsweise werden in HKUST-1 und MOF-11 durch die Entfernung, der an den apikalen Positionen der Cu-paddle-wheel-SBU koordinierenden Wasser Moleküle, offene Metallstellen erhalten. Die zu HKUST-1 isostrukturelle Verbindung $[Zn_3(btc)_2(L^A)_2]$ geht infolge des Aktivierungsprozesses (thermische Aktivierung bei 180°C) in eine amorphe Phase über.[53] Dieses Phänomen kann auf die potentiell ungünstige Transformation der Koordinationsgeometrie von Zn^{2+} beim Entfernen axial koordinierender Lösungsmittelmoleküle von quadratisch pyramidal zu einer ungünstigen quadratisch planaren Geometrie zurückgeführt werden. Die einfache Entfernung der apikalen Liganden und die Stabilität der Cu^{2+}-OMS sind durch die schwächere Bindung in Form längerer apikaler Metall-Ligand-Bindungen des quadratisch-pyramidalen d^9-Ions mit der Kombination der potentiellen Stabilisierung der quadratisch-planaren Geometrie zurückzuführen.

Die Speicherung und Trennung eines gewünschten Gases zählen zu den fundamentalen Eigenschaften von porösen Materialien. Zahlreiche Studien konzentrieren sich seit Ende des 20. Jahrhinderts auf die Synthese von starren MOFs, um eine permanente Porosität zu erreichen. Im Allgemeinen versteht man unter permanenter Porosität, dass mindestens eine Kristallphase für Gastmoleküle zugänglich und die Gasadsorption reproduzierbar ist.[61] Hinsichtlich des aktivierten Zustandes, klassifizierten Kitagaewa *et al.* poröse Koordinationspolymere in drei Generationen.[54,55] Materialien der ersten Generation weisen keine dauerhafte Porosität auf, ihr Gerüst bricht nach dem Entfernen von Gastmolekülen zusammen. Materialien der zweiten Generation basieren auf robusten Gerüsten und behalten ihre ursprüngliche potentiell poröse Struktur auch nach der Gastmolekülentfernung bei und können folglich Gastmoleküle reversibel aufnehmen und wieder abgeben. Diese starren porösen Feststoffe haben sich insbesondere dadurch etabliert, dass sie eine große Menge an Gastmolekülen adsorbieren können.[56] Kitagawa *et al.* definierten Materialien der dritten Generation als weiche poröse Kristalle (soft porous crystals, SPCs), welche ein flexibles oder dynamisches Verhalten der Gerüste aufweisen sollten. Nachfolgende Arbeiten von Férey und

Kitagawa *et al.* zu flexiblen MOFs, weckten ein großes Interesse in der Synthese und Erforschung dieser Materialien.[57,58] Die Gerüste von flexiblen MOFs unterliegen unter anderem verhältnismäßig schwachen supramolekularen (wie z.B. Wasserstoffbrücken-, π-π-) oder Koordinationswechselwirkungen, was zu einer erhöhten Anzahl intermolekularer Freiheitsgrade führt.[59,60] Die Flexibilität von MOFs, beruht auf einer reversiblen Transformierbarkeit der Gerüststruktur,welche sich durch Beibehaltung der Verknüpfungen trotz Phasenänderungen auszeichnet.[61] Zum einen kann die Phasenumwandlung unter Beibehaltung des kristallinen Zustandes erfolgen, zum anderen kann die Kristallinität eines MOFs während der Phasenumwandlung abnehmen. Das letztere Phänomen wird dadurch erklärt, dass die Fernordnung des Gerüsts verloren geht, ohne dass das Netzwerk zusammenbricht bzw. in eine amorphe Phase übergeht. Dieses dynamische Merkmal von porösen Kristallen wird durch externe Reize, wie Temperatur, Druck, Gastadsorption/-desorption, sowie mechanische oder photochemische Einflüsse ausgelöst.[61,62,63] Unter den geeigneten Bedingungen kann somit eine hohe selektive Aufnahme von Gastmolekülen erzielt werden.[64] Im Jahre 2005 stellte Kitagawa *et al.* eine Beziehung zwischen dem dynamischen Porenverhalten in Abhängigkeit von der Anwesenheit und Abwesenheit von Gastmolekülen her.[65] Im Allgemeinen unterscheidet man zwischen den Poren, welche während der Aufnahme oder dem Austausch von Gastmolekülen eine Verformung aufweisen, wobei die strukturelle Topologie des Gerüstes erhalten bleibt und Poren, welche infolge der Gastadsorption eine strukturelle Transformation von einer geschlossenen in eine offenere Form durchlaufen. Zu den Letzteren gehören MOFs mit den sogenannten „atmenden Poren“ („breathing pores“).[59] Fischer *et al.* beschrieben den Effekt der „Atmung“ als eine Verschiebung von Atomen des Gerüstes, welche mit einer Änderung des Einheitsvolumens begleitet wird.[62] Die unterschiedlichen Phasen (np = narrow pore, lp = large pore) können sich in den charakteristischen Abständen und Winkeln der Elementarzelle und den kristallographischen Raumgruppen unterscheiden. Eines der meist studierten MOFs mit „atmenden“ Eigenschaften ist das [M(X)][bdc], MIL-53(M), (M = Cr, Al, Fe, Ga, Sc, In; X = OH, F) (MIL = Material of Institute Lavoisier).[66,67,68,69,70,71,72,73] Die SBU in MIL-53 basiert auf eckenverknüpften Oktaedern (Abbildung 8 a). Jedes Metallatom ist äquatorial von vier Sauerstoffarmen der jeweils vier verschiedenen BDC^{2-}-Linkern umgeben, während die axial koordinierten Sauerstoffatome von μ_2-Hydroxylgruppen stammen. MIL-53 zeigt einen „Atmungseffekt“ bei Adsorption/Desorption von Gastmolekülen in bestimmten Temperaturbereichen (Abbildung 8 d, e). Die resultierende kristallographische Phasenänderung (Änderung der Gerüstgeometrie und der Porengröße) beruht dabei auf der O–O-Achse jeder Carboxylatgruppe, welche als „Kniescheibe“ mit Linkerrotation wirkt (Abbildung 8 b).[59]

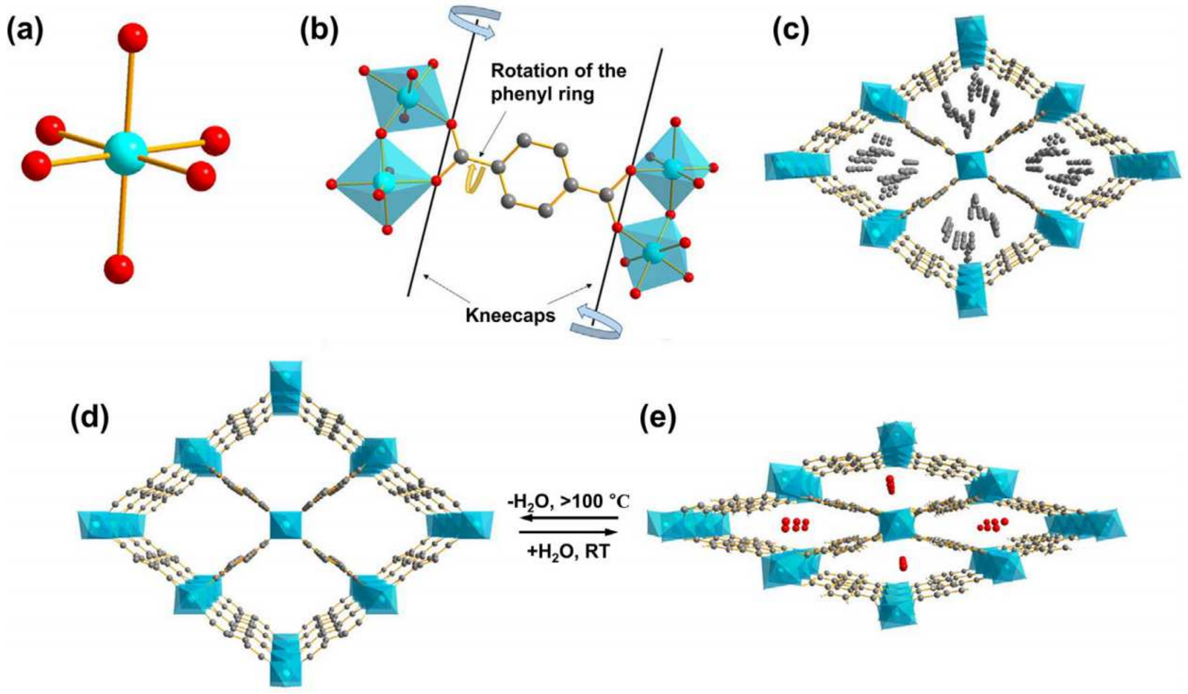

Abbildung 8 (a) Oktaedrische SBU von MIL-53; (b) schematische Darstellung der „kniescheibenartigen“ Bewegung mit Rotation des Phenylrings, die für das Atemverhalten von MIL-53 verantwortlich ist. Die drei häufigsten Formen von MIL-53 (c) MIL-53-*as* (*as* = as-synthesised), (d) MIL-53-*ht* (*ht* = high-temperature), (e) MIL-53-*lt* (*lt* = low-temperature). Darstellung wurde entnommen aus der Literatur 59 mit Genehmigung von Elsevier B.V. 2019.

Gemischt-Liganden MOFs, die auf einer paddle-wheel-SBU basieren, wurden weitgehend hinsichtlich ihrer strukturellen Flexibilität untersucht.[74,75] Diese 3D MOFs bilden 2D-Gitter aus zweikernigen paddle-wheel-SBUs, welche über neutrale verbrückende Liganden, meistens N-Donor-Liganden verschiedener Länge, zu einem 3D-Gitter verbunden sind.[76,77] Im Gegensatz zu MIL-53, bei dem die SBU nicht aktiv am Atemprozess beteiligt ist, hat die paddle-wheel-SBU einen erheblichen Einfluss auf die Transformation des Gerüstes und ist von der verwendeten Metallquelle abhängig. Fischer *et al*. zeigten, dass die CO_2-Adsorptionsisotherme von $[M_2(BME\text{-}BDC)_2(DABCO)]$ (M = Zn, Co, Ni, Cu; $BME\text{-}BDC^{2-}$ = 2,5-bis(2-Methoxyethoxy)-1,4-benzoldicarboxylat; DABCO = Diazabicyclo[2.2.2]octan) bei 195 K in Abhängigkeit des Metallzentrums jeweils verschiedene Phasenübergänge aufweist (Abbildung 9 a).[78]

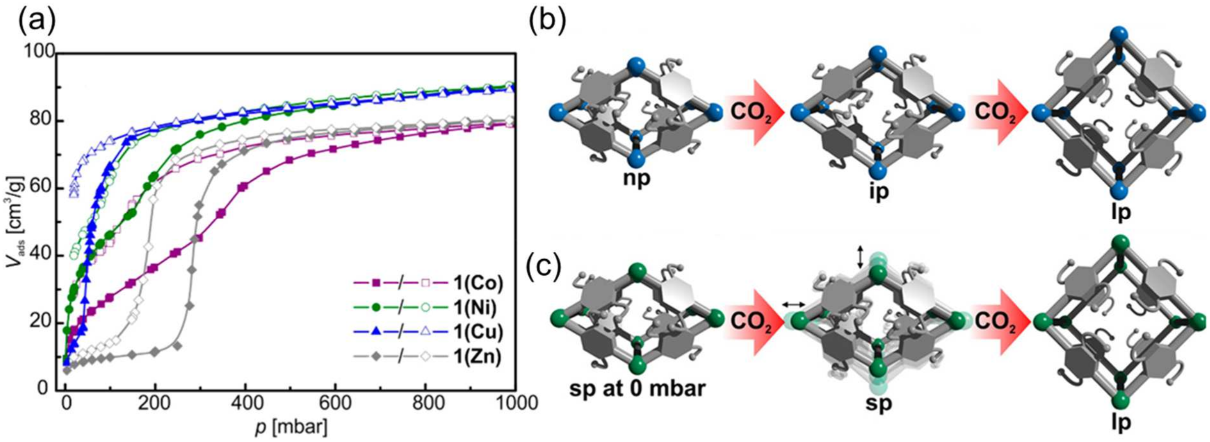

Abbildung 9 (a) CO_2 Adsorptions/Desorptions-Isothermen bei 195 K. Schematische Darstellung der verschiedenen Phasenübergänge in $M_2(BME\text{-}BDC)_2(DABCO)]$ für (b) M = Cu und Zn, (c) M = Co und Ni. Darstellung wurde reproduziert aus der Literatur 78 mit Genehmigung von American Chemical Society 2018.

Alle MOFs weisen CO_2-Isothermen mit einer signifikanten Hysterese auf, zeigen aber für das gegebene Metall einen unterschiedlichen Verlauf der Adsorptionsisotherme. Für $[Zn_2(BME\text{-}BDC)_2(DABCO)_n]$ und $[Cu_2(BME\text{-}BDC)_2(DABCO)]$ wurde eine S-förmige Isotherme mit einem steilen Anstieg beobachtet. Die Stufe bei 40 mbar für $[Cu_2(BME\text{-}BDC)_2(DABCO)]$ und 250 mbar für $[Zn_2(BME\text{-}BDC)_2(DABCO)]$ wurden dem Phasenübergang np → lp während der CO_2-Aufnahme zugeschrieben. Die Isothermen für $[Ni_2(BME\text{-}BDC)_2(DABCO)]$ und $[Co_2(BME\text{-}BDC)_2(DABCO)]$ zeigen einen nahezu gleichmäßigen Anstieg der Aufnahme über einen sehr weiten Druckbereich und die Steigung der Isotherme ist vergleichsweise flacher. Anhand von In-situ-Pulver-XRD-Messungen konnte gezeigt werden, dass die Verbindungen mit Zn und Cu während der CO_2-Adsorption einen Übergang von einer ausgeprägten engen, über eine mittlere (intermediate pore = ip) zu einer großen Pore durchlaufen (Abbildung 9 b). Die Verbindungen mit Ni und Co zeigen ein langsames Aufquellen (swell pore = sp) von der np-Phase zur lp-Phase (Abbildung 9 c). Es wurde beobachtet, dass die Größe der Porenkontraktion bei dem Übergang von einer lp-Phase zu einer np-Phase der Reihenfolge Co ≈ Zn > Ni > Cu folgt. Diese Tendenz kann den unterschiedlichen elektronischen Strukturen der Metallzentren zugeschrieben werden. Im Allgemeinen sind Verbindungen auf Cu-Basis im Vergleich zum Zn-, Ni- und Co-Analogon starrer. Für das Zn^{2+}-Ion (d^{10}) ist im Vergleich zum Cu^{2+}-Ion (d^9) eine höhere Verzerrung der Koordinationsumgebung zu erwarten. Um die Sorptionskapazität und spezifische Oberfläche eines porösen Materials zu ermitteln, werden experimentell Sorptionsisothermen aufgenommen, anhand derer poröse Materialien beschrieben und untereinander verglichen werden können. Nach IUPAC wurden hierfür Sorptionsklassifikationen aufgestellt, die für mikroporöse Materialien charakteristisch sind.[79] Beispielsweise kennzeichnet der Verlauf einer Typ-I-Adsorptionsisotherme starre poröse Materialien (Abbildung 10).

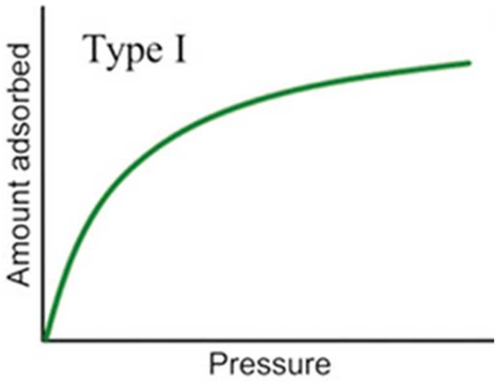

Abbildung 10 Profil einer Typ I Adsorptionsisotherme, die für starre mikroporöse MOFs charakteristisch ist. Darstellung wurde entnommen aus der Literatur 80 mit Genehmigung von John Wiley & Sons, Inc.1999-2020.

Infolge der Änderung ihrer Porengeometrie weisen die Adsorptionsisothermen von flexiblen Materialien einen S-förmigen bzw. stufenförmigen Verlauf auf und lassen sich nicht nach den klassischen Sorptionsklassifikationen einordnen. Eine Klassifizierung der Isothermen für flexible mikroporösen Materialien wurde im Jahre 2018 von Zaworotko *et al*. vorgeschlagen (Abbildung 11).[80] Demzufolge wird ein flexibles MOF, welches einer sukzessiven strukturellen Transformation von einer kleineren in eine größere Pore unterliegt („breathing“) mit einer Typ F-I-Isotherme gekennzeichnet. Wenn dieser Übergang plötzlich auftritt, spricht man von einer Typ F-II-Isotherme. Flexible Materialien welche einen allmählichen Übergang von einer nicht-porösen (geschlossenen) Phase zu einer porösen (offenen) Phase aufweisen („gate-opening“) werden durch eine Typ F-III-Isotherme charakterisiert. Eine Typ F-IV-Isotherme weist eine abrupte Aufnahme über einen engen Druckbereich auf.

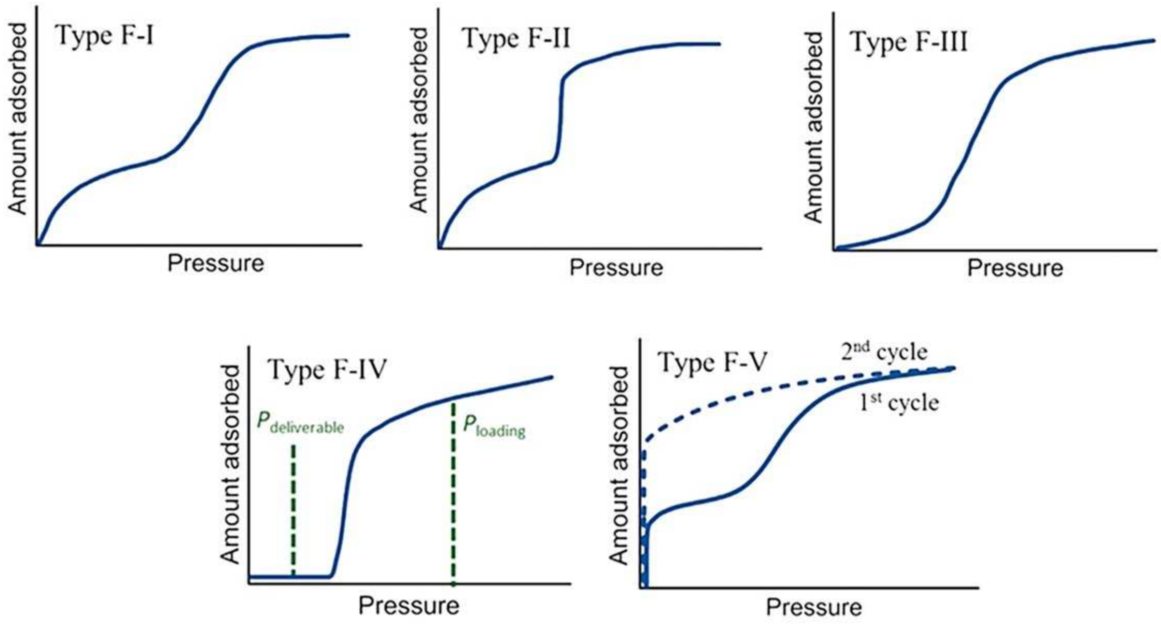

Abbildung 11 Von Zaworotko *et al*. vorgeschlagene Klassifizierung der Isothermen für flexible mikroporösen Materialien: Typ F-I = allmähliche Öffnung von kleinen Poren zu großen Poren; Typ F-II = plötzliche Öffnung von kleinen Poren zu größeren Poren; Typ F-III = allmähliche Öffnung von nicht-porös zu porös; Typ F-IV = plötzliche Öffnung von nicht-porös zu porös; Typ F-V = zeigt einen Formgedächtniseffekt. Darstellung wurde reproduziert aus der Literatur 80 mit Genehmigung von Wiley-VCH Verlag GmbH &Co. KGaA, Weinheim 2018.

Das von Millan *et al*. vorgestellte flexible paddle-wheel-MOF **rtl**-[Cu(HIsa-az-dmpz)] H_3Isa-az-dmpz, 5-(4-(3,5-Dimethyl-1*H*-pyrazolyl)azo)isophthalsäure) weist bei der Aktivierung eine reversible Phasenänderung in eine geschlossene Form auf und zeigt eine S-förmige F-IV-Adsorptionsisotherme für N_2 und CO_2 infolge eines Übergangs von einer nicht porösen in eine poröse Phase.[81] MOFs bei denen dieses Sorptionsverhalten beobachtet werden kann, sind besonders interessant, da sie im Vergleich zu starren MOFs, eine abrupte Gastaufnahme und folglich eine erhöhte Arbeitskapazität zwischen dem Gastaufnahme- und Abgabedruck aufweisen.[58,82]

1.2 Koordinationspolymere und Metall-organische Gerüstverbindungen auf der Basis von Phosphonat- und Phosphonatemonoester-Liganden

Der Erfolg von MOFs führte in den letzen Jahren zu einem ansteigenden Interesse an der Synthese von porösen Metallphosphonaten. Im Vergleich zu der Carboxylat-Linkern weisen Phosphonate stärkere koordinative Bindungen zu Metallen auf, was zu chemisch und thermisch stabileren Verbindungen führt. Die höhere Koordinationsaffinität ist auf die hohe Acidität von Phosphonsäuren ($pK_{s1} \sim 2.0$, $pK_{s2} \sim 6.0$) zurückzuführen.[83,84] Zusätzlich führt das Vorhandensein von drei Sauerstoffatomen innerhalb der Phosphonatgruppe zu einer Vielzahl von Koordinationsmodi, was einen Zugang zu neuen Netzwerk-Topologien eröffnet. Obwohl die Erforschung von porösen Metallphosphonaten auf mehr als ein Jahrzehnt zurückreicht, stellt die Synthese von kristallinen, ausgedehnten und porösen Netzwerkstrukturen stets eine Herausforderung dar. Aufgrund der relativ hohen Dentizität der Phosphonatgruppe dominiert tendenziell die Ausbildung von Verbindungen mit dichten Schichtstrukturen, die keine oder nur sehr geringe Porosität aufweisen.[85]

Die Erforschung von mikro- und mesoporösen Metallphosphonat-Materialien findet ihren Uhrsprung in den Arbeiten von Clearfield und Alberti zu der Synthese von 2D-geschichteten Zirconium(IV)-Phosphaten.[86] Einen entscheidenden Fortschritt auf diesem Bereich setzte Clearfield *et al.* mit der Kristallstrukturaufklärung von α-Zirkonium-bis(monohydrogen orthophosphat)monohydrat $[Zr(HPO_4)_2 \cdot H_2O]$, (kurz α-ZrP) mittels Einkristallröntgendiffraktometrie.[87]

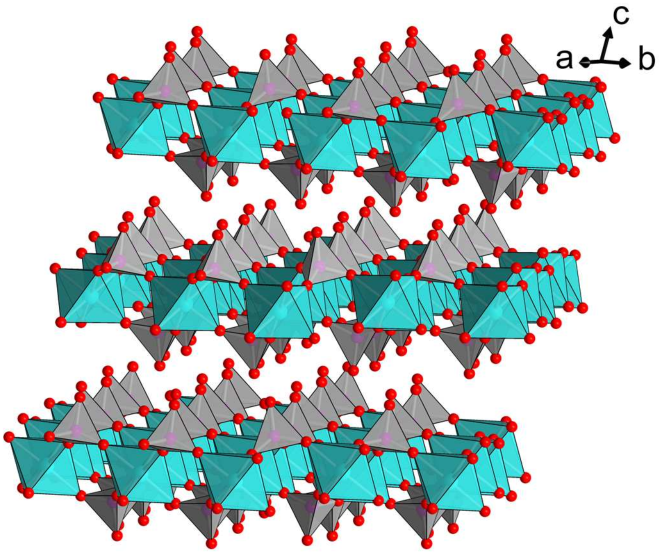

Abbildung 12 Schichtstruktur von α-ZrP. Farbcodes: Sauerstoff (rot), Phosphor (lila), ZrO_6-Oktaeder, blau; PO_4-Tetraeder, grau. Kristallstrukturinformationen wurden entnommen aus der Literatur 87 (CSD Refcode ICSD 10258).

α-ZrP basiert auf einer Schichtstruktur aus 1D-Ketten, in denen die Zr-Atome oktaedrisch von Monohydrogenphosphatgruppen koordiniert sind. Zwischen den Schichten ragen die freien OH-Gruppen in die Hohlräume. Nachfolgende Studien verfolgten den Austausch der OH-Gruppe durch eine organische Einheit, um den Zwischenabstand der geschichteten Materialien zu vergrößern.[88,89,90,91] Eine Strategie, starre Diphosphonat Säulenliganden zu verwenden um die anorganischen $ZrPO_3$-Schichten zu vernetzen wurde erstmals von Dines *et al*. vorgeschlagen.[92] Bedingt durch die schlechte Löslichkeit und direkte Ausfällung der auf dem vierwertigen Zirkonium basierenden Materialien konnten jedoch keine geeigneten Kristalle für die Kristallstrukturanalyse erhalten werden. Dies erschwert die Vorhersage der Koordinationschemie von Organophosphon-Liganden sowie eine gezielte Synthese.

In den späten 1970er und 1980er Jahren lenkte sich das Forschungsfeld auf die Synthese und Untersuchung zweiwertiger Metallphosphonate.[93] Es zeigte sich, dass mit Phenylphosphonaten und zweiwertigen Übergangsmetallen (Mn^{2+}, Fe^{2+}, Co^{2+}, Ni^{2+}, Cu^{2+}, Zn^{2+} und Cd^{2+}) kristalline Feststoffe der Zusammensetzung $M(C_6H_5PO_3)$, die überwiegend auf Schichtstrukturen basieren zugänglich sind.[94,95,96,97] In den 1990er Jahren wurden die ersten offenen zeolithartigen Gerüststrukturen *β*-$Cu(CH_3PO_3)$ (Methylphosphonat),[98] $Zn(O_3PC_2H_4NH_2)$ (2-Aminoethylphosphonat),[99] und α-, β-$Al(CH_3PO_3)$[100,101] mit kanalartigen Strukturen synthetisiert. (Abbildung 13).

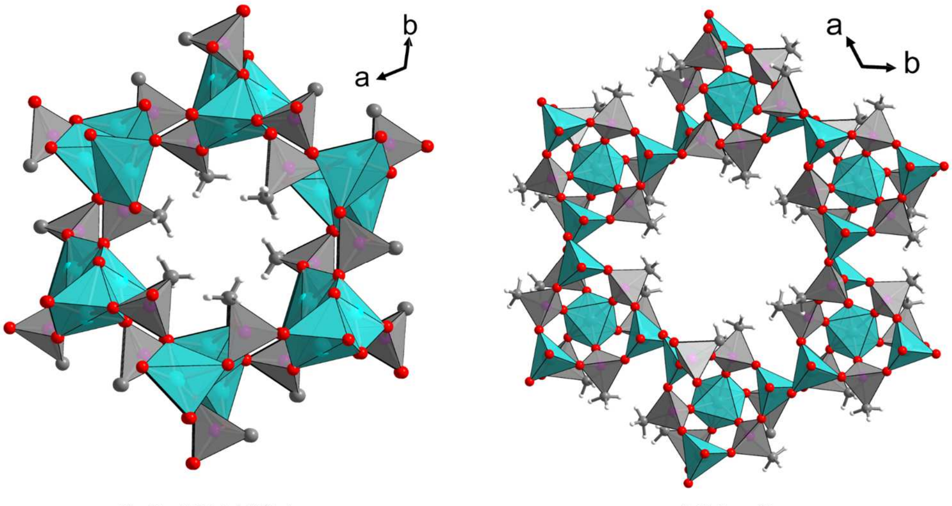

Abbildung 13 Kristallstrukturen von *β*-$Cu(CH_3PO_3)$ und α-$Al(CH_3PO_3)$. Farbcodes: Sauerstoff (rot), Phosphor (lila), Kohlenstoff (grau), Wasserstoff (weiß), Metallpolyeder (CuO_4, AlO_4, AlO_6) (blau), PO_3C-Tetraeder (grau). Kristallstrukturinformationen wurden entnommen aus der Literatur 98 (CSD Refcode YELWOB) für *β*-$Cu(CH_3PO_3)$ und 100 (CSD Refcode YUKBIP01) für α-AlMepO.

Die Literatur umfasst seit Anfang der 2000er Jahre zahlreiche Studien zu der Synthese von Metall-organischen Gerüstverbindungen auf der Basis von Arylphosphonat-Liganden mit definierten SBUs, die ein Zugang zu isoretikulären Verbindungen ermöglichen. Serre *et al.* synthetisierten mit dem bifunktionellen Linker *N,N'*-Piperazindi(methylenphosphonsäure) (H_4PBMP), zwei isostrukturelle MOFs (MIL-91(Ti, Al)) mit einer kettenförmigen SBU.[102] Die SBUs setzen sich aus eckenverknüpften TiO_6- oder AlO_6-Oktaedern zusammen, die über die Diphosphonatliganden zu einem 3D-Netzwerk verknüpft sind (Abbildung 14). Das Netzwerk enthält Kanäle (Porengröße ~3,5 × 4,0 Å^2), welche mit Wassermolekülen gefüllt sind. Die aktivierten Verbindungen zeigen eine N_2-Langmuir-Oberfläche von etwa 500 $m^2\ g^{-1}$ sowie ein Porenvolumen von 0,20 $cm^3\ g^{-1}$.

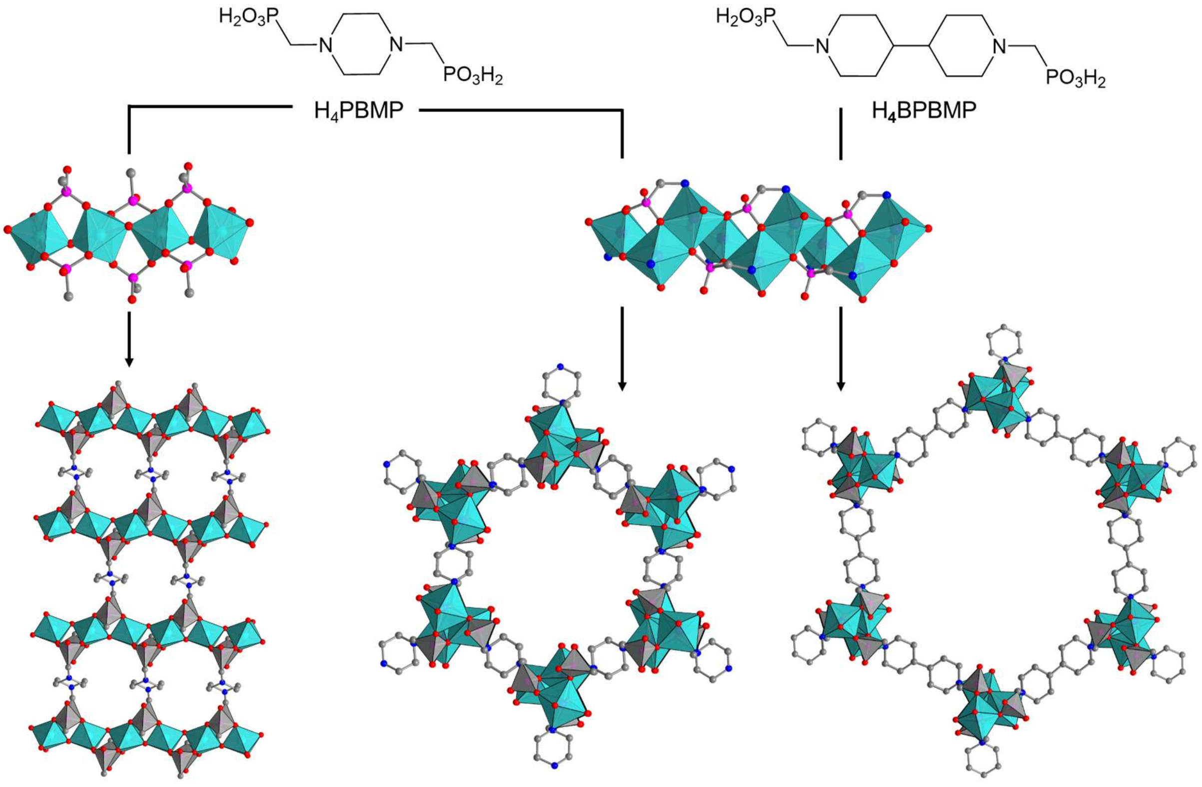

MIL-91(M) (M = Ti, Al) STA-12(M) (M = Mn, Fe, Co, Ni) STA-16(M) (M = Co, Ni)

Abbildung 14 Kristallstrukturen von MIL-97; STA-12 und STA-16 basierend auf Kettenförmigen SBUs. Farbcodes: Sauerstoff (rot), Stickstoff (blau), Phosphor (lila), Kohlenstoff (grau), Wasserstoff (weiß), MO_6-Oktaeder (blau). Kristallstrukturinformationen wurden entnommen aus der Literatur 102 (CSD Refcode IVEQAC) für MIL-97, Literatur 103 (CSD Refcode XESLAK) für STA-12 und Literatur 105 (CSD Refcode ATIJUJ) für STA-16.

Das erste und bislang einziges Beispiel für isoretikuläre Chemie in der Synthese von Phosphonat MOFs, wurde von der Arbeitsgruppe um Wright *et al.* vorgestellt. Basierend auf dem Linker H_4PBMP wurde die STA-12 Serie (STA = St. Andrews microporous material) mit den zweiwertigen Metallen Mn, Fe, Co und Ni synthetisiert.[103,104] Die isoretikulären Analoga mit der Bezeichnung STA-16, wurden unter der Verwendung des verlängerten Linkers *N,N'*-Bipiperidinbis(methylenephosphonsäure) (H_4BPBMP) mit Ni und Co erhalten.[105] Diese MOFs basieren auf unendlichen, kettenförmigen $[M_3(P(O)O_2)_3(N)_3]_\infty$ SBUs, in denen die

Metallionen oktaedrisch von Phosphonat, sowie Sauerstoffatomen und Stickstoffatomen vom zentralen Piperidin koordiniert sind. Letzteres dient als Verlängerungspunkt zu benachbarten Ketten, wodurch ein **etb**-Netz mit hexagonalen Kanälen resultiert. Der Ansatz zur Beschreibung von MOFs auf Basis der **etb**-Topologie mit dreizähligen helikalen kettenförmigen SBUs und ditopischen Linkern wurde von Yaghi *et al.* vorgeschlagen.[106] Nach diesem Konzept werden die SBUs zu Helices dekonstruiert. Diese können durch ditopische Linker zu 3D MOFs verknüpft werden. Die helikalen SBUs basieren auf 3-c Knoten, wobei zwei Verknüpfungen innerhalb der SBU liegen und eine Verknüpfung zum Linker stattfindet.

Die Verwendung von Phosphonatmonoester Liganden ist in der MOF-Chemie weitgehend begrenzt und überschaubar im Vergleich zu anderen Ligandenklassen. Strukturell sind Phosphonatmonoester-Liganden für die Synthese von neuartigen MOF-Strukturen höchst interessant. Im Vergleich zu Phosphonaten sind sie bidentat, wodurch ähnliche Koordinationsmodi zu der Carboxylatfunktionalität erzielt werden können. Der Alkylgruppe in Phosphonatmonoester MOFs wird eine strukturdirigierende und gegenüber Feuchtigkeit stabilisierende Wirkung sowie eine Adsorptionspräferenz der kleineren CO_2-Moleküle gegenüber N_2 und CH_4 zugeschrieben.[107] Eine der frühsten strukturellen Arbeiten zu der Synthese von MOFs auf der Basis der Phosphonatmonoethyl-Funktionalität wurde im Jahre 2002 von Lin *et al.* vorgestellt.[108] Unter der Umsetzung eines chiralen 2,2′-Diethoxy-1,1′-binaphthalen-6,6′-diphosphonsäure (L-$(H_2PO_3)_2$) Liganden mit einem Kupfersalz in Ethanol bei 130 °C, wurde [Cu(L-$(PO_3Et)_2$)] synthetisiert. Die Reaktionsbedingungen (erhöhte Temperatur, wasserfreie Lösungsmittel) erwiesen sich als ausschlaggebend für eine *In-situ*-Veresterungsreaktion zwischen L-$(H_2PO_3)_2$ und Ethanol, die zu der Bildung der L-$(PO_3Et)_2$ Einheit führte. [Cu(L-$(PO_3Et)_2$)] basiert auf der kettenförmigen $\{[Cu(PO_3Et)_2]\}_n$ SBU, in der die Cu(II)-Zentren durch die Koordination von vier Sauerstoffatomen vierer unterschiedlicher L-$(PO_3Et)_2$-Einheiten eine verzerrte quadratisch planare Koordinationsumgebung annehmen. Durch die Verknüpfung der $\{[Cu(PO_3Et)_2]\}_n$-Kette zu vier benachbarten Ketten über L-$(PO_3Et)_2$-Brücken, resultiert ein 3D MOF mit rhomboedrischen Kanälen. Die Ethoxygruppen ragen in die Kanäle und verschließen dabei die Hohlräume.

Weitere wegweisende Beiträge auf dem Gebiet der Phosphonatmonoester Koordinationspolymere/MOFs liefern die Arbeiten um Iremonger *et al.*[109] Im Jahre 2011 synthetisierten sie zwei isostrukturelle MOFs [Cu(Me_2BDP)] und [Cu(Et_2BDP)] (Me_2/Et_2BDP^{2-} = 1,4-Benzoldiphosphonatbis(mono(methyl/ethyl)ester)) durch die direkte Verwendung von zwei Monoalkylphosphonatgruppen-tragenden Linkern.[110] Die Strukturen setzen sich aus unendlichen 1D-$\{[Cu_2(PO_2(OEt/Me))_2]\}_n$ kettenförmigen SBUs zusammen, die über lineare Linker zu einem 3D-Netzwerk verknüpft sind (**Abbildung 15**).

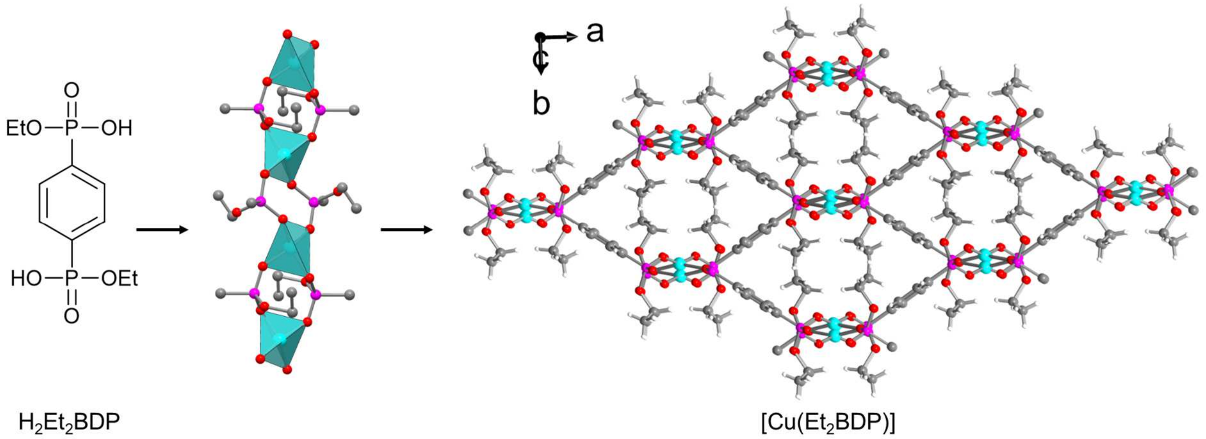

Abbildung 15 3D-Netzwerkstruktur von [$Cu(Et_2BDP)$] ausgehend vom ditopischen H_2Et_2BDP Linker. Die Struktur basiert auf einer kettenförmigen 1D-{[$Cu_2(PO_2(OEt/Me))_2$]}$_n$ SBU in der die Cu^{2+}-Ionen eine verzerrt tetraedrische Koordinationsumgebung haben. Farbcodes: Sauerstoff (rot), Phosphor (lila), Kohlenstoff (grau), Wasserstoff (weiß), CuO_4-Tetraeder (blau). Kristallstrukturinformationen wurden entnommen aus der Literatur 110 (CSD Refcode KASPIF).

Abhängig von der Größe der Alkylgruppe konnte ein Einfluss auf die CO_2-Aufnahmefähigkeit festgestellt werden. Für [$Cu(Et_2BDP)$] wurde keine CO_2 Aufnahme beobachtet, da die Kanäle weitgehend von Ethylgruppen blockiert sind. Infolge der kleineren Methylgruppe zeigt [$Cu(Me_2BDP)$] dagegen eine mäßige CO_2-Aufnahme von 30 cm^3(STP) g^{-1}, 1,38 mmol g^{-1}, bei 273 K und 1,2 bar, jedoch keine Aufnahme von N_2, H_2 oder CH_4. Eine spätere Arbeit zeigt, dass die Verwendung des linearen $H_2{}^iPr_2BDP$ Liganden mit dem sperrigen Isopropylester der Ausbildung eines 3D-Netzwerkes entgegenwirkt und stattdessen zur Ausbildung von isolierten zweidimensionalen Schichten führt.[111] Die Einführung zusätzlicher N-Donor-Liganden (wie zum Beispiel 2,2'-Bipyridin, 1,10-Phenanthrolin, 4,4'-Bipyridin oder 4,4'-Trimethylendipyridin) hat sich als wirksam erwiesen um 1D-Ketten auf verschiedene Gerüstdimensionen zu erweitern. In diesem Zusammenhang synthetisierten Jiang *et al.* unter Umsetzung des Liganden 4,4'-Biphenyldiphosphonatbis(monoethylester) (H_2BPDP) mit den N-Donor-Liganden Bis(1*H*-imidazol-1-yl)methan (BIM) oder 1,3,5-Tri(1*H*-imidazol-1-yl)benzol (TIB) eine Reihe von MOFs, wie [$Cd(BPDP)(BIM)(H_2O)_2$], [$Cd(BPDP)(BIM)$]$\cdot 7H_2O$, [$Co(BPDP)(TIB)(H_2O)$]$\cdot 7H_2O$ und [$M(BPDP)(TIB)(H_2O)_2$]$\cdot 6H_2O$ (M = Cd, Co und Cu), welche Schichtstrukturen bzw. isomorphe 3D-Gerüste aufweisen.[112] Die 3D-MOFs [$M(BPDP)(TIB)(H_2O)_2$]$\cdot 6H_2O$ (M = Cd und Cu) zeigen eine permanente Porosität sowie eine geringe Affinität für CO_2 mit Aufnahmen von 30 cm^3 g^{-1} und 40 cm^3 g^{-1} bei 195 K. Um die Topologie eines dichten Netzwerks in eine offene 3D-Gerüsttopologie zu lenken, wurde der Ansatz verfolgt, trigonale Liganden einzubauen.[111,113,114] Nach diesem Ansatz konnte durch die Umsetzung von 1,3,5-Benzoltriphosphonatmonoisopropylester ($H_3{}^iPrBTP$) und $Cu(NO_3)_2$ infolge einer hydrothermalen Synthese [$Cu_3({}^iPr_3BTP)_2$], CALF-30 (CALF = Calgary Framework) synthetisiert werden.[111] Es basiert auf einer offenen wabenartigen Struktur mit hexagonalen Poren (3,57 Å, einschließlich Van-der-Waals-Radien, mit einem Hohlraumvolumen von 15,1%). CALF-30 zeigt eine CO_2-Adsorption von ca. 60 cm g^{-1} bei 195 K, jedoch keine Aufnahme von N_2 oder CH_4. Die Verwendung eines größeren Triphenylbenzol-Liganden H_3Et_3(BTBP) führte schließlich zu der Entdeckung des permanent porösen CALF-33-Et_3, mit einer der bislang höchsten Oberflächen von 1000 m^2 g^{-1} für Phosphonat MOFs.[114]

2 Zielsetzung und Motivation

Das vorrangige Ziel dieser Arbeit liegt in der Synthese und Charakterisierung von Metall-organischen Gerüstverbindungen (MOFs) auf Basis von bifunktionellen Monoalkylphosphonat-Carboxylat-Liganden. Dreizähnige Phosphonate besitzen eine vielfältige Komplexchemie und erfüllen die Voraussetzungen durch die Koordination an Metallen, thermodynamisch stabile Koordinationsverbindungen auszubilden. Bedingt durch die relativ hohe Dentizität der Phosphonatgruppe weisen Metallphosphonate selten diskrete sekundäre Baueinheiten (SBUs) auf und begünstigen die Ausbildung unendlicher 1D- oder 2D-Ketten. Aufgrund der starken Tendenz zur Bildung dichter Schichtstrukturen, sind poröse Metallphosphonate selten in der Fachliteratur zu finden. Die Koordinationschemie von bitopischen linearen Arylphosphonaten mit Alkali-, Hauptgruppen-, Übergangs- und Seltenerdmetallen weist ein breites Spektrum mit weitreichenden Eigenschaften auf, einschließlich Lumineszenz, Magnetismus, katalytische Aktivität, thermische Stabilität und Wasserstabilität. Diese Studien zeigen, dass die parallele Stapelung der Aryleinheit die Formation von dichten Packungen verstärkt, weshalb für die meisten Verbindungen keine dauerhafte Porosität nachgewiesen wurde.

Im Rahmen dieser Arbeit wurden systematische Strategien verfolgt um dichte Strukturen zu vermeiden und neuartige ausgedehnte Phosphonat-MOFs zu synthetisieren.

Die Forschung wurde dabei von folgenden Strategien inspiriert: die Verwendung von bifunktionellen Monoalkylphosphonat-Carboxylat-Liganden, deren Potential zur synergistischen Kombination mit der Carboxylatfunktionalität in einem Liganden und die Verwendung von N-Donor-Co-Liganden. Monoester von Phosphonsäuren sind zweizähnig, wodurch diese eine zu der Carboxylatfunktionalität analoge Koordination annehmen können. In diesem Zusammenhang wird die Ausbildung definierter SBUs angestrebt. Des Weiteren hat sich der Einbau von N-Donor-Co-Liganden als eine effiziente Strategie zur Verbrückung 2D Netze durch die Verknüpfung benachbarter SBUs erwiesen. Die synthetisierten MOFs sollen mit den gängigen Charakterisierungsmethoden analysiert und mit ihren zugrundeliegenden Topologien beschrieben werden. Des Weiteren sollen die MOFs hinsichtlich ihrer Sorptionseigenschaften untersucht und der Einfluss der Alkylgruppe auf die Adsorption ermittelt werden.

In der Entwicklung von MOFs haben sich zur Steigerung ihrer Anwendungspotentiale weitreichende Funktionalisierungsstrategien ergeben. Die Synthese von MOFs mit offenen Metallstellen (open metal sites, OMS) ist eines der vielversprechendsten Aspekte um erhöhte (supramolekulare) Wechselwirkungen mit Gastmolekülen zu erzielen. Die Literatur umfasst eine Vielfalt an Forschungsschwerpunkten, (einschließlich der Synthese von OMS, deren Quantifizierung, Computerstudien, potentielle Eigenschaften, Post-Funktionalisierung, Gasadsorption, (Photo-) Katalyse und Sensing) welche die Entwicklung von OMS-MOFs mit verbesserten Leistungsfähigkeiten gegenüber MOFs ohne OMS aufzeigen. Anhand der Literatur soll im zweiten Teil dieser Arbeit eine Übersicht der möglichen Synthesestrategien für eine verifizierte Bildung von offenen Metallstellen in MOFs zusammengestellt werden. Die Wirkung von OMS auf die unterschiedlichen Anwendungen sollen vorgestellt werden. Als Grundlage für die Erforschung und Vorhersage der Sorptionseigenschaften und Anwendungen von OMS-MOFs soll außerdem ein Fokus auf die Computerstudien gesetzt werden. Die Übersicht soll helfen, das Design von OMS-MOFs für gewünschte Anwendungen voranzutreiben.

Die Generierung von SBUs wird unter anderem durch die Koordinationsumgebung der Metallquellen und der Orientierung der verbrückenden Donoratome in organischen Linkern beeinflusst. Abhängig von den Synthesebedingungen kann die Ausbildung von SBUs mit einer unterschiedlichen Anordnung und Konnektivitäten für ein gegebenes Metall gebildet werden. In der Literatur wurden verschiedene Strategien zur Synthese MOFs (solvothermal, mechanochemisch, sonochemisch, Trockengelumwandlung) verwendet. Ein aussichtsvolles Verfahren zur Synthese von MOFs ist auch die Verwendung von ionischen Flüssigkeiten (ILs) als Lösungsmittel oder als Additive. Sie können einen strukturdirigierenden Effekt (z.B. Templating) auf den Kristallisationsprozess von MOFs ausüben. Die Konstruktion von MOFs auf der Basis von Cobaltcarboxylat-SBUs ist schwierig vorherzusagen, da die Koordinationszahl und Anordnung von Cobalt(II) von vier (tetraedrisch) bis sechs (oktaedrisch) reichen kann. Zum Beispiel zeigt Cobalt eine tetraedrische Koordination in Co-MOF-5, eine quadratisch-pyramidenförmige Koordination in MOFs basierend auf paddle-wheel SBUs oder Ketten aus eckenverknüpften CoO_6-Oktaedern in Co-MOF-71. Unter der Prämisse, dass polynukleare Cobaltcarboxylate geeignete Kandidaten für die Strukturierung neuer Koordinationsfeststoffe mit interessanten Netzwerkarchitekturen darstellen, soll im zweiten Teil dieser Arbeit der Einfluss einer IL auf den Kristallisationsprozess und die Strukturbildung bei der Umsetzung von Cobalt(II)-Salzen mit Terephthalsäure untersucht werden.

3 Kumulativer Teil

Die folgenden Kapitel beinhalten die Ergebnisse dieser Dissertation, die in Form von Erstautorschaften in internationalen Journalen veröffentlicht wurden.
Jede Veröffentlichung steht für sich und enthält ein separates Literaturverzeichnis. Die Abbildungen, Tabellen und Schemata folgen der Nummerierung der Publikation. Die Publikationen werden in zeitlich chronologischer Reihenfolge aufgezeigt.
Die jeweiligen Veröffentlichungen werden durch den Titel, die Namen der Autoren, den Namen des Journals, eine kurze Zusammenfassung und die Anteile der Autorschaften eingeleitet.

3.1 Flexible bifunctional monoethylphosphonate/ carboxylates of Zn(II) and Co(II) reinforced with DABCO co-ligand: paradigmatic structural organization with pcu topology

Anna Goldman,[a] Beatriz Gil-Hernández,[b] Simon Millan,[a] Serkan Gökpinar,[a] Christian Heering,[a] Ishtvan Boldog[*a] and Christoph Janiak[*a], *CrystEngComm*, 2020, **22**, 2933–2944.

DOI: 10.1039/D0CE00275E

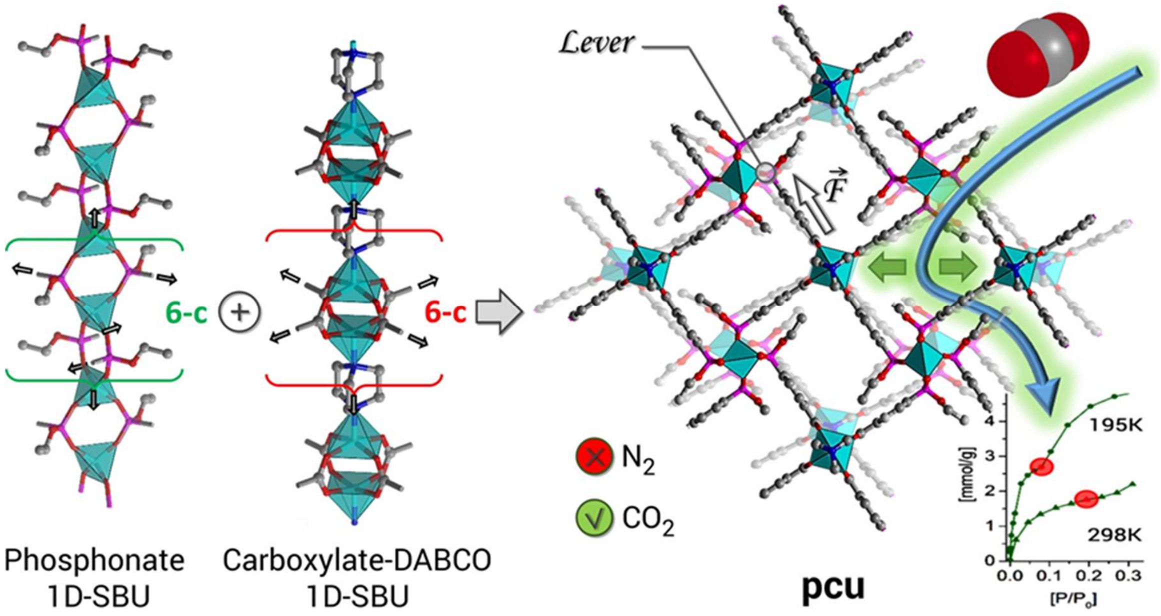

Die folgende Publikation berichtet über zwei neue isostrukturelle Metall-organische Gerüstverbindungen basierend auf einem bifunktionellen Carboxylat-Monoethylphosphonat Liganden. Der Ligand *O*-Ethyl-P-(4-carboxyphenyl)phosphonsäure (H_2EtBCP) wurde in zwei Schritten synthetisiert. Der Vorläufer Diethyl-P-(4-carboxyphenyl)phosphonat wurde durch eine Ni(II)-katalysierte Michaelis-Arbuzov-Reaktion mit Methyl-4-Iodbenzoat und Triethylphosphit synthetisiert. Durch partielle Hydrolyse unter milden Bedingungen in einer 2 mol L^{-1} wässrigen NaOH Lösung wurde der Monoester H_2EtBCP erhalten. Die Umsetzung von $Zn(NO_3)_2 \cdot 6H_2O$ und H_2EtBCP in DMF ergab eine Vorgängerstruktur, $[Zn_2(EtBCP)_2(Solv)]\cdot Solv'$. Das Motiv der 3D-Gerüststruktur basierend auf einem $\{Zn_2(RCOO)_2\}$ paddle-wheel und einer $\{Zn_2(PO_2(OEt))_2\}_n$ 1D-Kette konnte mittels Einkristall-Röntgenstrukturanalyse identifiziert werden. Das paddle-wheel Motiv in **1** diente als Grundlage für die Verwendung von DABCO als N-Donor-Co-Liganden, mit dem Ziel die Struktur durch zusätzliche „Vernetzung“ benachbarter paddle-wheel-SBUs zu stabilisieren.

Die Reaktion von H_2EtBCP, DABCO und $Zn(NO_3)_2 \cdot 6H_2O$ oder $Co(NO_3)_2 \cdot 6H_2O$ (Molverhältnis 2: 2: 1) in *N,N*-Dimethylacetamid (DMA) bei 100 °C führt zur Bildung von zwei isostrukturen MOFs mit der Zusammensetzung $[M_2(EtBCP)_2(DABCO)_{0.5}]\cdot 2DMA$ (M = Zn, Co).

Die MOFs basieren auf einem prototypischen **pcu**-Netz, in dem die kettenförmigen $\{M_2(PO_2(OEt))_2\}_n$-Monoethylphosphonat und $\{M_2(COO)_4(DABCO)\}$-Carboxylat SBUs 6-c Knoten bilden. Die aktivierten MOFs weisen ein interessantes S-förmiges Adsorptionsprofil vom F-I Typ für CO_2 bei 195 K auf, was auf die strukturelle Flexibilität des Netzwerks schließen lässt.

Eigenanteile an der Veröffentlichung:

- Synthese und Charakterisierung des Liganden und der MOFs sowie Durchführung der der Sorptionsmessungen.
- Auswertung, Interpretation und Verschriftlichung der Ergebisse in Form einer wissenschaftlischen Veröffentlichung.
- Frau Dr. Gil-Hernández führte die kristallographische Strukturverfeinerung durch.
- Aufnahme der Hochdrucksorptionsmessungen erfolgte durch Herr Dr. Serkan Gökpinar.
- Herr Dr. Ishtvan Boldog und Herr Dr. Simon Millan halfen bei der Interpretation der Ergebisse und Überarbeitung des Manuskripts.
- Finale Überarbeitung und Abstimmung des Manuskripts und der Revision in Zusammenarbeit mit Herrn Dr. Ishtvan Boldog und Herrn Prof. Christoph Janiak.

The work presented in this chapter has been published in:

Flexible bifunctional monoethylphosphonate/ carboxylates of Zn(II) and Co(II) reinforced with DABCO co-ligand: paradigmatic structural organization with pcu topology†

Anna Goldman,[a] Beatriz Gil-Hernández,[b] Simon Millan,[a] Serkan Gökpinar,[a] Christian Heering,[a] Ishtvan Boldog*[a] and Christoph Janiak*[a], *CrystEngComm.*, 2020, **22**, 2933–2944. DOI: 10.1039/D0CE00275E

The article is reproduced from Ref. 115 with permission from The Royal Society of Chemistry 2020.

Abstract

Two novel isostructural phosphonate-monoethylcarboxylate MOFs with the structural formula of $[M_2(EtBCP)_2(DABCO)_{0.5}]\cdot 2DMA$ (M = Zn (**2**), Co (**3**); H_2EtBCP = *O*-ethyl-P-(4-carboxyphenyl)phosphonic acid, DABCO = 1,4-diazabicyclo[2.2.2]octane, DMA = N,N-dimethylacetamide) were synthesized and characterized. The frameworks of **2** and **3** are sustained by $\{Zn_2(PO_2(OEt))_2\}_n$ metal-phosphonate- and DABCO-extended $\{Zn_2(COO)_4(DABCO)\}_n$ paddle-wheel carboxylate chain-SBUs. The chains providing connectivity in three, mutually orthogonal directions are running parallel and are combined in a framework, which could be interpreted as having a **pcu** topology. The simple structure-organization principle, which suggests the possibility of the elongation of the bifunctional ligand with scaling in two directions, allows to view the structures of **2** and **3** as prototypes for an isoreticular series. The porosity of both compounds, based on a relatively short ligand, is low: no adsorption of N_2 was registered, however, CO_2 is adsorbed readily allowing to estimate the surface area at ~330 $m^2\ g^{-1}$ (~900–1060 $m^2\ g^{-1}$ geometric estimate). The compounds demonstrate a two-step CO_2 adsorption isotherm both at 195 K (0–1 bar) and 298 K (0-20 bar). The adsorption isotherms are characterized by a gradual (type "F-I"), albeit still relatively steep onset of the second step, associated with structural flexibility/bistability. The estimated pore volumes at the start of the transformation (195 K) for **2** and **3** are ~0.11 ($0.08P/P_0$) and 0.12 $cm^3\ g^{-1}$ ($0.12P/P_0$) respectively, which corresponds considerably well to the geometrically calculated accessible volume of ~0.07 $cm^3\ g^{-1}$ for the experimental structure (3.3 Å probe diameter). The structural prerequisites of the observed flexibility of the framework, which might be associated with the non-planarity of the metal-phosphonate moieties, acting as 'levers' for propagating mechanical stress, are discussed.

Introduction

The field of metal–organic frameworks (MOFs) witnessed explosive growth during the last two decades. The ‘hybrid’ nature of the coordination polymers, consisting of both inorganic and organic constituents, their crystallinity and high attainable surface areas are among the primary factors behind the great expectations. The structural versatility and functional tunability[1–3] of MOF materials are indeed superior and a range of possible applications are demonstrated, including gas storage, small molecule separation, catalysis, sensing etc.[4–7] On the other hand, the relatively low chemical/hydrolytic stability is a hindrance to their real-world use. Nearly all of the most stable MOFs are M(III, IV) = Cr, Fe, Al, Zr carboxylates and M(I, II) = Ag, Cu, Zn, Co azolates. The bidentate phosphinates[8] and particularly the tridentate phosphonates of oxophilic[9] metals possess the thermodynamic prerequisites to be more stable than carboxylates (even if the kinetic factors could often prevail). Porous organo-phosphonates are actively researched for more than a decade, however the achievements were modest until recently. There is a strong tendency towards formation of dense layered structures,[10] partly evident for linear arylphosphonates (the stacking of the aryl-moiety reinforces the dense parallel packing; the use of non-acrylic ligand platforms, namely (bi)piperidines, led to one of the most successful early phosphonate MOFs, the isoreticular STA-12, −16 (ref. 11 and 12)). Discrete secondary building units (SBUs) tend to be less frequent compared to infinite 1D or 2D cases, which favor dense packing, due to relatively high denticity of the phosphonate group.[13]

The analysis of the relatively rare phosphonates with high porosity suggests a few strategies to avoid dense structures. The use of large rigid molecules with non-collinear phosphonate branches, *e.g.* trigonal shaped[14] or even better non-coplanar, e.g. tetragonal shaped molecules,[15] is one of the approaches.[16,17] The recent report of the ultrastable highly porous zirconium-based SZ series (S_{BET} up to ~600 m^2 g^{-1} for [N-Et-pyridinium]$_2$[Zr$_{3.5}$(LH)F$_9$])[15] with nearly fully deprotonated tetrahedral adamantane tetraphosphonic acids (H_8L) crowned the efforts of this type and the use of ionic liquids as a medium suggests the possibility of templating. The microporous CAU-14 copper phosphonate[14] with modest CO_2 adsorption is also worth mentioning. Alternatively, the introduction of synergistic co-ligands, *e.g.* N-donor ligands, or the use of monoalkylphosphonates for the decrease of the ligand's denticity were proven also efficient.

The use of N-donor co-ligands was shown to be partially productive leading to 3D framework compounds incorporating 2,2′-bipyridine, 1,10-phenanthroline, 4,4′-bipyridine or 4,4′-trimethylenedipyridine.[18–21] For most of the compounds no permanent porosities were demonstrated, however, extensive reports on properties including luminescence,[22–25] magnetism,[26–28] catalysis,[29] thermal stability[30,31] and water stability[32,33] were published. It is important to note, that the combination of carboxylate and N-donor ligands for divalent 3d metals is a viable strategy for the increase of stability. An illustrative example are the [M(BDC)$_2$(DABCO)], M = Cu, Zn MOFs, which demonstrate significantly higher hydrolytic stability than the carboxylateonly peers.[34,35] The role of the N-donor ligands could also be interpreted as a means of decreasing the average local connectivity of the networks. Other, more synergistic cases could be also foreseen. Monoesters of phosphonic acids and phosphinates are both bidentate and could function analogously to carboxylate groups.[36] The seminal works of Shimizu et al.,[36–38] eventually lead to the discovery of the permanently porous copper monoesterphosphonate framework CALF-33-ET$_3$ (CALF = Calgary Framework) with one of the highest surface areas at 1000 m^2 g^{-1} for a phosphonate-based MOF.[31,39] It is expected, that the alkyl substituent could tune the adsorption preference of the smaller CO_2 molecules over N_2 and CH_4.[40,41]

The use of phosphonate-monoesters as ligands for the synthesis of MOFs with significant porosity is also known; the reported materials are often characterized by high moisture and water-vapor stability.[42–44] Selected examples of the respective monoesterphosphonic acids used for the syntheses of coordination polymers/MOFs are summarized in Fig. 1.

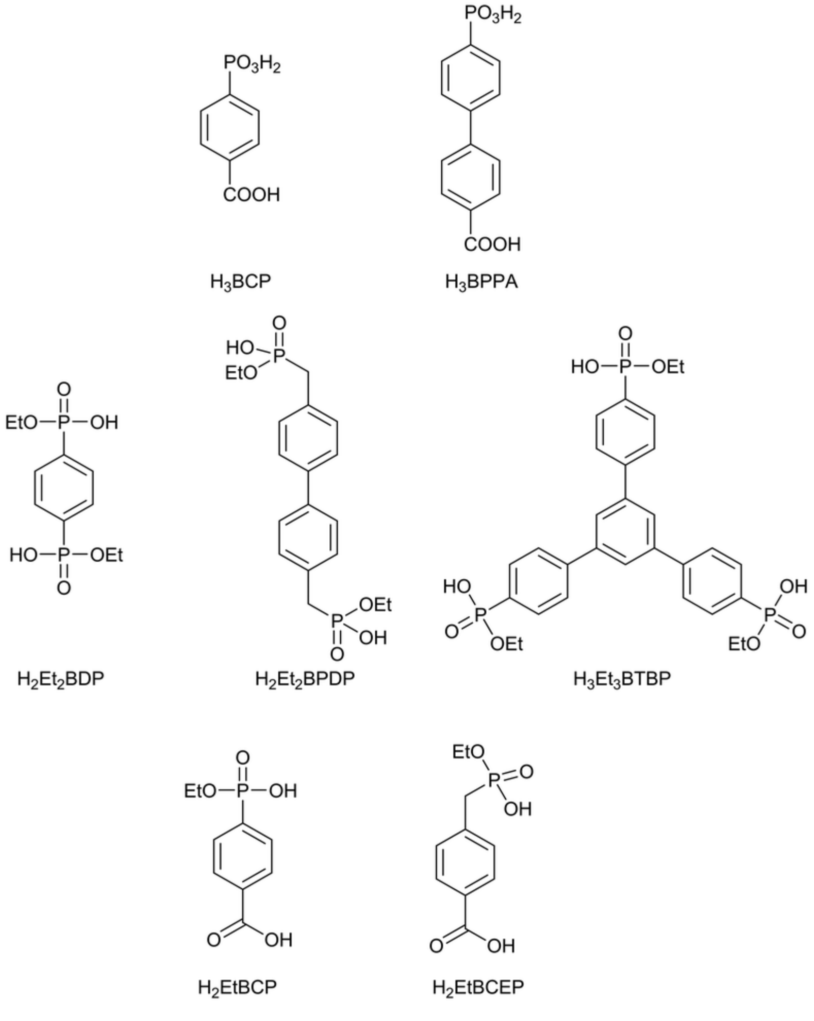

Fig. 1 The most relevant phosphonic and monoesterphosphonic acids reported in the literature as building-blocks for MOFs.[21,32,36,39,41]

Our research was inspired by all the three mentioned strategies aiming for robust phosphonate MOFs: the use of bifunctional (monoalkyl)phosphonates, their potentially synergistic combination with carboxylate functions in one ligand, and the use of N-donor co-ligands. Herein, were report two novel isostructural monoethylphosphonate-carboxylate MOFs obtained using that strategy: $[Zn_2(EtBCP)_2(DABCO)_{0.5}]\cdot 2DMA$, **2** and $[Co_2(EtBCP)_2(DABCO)_{0.5}]\cdot 2DMA$, **3**, with H_2EtBCP = *O*-ethyl-P-(4-carboxyphenyl)phosphonic acid, the second only known ligand of this class used for the syntheses of coordination polymers. The implications, originating from the potentially general importance of their special structures and the structural flexibility observed from the CO_2 adsorption data are discussed.

Results and discussion

Synthesis and structural characterization

The ligand, *O*-ethyl-P-(4-carboxyphenyl)phosphonic acid (H_2EtBCP), was synthesized in two steps. The intermediary diethyl *P*-(4-carboxyphenyl)phosphonate was obtained by the Ni(II)-catalyzed Michaelis–Arbuzov reaction between the methyl 4-iodobenzoate with triethylphosphite. Partial hydrolysis in 2 mol L^{-1} aqueous NaOH under mild conditions yielded the aimed monoester, H_2EtBCP (see the experimental section for details). While H_2EtBCP was reported before,[45–47] it was never used for the synthesis of coordination polymers. It is a rigid ligand, which is the second only representative of the monoalkylphosphonic–carboxylic acid class used in the synthesis of coordination polymers/MOFs after the flexible *O*-ethyl-*P*-(4-carboxyphenylmethyl)phosphonic acid ($H_2EtBCEP$) used for the preparation of non-porous luminescent cadmium based compounds (Fig. 1).[21] The initial screening for the best crystallization conditions was performed using the solutions of $Zn(NO_3)_2\cdot 6H_2O$ and H_2EtBCP in DMF. One of the experiments, (130 °C, 72 h see ESI† for further details) yielded a poorly crystalline material, nonetheless containing single crystals with a quality barely enough for a standard diffraction experiment. A 'predecessor' structure, $[Zn_2(EtBCP)_2(Solv)]\cdot Solv'$, **1**, was identified (Fig. S14 and S15; see ESI† for further details regarding this 'predecessor' structure). Repeated attempts to improve the quality of the measurement were only partially successful. However, the motif of the 3D framework structure sustained by $\{Zn_2(RCOO)_2\}$ paddle-wheel and $\{Zn_2(PO_2(OEt))_2\}_n$ 1D chain SBUs was clearly established (for the latter see Fig. 5a). The nature of the solvent molecule in **1** remains unclear and might be a minor impurity, possibly formed in situ. In this case, it might be a true bidentate ligand, which cannot be removed after activation (the possible role of formic acid/formate was checked in comparative experiments with a negative result, see ESI†). The observance of the paddle-wheel motif in **1** was an additional incentive, which stimulated us to use spacer N-donor (L^N) co-ligands molecules, aiming stabilization of the structure *via* additional 'cross-linking' through the formation of $\{Zn_2(RCOO)_2(L^N)_2\}$, the stable N-capped paddle-wheel SBU.[48] The approach seemed particularly suitable because the distance between the paddle-wheel units in **1** was estimated to be 6.3 Å (Fig. S15†), which corresponds well to the length of the DABCO molecule(Fig. 2).[49]

The DABCO ligand along with pyrazine or 4,4′-bipyridine is frequently used for a pillaring design-strategy of joining planar topologies sustained by paddle-wheel units.[35,50–55] The typical distances between paddle-wheel units determined from experimental structures are 6.7 Å for DABCO,[56] 7.1 Å for pyrazine[57] and 11.2 Å for 4,4′-bipyridine[58] (Fig. 2).

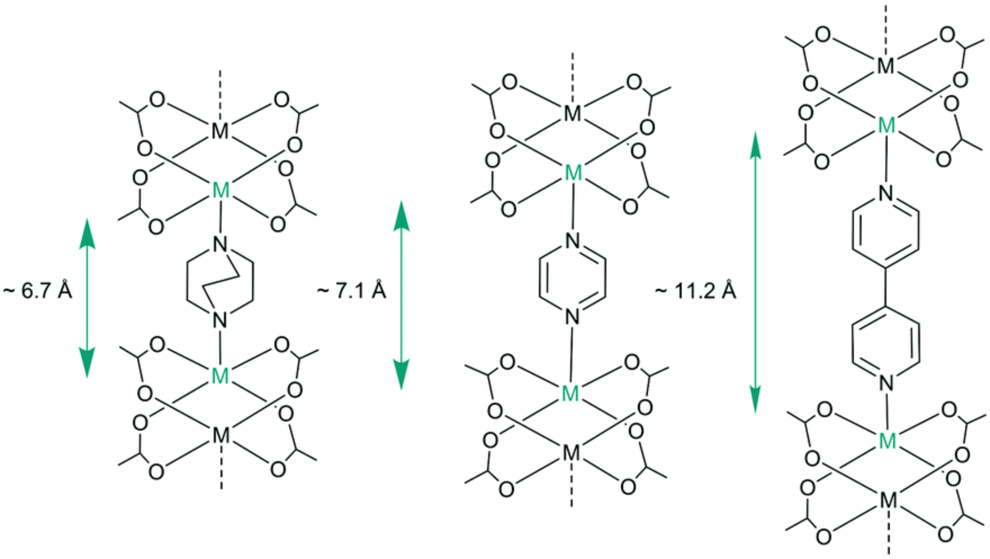

Fig. 2 Distances between the paddle-wheel units bridged with pillaring ligands DABCO, pyrazine and 4,4′-bipyridine, found in experimental crystal structures.[56–58]

The reaction of H_2EtBCP, DABCO, and $Zn(NO_3)_2{\cdot}6H_2O$ or $Co(NO_3)_2{\cdot}6H_2O$ (2 : 2 : 1 molar ratio) in N,N-dimethylacetamide (DMA) at 100 °C lead to the formation of two isostructural MOFs with a composition of $[M_2(EtBCP)_2(DABCO)_{0.5}]{\cdot}2DMA$ (M = Zn, Co; compounds **2** and **3** respectively). Notably, no products of appreciable crystallinity were obtained with the use of *N,N*-dimethylformamide (DMF). The single crystal structure of **2**, discussed in detail below, showed the incorporation of the DABCO ligand precisely at the allotted place, stitching the adjacent paddle-wheel units. The similarity of structures **2** and **3**, as well as the phase purity of the two latter, could be observed from the comparison of the experimental and simulated PXRD patterns (Fig. 3).

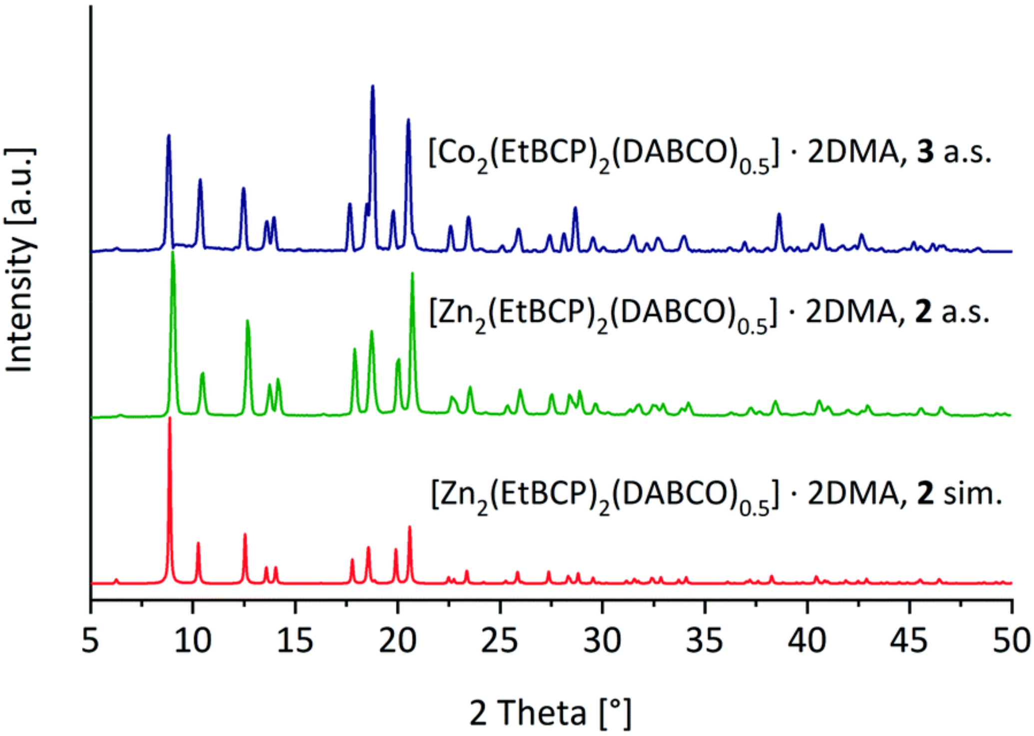

Fig. 3 PXRD patterns of [Zn_2(EtBCP)$_2$(DABCO)$_{0.5}$]·2DMA, **2** (red) simulated from X-ray crystal diffraction data and measured for the as-synthesized **2** (green) and for the as-synthesized [Co_2(EtBCP)$_2$(DABCO)$_{0.5}$]·2DMA, **3** (blue).

The isostructural compounds **2** and **3** crystallize in the *I4/m* space group, when the synthesis is done in DMA (interestingly, no product was obtained from DMF, and vice versa, **1** was not possible to obtain from DMA); the further description will be given on the example of **2**. The asymmetric unit contains two crystallographically independent metal ions, one deprotonated EtBCP^{2-} ligand, one DABCO ligand (the two latter represented by independent halves) and one uncoordinated DMA guest molecule (Fig. 4).

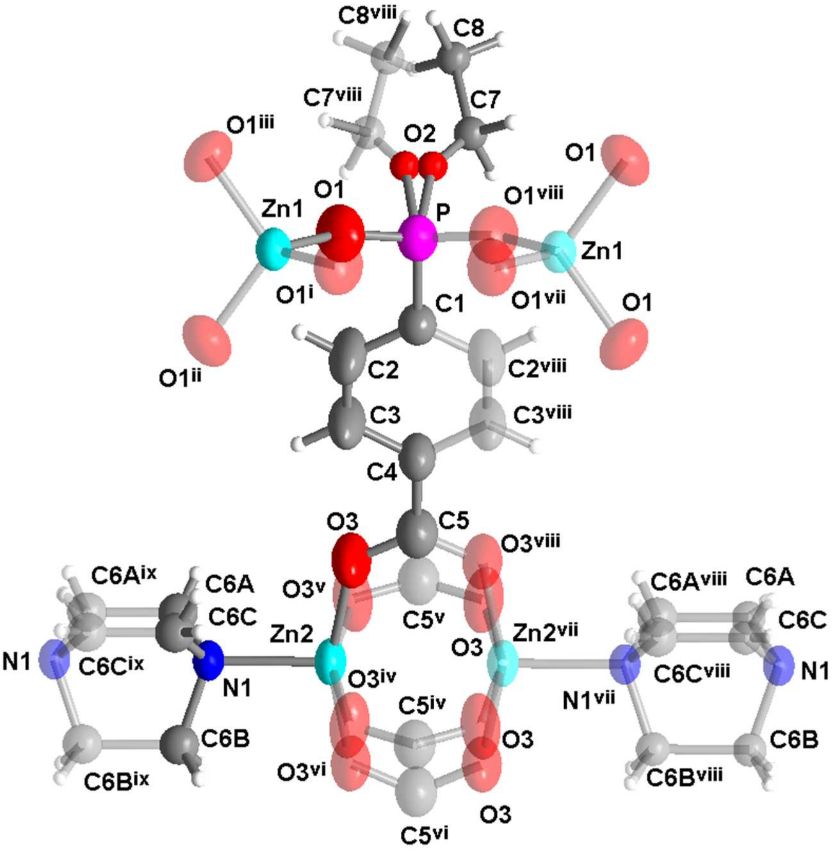

Fig. 4 The extended asymmetric unit of $[Zn_2(EtBCP)_2(DABCO)_{0.5}]\cdot 2DMA$, **2** in a thermal ellipsoid (50%) plot representation (with the exception of the disordered ethoxide group, which is plotted in ball and stick model for clarity). The DMA guest molecule and the disorder of the DABCO molecule is not given for clarity; see Fig. S16[†] for the disorder modelling. Symmetry-related atoms are depicted semitransparent. Symmetry transformations: (i) −x + 1, −y, z; (ii) −y + 1/2, x − 1/2, −z + 3/2; (iii) y + 1/2, −x + 1/2, −z + 3/2; (iv) y, −x + 1, z; (v) −y + 1, x, z; (vi) −x + 1, −y + 1, z; (vii) −x + 1,−y + 1, −z + 1; (viii) x, y, −z + 1; (ix) x, y, −z + 2.

The Zn1 atom has a tetrahedral environment consisting of four monoester phosphonate groups. Neighboring metal atoms are joined by the bridging monoester phosphonates, forming a linear 1D $\{Zn_2(PO_2(OEt))_2\}_n$ chain as an infinite SBU (Fig. 5a). This arrangement is relatively typical, and similar zinc and cobalt phosphonate chains are also known for instance in $[(enH_2)_2][Zn(PO_4)_2]$, $[C_{10}N_4H_{26}][Zn_5(H_2O)_4IJHPO_3)_6]\cdot 4H_2O$, $[C_6N_2H_{18}][Zn_3(HPO_3)_4]$ and $[C_5N_2H_{14}][Co(HPO_4)_2]$.[59–61] The Zn2 atom is pentacoordinated, adopting a $\{ZnO_4N\}$ square pyramidal environment. Together with the carboxylate and DABCO ligands, the Zn2 atoms constitute the DABCO ‘capped’ $\{[Zn_2(RCOO)_2(DABCO)]\}_n$ paddle-wheel unit, which is also well known.[35,50] The DABCO associates the paddle-wheel units in a chain, so it is possible to interpret the latter as a 1D SBU, instead of the interpretation on the level of discrete paddle-wheel units.

The structure of the framework is fully determined by the geometries of the two SBUs, connected by linear organic joints (Fig. 5c).

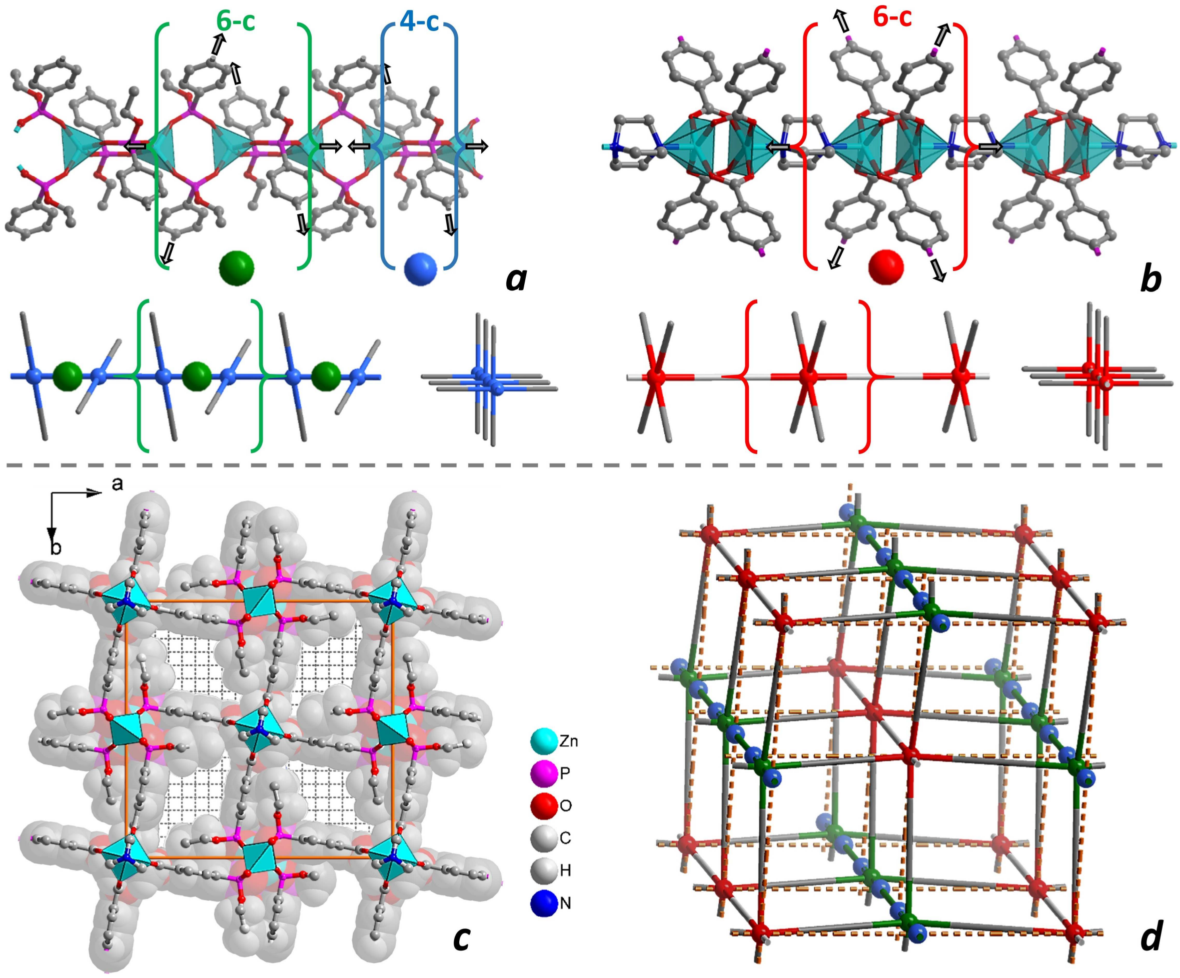

Fig. 5 The structural organization of **2** and **3**: (a) the $\{Zn_2(PO_2(OEt))_2\}_n$ phosphonate-monoester chain-SBU; the 4-c $\{Zn_2(PO_2(OEt))_2\}$ and the 6-c $\{[Zn_2(PO_2(OEt))_2]_2\}$ topological node interpretations are explained under the molecular drawing. (b) The $\{Zn_2(COO)_4(DABCO)\}_n$ extended paddle-wheel chain-SBU sustained by standard paddle-wheel units, joined axially by the bridging DABCO molecules. (c) The view on the framework along the c-axis (no H-atoms are shown for clarity) with an underlay-image of the ball-and-stick model image (with H-atoms shown) and a 1 Å grid, limited to the pores. (d) A topological representation of the framework, with the primary interpretation as a 6,6-c net (green and red nodes, **pcu**). The alternative connections on the level of the 4,6-c net interpretation (blue and red balls, $\{5^5{\cdot}6\}_2\{5^8{\cdot}6^4{\cdot}8^3\}$) are given in thin yellow dashed lines. Additional structure images for 2 are given in Fig. S17 and S18, ESI.†

There is a clear similarity between the two 1D SBUs. Their ‘cruciform’ projections along the main axis are indistinguishable in idealized high-symmetry representation. The idealized paddle-wheel unit represents 2 × 2 collinear directions (D_{4h} local symmetry), which are mutually orthogonal. The idealized prototype of the $\{[Zn_2(PO_2(OEt))_2]\}_n$ SBU (Fig. 5a; fragment in green brackets) features the same 2 × 2 mutually orthogonal pairs, lying not within a single, but within two parallel planes (D_{2d} local symmetry of a translationally independent part). A very simple and efficient synergism is possible because both SBUs ensure mutually orthogonal orientations of the connecting struts.

The two types of 1D SBUs, each possessing four, pairwise orthogonal, bonding directions run parallel in the structure of **2**. The resulting framework could be interpreted to have a primitive cubic underlying net, **pcu**, if the 6-connected {[$Zn_2(PO_2(OEt))_2]_2$} and extended paddle-wheel (*i.e.* including the DABCO-connectivity) moieties are taken as nodes (Fig. 5a, b, d and S17, ESI†). Other interpretations are possible as infinite SBUs could be fragmented to units of finite connectivity. The interpretation above is the most 'natural', taking into account the geometry of the fragments and the reduction of the framework to a frequent, fundamental and easily recognizable case. Under the simplest interpretation on the level of 4-c {$Zn_2(PO_2(OEt))_2$} and the 6-c paddle-wheel units the respective net is a two nodal $(4\text{-c})_2(6\text{-c})$ net with a $\{5^5{\cdot}6\}_2\{5^8{\cdot}6^4{\cdot}8^3\}$ point symbol (Fig. 5d and S17g; see ESI† for additional details).[62]

In comparison, the structure of **1** without the bridge of still unknown origin (equivalent to DABCO regarding the connectivity) represents the well-known 4,4-c **nbo** net on the level of the 4-c {$Zn_2(PO_2(OEt))_2$} and 4-c {$Zn_2(COO)_4$} paddle-wheel units (Fig. S17f, ESI†).

The experimental observation of **1**, which is not reinforced by DABCO, upholds the high resilience of the structural organization of **1–3**. However, the impossibility to synthesize **1** in a large quantity and in a phase-pure form indicates that the use of DABCO is practically essential. Due to the poor quality of **1**, the nature of bridging ligands between the paddle-wheel SBU is not clear. We hypothesize that trace impurities, which also might form during the synthesis, could act as bidentate bridging ligands, analogously to DABCO. It is potentially enough to have a small amount of such molecules to produce seeds of crystals with a structural type analogous to **2**. The crystal structure of **1** suggests a site sharing at the bridging ligand position, with a seemingly dominant contribution by solvent molecules.

The structure organization principle of **2** (Fig. 6) defines the acceptable length of the N-donor ligand with only a minor tolerance.

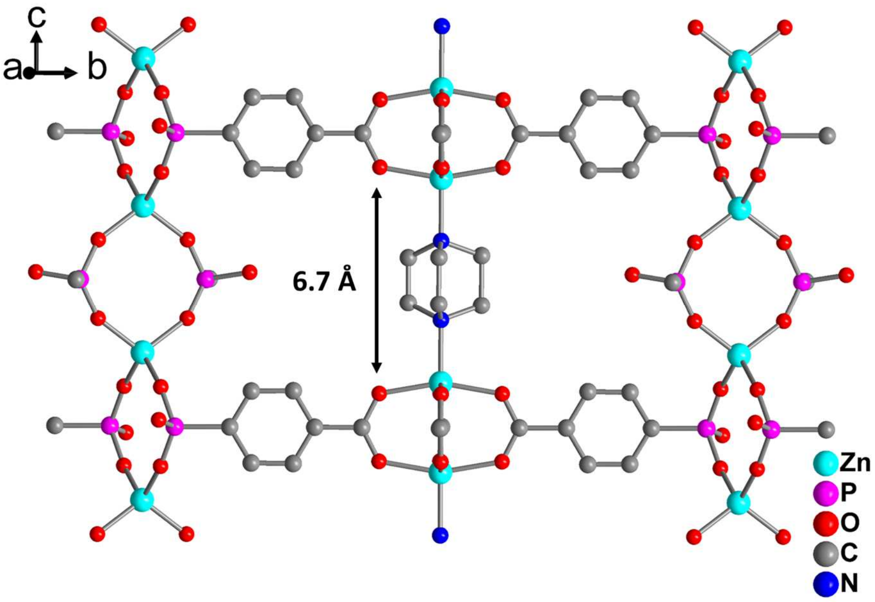

Fig. 6 A representative fragment of **2** showing the principles of structural organization. The length scaling for phosphonate ligand is potentially allowed, but not for the N-donor ligand-bridge.

The DABCO molecule fits nearly ideally the interstice of 6.0–7.0 Å (6.3 Å in **1** and 6.7 Å in **2**) between the paddle-wheel units. Theoretically, there is a chance also to incorporate a two-times longer ligand, like 4,4′-bipyridine (11.2 Å), when every second metal atom in the chain is absent. Such a structure is potentially possible, if every second phosphonate will not propagate the connectivity in the $\{[M_2(R'O)(R)PO_2][M_2(R''O)(R^T)PO_2]\}_n$ 1D chain-SBU. Half of the chelating ligands of the latter should be blocking monofunctional monoalkylphosphonates (with terminal substituent designated as R^T), or even monofunctional carboxylate terminal co-ligands (hence, they are potentially interesting modulators). The ‘terminated’ half of the rings would not propagate connectivity, which continues for those fragments only along the 1D phosphonate chain. As a result, a **pcu** topology would ensue again, but with longer edges, compared to the underlying net of **2**.

On the other hand, the arbitrary length-scaling of the phosphonate ligand in the structure type of **2** is in principle allowed without any special conditions. The structure would scale in two out of the three directions. The retained scale along the c-axis should provide enough mechanical stability (MOFs with ultra-large pores, like in IRMOF-74-XI representative of the MOF-74 isoreticular series, d_{pore} > 80 Å, are build according to similar principles, *i.e.* geometric scaling in two out of three directions). Therefore, the structure type of **2** appears to be of general importance, as a paradigmatic instance of a potential isoreticular series.

Thermogravimetric and gas adsorption analyses

Thermogravimetric analysis (TGA) of the as-synthesized $[Zn_2(EtBCP)_2(DABCO)_{0.5}]\cdot 2DMA$, **2** shows a weight loss of 23.9% up to 150 °C (calc. 21.3% for two DMA molecules of the ascribed formula unit; Fig. 7a). The chemical decomposition of the compound takes place at 320 °C (Fig. 7b).

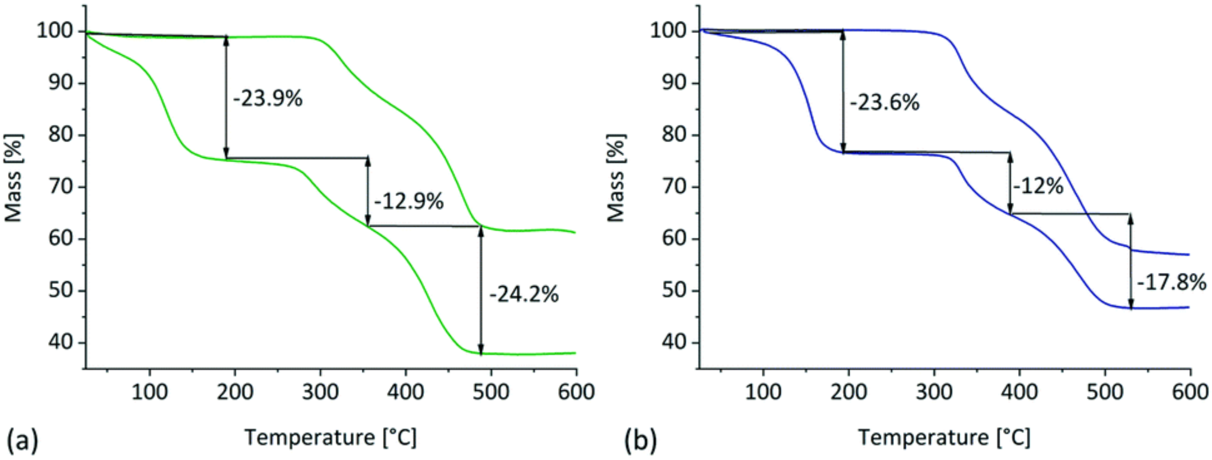

Fig. 7 TGA curves, 20–600 °C with a heating rate of 5 K min^{-1} under N_2 atmosphere for (a) the as-synthesized $[Zn_2(EtBCP)_2(DABCO)_{0.5}]\cdot 2DMA$, **2** (top curve) and the activated $[Zn_2(EtBCP)_2(DABCO)_{0.5}]$, **2′** (bottom curve) (b) for the Co-analogues, **3** and **3′**.

The structures of **2** and **3** feature roughly rectangular channels, running along the c-axis, and forming a 3D pore network *via* interconnections along other axes as well. The maximum included sphere diameter is 5.9 Å, while the maximum passable sphere diameter is 4.6 Å (as calculated by Zeo^{++};[63] here and below 3.68 Å probe diameter corresponding to N_2 is implied, if not given otherwise). The channels would be significantly larger if not the protruding ethyl groups of the ligand. However, there is a residual porosity, with a formal calculated surface area of 904–1057 m^2 g^{-1}. The geometrically calculated potential solvent accessible void volume is only 4.8% for N_2, but quickly grows to 7.3% for CO_2 (3.30 Å probe), 15.7% for H_2O (2.40 Å) and 36.7% for a formal probe of 1.0 Å diameter (Table S4†). The fast growth of the void volume is due to the narrow and curved pores, which accepts only a small amount of guest molecules with sizes approaching the pore diameter. All the data in this paragraph was calculated using the single crystal structure of **2** with removed solvent molecules and collapsed disorder $[Zn_2(EtBCP)_2(DABCO)_{0.5}]$ (Table S4, see also the comments in the ESI†).

It is important to note for the further discussion that the structural organization of **2** and **3** allows expecting enhanced flexibility due to the rotation of the phosphonate and carboxylate moieties around the axis of the 1D rod-like SBUs. Such type of flexibility is well known for carboxylate MOFs, e.g. for MIL-53, where the channels, running along the rod-like SBUs are already partially asymmetric (for example having rather a lozenge than a square shape; the latter case corresponds to a formal state of mechanic equilibrium and is much more resistant to deformation). The monoethylphosphonate differs from carboxylate by geometry (tetrahedral *vs.* trigonal). The {$P(OEt)O_2M_2$} arrangement constituting the chain SBU is out of the plane of the ligand, while the carboxylate based {CO_2M_2}, in contrary, remains coplanar, or at least co-axial, with the phenyl group after coordination. Hence, the mechanical strain, propagating along the ligand is displaced relatively to the axis of the 1D rod-like SBU and acts as a lever with ~2.0 Å length (for carboxylates the offset lever length is zero; the difference is very clear from Fig. 5c), which is a structural level argument for increased flexibility.

Compounds **2** and **3** were washed after the synthesis with DMA and activated at 160 °C under vacuum. The removal of the DMA guest molecules in **2** or **3** leads to a phase transition and formation of products **2′** or **3′** respectively, characterized by quite different PXRD patterns. We were not able to elucidate their structures, but the samples remain at least partially crystalline. Moreover, the soaking of **2′** or **3′** in DMA reinstates the initial structures of **2** and **3**, as witnessed by PXRD (Fig. 8 and S20, ESI†). Complete reversibility of the solvent removal is a supporting argument for retained integrity of the framework in the degassed structures, as well as for its significant flexibility.

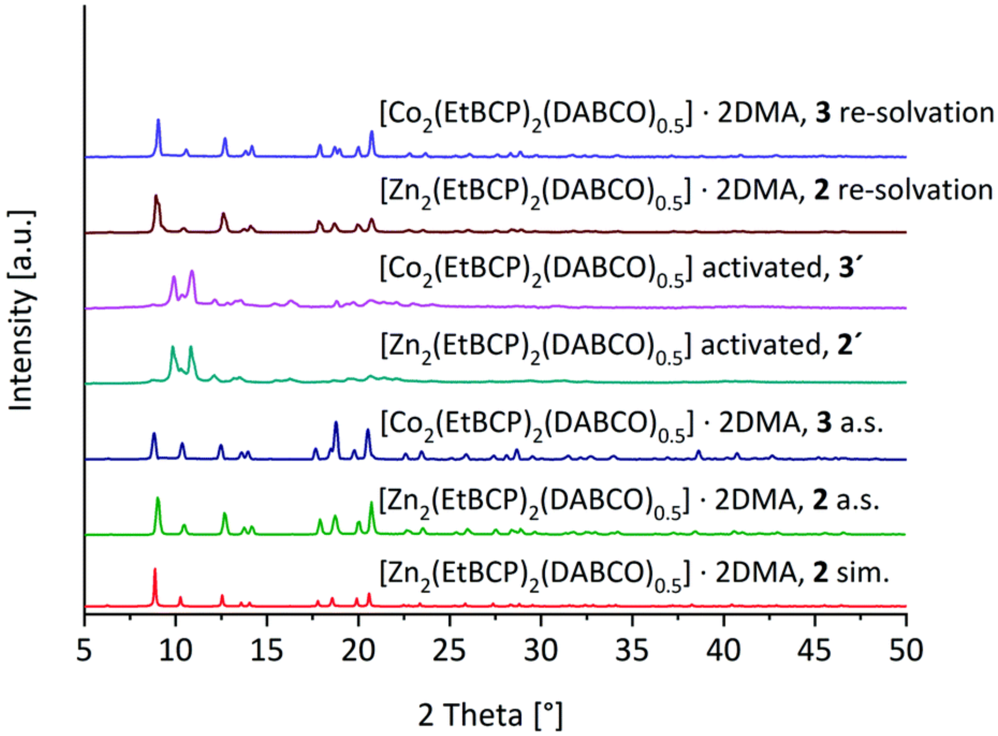

Fig. 8 Comparison of the PXRD patterns: simulated for the SCXRD structure of **2**; as-synthesized bulk **2** and **3**; activated **2′** and **3′**; re-solvated after the soaking of the activated samples in DMA.

The gas adsorption behavior of the activated [$Zn_2(EtBCP)_2(DABCO)_{0.5}$], **2′**, and [$Co_2(EtBCP)_2(DABCO)_{0.5}$], **3′**, materials was studied for N_2 (77 K) and Ar (87 K), CO_2 (195 K, 273 K, 293 K) and CH_4 (273 K, 293 K).

The adsorption of N_2 is negligible, which is expected for compounds with narrow pores (Fig. 9a and b). The maximum thorough sphere pore radius of 4.6 Å, assessed for the solvated structure of **2** (Table S4†), is only ~1 Å larger than the kinetic diameter of the N_2 molecule.

The respective adsorption kinetics should be very slow, which is aggravated by a low accessible pore volume, estimated at ~4.8% of the total volume (Table S4†). Furthermore, even slight flexibility of the structure could decrease the pores further, rendering the compound to be non-porous. In contrary, the uptake of the kinetically slightly smaller CO_2 was significant (115 $cm^3\ g^{-1}$ for **2′** and 128 $cm^3\ g^{-1}$ for **3′** at 1 bar, 195 K; Fig. 9), which allowed making a crude estimation of the Langmuir surface area (P/P_0 = 0.004–0.04 range, 195 K). The surface area of **2′** and **3′** are estimated to be 330 $m^2\ g^{-1}$ and 327 $m^2\ g^{-1}$, respectively (see ESI† for details and also for the even more imprecise BET estimation, which is, nevertheless provides comparable values).

More interestingly, the CO_2 adsorption isotherms at 195 K demonstrate two distinctive steps. The second step, starting at P/P_0 = ~0.1 could be associated with pore opening from small to larger pore size.[64] It is rather a gradual process with a relatively narrow ~0.1P/P_0 interval and could be classified as F-I type (the sudden opening, *i.e*. a strong rise of adsorption in a small P/P_0 is classified as F-II; the cases of **2′** and especially **3′**, with a slightly narrower interval, are approaching the latter type).[64] The Gurvich rule was used to determine the pore volume from the CO_2 adsorption isotherms at 195 K (Fig. 9a and b).[65] The micropore volume corresponding to the first step is 0.11 and 0.12 $cm^3\ g^{-1}$ for **2′** and **3′** (P/P0 < 0.08 and < 0.12 respectively). The total values for the combined two steps are ~0.21 and 0.23 $cm^3\ g^{-1}$ (maximum estimate, P/P_0 = 1.0) for **2′** and **3′** respectively.

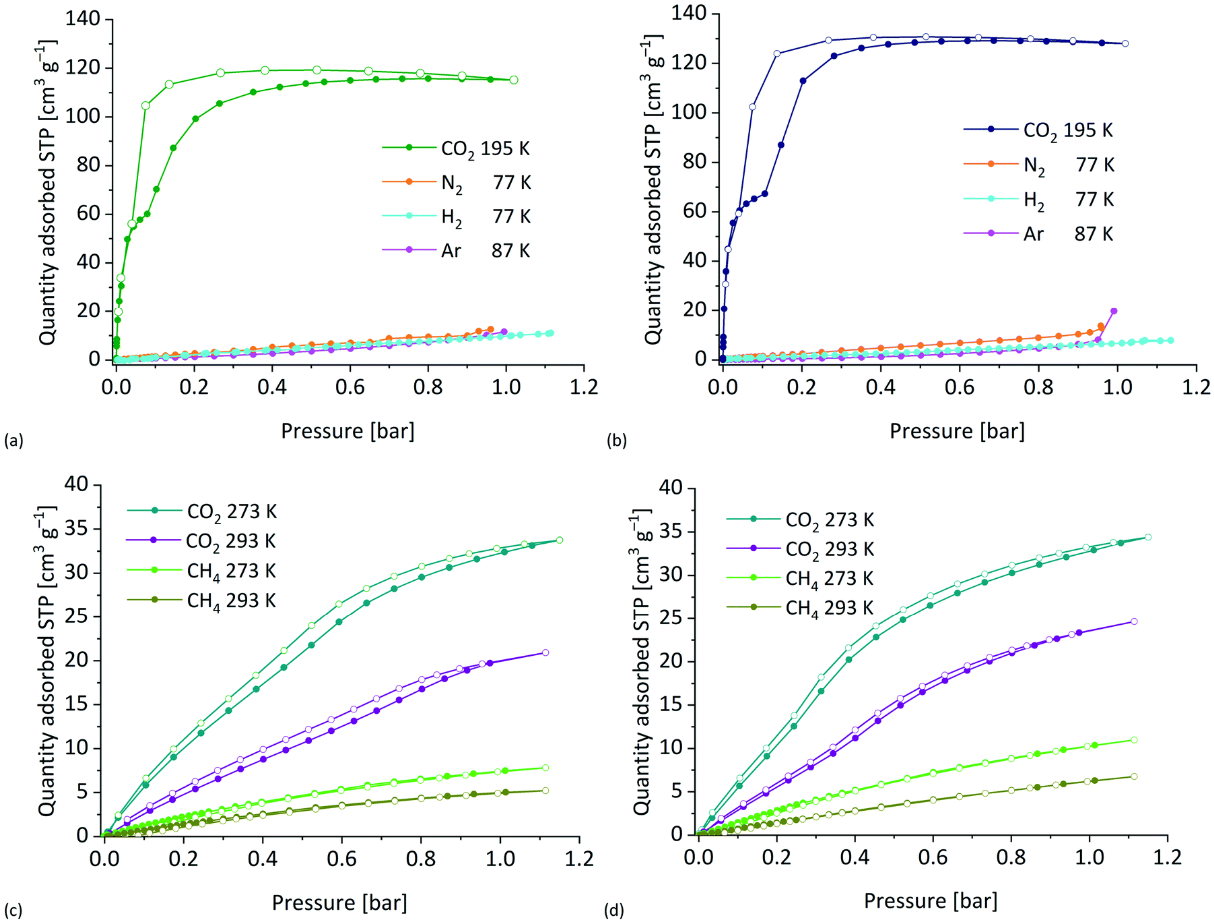

Fig. 9 Adsorption isotherms (the desorption branches are not shown for clarity in the cases of N_2, H_2 and Ar, see Fig. S23† for further details) for (a) [$Zn_2(EtBCP)_2(DABCO)_{0.5}$], **2′**; (b) [$Co_2(EtBCP)_2(DABCO)_{0.5}$], **3′**; (c) **2′**; (d) **3′**.

Therefore, significant framework flexibility, manifesting itself in a structural transformation, was found at a low temperature (the flexible behavior was also observed for carboxylate MOFs with DABCO as a co-ligand).[35,49,66,67] The steep rise of the second step (tendency towards “F-II” type) suggests rather an existence of bistability than a continuity of states, which correlates well with the observed crystallinity of the as-synthesized and degassed 2 (and 3), and yet with the strong differences of the respective PXRD patterns.

The hysteresis observed on the CO_2 adsorption isotherms for **2′** and **3′** at low pressures is kinetically conditioned. It was checked on the example of **3′** that as the equilibration time increases, the hysteresis width decreases. For the longest adsorption experiment (~5+ times longer equilibration time per acquisition point) the adsorption and desorption branches for the first step nearly coincide, while the remaining hysteresis is nearly solely limited to the second step (see Fig. S28 and Table S5 and short corresponding discussion in the ESI†). Hence, the desorption branch cannot be associated with a “metastable opened form”: longer equilibration times demonstrate full reversibility at least at $P/P_0 < 0.1$ pressures. The heat of adsorption for CO_2 from adsorption isotherms at 273–293 K is calculated to be 33.0 and 21.0 kJ mol^{-1} for **2′**

and **3′** at zero coverage (Fig. S22†). The energy difference is significantly higher than expected, and we believe that the lower crystallinity of **3** should at least partially be held responsible. The sorption data for CO_2 at 195 K, 273 K and 293 K are summarized in Table 1.

Table 1 CO_2 adsorption data for $[Zn_2(EtBCP)_2(DACO)_{0.5}]$, **2′** and $[Co_2(EtBCP)_2(DABCO)_{0.5}]$, **3′** at 1 bar

Data	**2′**			**3′**		
Temperature, K	195	273	293	195	273	293
Quantity adsorbed, $cm^3\ g^{-1}$	115	32	20	128	33	23
($mmol\ g^{-1}$)	(5.1)	(1.4)	(0.9)	(5.7)	(1.5)	(1.0)

CO_2 adsorption at 298 K and 20 bar shows a larger uptake for **3′** with 147 mg g^{-1} compared to **2′** with 97 mg g^{-1} (Fig. 10).

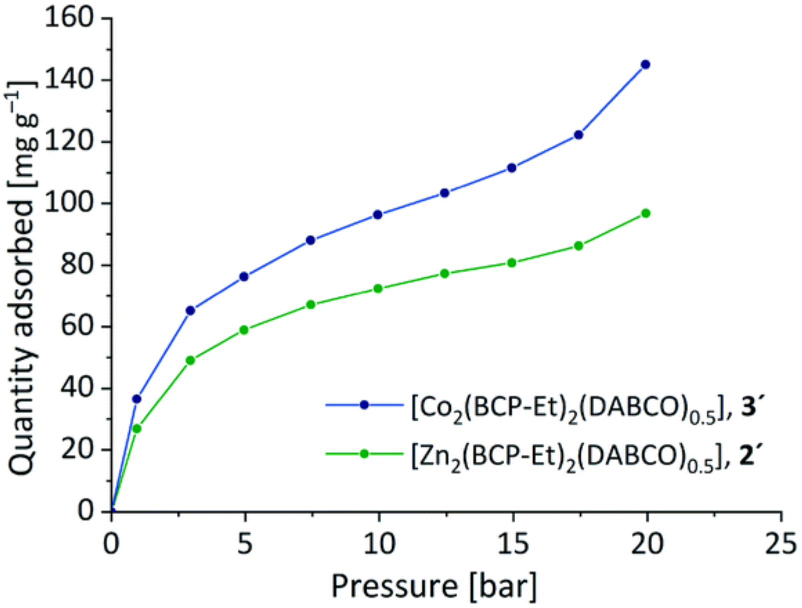

Fig. 10 High-pressure CO_2 adsorption isotherms at 298 K for **2′** (green) and **3′** (blue).

Both isotherms demonstrate inflection points at approximately 12 bar indicating possible gradual structural transformations. The dissimilarity of the transformation energetics is the only evident explanation of such a strong difference. The pore-sizes for **2′**, **3′** are similar at low pressures at room temperature, but start to diverge at elevated pressures (note that minor, but evident dissimilarities between **2′** and **3′** are visible at low pressures and low temperatures, as discussed above). The adsorption conditions (*P, T*) are approaching the supercritical state of CO_2 and hence the use of the Gurvich rule for the determination of the pore volume is highly questionable. Still, we have used it as an estimate: at 298 K the pore volume at the first step was calculated to be 0.11 $cm^3\ g^{-1}$ for **2′** and 0.15 $cm^3\ g^{-1}$ for **3′** (12 bar or $P/P_0 = 0.19$ in both cases) (Fig. S21, ESI†). It is presumed that after the pores are filled to a certain extent, not very different for the low (195 K) or high temperatures (298 K), a structural transformation occurs.

The notable affinity to CO_2 might partially explain another, not quite clear observation, namely the negligible adsorption of Ar, which is similar to N_2. It is possible, that the increased adsorbent–adsorbate affinity is necessary for opening up the initially closed pores of the flexible framework.

It is interesting to compare the experimentally derived micropore volumes at the transformation points with values calculated for the structures of **2**/**3** (CO_2 adsorption at 195 K). The values are respectively 0.11/0.12 $cm^3\,g^{-1}$ (P/P_0 = ~0.1, 195 K), 0.11/0.15 and $cm^3\,g^{-1}$ (P/P0 = ~0.19, 195 K) **3′** *vs.* 0.065 $cm^3\,g^{-1}$ calculated geometrically (Table S4, ESI†). The transformations take place at an adsorption value, which corresponds reasonably well to the calculated maximum accessible pore volume for the structure of **2** with removed solvent molecules (0.065 $cm^3\,g^{-1}$). This observation supports the viewpoint that the transformation is stimulated by complete pore filling of the less porous variant of the structure. The low precision of the estimated value should not be surprising: the calculated accessible volume in the structure of **2** quickly grows with the decrease of the size of the probe and reaches 37% for a probe of ~1.0 Å. While such probe size is much smaller than a molecular size, the steep growth of the void volume shows that there is potentially available space, which could, possibly, be partially accessed upon minor structural deformations. This is what, evidently, takes place.

Moisture stability, water vapor adsorption, and liquid solvent stability tests

Both the non-degassed **2** and **3**, as well as the non-degassed **2′** and **3′** demonstrated only a minor change of PXRD patterns upon two days of exposure to ambient air (Fig. S29†). The satisfactory stability allowed to measure the water-vapour adsorption at 293 K in the range of 0–0.95P/P_0 for the single case of **3′**, representative enough for the case of isostructural compounds. Relatively low affinity (IUPAC isotherm type III) and a maximum uptake of 48 mg g^{-1} was observed (Fig. S30†), however the very well-defined hysteresis indicates that the binding of the adsorbed water associated with the second coordination sphere of the metal ions is substantial. The relatively low affinity is in line with the hydrophobic ‘padding’ of the pores by the organic ligands and not the least by the ethyl substituent of the monoethylphosphonate, protruding into the channels. The small maximum uptake correlates well with the low accessible pore volume. The crystallinity of the sample did not change significantly during the experiment as witnessed by PXRD.

The long-term solvent exchange of **2** with chloroform, ethanol, acetone (~3 days each), and water (~1 day) was called to check the stability of the framework against liquid solvents (no prior degassing was carried out; the degassing itself is responsible for some loss of crystallinity, associated with PXRD peak broadening, which could mask finer effects, caused by the action of moisture). After PXRD measurements, the samples were exchanged again by DMA, in order to test the possibility to return to the state of crystallinity of the as-synthesized **2** (Fig. S31†). The exchange with chloroform caused minor changes, with ethanol moderate, and with acetone a transformation to another phase. However, the subsequent exchange with DMA reinstated the initial crystallinity in full, providing another argument for flexibility of the framework of **2**, this time upon the action of solvent molecules (see ESI†). On the other hand, water causes an irreversible transformation to a phase with an appreciable crystallinity, and hence **2** should be regarded as instable to the action of liquid water for prolonged time. It is worth to stress that this instability is rather not an irreversible hydrolysis into an amorphous phase as in the majority of other MOFs, but a crystal-to-crystal transformation.

Conclusions

Two new isostructural zinc and cobalt monoethylphosphonate-carboxylate MOFs, $[Zn_2(EtBCP)_2(DABCO)_{0.5}]\cdot 2DMA$, **2** and $[Co_2(EtBCP)_2(DABCO)_{0.5}]\cdot 2DMA$, **3** including DABCO as a co-ligand were synthesized. The structures are built upon the $\{M_2(PO_2)OEt))_2\}_n$ chains already observed in phosphonate-monoester coordination polymers and on DABCO-expanded archetypal paddle-wheel carboxylate units. A potentially very important observation for structure-design heuristics is the nearly equal length of the six-connected $\{[Zn_2(PO_2)OEt))_2]_2\}$-phosphonate-monoester- and the $\{Zn_2(COO)_4(DABCO)\}$ SBU-fragments (in this work only the simplest, **pcu** framework is demonstrated, but due to the equivalence in dimensions a number of other framework topologies could also be expected). The structural organization shows high resilience, as the ‘parent’ compound, the $[Zn_2(EtBCP)_2(Bridge/Solv)]\cdot(Solv')$, **1**, was also observed as a minor product in a DABCO-free synthesis; the structural motif for **1**, similar to **2** and **3** was experimentally confirmed. Importantly, the compounds **2** and **3** represent a structural type, which permits the elongation of the monoalkylphosphonate ligand, leading to metrical scaling in two directions in isoreticular analogues (see Fig. S19†). Such scaling is preferable, comparing to the scaling in all directions, for structural stability and avoiding interpenetration. The activated compounds **2′** and **3′** show two-step CO_2 adsorption at low-pressure (195 K) and an analogous behavior with an inflection point on the isotherm at high pressure (298 K). The effects could be explained by structural flexibility, which is supported by the analysis of the structure (the ‘lever’ effect of the trigonal phosphonate, in contrary to trigonal-planar carboxylate, remaining in-plane with the 1D rod-like SBU as well as the particularly steep calculated growth of accessible volume in the structure by decrease of the probe size, indicating the capacities for structural rearrangement).

Experimental section

Materials and measurements

All the chemicals (purity equivalent to ACS grade or higher) were obtained from commercial sources and used without future purification.

The CHN elemental analysis was performed using Perkin Elementar Vario EL III analyzer. IR-spectra were recorded on a Bruker Tensor 37 IR spectrometer (Bruker Optics, Germany) equipped with an ATR unit. ESI-MS spectra were recorded with a Thermo-Quest Ion Trap API mass spectrometer Finnigan LCQ Deca. Thermogravimetric analysis (TGA) was performed with a Netzsch TG 209 F3 Tarsus using an aluminium crucible in the 20–600 °C range at 5 K min^{-1} rate under N_2 atmosphere. The powder X-ray diffraction patterns (PXRDs) were obtained on a Bruker D2 Phaser diffractometer using Cu-Kα radiation (λ = 1.5418 Å; 30 kV, 10 mA source supply parameters) and a flat low-background silicon sample holder.

The low pressure gas adsorption isotherms for CO_2, CH_4 and H_2 were measured using a Micromeritics ASAP 2020 automatic gas sorption analyzer, equipped with one vacuum pump for the sample preparation and one for the analysis ($\sim10^{-6}$ Torr ultimate vacuum in the manifold).

The samples were degassed at the preparation port of the analyzer until the pressure rising rate in the temporarily closed manifold was less than 2 µTorr min^{-1} at 160 °C. After degassing, the sample tube was weighted (seal frits were used for permanent sealing) and transferred to the analysis port of the sorption analyzer. Before the sorption experiments, the compounds were subjected to a short, repeated degassing to remove remaining gas molecules. Helium gas was used for the determination of the warm and cold free-space of the sample tubes. The volumes of the adsorbed gases are given at standard temperature and pressure, STP (293.15 K, 101.325 kPa). The adsorption isotherms were measured for CO_2 at 195, 273, 293 K; for CH_4 at 273, 293 K and for H_2 at 77 K. The isosteric heat of adsorption values for CO_2 from the isotherms at 273.15 K and 293.0 K were calculated using Clausius–Clapeyron equation as implemented in the ASAP 2020 v3.05 software. The N2 and Ar sorption isotherms were additionally measured on a Quantachrome Autosorb iQ MP automatic gas sorption instrument, using parameters, similar to described for the measurement with the ASAP 2020. All used gases (He, N_2, H_2, CO_2, Ar, CH_4) were of ultra-high purity (UHP, grade 5.0, 99.999%). The CO_2 gas adsorption isotherms for 0–20 bar pressures at 298 K were measured using Rubotherm IsoSorb Static instrument, which employs a gravimetric principle. The weight change was measured with a magnetic suspension balance (resolution 0.01 ± 0.03 mg).

The water vapor sorption isotherm was measured on a Quantachrome VSTAR vapor sorption analyser at 293 K.

The single crystal X-ray diffraction data were collected on a Bruker Kappa APEX II DUO equipped with an APEX II CCD area detector, using Mo-Kα radiation (λ = 0.71073 Å) generated by a microfocus sealed tube source. The data collection was performed by ω scans and controlled by APEX2 software.[68] The data reduction was performed using SAINT[68] and the experimental absorption correction using SADABS.[69] The structure was solved by direct methods (SHELXS-2016), the refinement was done by full-matrix least squares on F^2 using the SHELXL-2018 program suite,[70] and the graphical user interface (GUI) ShelXle.[71] The molecular graphics were prepared using Diamond.[72]

Ligand synthesis

Methyl 4-iodobenzoate. The procedure was adapted from Zhao et al.[73] Concentrated H_2SO_4 (5 mL) was carefully added to a solution of 4-iodobenzoic acid (10 g, 0.04 mol) in MeOH (200 mL). The mixture was refluxed for 14 h. After cooling to room temperature, the solvent was removed in vacuo and the residue was dissolved in dichloromethane (100 mL). The organic layer was washed with saturated $NaHCO_3$ solution (100 mL), brine (100 mL) and dried over $MgSO_4$. Methyl 4-iodobenzoate was obtained as a white solid after removal of the solvent under reduced pressure (9.6 g, 91%); ^{1}H NMR (300 MHz, $CDCl_3$): δ 7.80 (d, *J* = 8.6 Hz, 2H), 7.73 (d, *J* = 8.6 Hz, 2H), 3.91 (s, 3H); ^{13}C NMR (75 MHz, $CDCl_3$): δ = 166.7, 137.9, 131.2, 129.7, 100.9, 52.4.

Methyl 4-(diethoxyphosphoryl)benzoate. The procedure was adapted from Jaffrès et al.[74] A stirred mixture of $NiBr_2$ (0.87 g; 4 mmol), methyl 4-iodobenzoate (13.0 g, 50 mmol) and mesitylene (14 mL) were heated to 180 °C under nitrogen atmosphere. Triethylphosphite (12.8 mL, 75 mmol) was added dropwise for 4 h. During the addition of triethylphosphite, a color change of the solution from red to violet and finally to yellow was observed. After the addition, the solution was heated further at 180 °C for 2 h yielding a yellow suspension. Then, the solvent was removed in vacuo. Water (100 mL) was added to the residue and the mixture extracted with diethyl ether (2 × 50 mL). The organic phase was washed with brine (50 mL) and dried over $MgSO_4$. The reaction mixture was concentrated in vacuo to produce an orange viscous oil that was purified by silica gel column chromatography using (DCM/EtOH: 98/2) as eluent to give a colorless viscous oil of methyl 4-(diethoxyphosphoryl)benzoate (7.1 g, 52%); ^{31}P NMR (121 MHz, $CDCl_3$): δ = 17.68; 1H NMR (300 MHz, DMSO-d_6): δ 8.09 (dd, ^{3}J = 8.5, ^{4}*J* = 3.8 Hz, 2H), 7.86 (dd, ^{3}*J* = 12.8, 3*J* = 8.5 Hz, 2H), 4.14–3.97 (m, 4H), 3.88 (s, ^{3}H), 1.23 (t, *J* = 7.2 Hz, 6H); ^{13}C NMR (75 MHz, DMSO-d_6) δ 165.5, 133.4, 132.9, 131.7, 129.2, 62.0, 52.5.

***O*-Ethyl-P-(4-carboxyphenyl)phosphonic acid or 4-(ethoxyhydroxyphosphinyl)benzoic acid (H_2EtBCP).** The procedure is adapted from Lee et al.[45] Methyl-4- (diethoxyphosphoryl)benzoate (1.5 g, 5.5 mmol) was heated in a mixture of aqueous NaOH (2 mol L^{-1}, 33 mL) and EtOH (33 mL) at 80 °C during 3 h. The reaction mixture was then concentrated in vacuo to a third of the volume and acidified with cooled 1 N HCl to pH 1, followed by extraction with dichloromethane. The combined organic extracts were dried over Na_2SO_4 and the solvent was removed under reduced pressure, to afford the product as a white solid (0.71 g, 56%); ^{31}P NMR (121 MHz, DMSO-d_6): δ = 14.61; ^{1}H NMR (300 MHz, DMSO-d_6) δ 8.04 (dd, *J* = 8.4, *J* = 3.6 Hz, 2H), 7.81 (dd, *J* = 12.6, J = 8.4 Hz, 2H), 3.96–3.86 (m, 2H), 1.18 (t, *J* = 7.1 Hz, 3H); ^{13}C NMR (75 MHz, DMSO-d_6) δ 166.79, 135.9, 133.5, 131.3, 129.2, 61.0, 16.3.

MOF syntheses

Synthesis of $[Zn_2(EtBCP)_2(DABCO)_{0.5}]\cdot 2DMA$, **2**; $[Co_2(EtBCP)_2(DABCO)_{0.5}]\cdot 2DMA$, **3**. The compounds **2** and **3** were synthesized according to the same procedure (for the synthesis of $[Zn_2(EtBCP)_2(Solv)]\cdot Solv'$, **1**, see ESI†). $Zn_2(NO_3)_2\cdot 6H_2O$ (26.77 mg, 0.09 mmol) or $Co_2(NO_3)_2\cdot 6H_2O$ (26.2 mg, 0.09 mmol), DABCO (5 mg, 0.045 mmol) and H_2EtBCP (20 mg, 0.09 mmol) were dissolved in DMA (2 mL). The mixture was transferred in a thick-walled borosilicate glass tube, sealed with a screw-cap and heated up to 100 °C for 8 h. The temperature was held for 94 h and then decreased linearly to room temperature within 4 h. 34.6 mg (60%) of **2** consisting of considerably large colorless single crystals and 37.2 mg (66%) of **3** consisting of very small dark-blue single crystals, too small for a routine SCXRD experiment, were collected. The syntheses were reproduced six times.

2 Elemental analysis [%] calc. for: $[Zn_2(EtBCP)_2(DABCO)_{0.5}]\cdot 2DMA$, $C_{29}H_{42}N_3O_{12}P_2Zn_2$: C 42.61, H 5.18, N 5.14, found: C 42.3, H 5.17, N 5.01. IR (KBr) $\tilde{v}_{max}$ [cm^{-1}]: 3440, 2982, 2937, 1644, 1556, 1414, 1190, 1156, 1129, 1090, 1046, 1014, 965, 868, 848, 807, 776, 732, 703, 520, 484.

2′ (degassed **2**). Elemental analysis [%] calc. for: $[Zn_2(EtBCP)_2(DABCO)_{0.5}]$, $C_{21}H_{24}NO_{10}P_2Zn_2$: C 39.22, H 3.76, N 2.18, found: C 38.48, H 3.68, N 2.14. IR (KBr) $\tilde{v}_{max}$ [cm^{-1}]: 3436, 3068, 2981, 2934, 2902, 1636, 1553, 1503, 1419, 1157, 1128, 1079, 1042, 948, 863, 771, 729, 702, 608, 476.

3 Elemental analysis [%] calc. for: $[Co_2(EtBCP)_2(DABCO)_{0.5}]\cdot 2DMA$, $C_{29}H_{42}N_3O_{12}P_2Co_2$: C 43.30, H 5.26, N 5.22, found: C 43.07, H 2.27, N 5.11. IR (KBr) $\tilde{v}_{max}$ [cm^{-1}]: 3435, 2981, 2936, 2902, 1649, 1553, 1450, 1413, 1264, 1189, 1155, 1129, 1088, 1046, 1014, 867, 846, 806, 505, 775, 732, 703, 591, 491.

3′ EA [%] calc. for: $[Co_2(EtBCP)_2(DABCO)_{0.5}]$, $C_{21}H_{24}NO_{10}P_2Co_2$: C 40.02, H 3.84, N 2.22, found: C 39.28, H 3.91, N 2.15. IR (KBr) $\tilde{\nu}_{max}$ [cm^{-1}]: 3433, 3065, 2980, 2935, 2900, 1620, 1551, 1503, 1413, 1287, 1157, 1128, 1076, 1043, 948, 863, 771, 729, 704, 608, 482.

Structure refinement details

The DABCO molecule is located on the 4-fold axis special position. The trigonal molecule has a lower symmetry than the symmetry of the special position. The disorder was modeled using a four-component model with equal weights. The ethyl group of the ligand was refined using a two-component disorder model with equally populated components related by a mirror plane. The disordered DMA molecule was modeled similarly. All atoms in the structure except the DMA guest molecule were refined anisotropically. A part of the C–O, C–N, C–C, and N–O bond lengths in the OEt moiety and the guest solvent molecule were restrained. The hydrogen atoms of DABCO, DMA and the ethyl group of the ligand were positioned geometrically and refined using a riding model: d(C–H) = 0.96 Å (CH_2), 0.97 Å (CH_3), 0.95 Å ($C_{Ar}H$); $U_{iso}(H) = 1.2 \times U_{eq}$. The crystal data and structure refinement details are given in Table 2.

Table 2 Crystal data and refinement details for $[Zn_2(EtBCP)_2(DABCO)_{0.5}]\cdot 2DMA$, **2**[a]

Empirical formula	$C_{29}H_{42}N_3O_{12}P_2Zn_2$
M/g mol^{-1}	817.33
Crystal dimensions /mm	0.20 × 0.03 × 0.03
T /K	293
Crystal system	Tetragonal
Space group	$I4/m$
a, b, c /Å	19.912 (4), 19.912 (4), 9.5338 (17)
V /Å³	3779.9 (16)
Z	4
ρ /g cm^{-3}	1.436
μ (Mo Kα) /mm^{-1}	1.41
F(000)	1692
T_{min}, T_{max}	0.950, 0.958
$\Delta\rho_{max}$, $\Delta\rho_{min}$ / e Å^{-3}	0.81, −0.50
No. of measured, independent and observed [I > 2σ(I)] reflections	23360, 1947, 1145
R_{int}	0.094
$R[F^2 > 2\sigma(F^2)]$, $wR(F^2)$,[b] S	0.075, 0.223, 0.98

[a] The CCDC reference number is 1985571. [b] $w = 1/[\sigma^2(F_o^2) + (0.1387{*}P)^2]$ where $P = (F_o^2 + 2F_c^2)/3$. Goodness-of-fit $S = [\Sigma[w(F_o^2-F_c^2)^2]/(n-p)]^{1/2}$.

Conflicts of interest

There are no conflicts to declare.

Acknowledgements

The authors thank one of our anonymous referee, who posed interesting questions regarding the role of the in situ formed formic acid, as well as the hysteresis and kinetic effects for the CO2 adsorption, which allowed to improve the manuscript. We thank Dr. Gamall Makhloufi, then a doctoral student in the group of CJ, for collecting preliminary data for the “predecessor” structure of **1**.

References

1 W. Lu, Z. Wei, Z. Y. Gu, T. F. Liu, J. Park, J. Park, J. Tian, M. Zhang, Q. Zhang, T. Gentle III, M. Bosch and H. C. Zhou, *Chem. Soc. Rev.*, 2014, **43**, 5561–5593.

2 G. K. Shimizu, R. Vaidhyanathan and J. M. Taylor, *Chem. Soc. Rev.*, 2009, **38**, 1430–1449.

3 J. P. Zhang, Y. B. Zhang, J. B. Lin and X. M. Chen, C*hem. Rev.*, 2012, **112**, 1001–1033.

4 M. F. de Lange, K. J. Verouden, T. J. Vlugt, J. Gascon and F. Kapteijn, *Chem. Rev.*, 2015, **115**, 12205–12250.

5 Y. B. Huang, J. Liang, X. S. Wang and R. Cao, *Chem. Soc. Rev.*, 2017, **46**, 126–157.

6 J.-R. Li, R. J. Kuppler and H.-C. Zhou, *Chem. Soc. Rev.*, 2009, **38**, 1477–1504.

7 L. E. Kreno, K. Leong, O. K. Farha, M. Allendorf, R. P. Van Duyne and J. T. Hupp, *Chem. Rev.*, 2012, **112**, 1105–1125.

8 J. Hynek, P. Brázda, J. Rohlíček, M. G. S. Londesborough and J. Demel, *Angew. Chem.*, Int. Ed., 2018, **57**, 5016–5019.

9 P. Deria, W. Bury, I. Hod, C. W. Kung, O. Karagiaridi, J. T. Hupp and O. K. Farha, *Inorg. Chem.*, 2015, **54**, 2185–2192.

10 Y.-P. Zhu, T.-Y. Ma, Y.-L. Liu, T.-Z. Ren and Z.-Y. Yuan, *Inorg. Chem. Front.*, 2014, **1**, 360–383.

11 S. R. Miller, G. M. Pearce, P. A. Wright, F. Bonino, S. Chavan, S. Bordiga, I. Margiolaki, N. Guillou, G. Férey, S. Bourrelly and P. L. Llewellyn, *J. Am. Chem. Soc.*, 2008, **130**, 15967–15981.

12 M. T. Wharmby, J. P. Mowat, S. P. Thompson and P. A. Wright, *J. Am. Chem. Soc.*, 2011, **133**, 1266–1269.

13 Y. Zorlu, D. Erbahar, A. Cetinkaya, A. Bulut, T. S. Erkal, A. O. Yazaydin, J. Beckmann and G. Yucesan, *Chem. Commun.*, 2019, **55**, 3053–3056.

14 N. Hermer and N. Stock, *Dalton Trans.*, 2015, **44**, 3720–3723.

15 T. Zheng, Z. Yang, D. Gui, Z. Liu, X. Wang, X. Dai, S. Liu, L. Zhang, Y. Gao, L. Chen, D. Sheng, Y. Wang, J. Diwu, J. Wang, R. Zhou, Z. Chai, T. E. Albrecht-Schmitt and S. Wang, *Nat. Commun.*, 2017, **8**, 15369–15379.

16 Z. Hassanzadeh Fard, N. E. Wong, C. D. Malliakas, P. Ramaswamy, J. M. Taylor, K. Otsubo and G. K. H. Shimizu, *Chem. Mater.*, 2018, **30**, 314–318.

17 Z. H. Fard, Y. Kalinovskyy, D. M. Spasyuk, B. A. Blight and G. K. H. Shimizu, C*hem. Commun.*, 2016, **52**, 12865–12868.

18 T. Zeng, L. Wang, L. Feng, H. Xu, Q. Cheng and Z. Pan, *Dalton Trans.*, 2019, **48**, 523–534.

19 L.-L. Dai, Y.-Y. Zhu, C.-Q. Jiao, Z.-G. Sun, S.-P. Shi, W. Zhou, W.-Z. Li, T. Sun, H. Luo and M. X. Ma, *CrystEngComm*, 2014, **16**, 5050–5061.

20 D. Kong, J. Zon, J. McBee and A. Clearfield, *Inorg. Chem.*, 2006, **45**, 977–986.

21 Z. Zhao, D. Yang, B. Xing, C. Ma, Z.-G. Sun, Y.-Y. Zhu, H.-Y. Li and J. Li, *RSC Adv.*, 2016, **6**, 92175–92185.

22 C. Ma, C.-Q. Jiao, Z.-G. Sun, Y.-Y. Zhu, X.-W. Zhang, M. L. Wang, D. Yang, Z. Zhao, H.-Y. Li and B. Xing, *RSC Adv.*, 2015, **5**, 79041–79049.

23 Z. Chen, H. Yang, M. Deng, Y. Ling, L. Weng and Y. Zhou, *Dalton Trans.*, 2012, **41**, 4079–4083.

24 S.-P. Shi, Y.-Y. Zhu, Z.-G. Sun, W. Zhou, L.-L. Dai, M.-X. Ma, W.-Z. Li, H. Luo and T. Sun, *Cryst. Growth Des.*, 2014, **14**, 1580–1590.

25 K. Chen, Z.-G. Sun, Y.-Y. Zhu, Z.-M. Liu, F. Tong, D.-P. Dong, J. Li, C.-Q. Jiao, C. Li and C.-L. Wang, *Cryst. Growth Des.*, 2011, **11**, 4623–4631.

26 T.-H. Zhou, Z.-Z. He, X. Xu, X.-Y. Qian and J.-G. Mao, *Cryst. Growth Des.*, 2013, **13**, 838 843.

27 A. M. Putz, L. M. Carrella and E. Rentschler, *Dalton Trans.*, 2013, **42**, 16194–16199.

28 J.-T. Li, T. D. Keene, D.-K. Cao, S. Decurtins and L.-M. Zheng, *CrystEngComm*, 2009, **11**, 1255–1260.

29 X. Chen, Y. Peng, X. Han, Y. Liu, X. Lin and Y. Cui, *Nat. Commun.*, 2017, **8**, 2171.

30 Y.-J. Qi, J.-H. Liu, W.-X. Zheng, X.-X. Li and S.-T. Zheng, *Chin. Chem. Lett.*, 2018, 959–962.

31 C. Serre, N. Stock, T. Bein and G. Férey, *Inorg. Chem.*, 2004, **43**, 3159–3163.

32 C. Heering, B. Francis, B. Nateghi, G. Makhloufi, S. Lüdeke and C. Janiak, *CrystEngComm*, 2016, **18**, 5209–5223.

33 C. Zhang, H. Shi, L. Sun, Y. Yan, B. Wang, Z. Liang, L. Wang and J. Li, *Cryst. Growth Des.*, 2018, **18**, 7683–7689.

34 K. Seki and W. Mori, *J. Phys. Chem. B*, 2002, **106**, 1380–1385.

35 D. N. Dybtsev, H. Chun and K. Kim, *Angew. Chem., Int. Ed.*, 2004, **43**, 5033–5036.

36 S. S. Iremonger, J. Liang, R. Vaidhyanathan, I. Martens, G. K. H. Shimizu, T. D. Daff, M. Z. Aghaji, S. Yeganegi and T. K. Woo, *J. Am. Chem. Soc.*, 2011, **133**, 20048–20051.

37 K. Bladek, M. Reid, H. Nishihara, F. Akhtar, B. Gelfand and G. K. H. Shimizu, *Chem. – Eur. J.*, 2018, **24**, 1533–1538.

38 B. Gelfand, J. Taylor and G. K. H. Shimizu, *CrystEngComm*, 2017, **19**, 3727–3736.

39 B. S. Gelfand, R. P. Huynh, R. K. Mah and G. K. H. Shimizu, *Angew. Chem., Int. Ed.*, 2016, **55**, 14614–14617.

40 B. Gelfand, J.-B. Lin and G. K. H. Shimizu, *Inorg. Chem.*, 2015, **54**, 1185–1187.

41 B. Gelfand, R. P. S. Huynh, S. Collins, T. Woo and G. K. H. Shimizu, *Chem. Mater.*, 2017, **29**, 10469–10477.

42 S. S. Iremonger, J. Liang, R. Vaidhyanathan and G. K. H. Shimizu, *Chem. Commun.*, 2011, **47**, 4430–4432.

43 J. M. Taylor, R. Vaidhyanathan, S. S. Iremonger and G. K. H. Shimizu, *J. Am. Chem. Soc.*, 2012, **134**, 14338–14340.

44 J.-W. Zhang, C.-C. Zhao, Y.-P. Zhao, H.-Q. Xu, Z.-Y. Du and H.-L. Jiang, *CrystEngComm*, 2014, **16**, 6635–6644.

45 Y. Park, I. Jeon, S. Shin, J. Min and P. H. Lee, *J. Org. Chem.*, 2013, **78**, 10209–10220.

46 Y. Park, J. Seo, S. Park, E. J. Yoo and P. H. Lee, *Chem. – Eur. J.*, 2013, **19**, 16461–16468.

47 R. W. Heidebrecht, M. Chenard, J. Close, W. K. Dahlberg, J. Fleming, J. B. Grimm, J. E. Hamill, A. Harsch, B. B. Haines, B. Hughes, A. M. Kral, R. E. Middleton, C. Mushti, N. Ozerova, A. A. Szewczak, H. Wang, K. Wilson, D. J. Witter, J. P. Secrist and T. A. Miller, *Bioorg. Med. Chem. Lett.*, 2009, **19**, 2053–2058.

48 T. N. Tu, K. D. Nguyen, T. N. Nguyen, T. Truong and N. T. S. Phan, *Catal. Sci. Technol.*, 2016, **6**, 1384–1392.

49 S. Henke, A. Schneemann, A. Wütscher and R. A. Fischer, *J. Am. Chem. Soc.*, 2012, **134**, 9464–9474.

50 H. Wang, J. Getzschmann, I. Senkovska and S. Kaskel, M*icroporous Mesoporous Mater.*, 2008, **116**, 653–657.

51 B. Chen, S. Ma, F. Zapata, F. R. Fronczek, E. B. Lobkovsky and H. C. Zhou, *Inorg. Chem.*, 2007, **46**, 1233–1236.

52 B.-Q. Ma, K. L. Mulfort and J. T. Hupp, *Inorg. Chem.*, 2005, **44**, 4912–4914.

53 S. Bureekaew, H. Sato, R. Matsuda, Y. Kubota, R. Hirose, J. Kim, K. Kato, M. Takata and S. Kitagawa, *Angew. Chem., Int. Ed.*, 2010, **49**, 7660–7664.

54 H. Chun, D. N. Dybtsev, H. Kim and K. Kim, *Chem. – Eur. J.*, 2005, **11**, 3521–3529.

55 V. Guillerm, D. Kim, J. F. Eubank, R. Luebke, X. Liu, K. Adil, M. S. Lah and M. Eddaoudi, *Chem. Soc. Rev.*, 2014, **43**, 6141–6172.

56 K. Uemura, Y. Yamasaki, Y. Komagawa, K. Tanaka and H. Kita, *Angew. Chem., Int. Ed.*, 2007, **46**, 6662–6665.

57 S. Takamizawa, T. Akatsuka and R. Miyake, *CrystEngComm*, 2010, **12**, 82–84.

58 M. Kondo, Y. Takashima, J. Seo, S. Kitagawa and S. Furukawa, *CrystEngComm*, 2010, **12**, 2350–2353.

59 K. Yanxiong, L. Jianmin, Z. Yugen, H. Gaofei, J. Zheng and L. Zhibin, *Cryst. Res. Technol.*, 2002, **37**, 169–175.

60 W. Fu, D. Zhang, Z. Shi, L. Yang and S. Feng, *Inorg. Chim. Acta*, 2006, **359**, 369–373.

61 A. Choudhury, S. Natarajan and C. N. R. Rao, *J. Chem. Soc., Dalton Trans.*, 2000, 2595–2598.

62 V. A. Blatov, A. P. Shevchenko and D. M. Proserpio, *Cryst. Growth Des.*, 2014, **14**, 3576–3586.

63 T. F. Willems, C. H. Rycroft, M. Kazi, J. C. Meza and M. Haranczyk, M*icroporous Mesoporous Mater.*, 2012, **149**, 134–141.

64 Q.-Y. Yang, P. Lama, S. Sen, M. Lusi, K. J. Chen, W.-Y. Gao, M. Shivanna, T. Pham, N. Hosono, S. Kusaka, J. J. Perry IV, S. Ma, B. Space, L. J. Barbour, S. Kitagawa and M. J. Zaworotko, *Angew. Chem., Int. Ed.*, 2018, **57**, 5684–5689.

65 L. Gurvich*, Zh. Russ. Fiz.-Khim. O-va.*, 1915, **47**, 805–827.

66 A. Schneemann, P. Vervoorts, I. Hante, M. Tu, S. Wannapaiboon, C. Sternemann, M. Paulus, D. C. F. Wieland, S. Henke and R. A. Fischer, *Chem. Mater.*, 2018, **30**, 1667–1676.

67 K. Uemura, Y. Yamasaki, Y. Komagawa, K. Tanaka and H. Kita, *Angew. Chem.*, 2007, **119**, 6782–6785.

68 Bruker AXS, *APEX2*, Bruker AXS Inc., Madison, Wisconsin, USA, 2012.

69 G. M. Sheldrick, *In Program SADABS*:, *Area-detector absorption correction*, University of Göttingen, Germany, 1996.

70 G. M. Sheldrick, Crystal structure refinement with SHELXL, *Acta Crystallogr., Sect. C: Struct. Chem.*, 2015, **71**, 3–8.

71 C. B. Hübschle, G. M. Sheldrick and B. Dittrich, ShelXle: a Qt graphical user interface for SHELXL, *J. Appl. Crystallogr.*, 2011, **44**, 1281–1284.

72 K. Brandenburg, *Diamond (Version 3.2), Crystal and Molecular Structure Visualization, Crystal Impact*, K. Brandenburg & H. Putz Gbr, Bonn (Germany), 2009, http://www.crystalimpact. com/diamond.

73 M. Shao and Y. Zhao, *Tetrahedron Lett.*, 2010, **51**, 2892–2895.

74 J.-M. Rueff, N. Barrier, S. Boudin, V. Dorcet, V. Caignaert, P. Boullay, G. Hix and P.-A. Jaffrès, *Dalton Trans.*, 2009, 10614–10620.

The article is reproduced from Ref. 115 with permission from The Royal Society of Chemistry 2020.

Electronic Supplementary Information (ESI)

Flexible bifunctional monoethylphosphonate/carboxylates of Zn(II) and Co(II) reinforced with DABCO co-ligand: paradigmatic structural organization with pcu topology

Anna Goldman,[a] Beatriz Gil-Hernández,[b] Simon Millan,[a] Serkan Gökpinar,[a] Christian Heering,[a] Ishtvan Boldog*[a] and Christoph Janiak*[a]

[a] Institut für Anorganische Chemie und Strukturchemie, Heinrich-Heine-Universität Düsseldorf, Universitätsstraße 1, 40225 Düsseldorf, Germany. E-mail: janiak@uni-duesseldorf.de

[b] Departamento de Química, Facultad de Ciencias de La Laguna, Sección Química, Universidad de La Laguna, 38206 La Laguna, Tenerife, Spain

** Corresponding authors: ishtvan.boldog@gmail.com, janiak@hhu.de*

Additional email addresses: anna.goldman@hhu.de, beagher@ull.es, simon.millan@hhu.de, serkan.goekpinar@hhu.de, cheering@mmm.com

Contents

1 ^1H, ^{13}C, and ^{31}P NMR spectra 53

  1.1 Methyl 4-iodobenzoate 53
  1.2 Methyl-4-(diethoxyphosphoryl)benzoate 54
  1.3 *O*-ethyl-*P*-(4-carboxyphenyl)phosphonic acid, H_2EtBCP 55

2 Overview of surface area and CO_2 adsorption data for (monoalkyl)-phosphonate MOFs based on selected ligands. 57
3 Synthesis, verification of the role of formic acid, and PXRD patterns for $[Zn_2(EtBCP)_2(Solv)]·Solv'$, **1** 60

  3.1 Synthesis and the PXRD patterns 60
  3.2 The potential role of *in-situ* formed formic acid 61

4 Crystallographic data and structure refinement for $[Zn_2(EtBCP)_2(Solv)]·Solv'$, **1** 63
5 Crystallographic details for $[Zn_2(EtBCP)_2(DABCO)_{0.5}]·2DMA$, **2** 65
6 Topological analysis of **2** 67

  6.1 Topos-output for the topology of **2** on the level of 4,6-c net 69
  6.2 Res-file input in *P*4 symmetry for different levels of topological interpretation 69
  6.3 Illustration of the possible isoreticular expansion of **2** 70

7 Geometrical surface area and pore volume based on structural data 71
8 BET and Langmuir surface areas and the respective experimental adsorption raw data 75

  8.1 Langmuir report for $[Zn_2(EtBCP)_2(DABCO)_{0.5}]$, **2´** 76
  8.2 BET report for $[Zn_2(EtBCP)_2(DABCO)_{0.5}]$, **2´** 77
  8.3 Langmuir report for $[Co_2(EtBCP)_2(DABCO)_{0.5}]$, **3´** 78
  8.4 BET report for $[Co_2(EtBCP)_2(DABCO)_{0.5}]$, **3´** 79

9 Comparison of low pressure CO_2 adsorption isotherms collected using different equilibration times for **3′** (assessing kinetic effects) 80
10 Stability tests in air and the water vapor adsorption by **3′** 82
11 Solvent stability tests performed on **2** 83
12 References 84

1 ^{1}H, ^{13}C, and ^{31}P NMR spectra

1.1 Methyl 4-iodobenzoate

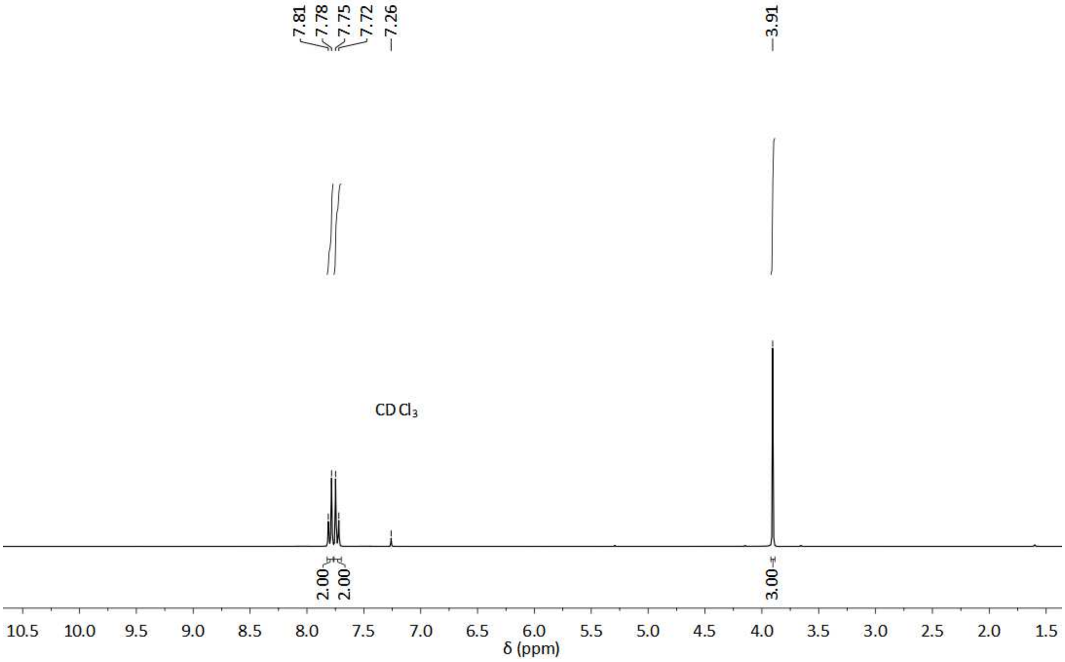

Fig. S1 ^{1}H NMR spectrum (300 MHz, $CDCl_3$) of methyl 4-iodobenzoate.

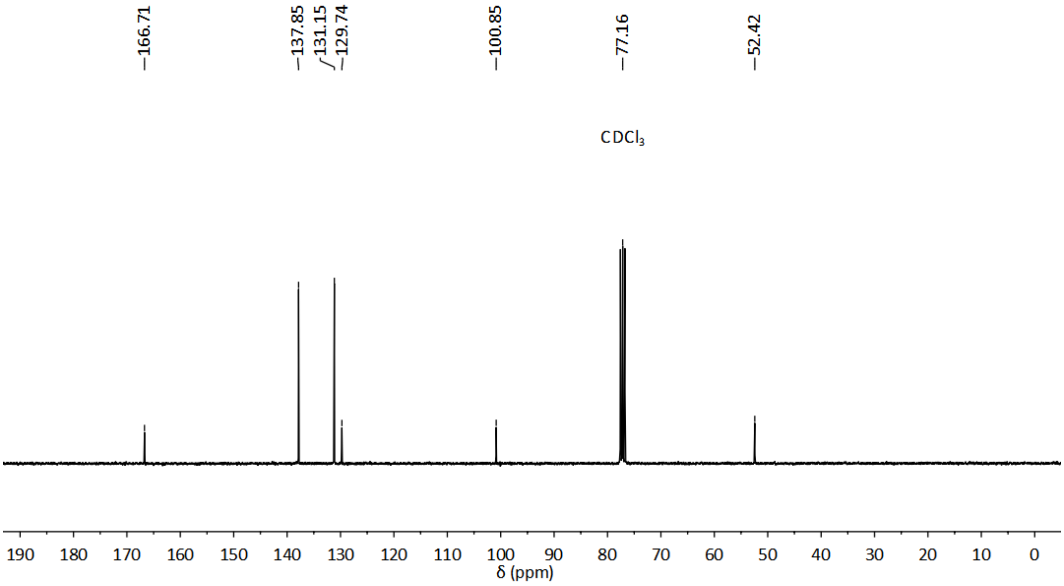

Fig. S2 ^{13}C NMR spectrum (75 MHz, $CDCl_3$) of methyl 4-iodobenzoate.

1.2 Methyl-4-(diethoxyphosphoryl)benzoate

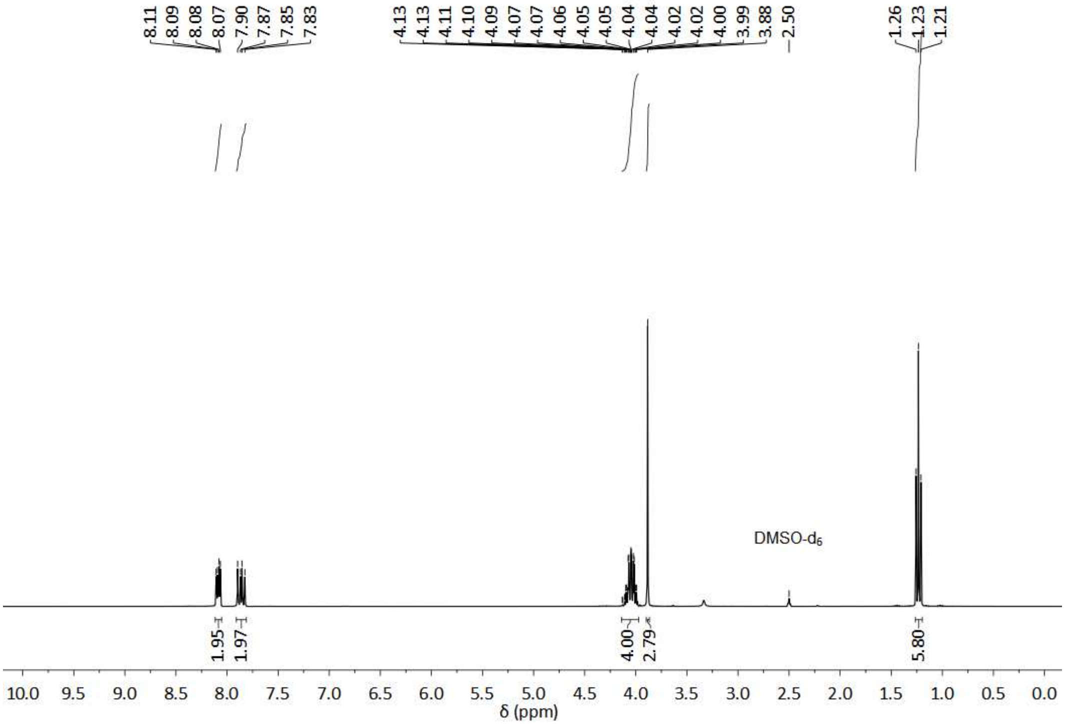

Fig. S3 ^{1}H NMR spectrum (300 MHz, DMSO-d$_6$) of methyl-4-(diethoxyphosphoryl)benzoate.

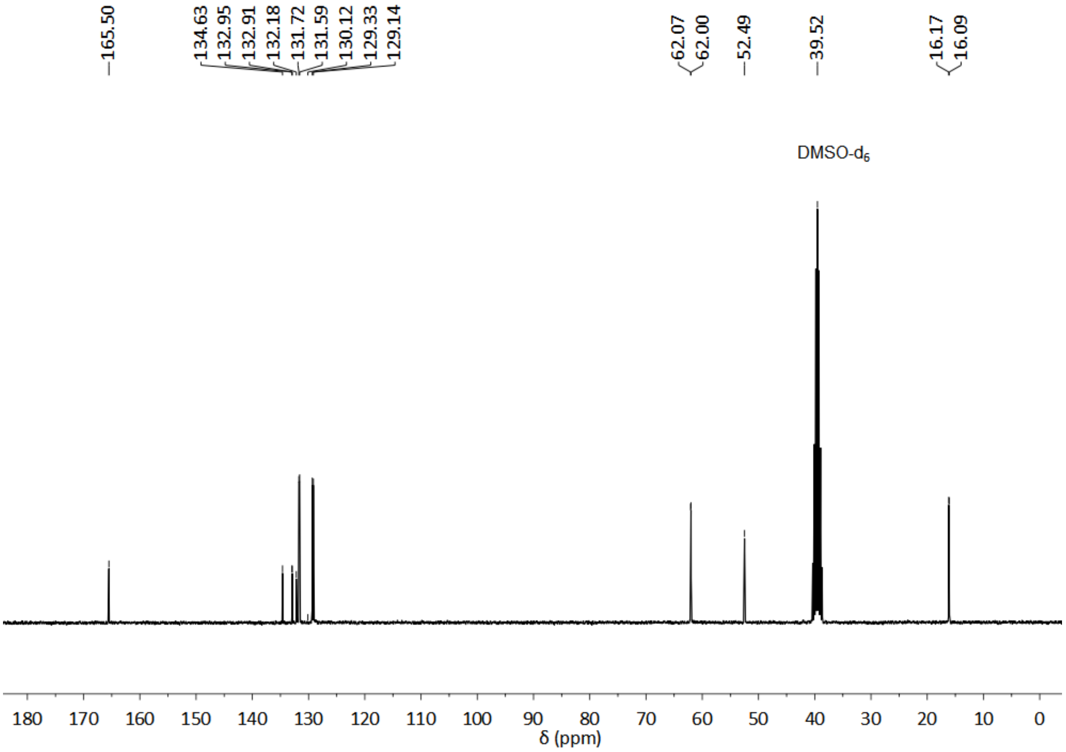

Fig. S4 ^{13}C NMR spectrum (75 MHz, DMSO-d$_6$) of methyl-4-(diethoxyphosphoryl)benzoate.

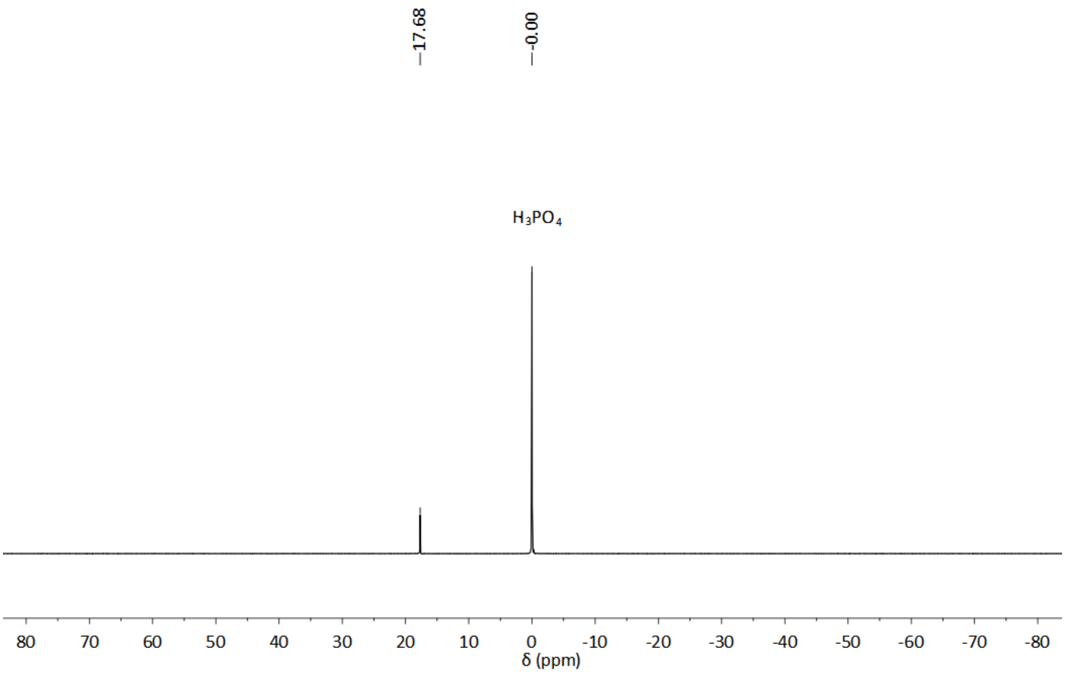

Fig. S5 ^{31}P NMR spectrum (121 MHz, $CDCl_3$) of methyl-4-(diethoxyphosphoryl)benzoate.

1.3 *O*-ethyl-*P*-(4-carboxyphenyl)phosphonic acid, H_2EtBCP

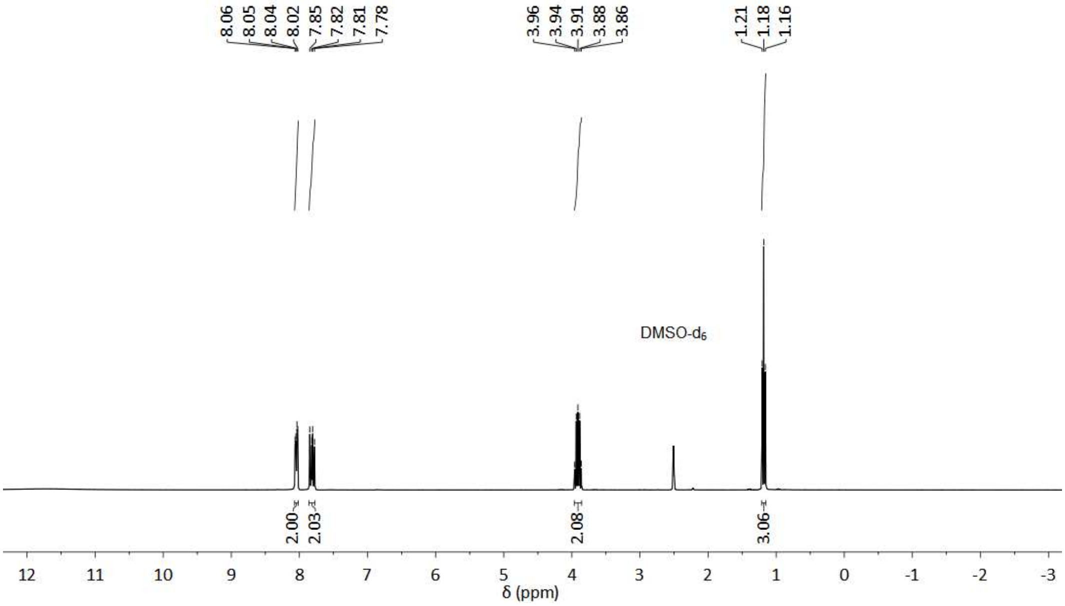

Fig. S6 ^{1}H NMR spectrum (300 MHz, DMSO-d_6) of H_2EtBCP.

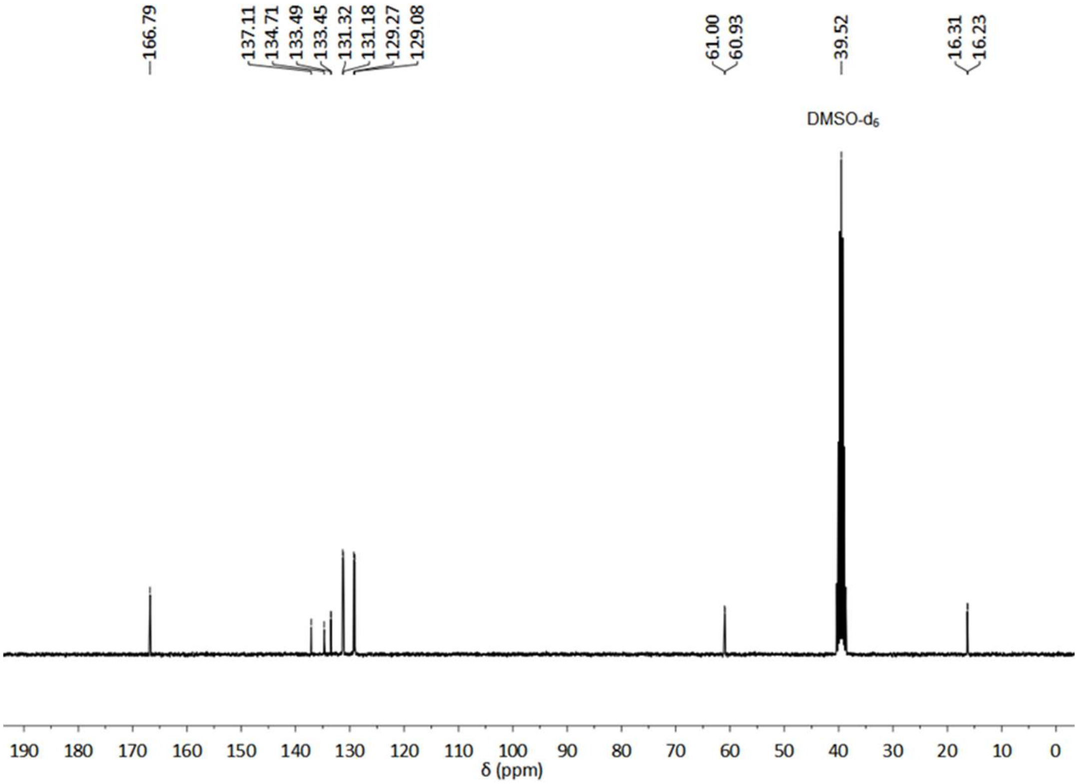

Fig. S7 ^{13}C NMR spectrum (75 MHz, DMSO-d_6) of H_2EtBCP.

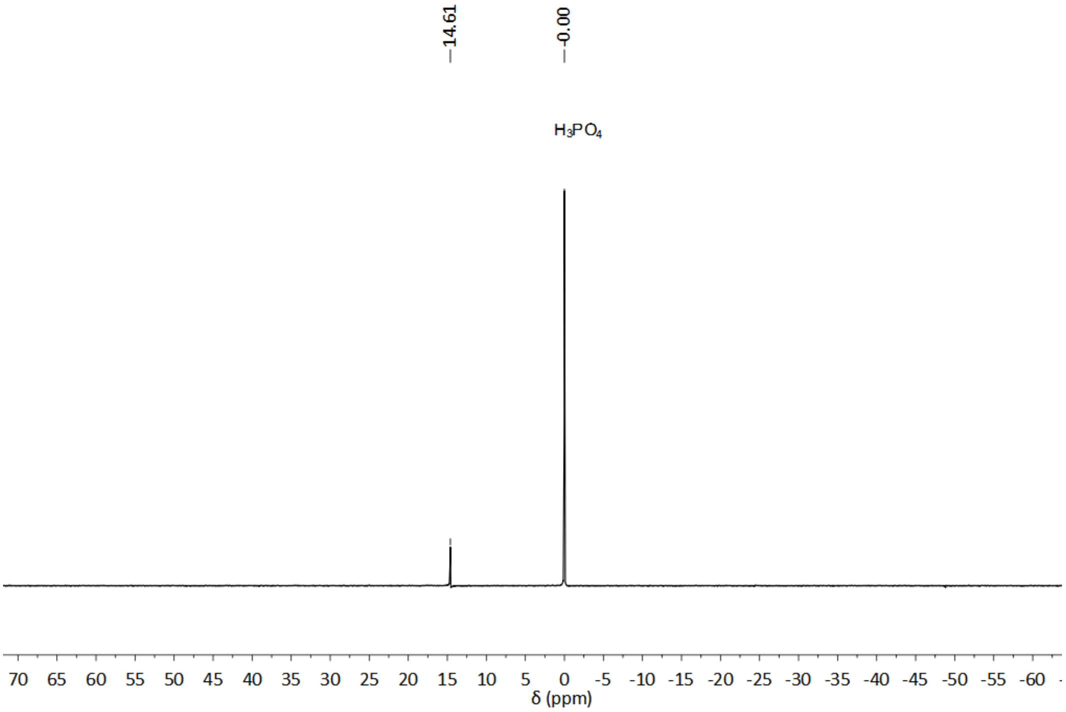

Fig. S8 ^{31}P NMR spectrum (242 MHz, DMSO-d_6) of H2EtBCP.

2 Overview of surface area and CO_2 adsorption data for (monoalkyl)-phosphonate MOFs based on selected ligands.

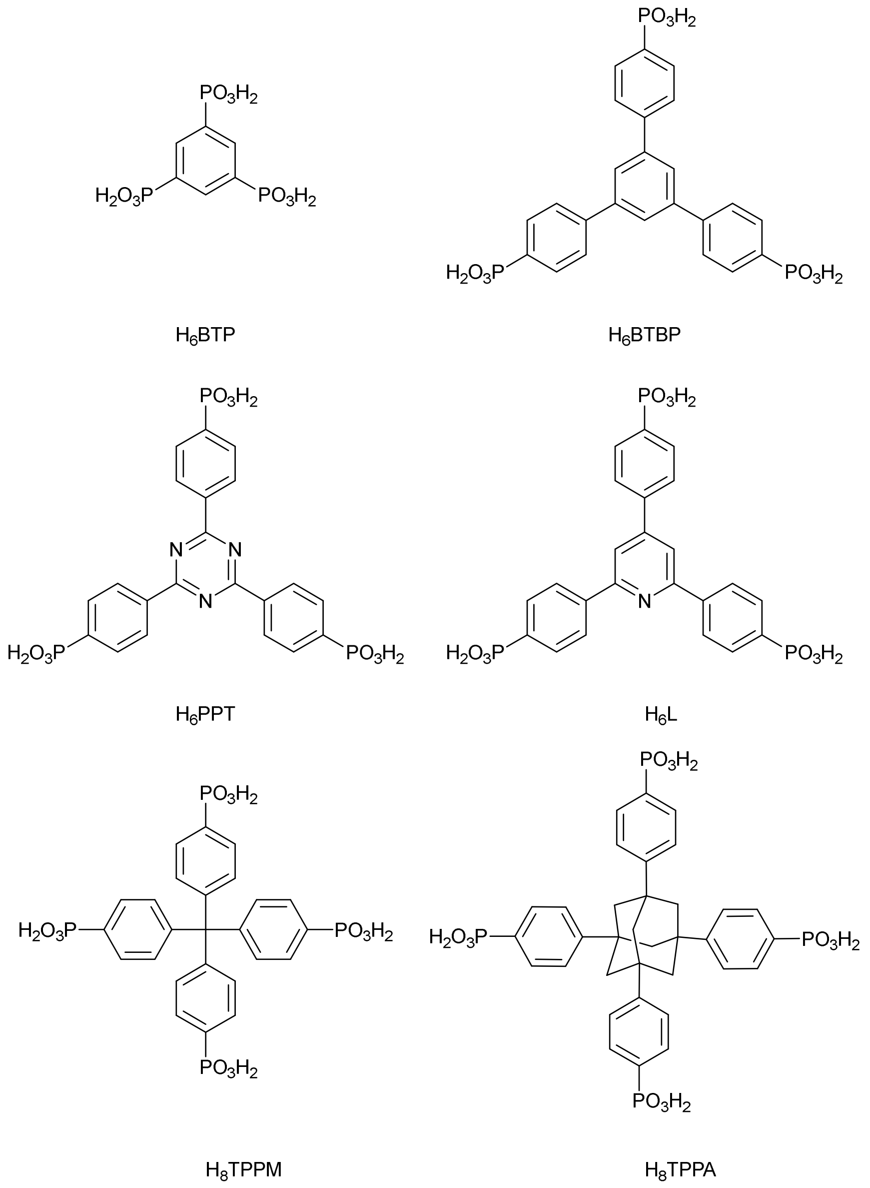

Fig. S9 Overview of high symmetry trigonal and tetragonal ligands used for the synthesis of MOFs.[1,9,10,11,12]

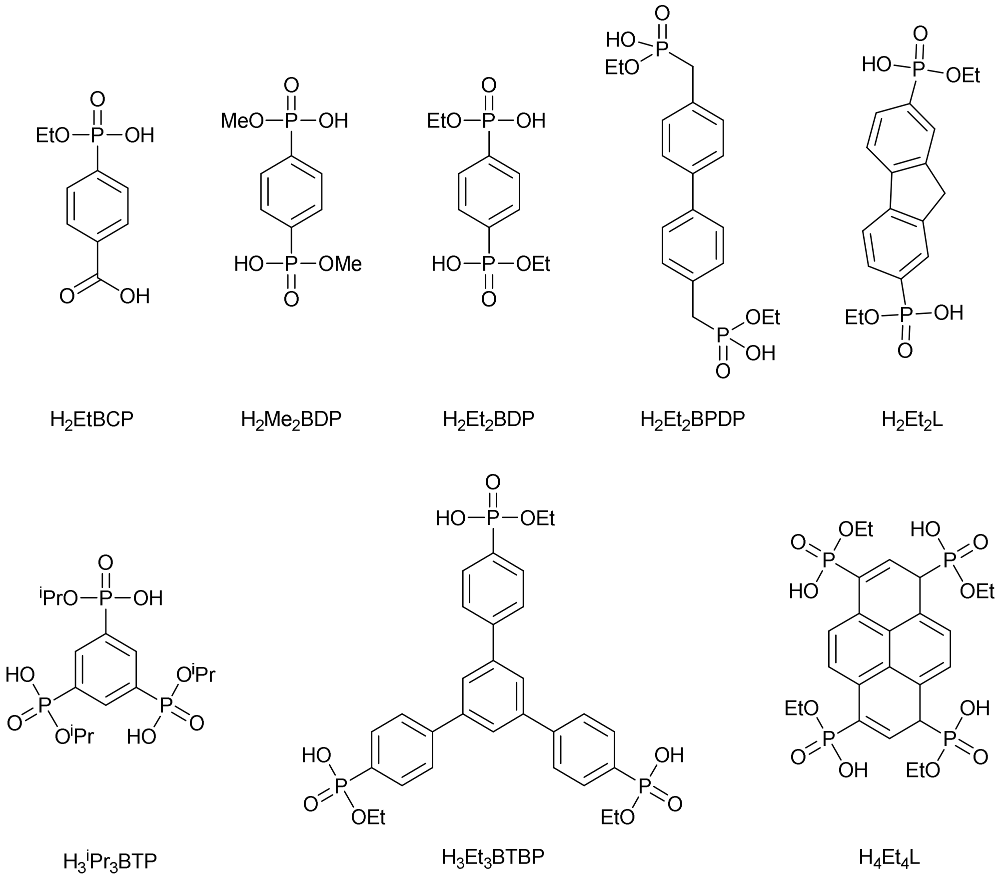

H_2EtBCP H_2Me_2BDP H_2Et_2BDP H_2Et_2BPDP H_2Et_2L

$H_3{}^iPr_3BTP$ H_3Et_3BTBP H_4Et_4L

Fig. S10 Overview of monoalkyl-phosphonate ligands used for the synthesis of MOFs.[2,3,4,5,6,7,8]

Table S1. Surface area and CO_2 adsorption data for selected monoalkyl-phosphonate and phosphonate-based MOFs.

Ligand	**MOF**	**Metal**	**Surface Area [m^2 g^{-1}]**	**CO_2 uptake [mmol g^{-1}]**			**Ref.**
				293 K	**273 K**	**195 K**	
Monoalkyl-phosphonate-carboxylate MOFs							
H_2EtBCP	$[M_2(EtBCP)_2(DABCO)_{0.5}]\cdot 2DMA$	Co	327[a,c]; 310[b,c]	1.0	1.5	5.7	This work
		Zn	330[a,c]; 310[b,c]	0.9	1.4	5.1	
Monoalkyl-phosphonate MOFs							
H_2Et_2L	CALS-4	Co	140[a]; 139[b]	/	/	1.9	2
H_2Et_2BDP	$[M(Et_2BDP)]$	Cu	/	/	0.1	/	3
		Zn	312[a,c]; 264[b,c]	/	1.1	2.8	4
H_2Me_2BDP	$[Cu(Me_2BDP)]$	Cu	153[a,c]; 150[b,c]	/	1.4	/	3
H_2Et_2BPDP	$[M(Et_2BPDP)(TIB)(H_2O)_2]\cdot 6H_2O$	Cd	16[a,c]	/	/	1.3	5
		Cu	70[a,c]	/	/	1.8	
H_4Et_4L	CALF-25	Ba	385[b]	/	0.9	4.0	6
$H_3{}^iPr_3BTP$	CALF-30	Cu	312[a,c]; 244[b,c]	/	/	1.0	7
H_3Et_3BTB	CALF-33Et_3		1030[a]; 842[b]	~0.6	0.9	/	8
H_4Et_2BTB	CALF-33Et_2H		950[a]; 810[b]	~1.2	1.8[d]	/	
Phosphonate-MOFs							
H_6L	PCMOF20	Zr	180[b]	/	1.9	/	9
H_8TPPM	SZ-1		17[a]; 10[b]	/	/	0.8	10
H_8TPPA	SZ-2		357[a]; 225[b]	/	/	5.8	
	SZ-3		695[a]; 572[b]	/	/	5.3	
H_6PPT	CAU-14	Cu	647[b]	1.1[e]	/	/	11
H_6BTBP	$[Sr_2(H_2BTBP)\text{-}(CH_3OH)(H_2O)_4]$	Sr	146[b,d]	/	/	/	12

[a] Langmuir surface area; [b] BET surface area; [c] calculated from CO_2 adsorption isotherm at 195 or 273 K. [d] 278 K measurement temperature; [e] 298 K measurement temperature.

3 Synthesis, verification of the role of formic acid, and PXRD patterns for $[Zn_2(EtBCP)_2(Solv)]\cdot Solv'$, 1

3.1 Synthesis and the PXRD patterns

Synthesis of 1: a mixture of $Zn(NO_3)_2\cdot 6H_2O$ (51.7 mg, 0.17 mmol), H_2EtBCP (20 mg 0.09 mmol) , DMF (2 mL) and 0.1 mL conc. HNO_3 was transferred in a Pyrex tube. The tube was transferred to a programmable oven and heated up to 120 °C in 2 h. During the second step, the temperature was raised linearly to 130 °C within three days and then cooled down in 24 h to room temperature. A reasonably crystalline probe of $[Zn_2(EtBCP)_2(Solv)]\cdot Solv'$ consisting of single crystals suitable for SCXRD analysis was obtained in a yield of 26 mg (52%).

Unlike the reliable syntheses of **2** and **3**, the synthesis of **1** is very sensitive to admixtures and/or the regime of recrystallization. The crystallization outcome was not well-reproducible. Only once it was possible to obtain single crystals suitable for XRD structure determination, however the phase was not pure. A reasonably phase-pure sample was obtained in a few repeated experiments according to the reasonably good PXRD pattern matching with the simulated one (Fig. S1 demonstrates the comparison between the activated and the as-synthesized sample for the case when the best match was reached). The material lost its crystallinity to a significant extent after activation (Fig. S1), but it is the low reproducibility, which put an end to further investigations.

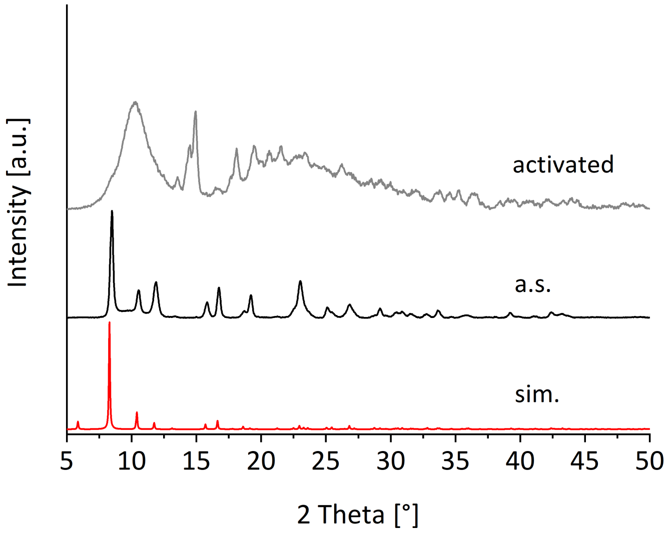

Fig. S11 The PXRD patterns of:
$[Zn_2(EtBCP)_2(Solv)]\cdot(Solv')$, **2** simulated from X-ray single crystal diffraction data (red);
2 bulk sample, as synthesized (black);
2´ activated sample (grey).

3.2 The potential role of *in-situ* formed formic acid

The single crystal XRD structure (see Chapt. 4) features a molecular moiety, which could be a bridging ligand, with a role, similar to the role of DABCO in **2**. The fragment could be potentially interpreted as a formate bridge, as formic acid is indeed present in the reaction medium due to the hydrolysis of DMF under elevated temperatures by the residual water impurities, including the water introduced by the metal salt hydrates. An indirect supporting argument is that the formation of **1** is DMF specific and could not be observed in DMA, which should kinetically be more stable towards hydrolysis.

The structural motif of **1** was reasonably well established, and the structure organization principle is similar to **2**, which imposes the presence of a non-charged bridge. Hence, formate could not be the dominant representative of the potentially site-sharing ligands instead of DABCO, but it might play an important role as a modulator, guiding the assembly of **1**.

In order to verify a possible role of the formic acid, we performed three comparative experiments. They were carried out under strictly the same conditions except the varied amount of formic acid (0, 10 and 65 molar equivalents compared to the amount of the ligand; in the latter case no HNO_3 was added). The amounts of other reactants were the same as in the standard synthesis, described above. After 3 days of linear temperature increase form 120 °C to 130 °C the sample with 65 equivalents of formic acid did not demonstrate the formation of a precipitate, so the reaction time for all samples was extended further for 3 days at 130 °C. The prolonged heating increased the yield of **1** in the experiment with 0 eq. and 10 eq. of formic acid and caused the formation of a crystalline precipitate in the experiment with 65 eq. of formic acid.

The micrographs (Fig. S2) and the comparative PXRD patterns (Fig. S3) demonstrate, that in the presence of formic acid a new phase forms. The new phase has a morphology of spherical “concretions” composed of very thin needles; the size of the crystallites is way below the necessary size for the single crystal XRD structure determination. The PXRD confirms that the new phase is significantly different from **1**, though it might bear some local similarities. No further investigation of the new phase was attempted.

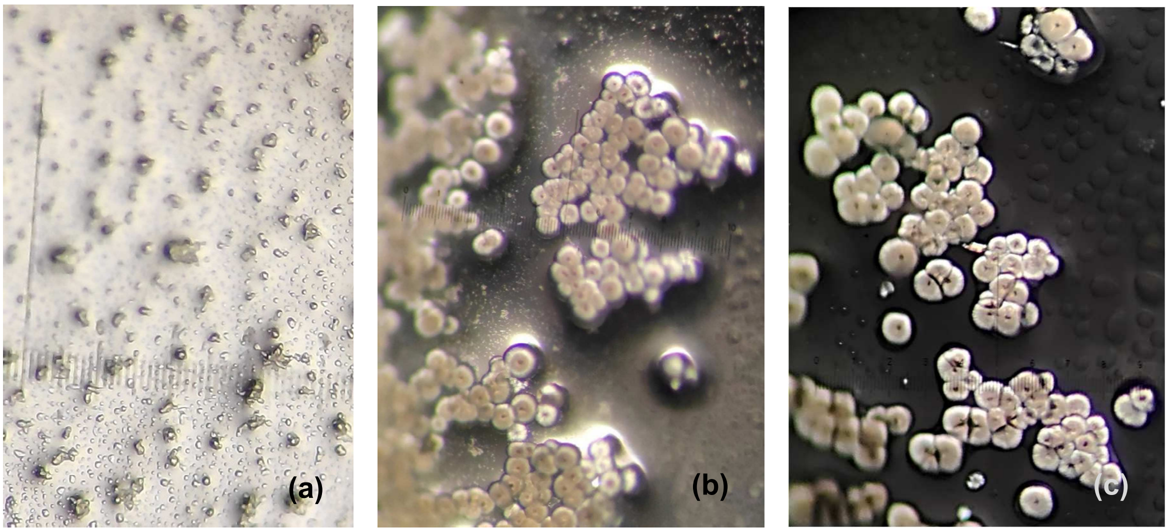

Fig. S12 Micrographs of the products in the comparative syntheses with (a) 0 equivalents of formic acid compared to H_2L; (b) 10 eq. of formic acid; (c) 65 eq. of formic acid.

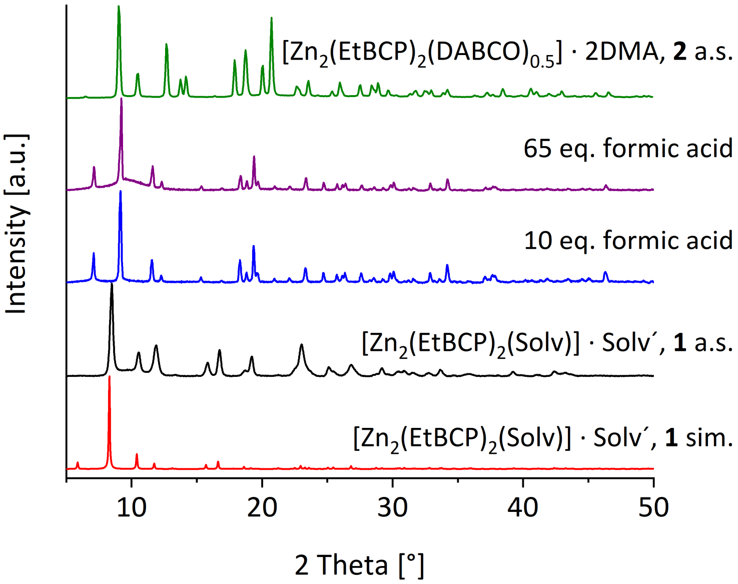

Fig. S13 Comparison of the PXRD patterns for: the simulated **1**, (red), derived from experimental SCXRD; the as-synthesized **1** (black); the as-synthesized comparative sample with 10 eq. of formic acid (blue); the as-synthesized comparative sample with 65 eq. of formic acid (purple); the as-synthesised $[Zn_2(EtBCP)_2(DABCO)_{0.5}]\cdot 2DMA$, **2**.

4 Crystallographic data and structure refinement for $[Zn_2(EtBCP)_2(Solv)]\cdot Solv'$,1

The *O*-ethoxyphosphonate group of the ligand is disordered over two mirror plane related positions. Its ethoxy fragment (OEt) was refined using distance and thermal displacement parameter restraints using DFIX and SIMU instructions. The latter was also applied for the C atoms of the phenyl group.

The aromatic hydrogen atoms of the ligand were positioned geometrically (C-H = 0.95 Å) and refined using a riding model (AFIX 43) with $U_{iso}(H) = 1.2U_{eq}(C)$. The ethylene and methylene hydrogen atoms of the phosphonate group of the ligand, H_2EtBCP, were positioned geometrically (d(C-H) are 0.96 Å for CH_2 and 0.97 Å for CH_3) and refined using a riding model (AFIX 23 for ethylene $-CH_2-$, AFIX 33 for CH_3), with $U_{iso}(H) = 1.2*U_{eq}$.

Unfortunately, it was not possible to establish the nature of the molecule coordinated to the apical position of the paddle-wheel unit in **1** (the hypothesis regarding the possible role of the formate anion, similar in size, was tested with a negative result; see Chapt. 3.2). The electron densities of the respective part of the structure were modeled by an "O(0.5)-P(0.25)"-fragment (the numbers in the brackets are the respective occupation factors). The atoms belonging to the fragment are marked with X and Y atoms on the picture of the extended asymmetric unit (Fig. S4).

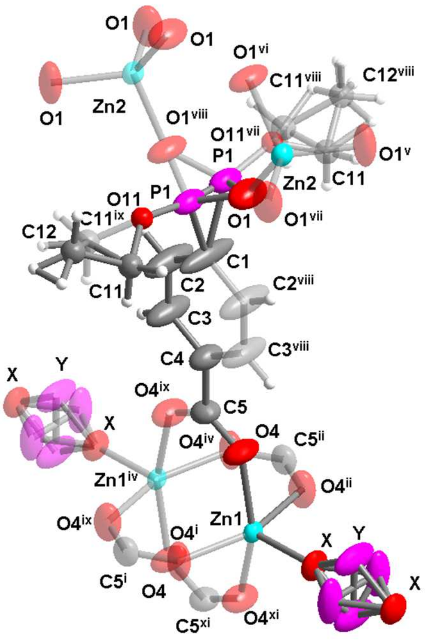

Fig. S14 The extended asymmetric unit of $[Zn_2(EtBCP)_2(Solv)]\cdot Solv'$, **1**, thermal ellipsoid plot representation (50%). Symmetry transformations: (i) *y*, −*x*+1, *z*; (ii) −*y*+1, *x*, *z*; (iii) −*x*+1, −*y*+1, *z*; (iv) −*x*+1, −*y*+1, −*z*+1; (v) *y*−1/2, −*x*+3/2, −*z*+1/2; (vi) −*x*+1, −*y*+2, *z*; (vii). −*y*+3/2, *x*+1/2, −*z*+1/2; (viii) −*x*+1, *y*, −*z*+1; (ix) *x*, *y*, −*z*+1; (x) *y*, −*x*+1, −*z*; (xi) −*x*+1, −*y*+1, −*z*.

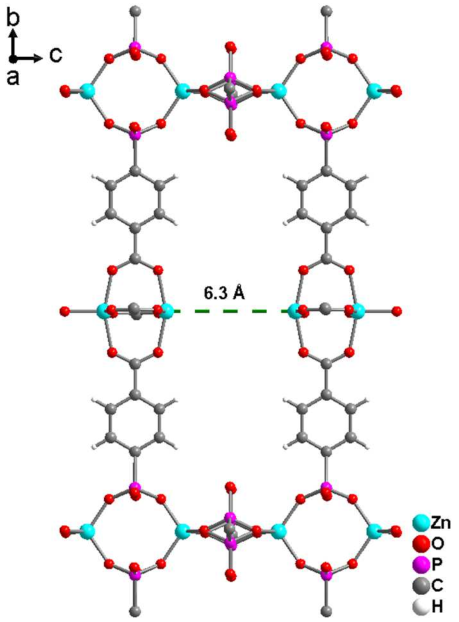

Fig. S15 The disposition of two adjacent paddle-wheel SBUs in [$Zn_2(EtBCP)_2(Solv)$]·Solv´, **1**, d(Zn2–Zn2) = 6.3 Å (the ethyl groups are not shown for clarity). The structure contains a bridge of still unknown origin (equivalent to DABCO regarding the connectivity). This unclear bridge might be a minor impurity, possibly formed in-situ from the used reactants or solvent molecule.

Table S2 Crystal data and refinement details for [$Zn_2(EtBCP)_2(Solv)$]·Solv´, **1**

CCDC deposition number	**1985570**
Empirical formula	$C_9H_9O_{5.50}P_{1.25}Zn$
M/g mol^{-1}	309.24
Crystal dimensions/mm	0.25 x 0.08 x 0.02
T /K	260
Crystal system	Tetragonal
Space group	$I4/mmm$
a, b, c /Å	21.4445 (11), 21.4445 (11), 9.3118 (5)
V /Å³	4282.2 (5)
Z	8
D_x /Mg m^{-3}	0.962
μ (Mo Kα) /mm^{-1}	1.24
F(000)	1254
T_{min}, T_{max}	0.887, 0.975
$\Delta\rho_{max}$, $\Delta\rho_{min}$ [e Å^{-3}]	1.72, –0.61
No. of measured, independent and observed [I > 2σ(I)] reflections	47819, 2112, 1636
R_{int}	0.044
$R[F^2 > 2\sigma(F^2)]$, $wR(F^2)$, S	0.059, 0.187, 1.10

w = 1/[$\sigma^2(F_o^2) + (0.1387P)^2$] where P = $(F_o^2 + 2F_c^2)/3$. Goodness-of-fit S = $[\Sigma [w(F_o^2–F_c^2)^2] /(n–p)]^{1/2}$.

5 Crystallographic details for [Zn$_2$(EtBCP)$_2$(DABCO)$_{0.5}$]·2DMA, 2

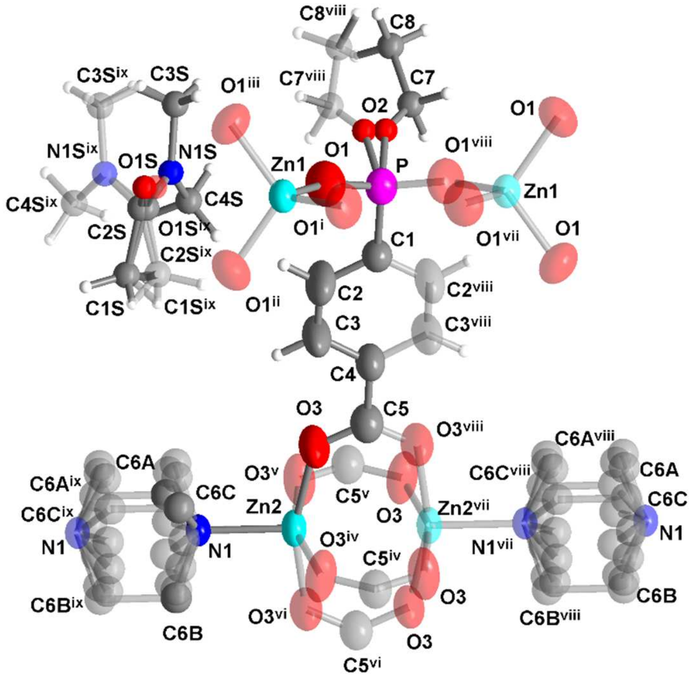

Fig. S16 The extended asymmetric unit of [Zn$_2$(EtBCP)$_2$(DABCO)$_{0.5}$]·2DMA, **2** thermal ellipsoid (50%) plot representation, with the exception of the disordered ethoxide group, which is plotted in ball-and-stick model for clarity. DABCO is given without hydrogen atoms for better visibility of the disordered components. Symmetry transformations: (i) −x+1, −y, z; (ii) −y+1/2, x−1/2, −z+3/2; (iii) y+1/2, −x+1/2, −z+3/2; (iv) y, −x+1, z; (v) −y+1, x, z; (vi) −x+1, −y+1, z; (vii) −x+1,−y+1, −z+1; (viii) x, y, −z+1; (ix) x, y, −z+2.

Table S3. Selected bond lengths [Å] and angles [°] for [Zn$_2$(EtBCP)$_2$(DABCO)$_{0.5}$]·2DMA, **2**.

Bond	Length, [Å]	Bond	Length, [Å]
Zn1—O1	1.913(4)	**C5—O3^{vii}**	1.231(6)
Zn1—O1^{i}	1.913(4)	**N1—C6C**	1.451(13)
Zn1—O1^{ii}	1.913(4)	**N1—C6A**	1.466(13)
Zn1—O1^{iii}	1.913(4)	**N1—C6B**	1.502(13)
Zn2—O3	2.021(5)	**C6A—C6A^{viii}**	1.53(4)
Zn2—O3^{iv}	2.021(5)	**C6B—C6B^{viii}**	1.63(4)
Zn2—O3^{v}	2.021(5)	**C6C—C6C^{viii}**	1.47(4)
Zn2—O3^{vi}	2.021(5)	**O1S—C2S**	1.293(10)
Zn2—N1	2.039(7)	**C2S—N1S**	1.342(10)
P—O1^{vii}	1.484(4)	**C2S—C1S**	1.508(9)
P—O1	1.484(4)	**N1S—C3S**	1.460(9)
P—O2	1.536(9)	**N1S—C4S**	1.460(9)
P—C1	1.786(8)	**C7—C8**	1.498(10)
O2—C7	1.392(10)	**C1—C2^{vii}**	1.357(8)
C1—C2	1.357(8)	**C4—C5**	1.527(13)
C2—C3	1.364(10)	**C5—O3**	1.231(6)
C3—C4	1.365(8)		

Angle	Value, [°]	Angle	Value, [°]
O1—Zn1—O1^{i}	109.6(3)	**O3^{vii}—C5—C4**	117.1(4)
O1—Zn1—O1^{ii}	109.40(15)	**C5—O3—Zn2**	127.0(5)
O1^{i}—Zn1—O1^{ii}	109.40(15)	**C6C—N1—C6A**	111.2(8)
O1—Zn1—O1^{iii}	109.40(15)	**C6C—N1—C6B**	108.0(8)
O1^{i}—Zn1—O1^{iii}	109.40(15)	**C6A—N1—C6B**	105.8(8)
O1^{ii}—Zn1—O1^{iii}	109.6(3)	**C6C—N1—Zn2**	112.3(8)
O3—Zn2—O3^{iv}	88.33(4)	**C6A—N1—Zn2**	110.9(9)
O3—Zn2—O3^{v}	88.33(4)	**C6B—N1—Zn2**	108.4(8)
O3^{iv}—Zn2—O3^{v}	160.3(2)	**N1—C6A—C6A^{viii}**	110.9(9)
O3—Zn2—O3^{vi}	160.3(2)	**N1—C6B—C6B^{viii}**	108.4(8)
O3^{iv}—Zn2—O3^{vi}	88.33(4)	**N1—C6C—C6C^{viii}**	112.3(8)
O3^{v}—Zn2—O3^{vi}	88.33(4)	**O1S—C2S—N1S**	115.1(18)
O3—Zn2—N1	99.83(12)	**O1S—C2S—C1S**	125.6(17)
O3^{iv}—Zn2—N1	99.83(12)	**N1S—C2S—C1S**	115.8(14)
O3^{v}—Zn2—N1	99.83(12)	**C2S—N1S—C3S**	118.3(15)
O3^{vi}—Zn2—N1	99.83(12)	**C2S—N1S—C4S**	119.3(14)
O1^{vii}—P—O1	119.4(4)	**C3S—N1S—C4S**	121.5(14)
O1^{vii}—P—O2	113.3(6)	**C2^{vii}—C1—P**	121.1(4)
O1—P—O2	97.9(6)	**C2—C1—P**	121.1(4)
O1^{vii}—P—C1	109.5(2)	**C1—C2—C3**	121.7(6)
O1—P—C1	109.5(2)	**C2—C3—C4**	119.9(6)
O2—P—C1	106.1(4)	**C3^{vii}—C4—C3**	118.9(8)
P—O1—Zn1	153.6(4)	**C3^{vii}—C4—C5**	120.5(4)
C7—O2—P	118.8(15)	**C3—C4—C5**	120.5(4)
O2—C7—C8	114(2)	**O3—C5—O3^{vii}**	125.7(9)
C2^{vii}—C1—C2	117.6(8)	**O3—C5—C4**	117.1(4)

Symmetry transformations: (i) −x+1, −y, z; (ii) −y+1/2, x−1/2, −z+3/2; (iii) y+1/2, −x+1/2, −z+3/2; (iv) y, −x+1, z; (v) −y+1, x, z; (vi) −x+1, −y+1, z; (vii) −x+1,−y+1, −z+1; (viii) x, y, −z+1; (ix) x, y, −z+2.

6. Topological analysis of 2

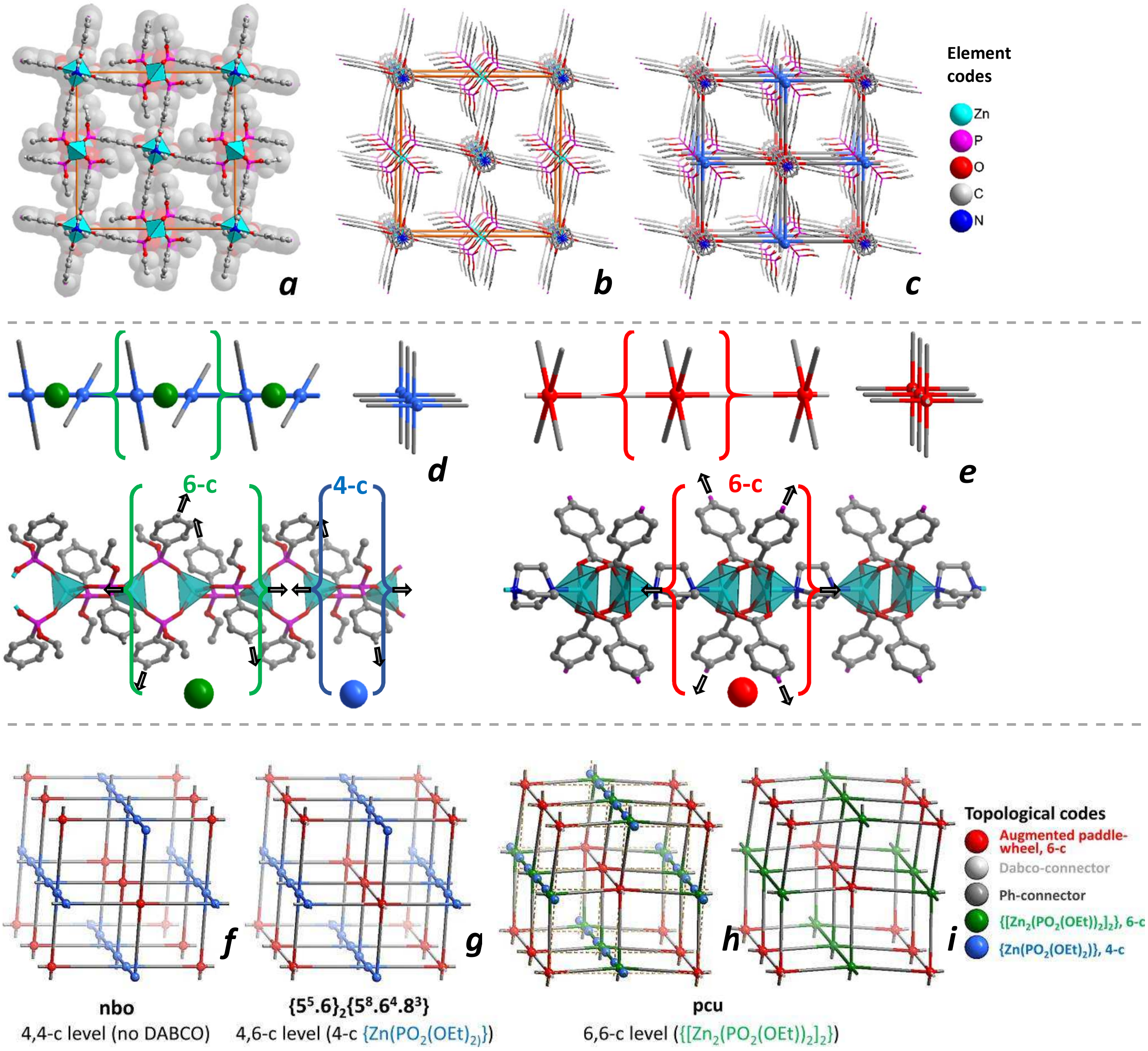

Fig. S17 The extended topological scheme for the structure of **2**.
(a) The view on the framework along the *c*-axis (no H-atoms are given for clarity) with an underlay-image of the ball-and-stick model image (with H-atoms). (b) The wireframe model of a representative part of the structure (the disorder is given explicitly). (c) As previous, but with the underlying net shown. (d) The $\{Zn_2(PO_2(OEt))_2\}_n$ phosphonate-monoester chain-SBU (note, that the attached phenyl groups are also shown for better assessment); the 4-c $\{Zn_2(PO_2(OEt))_2\}$ and the 6-c $\{[Zn_2(PO_2(OEt))_2]_2\}$ topological node interpretations are explained (e) The $\{Zn_2(COO)_4(DABCO)\}_n$ extended paddle-wheel chain-SBU sustained by standard paddle-wheel units, joined axially by bridging DABCO molecules (note, that the attached phenyl groups are also shown for better assessment). (f,g,h,i) Different levels of topological interpretations (see the legends).

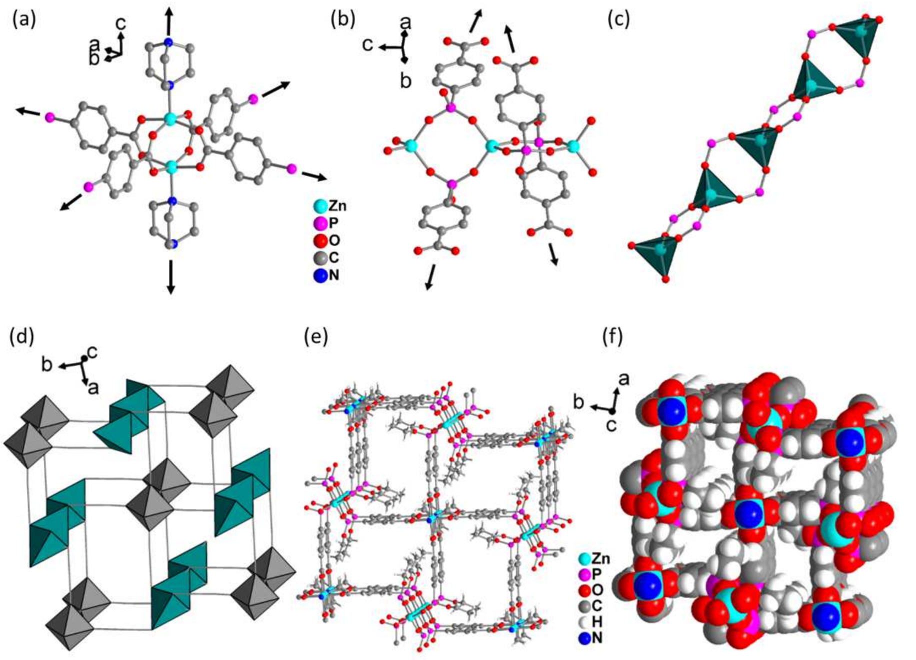

Fig. S18 Alternative, more conventional presentation on the structural organization of **2** (isostructural to **3**): (a) the $\{Zn_2(O_2C\text{-})_4\}$ standard paddle-wheel arrangement with four equatorial carboxylates (square-planar geometry) and two axial DABCO molecules; (b) the $Zn_2(PO_2(OEt))_2\}$ chain arrangement of the infinite phosphonate-monoester chain-SBU. (c) the 1D phosphonate-monoester chain-SBU in ball-and-stick and polyhedral representations; (d) a topological representation of the framework, based on 1D chains of axially connected 6-c units (e, f) the ball-and-stick and the space-filling representation of the framework respectively.

The topological assessment using the Topos software[13] was performed on structural input files with manually created dummy atoms, corresponding to the respective nodes. An important peculiarity is that the interpretation on the level of the 6-c $\{[Zn_2(PO_2(OEt))_2]_2\}$ node (marked green on Fig. S15) demanded a decrease of the symmetry of the structure from *I*4/m to *P*4. It was necessary, as in *I*4/m every neighboring pair of $\{Zn_2(PO_2(OEt))_2\}$ nodes (marked blue on Fig. S15) has a corresponding $\{[Zn_2(PO_2(OEt))_2]_2\}$ node between them. However, the joining of two 4-c $\{Zn_2(PO_2(OEt))_2\}$ nodes in one 6-c $\{[Zn_2(PO_2(OEt))_2]_2\}$ node essentially halves the amount of the latter, which is only compatible with the lowered symmetry.

All the topological interpretations were checked by Topos. The outputs for the **pcu** and **nbo** nets are trivial, while the output for the seemingly new 4,6-c net is the next chapter.

The crystallographic file in res-format (SHELX) for the nodes of the nets of different levels of interpretation in *P*4 symmetry is given in the penultimate subchapter of this section (note the comment sections after the “!” sign).

6.1 Topos-output for the topology of 2 on the level of 4,6-c net

The TOPOS output for the topology of **2** on the level of 4-c {[$Zn_2(PO_2(OEt))_2$]} and the 6-c augmented {$Zn_2(COO)_4(DABCO)$} paddle-wheel units:

```
“{Zn2(RCOO)4} paddle-wheel” Point symbol:{5^8.6^4.8^3}
Extended point symbol:[5.5.5.5.5.5.5.5.6(2).6(2).6(2).6(2).8(6).8(6).8(8)]
-------------------------------------
“{Zn2(PO2(OEt))2}” Point symbol:{5^5.6}
Extended point symbol:[5.5.5.5.5(2).6(2)]
-------------------------------------
Point symbol for net: {5^5.6}2{5^8.6^4.8^3}
4,6-c net with stoichiometry (4-c)2(6-c); 2-nodal net
```

6.2 Res-file input in *P*4 symmetry for different levels of topological interpretation

```
TITL 2_topol_symplified_in_P4
CELL 1.5478 19.9120 19.9120 9.5338 90.0000 90.0000 90.0000
ZERR 0.0000 0.0040 0.0040 0.0017 0.0000 0.0000 0.0000
LATT -1
SYMM -y, x, z
SYMM -x, -y, z
SYMM y, -x, z
SFAC Au Ag Al Br Bi Be
cn1a 1 0.50000 0.50000 0.50000 0.2500 0.05000  ! Paddle wheel, 4c
cn1b 1 0.00000 0.00000 0.00000 0.2500 0.05000  ! Paddle wheel, 4-c
ct2a 2 0.50000 0.50000 1.00000 0.2500 0.05000   ! DABCO ligand (connector)
ct2b 2 0.00000 0.00000 0.50000 0.2500 0.05000   ! DABCO ligand (connector)
ct1a  3 0.50000 0.25000 0.37500 1.0000 0.05000  ! {Zn2(PO2(OEt))2} node, 4c in 6,6-c net
! ot1a  6 0.50000 0.25000 0.50000 1.0000 0.05000! alternatively to ct1a in 4,6-c net
ct1b 3 0.00000 0.75000 0.12500 1.0000 0.05000   ! {Zn2(PO2(OEt))2} node, 4c in 6,6-c net
! ot1b  6 0.00000 0.75000 0.00000 1.0000 0.05000! alternatively to ct1a in 4,6-c net
jn1  4 0.50000 1.00000 0.25000 0.5000 0.05000    ! {[Zn2(PO2(OEt))2]2} node, 6c
! cn3a  5 0.50000 0.00000 0.50000 1.0000 0.05000          ! {Zn2(PO2(OEt))2} node, 4c in 4,6-c net
! cn3b  5 0.50000 0.00000 0.00000 1.0000 0.05000          ! {Zn2(PO2(OEt))2} node, 4c in 4,6-c net
! the jn1-jn1 distance in the 6,6-c net is ~9.5 Å, all other bonds are of ~4.5-5.5 Å lengths
END
```

6.3 Illustration of the possible isoreticular expansion of 2

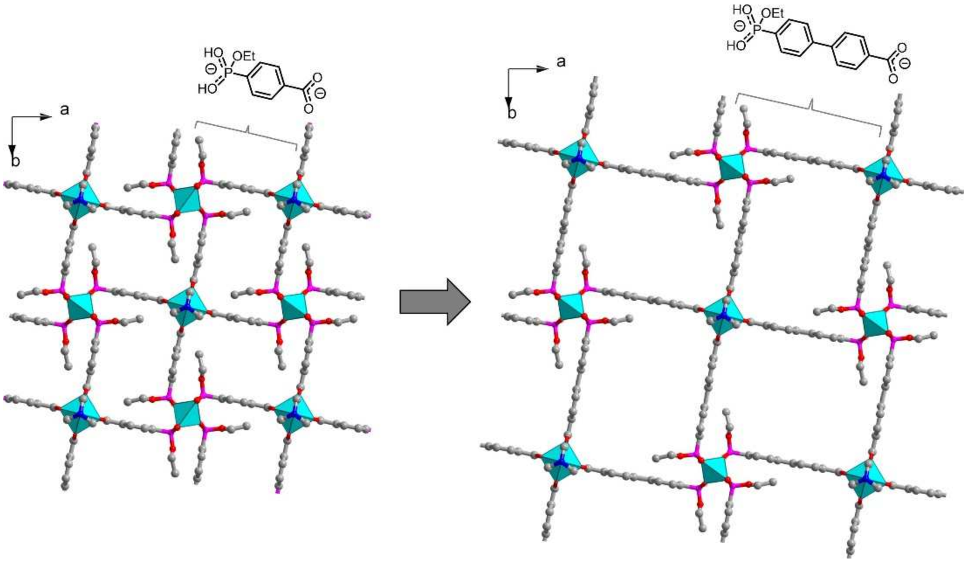

Fig. S19 Projections of the structure of **2** and its isoreticularly expanded analogue, based on a ligand with a biphenyl core, on the *ab* plane. Note that the monoethylphosphonate ligands are oriented parallel to the ab plane (though not coplanarly), and the connectivity along the *c*-axis is sustained by the 1D SBUs, also by means of the DABCO co-ligands. Hence, the isoreticular expansion *via* the elongation of the monoethylphosphonate ligand affects only two dimensions out of three.

7 Geometrical surface area and pore volume based on structural data

The geometrical (‘theoretical’, Connoly) surface area and the void volume (*i.e.* solvent/probe accessible pore volume) for [$Zn_2(EtBCP)_2(DABCO)_{0.5}$] **2´** were calculated using the program Surface Area Program (by Düren/Snurr)[14] and the Zeo++ program[15], both of which based on Monte-Carlo approach of volume-filling of the structure by probe-spheres. For comparison, the pore volume was also calculated with Platon,[16] using a simpler and less precise grid-point calculation-based approach (fixed “equivalent probe” diameter of 2.4 Å). The calculation results by Platon proved to be strongly overestimated, and rather approximate an asymptotic value to the integral void volume (*i.e.* equivalent for a void volume found for a probe, which size tends to zero). It is known situation for the Platon software, and thence the respective data is not reliable for very narrow pore structures.

The input files for all the programs were prepared as follows: the DMA solvent molecules were removed, the symmetry was lowered to *P*1 (*i.e.* all the symmetry equivalent atoms were generated) the disorder was collapsed to one component for both the DABCO and OEt moieties. If the disorder were not collapsed, which would be a mistake as the given programs do not account the occupation factors, the error is relatively modest (e.g. for Platon is relatively small, ~10%) as the rotational disorder of DABCO does not take away a lot of volume, while the disorder of OEt is relatively well localized. The calculated values are listed in Table S4.

Table S4. The geometrical surface areas and pore volumes calculated using different software for [$M_2(EtBCP)_2(DABCO)_{0.5}$] (M = Zn, **2´**) and the relevant experimental data (M = Zn, **2´**; M = Co, **3´**)

Surface Area Program[a]	
Total surface area, $m^2\ g^{-1}$	904
Zeo++ [a]	
Total accessible surface area, $m^2\ g^{-1}$	1057
Total non-accessible surface area, $m^2\ g^{-1}$	0
Maximum included sphere diameter	5.91
Maximum free sphere diameter (*i.e.* passable through the pore system), Å	4.62
Void volume (3.68 Å probe diam., equiv. to N_2), % {$cm^3\ g^{-1}$}	4.7 {0.041}
Void volume (3.30 Å probe diam., equiv. to **CO_2**), % {$cm^3\ g^{-1}$}	**7.3 {0.065}**
Void volume (2.40 Å probe diam., equiv. to H_2O), % {$cm^3\ g^{-1}$}	15.7 {0.139}
Void volume (1 Å probe diam., approximation of total free vol.), % {$cm^3\ g^{-1}$}	36.7 {0.325}
Platon 'Calc Void/Solv'	

Void volume (2.4 Å probe diam., equiv. to H_2O), % {cm^3 g^{-1}} [a]	44.6 {0.394}

Experimental CO_2 uptake

V_{pore} (cm^3 g^{-1}) (195 K) [b]	
First step (end)	M = Zn: 0.11 (P/P_0 = 0.08) M = Co: 0.12 (P/P_0 = 0.11)
Second step (end)	M = Zn: 0.21 (P/P_0 = 1.0) M = Co: 0.23 (P/P_0 = 1.0)
V_{pore} (cm^3 g^{-1}) (298 K) [b]	
First step	M = Zn: 0.11 (P/P_0 = 0.19) M = Co: 0.15 (P/P_0 = 0.19)

[a] Probe diameter is 3.681 Å, equals to the kinetic diameter of N_2 molecule (if not given otherwise explicitly), framework density is 1.13 g cm^{-3} (solvent molecules removed)

[b] Experimental pore volumes are calculated under the assumption of the validity of the Gurvich rule[17] according to (specific amount adsorbed)/(density of liquid CO_2) with $\rho_{CO2,\ 195\ K}$ = 1.10 g cm^{-3} and $\rho_{CO2,\ 298\ K}$ = 0.71 g cm^{-3}.

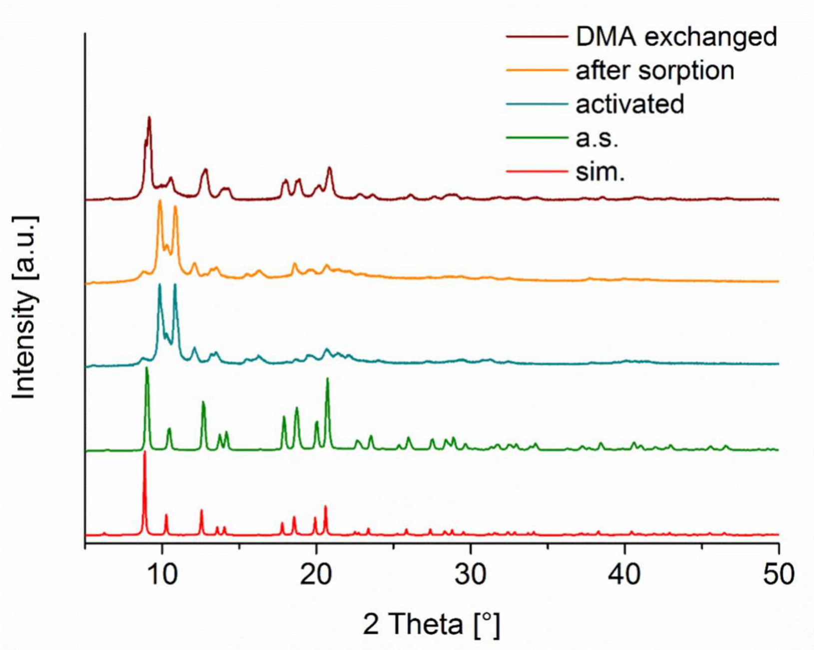

Fig. S20 PXRD patterns of:
$[Zn_2(EtBCP)_2(DABCO)_{0.5}]\cdot 2DMA$, **2**, simulated from X-ray crystal diffraction data (red);
the measured PXRD pattern for the as-synthesized sample of **2** (green);
the sample activated by 160°C, **2´** (teal);
the activated sample after sorption measurement, **2´**$_{abs}$ (orange);
the activated sample after re-solvation by DMA, **2**$_{resolv}$.

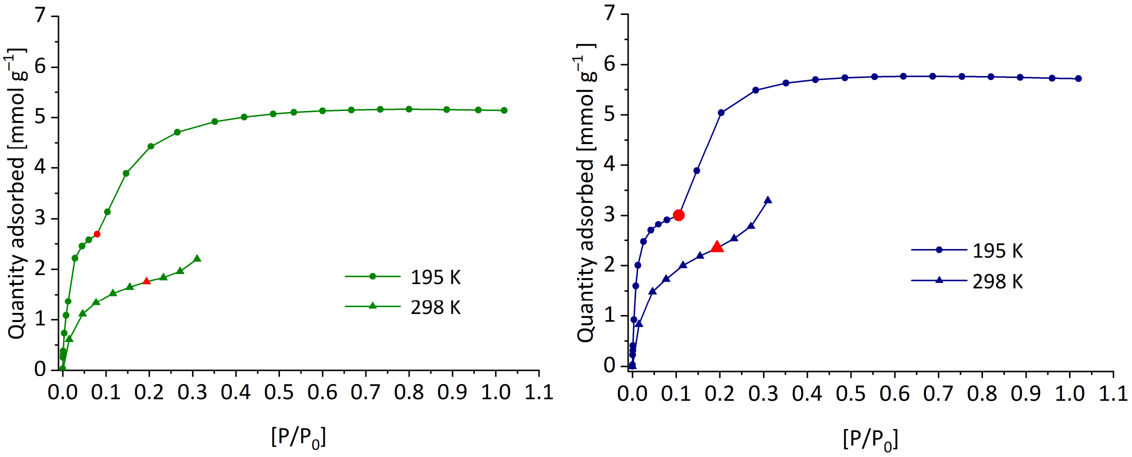

Fig. S21 Comparison of the low and high-pressure sorption isotherms for CO_2 at 195 K and 298 K respectively for $[Zn_2(EtBCP)_2(DABCO)_{0.5}]$, **2´** (green) and $[Co_2(EtBCP)_2(DABCO)_{0.5}]$, **3´** (blue). The red point symbolizes the first step which was used to calculate the maximal micropore volume for the particular isotherm before the assumed structural transformation.

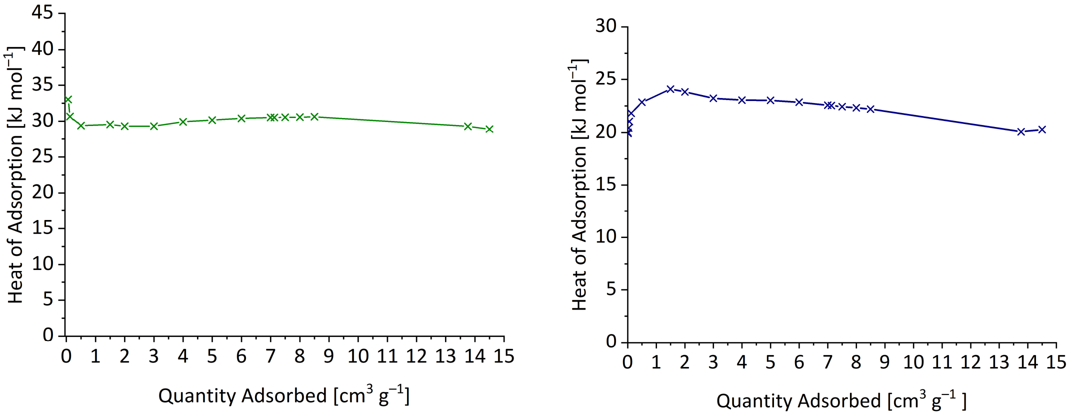

Fig. S22 Isosteric heat of adsorption of CO_2 for **2´** (left) and **3´**(right), derived from CO_2 adsorption isotherms at 273 and 293 K.

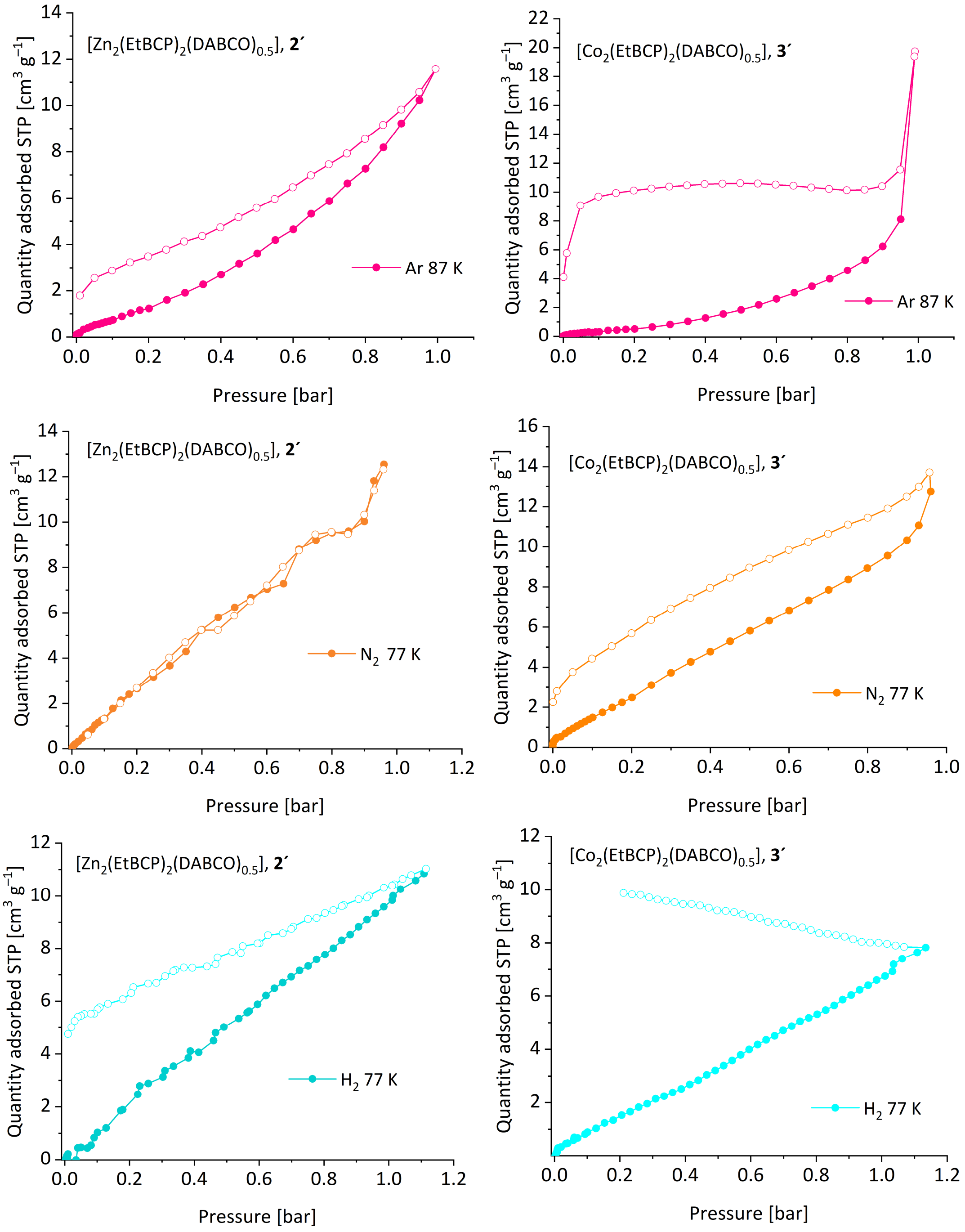

Fig. S23 Adsorption and desorption isotherms of Ar, N_2 and H_2 for [$Zn_2(EtBCP)_2(DABCO)_{0.5}$], **2´** (left) and [$Co_2(EtBCP)_2(DABCO)_{0.5}$], **3´** (right).

Notes: a) The Ar adsorption/desorption isotherm for **3´** at 87 K shows an effect of a very short equilibrium time. Argon is adsorbed to a small extent, but it is not desorbed fast enough. As in other cases, the measurement error is large due to the small amount adsorbed.

b) The H_2 adsorption/desorption isotherm for **3´** at 77 K demonstrates an artefact regarding the desorption branch. The appearance of such artefacts is quite possible for low amount adsorbed. The measurement is marked by poor-quality, but was not repeated due to the low amount adsorbed.

8 BET and Langmuir surface areas and the respective experimental adsorption raw data

The use of CO_2 gas adsorption data for the calculation of the BET area is controversial. CO_2 at low temperatures does not correspond well to the demands of the phenomenological BET model. Despite the low precision, the method is occasionally used in practice.[18,19,20,21] The discussion of the correctness of the approach is outside of the scope of this publication. We use the method as a crude estimate along with the Langmuir model. The latter is, in principle, suits better for the treatment of the experimental data, however also has precision issues due to the low acting relative pressures and hence the low adsorbed amounts.
Nevertheless, the results obtained *via* the use of the BET and Langmuir model are quite close and indicates consistency, even if the precision remains unclear.

8.1 Langmuir report for $[Zn2(EtBCP)_2(DABCO)_{0.5}]$, 2´

Langmuir surface area:	330.2708 ± 9,2532 m^2 g^{-1}
Slope:	0.013830 ± 0,000387 g cm^{-3} STP
Y-intercept:	0.157 ± 0.014 mmHg g cm^{-3} STP
b:	0.088088 1 $mmHg^{-1}$
Qm:	72.3086 cm^3 g^{-1} STP
Correlation coefficient:	0.998434
Molecular cross-sectional area:	0.1700 nm^2

Pressure, mmHg	**Quantity adsorbed (STP), cm^3 g^{-1}**	**P/Q (STP), mmHg cm^{-3}**
5.707641	24.2983	0.235
9.573032	30.5375	0.313
21.194822	49.6882	0.427
33.597107	54.9401	0.612
45.386738	57.7457	0.786
59.656086	60.1779	0.991

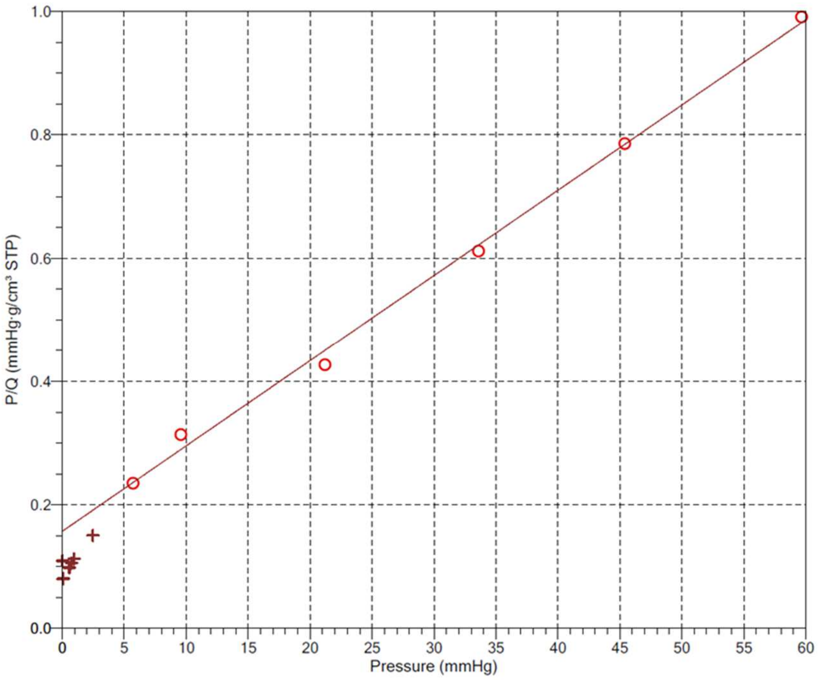

Fig. S24 Langmuir surface area plot for **2´**.

8.2 BET report for $[Zn_2(EtBCP)_2(DABCO)_{0.5}]$, 2´

BET surface area: 310.5327 ± 9.4466 $m^2\ g^{-1}$
Slope: 0.014602 ± 0.000447 g cm^{-3} STP
Y-intercept: 0.000107 ± 0.000011 g cm^{-3} STP
C: 138.080668
Qm: 67.9872 $cm^3\ g^{-1}$ STP
Correlation coefficient: 0.9981285
Molecular cross-sectional area: 0.1700 nm^2

Relative pressure, P/P_o	**Quantity adsorbed (STP), $cm^3\ g^{-1}$**	**$1/[Q(P_0/P - 1)]$**
0.004047972	24.2983	0.000167
0.006789385	30.5375	0.000224
0.015031789	49.6882	0.000307
0.023827735	54.9401	0.000444
0.032189176	57.7457	0.000576
0.042309281	60.1779	0.000734

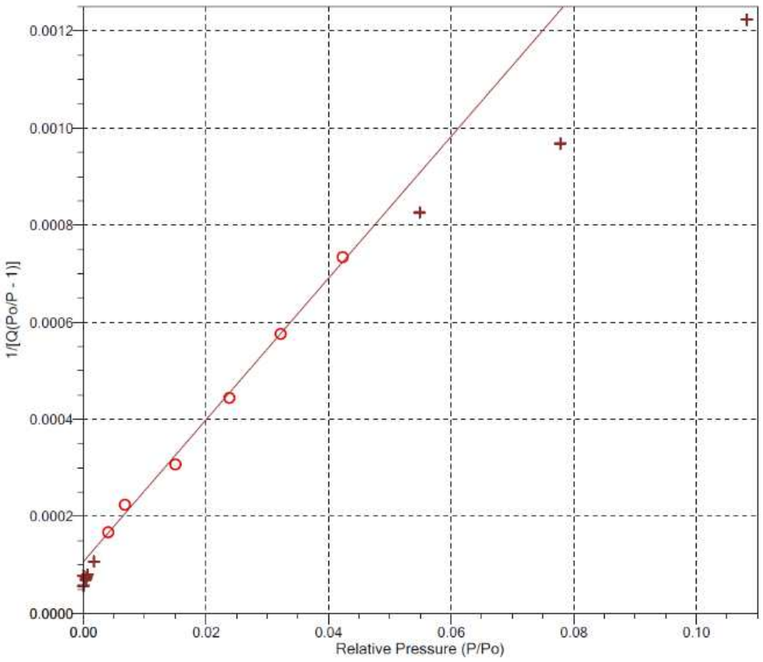

Fig. S25 BET surface area plot for **2´**.

8.2 Langmuir report for [$Co_2(EtBCP)_2(DABCO)_{0.5}$], 3´

Langmuir surface area: 326,8281 ± 1,2338 m^2 g^{-1}
Slope: 0.013975 ± 0,000053 g cm^{-3} STP
Y-intercept: 0.080 ± 0,002 mmHgKg cm^{-3} STP
b: 0.174252 1/mmHg
Qm: 71.5548 cm^3 g^{-1} STP
Correlation coefficient: 0.999971
Molecular cross-sectional area: 0.1700 nm^2

Pressure, mmHg	**Quantityadsorbed (STP), cm^3 g^{-1}**	**P/Q (STP), mmHg cm^{-3}**
5.984107	35.8666	0.167
9.519302	44.9481	0.212
19.044296	55.4762	0.343
31.617212	60.5244	0.522
44.528290	63.2270	0.704
59.221222	65.2755	0.907

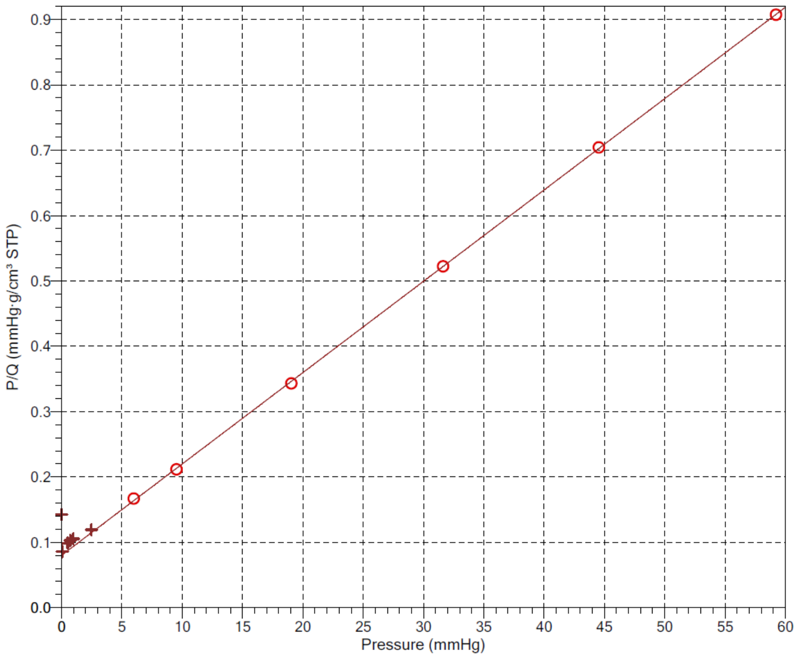

Fig. S26 Langmuir surface area plot for **3´**.

8.4 BET report for [Co_2(EtBCP)$_2$(DABCO)$_{0.5}$], 3´

BET surface area:	309.7723 ± 2.1570 m^2 g^{-1}
Slope:	0.014693 ± 0.000103 g cm^{-3} STP
Y-intercept:	0.000052 ± 0.000002 g cm^{-3}STP
C:	282.925279
Qm:	67.8207 cm^3 g^{-1} STP
Correlation coefficient:	0.9999024
Molecular cross-sectional area:	0.1700 nm^2

Relative pressure, P/P_o	**Quantity adsorbed (STP), cm^3 g^{-1}**	**$1/[Q(P_0/P - 1)]$**
0.004244048	35.8666	0.000119
0.006751278	44.9481	0.000151
0.013506593	55.4762	0.000247
0.022423555	60.5244	0.000379
0.031580347	63.2270	0.000516
0.042000867	65.2755	0.000672

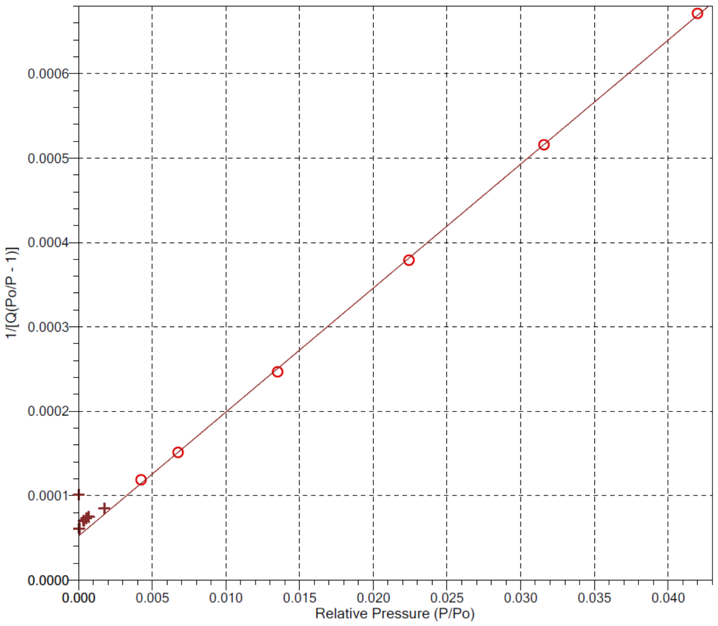

Fig. S27 BET surface area plot for **3´**.

9 Comparison of low pressure CO_2 adsorption isotherms collected using different equilibration times for **3′** (assessing kinetic effects)

In order to verify the influence of kinetic factors, we measured the CO_2 adsorption isotherms for **3′** using three different instrumental equilibration-time settings, 20 s, 40 s, and 100 s. Note that those numbers do not have very direct physical sense: they are only the time intervals after, which the instrument (Micromeritics ASAP 2020, in this case) checks the change of the pressure with time, and concludes, whether the acquisition of the data point is finished or a next equilibration-period should be applied. Hence, the real equilibration time consists of multiple time intervals. The precise acquisition times for the collected data points are given in Table S5.

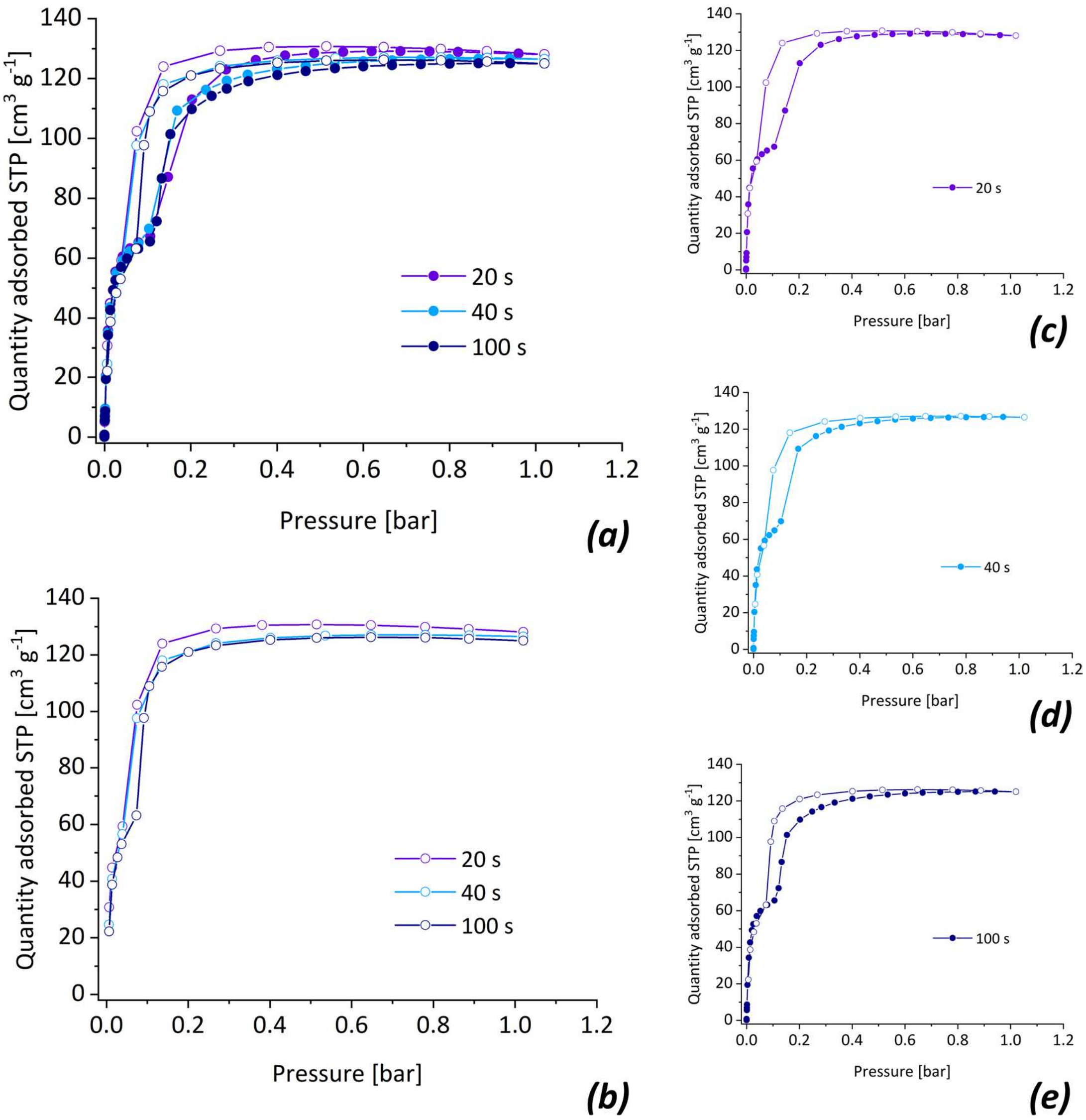

Fig. S28 Comparison of the CO_2 physisorption isotherms (195 K) of **3′** measured using different instrumental equilibration-time parameters (20 s, 40 s, 100 s). (a) Overlay of the three physisorption isotherms (b) overlay of the desorption branches only (c,d,e) complete individual physisorption isotherms.

The measurements clearly indicate that the presence of hysteresis is at least partially, but most probably entirely, kinetically conditioned for the analog materials **2′** and **3′**. For the longest equilibration-time parameter (100 s) the hysteresis width is roughly half of the one observed in the shortest time (20 s). The adsorption and the desorption branches of the physisorption isotherm become practically indistinguishable for the first adsorption step at the longest equilibration time, indicating that complete return to the initial framework geometry occurs.

Table S5. Data-points for the CO_2 physisorption isotherms measured with various equilibration-time parameters (20 s, 40 s and 100 s) for **3′** with acquisition times given.

20 s			40 s			100 s *		
Pressure, mbar	Quantity adsorbed, $cm^3\ g^{-1}$ STP	Elapsed time, h:min	Pressure, mbar	Quantity adsorbed, $cm^3\ g^{-1}$ STP	Elapsed time, h:min	Pressure, mbar	Quantity adsorbed, $cm^3\ g^{-1}$ STP	Elapsed time, h:min
0.0127	0.0671	1:55	0.0150	0.114	2:00	0.0187	0.1101	2:12
0.0808	0.704	2:06	0.0752	0.809	2:17	0.0842	0.8091	2:38
0.672	5.09	2:20	0.679	5.72	2:34	0.731	5.59	3:05
0.962	7.01	2:30	0.962	7.53	2:50	0.971	6.93	3:31
1.29	9.22	2:39	1.30	9.57	3:18	1.29	8.68	3:55
3.28	20.65	2:49	3.30	20.44	3:03	3.30	19.42	4:22
7.98	35.87	2:56	8.02	35.13	3:30	8.03	34.32	4:42
12.69	44.95	3:04	12.81	43.66	3:41	13.20	42.65	5:02
25.39	55.48	3:12	27.77	55.04	3:52	20.01	49.30	5:23
42.15	60.52	3:17	42.03	59.33	4:02	25.70	52.61	5:43
59.37	63.23	3:21	58.61	62.29	4:11	38.48	57.02	6:04
78.96	65.28	3:25	79.14	64.80	4:19	52.25	59.82	6:23
106.39	67.33	3:28	103.62	69.79	4:42	78.53	63.13	6:41
147.51	87.07	3:50	168.43	109.27	5:00	105.64	65.55	7:02
203.05	112.99	4:02	235.32	116.23	5:13	121.15	72.31	7:47
281.83	123.00	4:08	283.40	119.27	5:25	132.70	86.64	8:39
351.09	126.17	4:12	332.05	121.27	5:34	152.64	101.41	9:18
418.79	127.66	4:15	399.83	123.17	5:43	202.54	109.74	9:48
486.10	128.47	4:01	466.84	124.33	5:51	248.65	114.16	10:15
553.60	128.91	4:20	533.61	125.16	5:58	283.79	116.59	10:41
619.70	129.13	4:22	600.32	125.73	6:06	333.46	119.05	11:04
686.63	129.16	4:24	666.93	126.09	6:14	400.80	121.16	11:25
753.44	129.07	4:26	733.67	126.35	6:22	466.57	122.48	11:44
819.96	128.90	4:28	800.24	126.49	6:29	534.46	123.42	12:03
886.72	128.65	4:31	866.91	126.58	6:37	600.39	124.06	12:22
960.07	128.30	4:33	940.17	126.60	6:45	666.94	124.49	12:41
1019.90	128.05	4:35	1020.03	126.49	6:53	733.71	124.76	13:00
886.70	129.14	4:37	887.77	126.88	7:01	800.28	124.96	13:18
779.78	129.88	4:40	780.36	127.06	7:09	867.16	125.08	13:37
647.25	130.46	4:42	647.78	127.05	7:17	940.57	125.08	13:56
514.75	130.75	4:44	535.46	126.78	7:25	1020.33	125.01	14:15
381.19	130.50	4:47	401.50	126.01	7:33	887.21	125.71	14:34
267.88	129.31	4:50	267.97	124.13	7:42	780.23	126.06	14:53
136.83	123.97	4:57	137.00	118.04	8:02	647.59	126.22	15:11
74.91	102.38	5:22	74.57	97.64	9:42	514.58	125.96	15:30
39.44	59.31	5:34	39.02	56.54	10:06	401.06	125.29	15:49
13.59	44.77	5:46	13.53	40.76	11:00	268.26	123.34	16:12
6.55	30.74	5:58	6.21	24.62	11:57	200.83	121.01	16:43
						135.56	115.83	17:49
						105.10	108.96	19:38
						91.60	97.67	23:19
						73.29	63.12	23:52
						36.92	53.02	25:54:00
						27.24	48.37	27:17:00
						13.56	38.71	27:40:00
						6.56	22.22	31:08:00

[*] There were some additional data points measured for the desorption branch of the adsorption isotherm

10 Stability tests in air and the water vapor adsorption by 3′

The stability tests regarding moisture in air were performed *via* exposure of the samples to ambient air at ~ 295 K (~50% relative humidity, typical for indoors conditions. As the test is qualitative, no in-depth control of humidity was pursued). No significant changes were observed in all cases.

The starting sample for **2**, denoted as "**2**, a.s." in Fig. S29 was a different sample then the one used for the PXRD in Fig. 3 (MS). Hence, the slight changes in the peak intensities compared to Fig. 3. The starting sample for **3**, denoted as "**3**, re-solvated" was a sample which had been used for CO_2 and water vapor sorption studies. After the water vapor sorption measurement, the sample was re-solvated with DMA. Hence, again the slight changes in the peak intensities compared to Fig. 3 (MS).

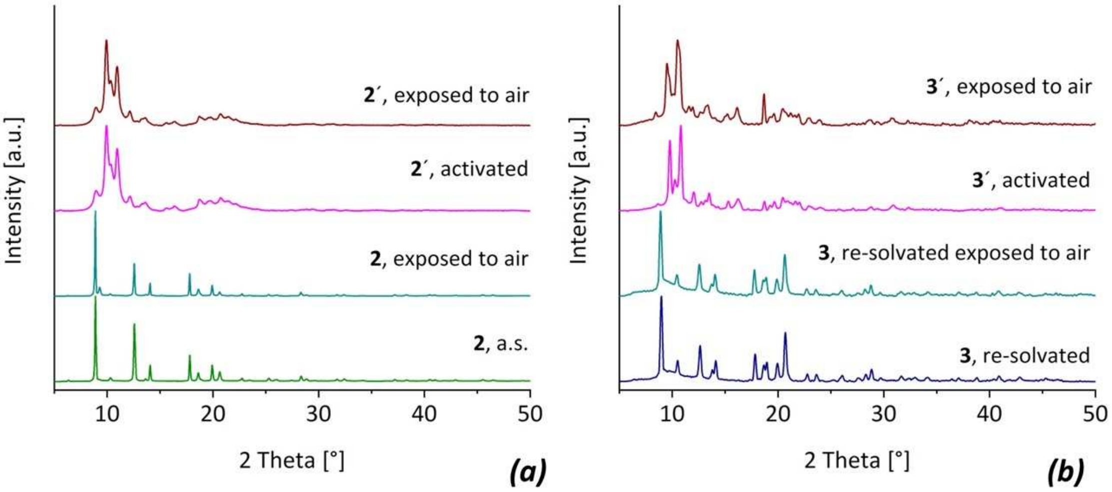

Fig. S29 PXRD stability tests for **2, 2′** (a) and **3, 3′** (b) in air for 2 days.

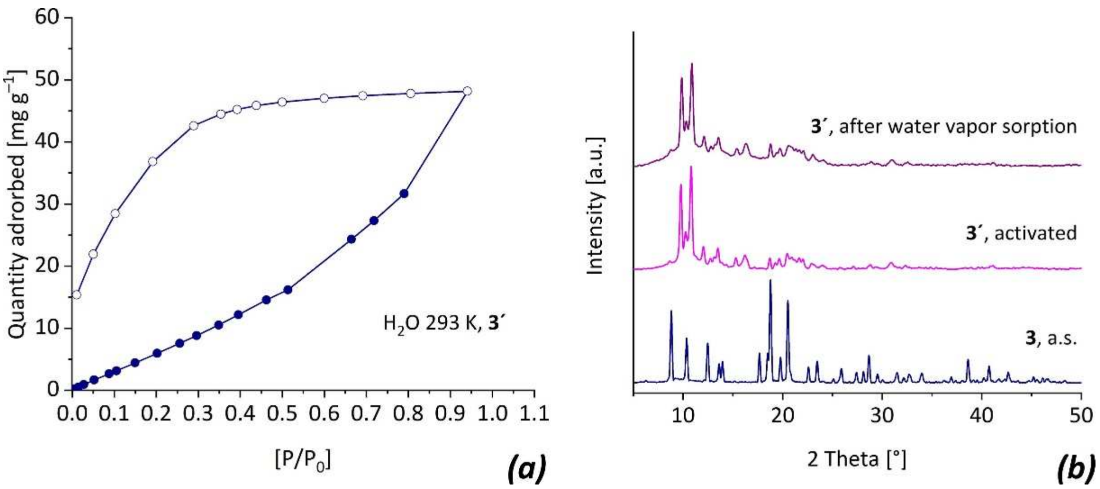

Fig. S30 (a) H_2O adsorption and desorption isotherm at 298 K for **3´** measured on the Quantachrome VSTAR vapor sorption analyser; (b) PXRD monitoring of the changes after activation (160 °C, vacuum) and after the performed water vapor adsorption.

11 Solvent stability tests performed on 2

In order to assess the solvent stability of **2**, a long-term soaking (~3 days) of the as-synthesized material in chloroform, ethanol, acetone and in water (~1 day) was carried out. The exchanged materials were subjected to additional "reverse exchange" *via* soaking in DMA (~3 days). While the treatment of the degassed samples would give a faster and to some extent more reliable result, the long-term soaking of the as-synthesized sample is also satisfactory, while the result is not affected by the crystallinity deterioration due to the degassing:

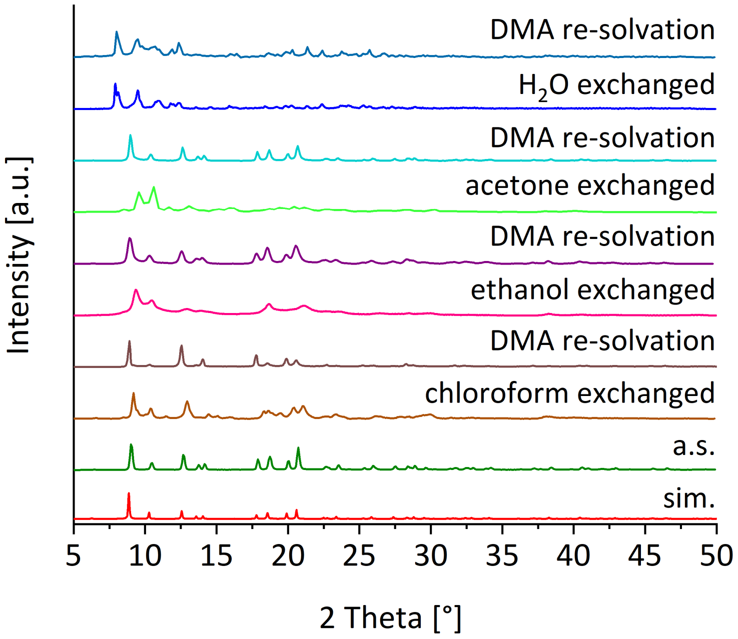

Fig. S31 PXRD patterns of **2** after soaking in different solvents, followed by "reverse-exchange" with *N,N*-dimethylacetamide (DMA).

Soaking in chloroform resulted only in a minor change of crystallinity according to the PXRD pattern, while ethanol caused a significant change. However, in both cases a complete return to the initial state took place after soaking the exchanged material in pure DMA. Interestingly, acetone caused a strong change, but the reversal was also complete. Finally, water caused a transformation to a different phase with an appreciable crystallinity, which did not return to the initial state after soaking in DMA.

The experimental observation suggests significant stability against the action of chloroform, ethanol and acetone. The exchange causes rather reversible deformation of the flexible framework without loss of crystallinity and with full recovery of the initial state after subsequent soaking in DMA. The situation with water is more complex: while the crystallinity is not lost completely, the transformation is irreversible. Hence, the conclusion is that **2** is not truly stable in contact with liquid water and in the best case transforms to another unknown crystalline phase with somewhat compromised crystallinity.

12 References

1 D. Kong, J. Zon, J. McBee and A. Clearfield, *Inorg. Chem.*, 2006, **45**, 977–986.

2 K. Bladek, M. Reid, H. Nishihara, F. Akhtar, B. Gelfand and G. K. H. Shimizu, *Chem. – Eur. J.*, 2018, **24**, 1533–1538.

3 S. S. Iremonger, J. Liang, R. Vaidhyanathan, I. Martens, G. K. H. Shimizu, T. D. Daff, M. Z. Aghaji, S. Yeganegi and T. K. Woo, *J Am. Chem. Soc.*, 2011, **133**, 20048–20051.

4 S. S. Iremonger, J. Liang, R. Vaidhyanathan and G. K. H. Shimizu, *Chem. Commun.*, 2011, **47**, 4430–4432.

5 J.-W. Zhang, C.-C. Zhao, Y.-P. Zhao, H.-Q. Xu, Z.-Y. Du and H.-L. Jiang, *CrystEngComm*, 2014, **16**, 6635–6644.

6 J. M. Taylor, R. Vaidhyanathan, S. S. Iremonger and G. K. H. Shimizu, *J. Am. Chem. Soc.*, 2012, **134**, 14338–14340.

7 B. Gelfand, J.-B. Lin and G. K. H. Shimizu, *Inorg. Chem.*, 2015, 54, 1185–1187.

8 B. S. Gelfand, R. P. Huynh, R. K. Mah and G. K. H. Shimizu, *Angew. Chem. Int. Ed.*, 2016, **55**, 14614–14617.

9 Z. Hassanzadeh Fard, N. E. Wong, C. D. Malliakas, P. Ramaswamy, J. M. Taylor, K. Otsubo and G. K. H. Shimizu, *Chem. Mater.*, 2018, **30**, 314–318.

10 T. Zheng, Z. Yang, D. Gui, Z. Liu, X. Wang, X. Dai, S. Liu, L. Zhang, Y. Gao, L. Chen, D. Sheng, Y. Wang, J. Diwu, J. Wang, R. Zhou, Z. Chai, T. E. Albrecht-Schmitt and S. Wang, *Nat. Commun.*, 2017, **8**, 15369–15379.

11 N. Hermer and N. Stock, *Dalton Trans.*, 2015, **44**, 3720–3723.

12 R. Vaidhyanathan, A. H. Mahmoudkhani and G. K. H. Shimizu, *Can. J. Chem.*, 2009, **87**, 247–253.

13 V. A. Blatov, A. P. Shevchenko, and D. M. Proserpio, *Cryst. Growth Des.*, 2014, **14**, 3576–3586.

14 T. Düren, F. Millange, G. Férey, K. S. Walton, and R. Q. Snurr, *J. Phys. Chem. C*, 2007, **111**, 15350– 15356

15 T. F. Willems, C. H. Rycroft, M. Kazi, J. C. Meza, and M. Haranczyk, *Microporous Mesoporous Mater.*, 2012, **149**, 134–141.

16 A. L. Spek, Structure Validation in Chemical Crystallography *Acta Crystallogr. D*, 2009, 65, 148– 155; PLATON – A Multipurpose Crystallographic Tool, Utrecht University, Utrecht, The Netherlands, A. L. Spek, 2008; Windows implementation: Farrugia, L. J. University of Glasgow, Scotland, Version **40608**, 2008.

17 L. Gurvich, *J. Phys. Chem. Soc. Russ.*, 1915, **47**, 805–827.

18 A.-X. Zhu, Q.-Y. Yang, A. Kumar, C. Crowley, S. Mukherjee, K.-J. Chen, S.-Q. Wang, D. O'Nolan, M. Shivanna and M. J. Zaworotko, *J. Am. Chem. Soc.*, 2018, **140**, 15572–15576.

19 S.-C. Xiang, Z. Zhang, C.-G. Zhao, K. Hong, X. Zhao, D.-R. Ding, M.-H. Xie, C.-D. Wu, M. C. Das, R. Gill, K. M. Thomas and B. Chen, *Nature Commun*, 2011, **2**, 204.

20 C. Hou, Q. Liu, T. Okamura, P. Wang, W.-Y. Sun, *CrystEngComm*, 2012, **14**, 8569–8576.

21 K. Roztocki, M. Szufla, M. Hodorowicz, I. Senkovska, S. Kaskel and D. Matoga, *Cryst. Growth Des.*, 2019, **19**, 7160–7169.

3.1. Coordinatively unsaturated metal sites (open metal sites) in metal–organic frameworks: design and applications

Ülkü Kökçam-Demir,‡a Anna Goldman,‡a Leili Esrafili,b Maniya Gharib,b Ali Morsali,‡*b Oliver Weingartc and Christoph Janiak‡*a, *Chem. Soc. Rev.*, 2020, **49**, 2751–2798. DOI: 10.1039/C9CS00609E

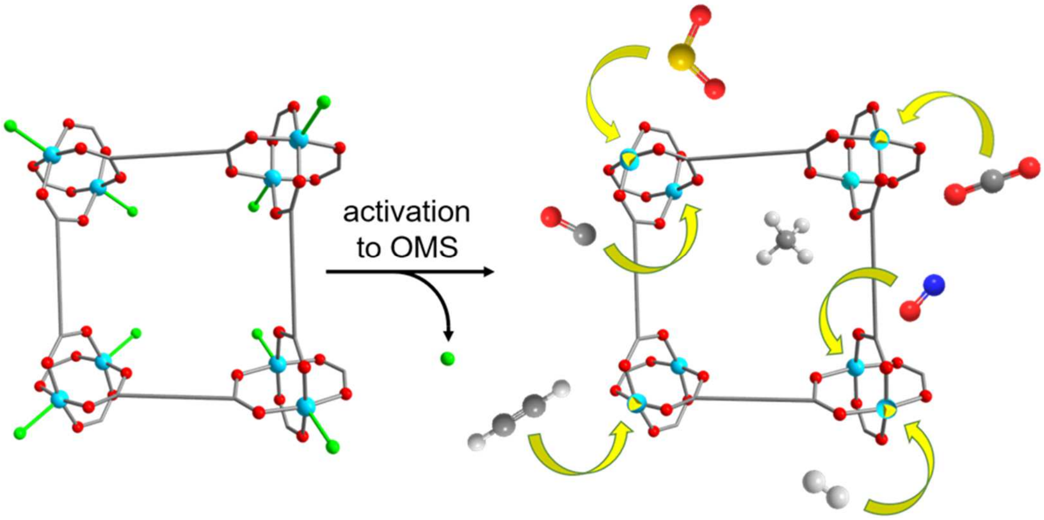

Die Forschung zu Metall-organischen Gerüstverbindungen (MOFs) mit offenen Metallstellen (open metal sites, OMS) hat sich in den letzten Jahren stark entwickelt. MOFs können offene Metallstellen oder koordinativ ungesättigte Stellen (coordinatively unsaturated sites, CUS) oder offene Koordinationsstellen (open coordination sites, OCS) enthalten, wenn freie Lewis-Säure-Stellen auf den Metallionen oder Clusterknoten generiert werden. Die definierte Synthese von OMS in MOFs ist die Basis einer gezielten Funktionalisierung für die Koordination schwach bindender Spezies und erhöhte (supramolekulare) Wechselwirkungen mit Gastmolekülen. Im Vergleich zu MOFs, bei denen die Metallstellen vollständig besetzt sind, wirken offene Metallstellen häufig als starke Bindungsstellen, was zu einer erhöhten Wechselwirkung mit verschiedenen Sorbatmolekülen führt. Daher sind OMS-MOFs vielversprechende Kandidaten für potenzielle Anwendungen der Gassorption und -trennung, Katalyse, Sensorik *etc*. MOFs mit OMS können unter anderem als feste Adsorbentien zur selektiven Entfernung von CO_2 aus Trockengasgemischen, zur Olefin/Kohlenwasserstoff-Trennung und als hochselektive Lewis-Säure Katalysatoren verwendet werden. Dieses Review gibt einen umfassenden Überblick zu unterschiedlichen Synthesestrategien von MOFs mit offenen Metallstellen, theoretischen Studien zu den Auswirkungen von OMS auf Wirt-Gast-Wechselwirkungen und verschiedenen potentiellen OMS-MOF-Anwendungen. Im experimentellen Teil liegt der Schwerpunkt dieses Reviews auf MOFs mit nachgewiesener OMS-Bildung, die durch analytische Methoden eindeutig verifiziert wurde.

Eigenanteile an der Veröffentlichung:

- Idee und Übergabe des Projekts erfolgte durch Herrn Prof. Dr. Ali Morsali.
- Konzeption, Aufbau und Verschriftlichung des Reviews auf der Basis einer ausgiebigen Literaturrecherche erfolgte in Zusammenarbeit mit Frau Ülkü Kökçam-Demir zu gleichen Anteilen.
- Eigenständige Darstellung der SBUs anhand von kristallographischen Daten.
- Anfertigung der Tabellen 1 und S1 – S3.
- Schreiben des Kapitels 3 (Computational studies), MOF-Struktur bezogene Abschnitte im Kapitel 2 (Synthetic and structural overview on typical SBUs for open metal sites and coordinated solvent removal strategies) sowie der Abschnitte „Gas sorption“, „CO_2 adsorption“, „CO adsorption“, „C_2H_2 sorption“, „CH_4 adsorption“, „SO_2 adsorption“ und „Separation“ im Kapitel 4 (Open metal site applications).
- Frau Ülkü Kökçam-Demir schrieb die Einleitung, das Kapitel 2 (Synthetic and structural overview on typical SBUs for open metal sites and coordinated solvent removal strategies) sowie die Abschnitte „Post functionalization of OMS in MOFs”, „H_2 adsorption”, „NO adsorption”, „SO_2 adsorption”, „Catalysis and photocatalysis” und „Sensing” im Kapitel 4 (Open metal site applications).
- Die Anfertigung der Tabellen 2 und 3 erfolgte durch Frau Ülkü Kökçam-Demir.
- Die Verschriftlichung des Abschnitts 2.IV (Quantifying OMS) erfolgte in Zusammenarbeit mit Frau Ülkü Kökçam-Demir und Herrn Prof. Dr. Christoph Janiak.
- Überarbeitung und Korrektur des theoretischen Kapitels „Computational studies“ erfolgte durch Herrn PD Dr. Oliver Weingart.
- Literaturrecherche und Durchsicht des Manuskripts erfolgte durch Frau Leili Esrafili, Frau Maniya Gharib und Herrn Prof. Dr. Ali Morsali.
- Überarbeitung und Korrektur des Manuskripts erfolgte durch Herrn Prof. Dr. Christoph Janiak.
- Finale Abstimmung und Bearbeitung der Revision des Manuskripts erfolgte in Zusammenarbeit mit Frau Ülkü Kökçam-Demir und Herrn Prof. Dr. Christoph Janiak.

The work presented in this chapter has been published in:

Coordinatively unsaturated metal sites (open metal sites) in metal–organic frameworks: design and applications†

Ülkü Kökçam-Demir,[‡a] Anna Goldman,[‡a] Leili Esrafili,[b] Maniya Gharib,[b] Ali Morsali,[‡*b] Oliver Weingart[c] and Christoph Janiak[‡*a], *Chem. Soc. Rev.*, 2020, **49**, 2751–2798. DOI: 10.1039/C9CS00609E

The article is reproduced from Ref. 116 with permission from the The Royal Society of Chemistry 2020.

Metal–organic frameworks (MOFs) can contain open metal sites (OMS) or coordinatively unsaturated sites (CUS) or open coordination sites (OCS) when vacant Lewis acid sites on the metal ions or cluster nodes have been generated. This review combines for the first time all aspects of OMS in MOFs, starting from different preparation strategies over theoretical studies on the effects of OMS with host–guest interactions up to distinct OMS-MOF applications. In the experimental part the focus of this review is on MOFs with proven OMS formation which are not only invoked but are clearly verified by analytical methods.

1. Introduction

Metal–organic frameworks are three-dimensional coordination networks containing potential voids.[1,2] This subcategory of coordination polymers is built from metal ions or metal clusters linked together by organic ligands. A key characteristic of MOFs should be their crystallinity for structure determination together with proven (micro-)porosity. An important feature of MOFs over other porous materials such as zeolites and porous carbons[3,4] is the ability to widely design the physiochemical inner surface properties, and thereby establish a large variety in topologies and structures by the deliberate design and selection of organic and inorganic molecular building blocks.[5] MOFs have been considered to be promising candidates for a diversity of potential applications such as gas sorption, including gas separation[6] and storage,[7–9] catalysis,[10–13] photocatalysis,[14] sensing,[15] drug delivery,[16] optical applications[17] and heat transformation.[18–21]

In classical coordination chemistry or organometal chemistry the concept of free coordination sites was already well established. A free coordination site exists in complexes with a lower than the normal coordination number of the metal atom. For those 3d metal atoms for which an octahedron with coordination number six would be expected, a missing ligand and only fivefold coordination would establish a free coordination site. Square-planar metal complexes which are often found for d^8 metal atoms have inherently two free coordination sites.[22,23] In ligand substitution reactions with metal complexes the dissociative pathway proceeds through a lower coordination number/free coordination site as the intermediate or transition state. Oxidative addition needs open metal sites with possibility to increase the coordination (and oxidation) number by two. A free coordination site is required *e.g.* for π-coordination of an olefin prior to insertion in the metal–carbon bond of the polymer chain end for olefin polymerization. Many metalloproteins and -enzymes have free coordination sites before the substrate coordination, *e.g.* the iron atom in hemoglobin is five-fold coordinated before the dioxygen coordination.[24] The "free coordination site" can be temporarily occupied by a labile water (aqua) ligand. Different to open metal sites in MOFs, the "free coordination sites" in classical coordination chemistry often present only intermediary or transition states. This is due to the presence of solvent molecules as coordination chemistry or catalysis is often conducted in solution. Hence, the potential free coordination sites will then be occupied by labile solvent molecules.[22,25]

Overall, the M–L bond in metal–ligand coordination complexes is often kinetically labile. Thus, in solution there will often be an equilibrium between the desired ligand and competing coordinating solvent molecules like water, alcohols, *etc.*[24] The lability of the metal–ligand bond is an inherent necessity of the use of metal atoms as catalytic centers in metallo-enzymes or technical catalysts. When the thermally activated ligand exchange will be very slow as for kinetically stable (inert) metal complexes, *e.g.* of Co^{3+} in $[Co(CN)_6]^{3-}$ or $[Co(NH_3)_6]^{3+}$ excitation with light can lead to an effective (fast) ligand exchange through the population of a photoactive excited state. When the light irradiation of the complexes is carried out in water, the CN or NH_3 ligand will initially be replaced by an aqua ligand (photoaquation).[22,25]

The M–L bond dissociation energy of the coordinative bond is usually lower than that of a covalent C–C or C–O bond.[24] From coordination chemistry principles, the thermodynamic stability of the M–L bond can be increased with high valence metal ions, such as Cr^{3+}, Fe^{3+}, and Zr^{4+}. With the coordination environments being equal, an increased charge will increase the electrostatic interaction between the metal ions and the ligands. A measure of the complex stability is the stability constant, which typically is not very large for monodentate ligands.[24,26]

In MOFs the metal ion which will be considered for the generation of the open metal site should be part of the metal node or metal secondary building unit. There are also MOFs which have metal ions as part of the linker, in so-called metalloligands.[27–30] The formation or presence of open metal sites in these metallo-ligands will not be the topic of this review as this is even more closely related to classical coordination chemistry.

In MOF structures any change to the metal ions in the metal SBU must ensure the integrity of the network. Importantly, the MOF structure must not collapse, and their crystallinity and porosity should be preserved, that is, a labile terminal ligand should be removed without damage to the framework. The obtained not fully coordinated metal ions are termed open metal sites (OMS) or coordinatively unsaturated sites (CUS) or occasionally also open coordination sites (OCS). Open metal site chemistry based on MOFs started in 1999, when HKUST-1 (Hong Kong University of Science and Technology, commercially available as Basolite C300 from BASF) was reported by Williams et al.[31] as the first MOF with an obviously easily obtainable OMS. The first report of a Zn-MOF with an open metal site was confirmed in 2000 by Yaghi *et al.*[32,33] with $[Zn_2(btc)(NO_3)(C_2H_5OH)_3](C_2H_5OH)_2(H_2O)$, also named as MOF-4 which is converted to $[Zn_2(btc)(NO_3)]$ after activation.[34,35]

We note that this review is only on MOFs with proven OMS formation. Thus, we solely considered work in which OMS are not only invoked but are clearly verified by analytical methods. The large number of publications which refer to OMS with no definitive proof were not assessed for this review.

The activation of open metal sites in MOFs is often seen as a key in applications. The OMS in MOFs represent often the strongest binding sites, which leads to an increased interaction with different sorbate molecules, compared to MOFs where the metal sites are fully occupied.[36,37] Hence, such OMS-MOFs are very promising candidates for applications, like catalysis,[38–40] sensing,[41] gas separation (*e.g.* alkene/alkane,[42–45] C_2H_2/CO_2,[46–48] CO_2/CH_4,[47] C_2H_2/CH_4,[48,49] C_2H_4/CH_4,[49] CO_2/CH_4,[49,50] 1-butene from other butene isomers51),[52–54] and gas sorption, *e.g.* H_2,[55–65] CO_2,[49,66–71] O_2,[72] CO,[73] NO,[74] N_2O,[75] acetylene C_2H_2,[49,76–78] SO_2,[79] CH_4,[80,81] olefins (ethylene,[49,82] propylene[82]) and alkanes (ethane,[82] propane[82]), ammonia,[83] sulfonamide,[84] phosphine.[85] The most commonly associated potential applications to open metal sites are shown in Fig. 1.

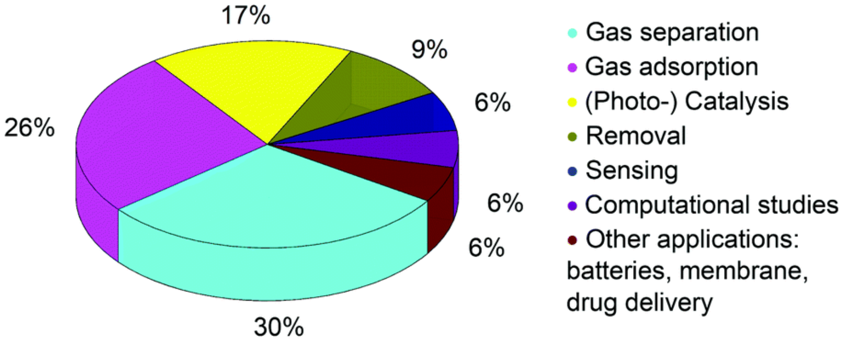

Fig. 1 Most commonly associated potential applications to open metal site MOFs in percent [%] of its number of publications. Taken from SciFinder – CAS by literature search. (Source: https://sso.cas.org/as/jUgiM/resume/as/authorization.ping. Search term: metal–organic frameworks, open metal sites (486 hits, approx. 100%): gas separation (146 hits, 30%), gas adsorption (125 hits, 26%), (photo-) catalysis (84 hits, 17%), removal (46 hits, 9%), sensing (30 hits, 6%), computational studies (27 hits, 6%), other applications: batteries, membrane and drug delivery (28 hits, 6%). Search day: 17.06.2019).

The largest number of potential applications in connection with OMS by the number of publications is gas separation and adsorption. The first connection of OMS to gas adsorption for H_2 was reported in 2005 by Yaghi *et al.*[86] Following the already well-established coordination chemistry and catalysis principles for free coordination sites (see above) OMS-MOFs show an increase in H_2 uptake capacity and improved isosteric heat of adsorption (Q^0_{st}), due to the dihydrogen affinity of the metal atom (akin to the formation of metal–H_2 complexes).[87–92]

Furthermore, OMS can give p-interactions with olefins (formation of metal–olefin complexes) and feature a high adsorption enthalpy of CO_2 which is advantageous for its gas sorption, and separation.[52,93–97] In addition, OMS of electron-deficient metal atoms can act as Lewis acid sites, *e.g.* in catalytic reactions.[32,39] The post-functionalization of OMS, in other words ligand substitution through first formation of an OMS followed by a new ligand coordination to the OMS in MOFs, can be used to postsynthetically functionalize MOFs in general.[98]

In this review, we focus on the synthetic strategies for the verified formation of OMS in MOFs and on applications where a strong evidence for the effect of OMS was provided. Moreover, we also summarize computational studies, because they are an important foundation for studying and predicting sorption properties and applications of OMS-MOFs. Therefore, this overview should help to advance the design of OMS-MOFs for desired applications.

2. Synthetic and structural overview on typical SBUs for open metal sites and coordinated solvent removal strategies

From the initial MOF synthesis, the (remaining) metal coordination sites and the MOF pores will be filled by the solvent which was used in the synthesis. This solvent will be a ligand at the metal atoms to reach their stable coordination number and act as a porogen for the formation of the framework structure. The stability of the SBU and thus the entire framework depends upon the coordination chemistry of the metal atom. A metal atom has a preferred or typical coordination geometry governed by coordination chemistry principles, such as the metal atom size and d-electron configuration (see above in Introduction). If the metal ions are not solely coordinated to the donor atoms of the bridging ligands, their coordination sphere is usually saturated with coordinating unidentate solvent molecules derived from the synthesis medium. The as-synthesized MOF will have initially all metal ions in the SBU in their fully coordinatively saturated state, that is, most stable coordination environment according to their usual coordination numbers, which are typically six (octahedral) or four (tetrahedral) for most 3d transition metal ions. In order to obtain open metal sites in the metal SBUs of MOFs (Table 1) an initial labile terminal ligand which may typically be a solvent molecule needs to be removed from its coordinating metal atom (Fig. 2).

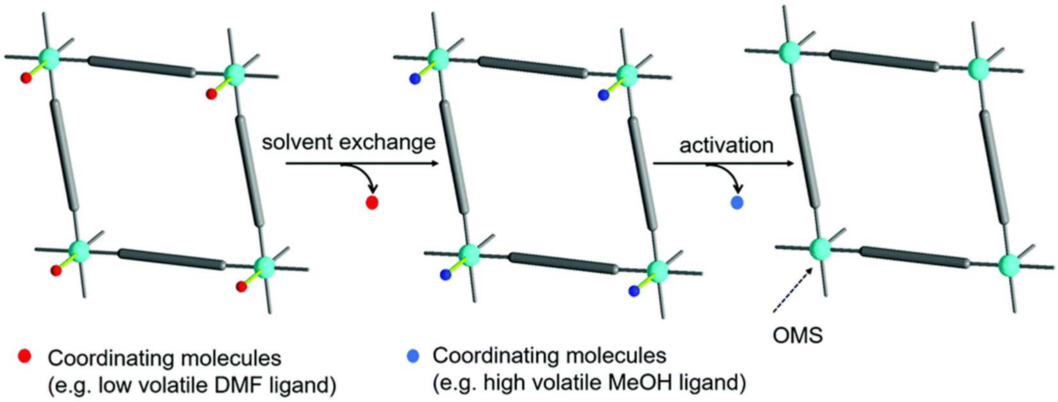

Fig. 2 Schematic presentation of the generation of unsaturated coordination environments on metal atoms in MOFs by replacing a low-volatile ligand (*e.g.* DMF) by a higher-volatile ligand (*e.g.* MeOH) through “solvent exchange” for the subsequent activation, that is, solvent removal.

The procedure for this ligand removal with OMS generation is usually solvent exchange and removal, which may be generally termed “activation”[68,96,99,100] and can be further differentiated into thermal, chemical[101–104] or photothermal[105] activation (Fig. 3).

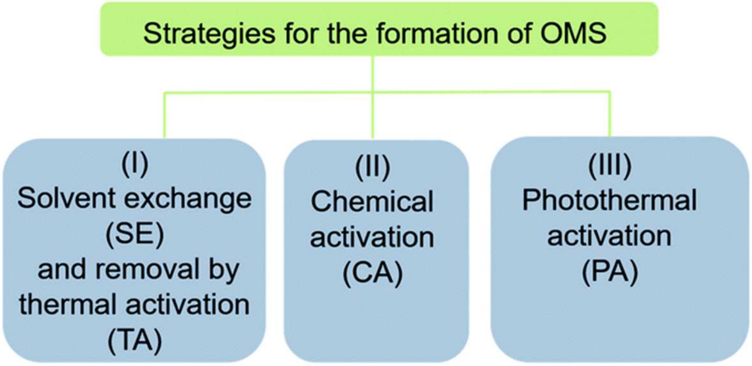

Fig. 3 Overview on the synthetic strategies for the formation of OMS in MOFs.

The synthesis of OMS in MOFs by the general removal of coordinated solvent molecules must proceed without causing a collapse of the network structure.[106,107] It should be noted, however that the salient features of MOFs, namely crystallinity and proven porosity must be retained upon OMS formation which is not always verified in the literature.

In general, the removal of these coordinated solvent molecules is accompanied by a change in the coordination geometry of the metal center.

The open metal sites in MOFs can be generated by the removal of coordinated labile solvent ligand molecules like water, alcohols (methanol and ethanol), acetonitrile, and DMF (*N,N′*-dimethylformamide). The attempt to simply remove the coordinated solvent ligand (and the solvent from the pores) by heating under vacuum, however, may often fail and result in framework degradation or complete decomposition. Some of the solvent ligands are low

volatile (*e.g.* DMF), therefore require high temperature or long evacuation times. Others are more strongly coordinated to the network (*e.g.* water through stronger metal coordination or hydrogen-bonding to the ligand donor atoms) and have a high surface tension in their liquid state and may lead to cavitation effects, that is, network collapse upon their removal.[10]
In order to ensure network retention there are several strategies and procedures in the literature to remove the coordinated solvent molecules (Fig. 3):[101–104,106]

(I) Solvent exchange and removal by thermal activation.[86,92] A less-volatile (higher boiling) solvent ligand is first exchanged with a more volatile (lower boiling) solvent. At the same time the less volatile solvent is thereby washed from the pores of the MOF. This solvent exchange procedure is then followed by thermal activation,[83,98–100,109–116] that is, by applying heat energy and/or (high) vacuum.

(II) (II) Chemical activation.[101–104] A less-volatile solvent is first exchanged by a (washing) treatment with highly volatile and only very weakly coordinating halogenated solvents. Different from (I) the final halogenated solvent removal occurs upon air-drying without using extra thermal energy (accept the energy provided by room temperature). Thereby, the final drying procedure is simpler and faster than in (I).

(III) Photothermal activation.[105] Especially for kinetically stable (inert) metal ions (*e.g.* Cr^{3+}) solvent ligand exchange and thermal ligand exchange will be very slow. Instead irradiation with (UV-vis) light then leads to a fast ligand exchange or removal through the population of a photoactive excited state. Selected papers will be presented, which describe the removal of the coordinated solvent molecules to form open metal sites in their MOFs, by using these three synthetic strategies. Table 2 gives an overview of the OMS-MOFs with their removal strategies in detail, which are reported in this review.

In the following we only reference work where OMS formation was confirmed in combination with framework stability.

Table 1 Overview presentation of selected prototypical OMS-MOFs with their linkers and SBUs discussed in this review[a]

Ligand	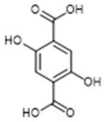	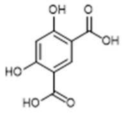	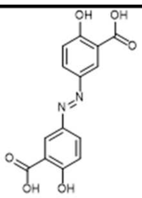	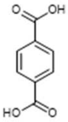	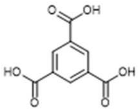	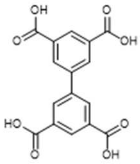	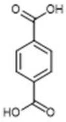	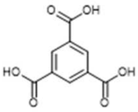
	H$_2$dobdc	H$_4$(*m*-dobdc)}	H$_4$Olz	H$_2$bdc	H$_3$btc	H$_2$bptc	H$_2$bdc	H$_3$btc
Selected MOF	M-MOF-74	[M$_2$(*m*-dobdc)]*	[M$_2$(olz)]	MOF-2	HKUST-1	MOF-505	MIL-101	MIL-100
M with OMS	Mg^{2+}, Mn^{2+}, Fe^{2+}, Co^{2+}, Ni^{2+}, Cu^{2+}, Zn^{2+}, Cd^{2+}	Mg^{2+}, Mn^{2+}, Fe^{2+}, Co^{2+}, Ni^{2+}	Mg^{2+}, Fe^{2+}, Co^{2+}, Ni^{2+}, Zn^{2+}	Cu^{2+}	Cr^{2+}, Cu^{2+}	Cu^{2+}	V^{3+}, Cr^{3+}, Fe^{3+}	Sc^{3+}, V^{3+}, Cr^{3+}, Fe^{3+}
SBU	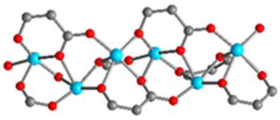			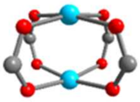			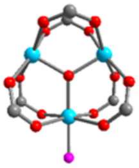 (• = F, OH)	

Ligand	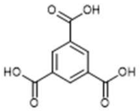	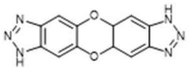	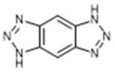	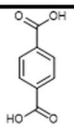	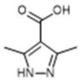
	H$_3$btc	H$_2$btdd	H$_2$bbta	H$_2$bdc	H$_2$dmcapz
Selected MOF	[Eu(btc)]	[M$_2$Cl$_2$btdd]	MAF-X27-Cl	UiO-66	[Cu$_2$(dmcapz)]
M with OMS	Eu^{3+}	Mn^{2+}, Co^{2+}, Ni^{2+}	Mn^{2+}, Co^{2+}	Zr^{4+}	Cu^{2+}
SBU	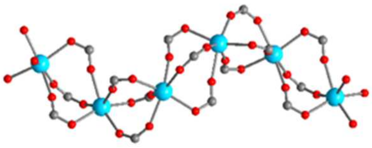	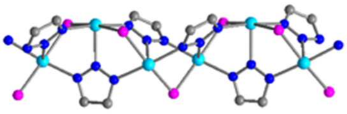 (• = Cl)		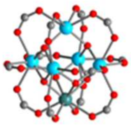	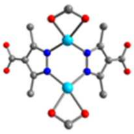

Ligand	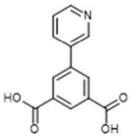	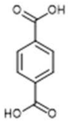	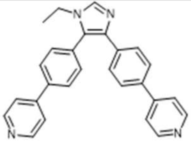	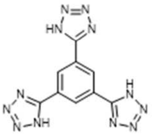
	H$_2$pyip	H$_2$bdc	L**	H$_3$btt
Selected MOF	NJU-Bai33	[Co$_3$(L)(bdc)$_{2.5}$(OAc)]		M-btt
M with OMS	Mn^{2+}	Co^{2+}		Cr^{2+}, Mn^{2+}, Fe^{2+}, Co^{2+}, Cu^{2+}, Cd^{2+}

SBU	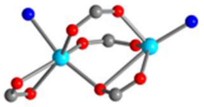	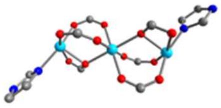	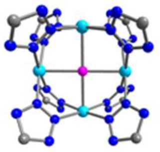 (• = Cl)

[a] The coordinated solvent molecules on the metal nodes, present in the X-ray structure, and the ligand hydrogen atoms are not shown for clarity. Atom color scheme: C grey; O red; N dark-blue; metal atoms pale blue; Cl, F, OH purple. Crystal structure information for the respective compounds was taken from the Cambridge crystallographic data center (CCDC). For a deciphering of the used acronyms such as HKUST, MIL, UiO, NJU, etc. See abbreviations at the end of this review. *For [M_2(*m*-dobdc)] and [M_2(olz)], the SBU of M-MOF-74 is representatively shown, since both compounds are isostructural. **L = 4,5-bis[4(4-pyridyl)phenyl]1-ethyl-1*H*-imidazole.

2.I Solvent exchange and removal by thermal activation

The most used strategy for forming OMS is by removing the coordinated solvent molecules from the metal atoms in MOFs by the solvent exchange (SE) method, followed by thermal activation (TA).[86,87,93,98–100,109–114,116]

Dinuclear paddle-wheel SBUs. The dinuclear paddle-wheel metal unit [$M_2(COO)_4(solvent)_2$] is of great interest, because these structures can be systematically tuned by carboxylate linkers of different lengths and geometries.[117–122] This unit is surrounded by four carboxylate groups in a 4-c square planar fashion (Fig. 4).

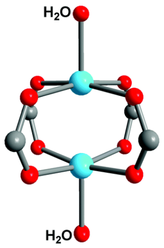

Fig. 4 Representation of the paddle-wheel unit of HKUST-1 [$Cu_3(btc)_2(H_2O)_2$], where the axial or apical sites of the Cu^{2+} ions are coordinated by water molecules. Crystal structure information from ref. 128 (CSD-Refcode DIHVIB01). The Cu···Cu distance is in the range of 2.5 Å.

The labile solvent molecules terminate the two axial positions of the metal handle. For Cu^{2+} the easy removal is due to the Jahn–Teller effect for the d^9 -ion which leads to weakly-bound apical ligands with long M–L bonds and a tendency towards formation of a square-planar geometry.[123–125]

The first MOF, that was examined for open Cu^{2+} sites, was HKUST-1, [$Cu_3(btc)_2(H_2O)_2$]. The framework is constructed of these dicopper paddle-wheel SBUs linked by trigonal 1,3,5-btc^{3-} (H_3btc = 1,3,5-benzentricarboxylate) linkers.[31] During the activation step the color changed from pale blue to dark blue due to the loss of the water molecules coordinated to the Cu centers as the coordination number of the Cu atoms decreased from five (square-pyramidal) to four (square planar).[126,127] Sometimes the dark-blue color of activated HKUST-1 is also referred to as deep-purple.[105]

Nair *et al*.[93] reported on the SE method to activate the Cu^{2+} sites in HKUST-1 for olefin/paraffin separation. They analyzed the removal of the solvent molecules and the availability of open metal sites in detail by *in situ* Fourier transform infrared spectroscopy (FT-IR), in situ mass spectrometry, and vapor-phase binary breakthrough experiments. The Cu-bound water exchange was based on removal and replacement by acetone through washing three times with fresh dry acetone over two days. Acetone was finally removed by drying at 70 °C for 1 h and evacuating at room temperature (RT) for 24 h in a vacuum oven to yield the solvent-exchanged and thermally activated sample (sample S2).[93]

For comparison, an only thermally activated sample (sample S1) was prepared by drying at 70 °C for 2 h and evacuating at RT for 24 h in a vacuum oven at 7×10^{-4} bar without previous SE. Nair *et al*. found that sample S2 had a 29% higher BE (Brunauer–Emmett–Teller) surface area of 1600 $m^2\ g^{-1}$ with a pore volume of 0.71 $cm^3\ g^{-1}$ than sample S1, which gave only 1240 $m^2\ g^{-1}$ with 0.55 $cm^3\ g^{-1}$ pore volume.[93] Fig. 5 shows the powder X-ray diffractions patterns (PXRD) of sample S1 and sample S2 at RT and the PXRDs at different temperatures of the thermally activated sample S1, where, the reflection at 6.51 disappeared, which was seen as a proof for the removal of the aqua ligands on Cu^{2+}.[93]

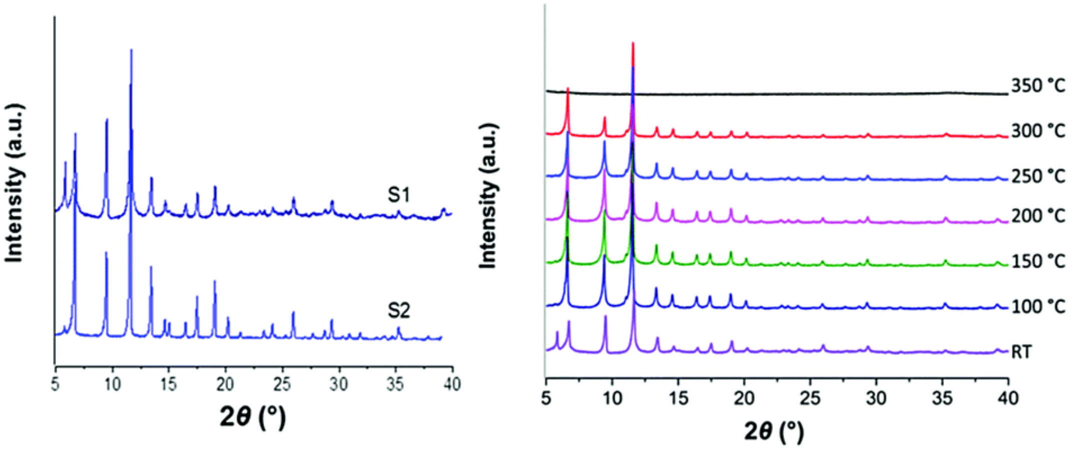

Fig. 5 Left: Powder X-ray diffraction patterns of thermally-only activated HKUST-1 (sample S1) and solvent-exchanged plus thermally-activated HKUST-1 (sample S2) at RT. Right: Powder X-ray diffraction patterns of a thermally-only activated HKUST-1 (sample S1) at different temperatures. Reproduced from ref. 93 with permission from the American Chemical Society, copyright 2016.

Furthermore, Nair *et al*. found that the total adsorption capacity and the equilibrium olefin selectivity in sample S2 was 44–55% and 10% higher, respectively, than in the thermally-only activated sample S1. The authors explained these results by using *in situ* FT-IR measurements to show that sample S2 has very few free carboxyl groups, hence, much less structure defects than sample S1. For the availability of OMS, they measured the amount of water desorbed from a known mass of completely dehydrated HKUST-1 and estimated the percentage of generated open metal sites (Fig. 6).

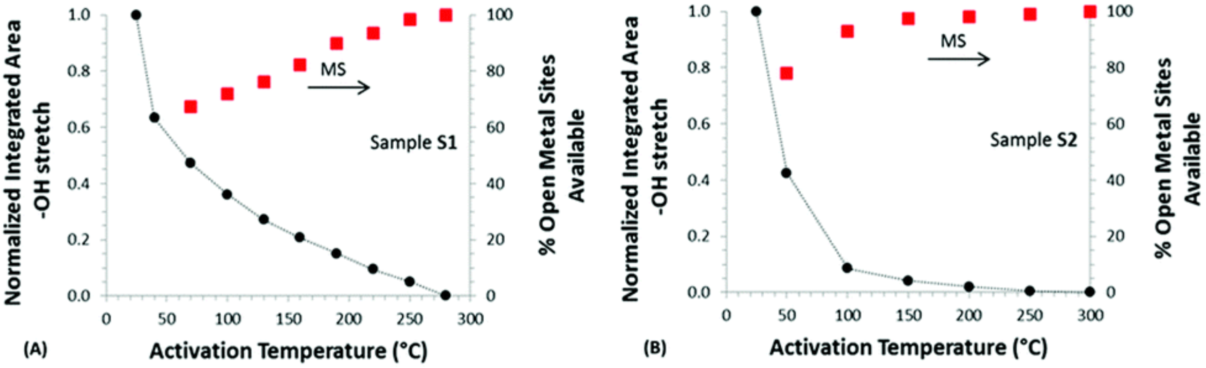

Fig. 6 Normalized mass of water lost from sample and percentage o OMS available for (A) sample S1 and (B) sample S2 at each activation step. Reproduced from ref. 93 with permission from the American Chemical Society, copyright 2016.

Nair *et al*. found that the availability of OMS increases with the activation temperature, *e.g.*, after activating at 70 °C for 12 h under a vacuum of 7 x 10^{-4} bar, the percentage of open metal sites in sample S1 was 69%. The fraction of 93% of OMS could be made available by TA up to 230 °C before the framework began to collapse. It was also concluded that the presence of defects in the material due to incomplete coordination of btc^{3-} linkers to the metal centers, led to stronger binding of the aqua ligands on the defective metal sites.[93] The percentage of OMS in samples S2 was already 78% after activating at 50 °C for 12 h, 9% higher than in sample S1 and increased further to 98% at 200 °C.[93]

Hong *et al.*[111] reported also on the activation of HKUST-1 at different temperatures. The as-synthesized HKUST-1 was dried at 378 K for 12 h under vacuum and activated in a nitrogen flow at different temperatures, 443, 473, 503, 523, and 553 K, to remove the coordinated water molecules. Hong and his co-workers followed this removal using thermogravimetric analysis (TGA) and differential scanning calorimetry (DSC). The first weight loss from room temperature to 378 K of 10.8 wt% was due to the loss of physisorbed H_2O and residual ethanol in the MOF channels. The second weight loss of 4.3 wt% from 378 and 473 K, and the third weight loss of 1.8 wt% from 473 and 558 K was eventually due to the dehydration of coordinated water in HKUST-1. The weight loss above 573 K represented the disintegration of the MOF structure. These experimental data were not in full agreement with the calculated mass change (4.1 wt% x 2) for two coordinated water molecules. Instead the two desorption steps for coordinated water molecules suggested the presence of two non-equivalent coordinated water molecules on the paddlewheel unit. The authors also reported that the crystallite size and morphology of the as-synthesized and the all-activated HKUST-1 MOFs did not show any changes in the

PXRD and of the morphology under the SEM (scanning electron microscope) until HKUST-1-553 K. From nitrogen adsorption measurements at 77 K the BET surface areas increased from 1382 (for HKUST-1- 443 K) over 1441 (for HKUST-1-503 K) to 1449 m^2 g^{-1} (for HKUST-1-523 K). We critically note that these differences are still within experimental error of about ±50 m^2 g^{-1} and values of 1441 and 1449 m^2 g^{-1} can be considered identical.[111] In 2016, Abbasi *et al.*[109] prepared microbelts of HKUST-1 as a heterogeneous catalyst for selective organic sulfide oxidation. After synthesis, the resulting solid was washed with water and methanol and dried under vacuum between 120 and 150 °C. Based on the TGA of these microbelts the removal of the coordinated water was assigned from the weight loss below 160 °C (Fig. 7).[129,130]

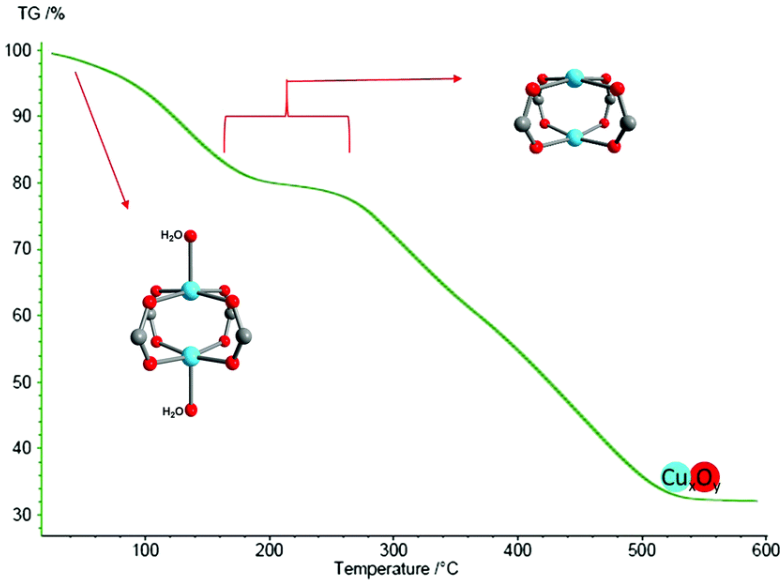

Fig. 7 Thermogravimetric analysis of HKUST-1 microbelts with the assigned weight losses for the aqua ligands giving the OMS-HKUST-1 network after 160 °C and before ~280 °C where the organic linkers start to degrade. Crystal structure information from ref. 128 (CSD-Refcode DIHVIB01). Reproduced from ref. 109 with permission of John Wiley & Sons, Ltd, copyright 2016.
2016.

Table 2 Open metal sites in metal–organic frameworks, which are reported in this review

				Formation of OMS			
OMS	Ligand	MOF-formula with solvent ligands (without pore solvent)	MOF-acronym	Removal strategies	Temp.[°C] (Time [h], vac)	Verification methods	Ref.
Mg	H_4dobdc	$[Mg_2(dobdc)(H_2O)_2]$	Mg-MOF-74	SE,^{f} TA, PA	200 (vac) 136 (30 min)	PXRD, TGA	70, 105 and 172
	H_4olz	$[Mg_2(olz)(solvent)_2]$	$[Mg_2(olz)]$	Se,^{c,f} TA	180 (12, vac)	PXRD, TGA	310
Sc	H_3btc	$[Sc_3(O)X_3(btc)_2(H_2O)_2]$	MIL-100(Sc)	SE^e	RT	PXRD	140 and 162
Zr	H_2bdc	$[Z_{r6}O_4(OH)_4(bdc)_6]$	UiO-66	TA PA	300 (vac); 300 (2, calcination) 57 (30 min)	PXRD, TGA	105, 114, 162 and 163
	H_2bdc-NH_2	$[Zr_6O_4(OH)_4(NH_2\text{-}bdc)_6]$	UiO-66-NH_2	SE,^{c,f} TA	150 (5, vac), 200 (16, vac)	–	164 and 284
V	H_2bdc	$[V_3(O)X(bdc)_3(H_2O)_2]$	MIL-101(V)	SE,^{c} TA	100 (12, vac), 150 (5, vac)	PXRD	143
	H_3btc	$[V_3(O)X_3(btc)_2(H_2O)_2]]$	MIL-100(V)	SE^{e,g}	100	PXRD	140 and 143
Cr	H_2bdc	$[Cr_3(O)X(bdc)_3(H_2O)_2]$	MIL-101(Cr)	TA	150 (24, vac); 150 (12, vac)	–	113 and 143–148
	H_3btc	$[Cr_3(btc)_2(H_2O)_2]$	$[Cr_3(btc)_2]$	SE,^{f} TA	160 (48, vac)	–	134
	H_3btc	$[Cr_3(O)X_3(btc)_2(H_2O)_2]$	MIL-100(Cr)	SE,^{e,g} TA	RT (16), 120-140 (12, vac); 200 (1, vac)	FTIR, NMR, PXRD, SEM	112, 138, 140 and 141
	H_3btt	$Cr_3[(Cr_4Cl)_3(btt)_{8(}DMF)_{12}]_2$	Cr-btt	SE,^{c,f} TA	150 (12, vac)	PXRD	159
Mn	H_2bbta	$[Mn_2Cl_2(bbta)(H_2O)_2]$	MAF-X25-Cl	SE,^{f,g} TA	100 (12, vac)	PXRD, TGA	183 and 184
	H_2btdd	$[Mn_2Cl_2(btdd)(H_2O)_2]$	$[Mn_2Cl_2(btdd)]$	SE,^{f} TA	100 (vac)	PXRD, TGA	83
	H_2pyip	$[Mn_2(pyip)_2DMF]$	NJU-Bai33	SE,^{a} TA	110 (10, vac)	PXRD, TGA, FTIR	137
	H_3btt	$Mn_3[(Mn_4Cl)_3(btt)_8(MeOH)_{12}]_2$	Mn-btt	SE,^{d} TA	150 (2, vac)	PXRD, TGA	160
	H_3tatb	$2H_3O^+$ $[Mn_4O(tatb)(H_2O)_4]_{8/3}$	PCN-9(Mn)	SE,^{b,f} TA	RT (12, vac), 60 (1, vac)	–	56 and 57
Fe	H_3btc	$[(Fe_3(O)F_{0.81}(OH)_{0.19})(btc)_2(H_2O)_2]$	MIL-100(Fe)	SE,^{e,g} TA	100 (12, vac) 150-250 (12, vac)	PXRD, FTIR	143
	H_3btt	$Fe_3[(Fe_4Cl)_3(btt)_8(MeOH)_{12}]_2$	Fe-btt	SE,^{f} TA	135 (24, vac)	TGA	157
	H_3tatb	$2H_3O^+$ $[Fe_4O(tatb)(H_2O)_4]_{8/3}$	PCN-9(Fe)	SE,^{b,f} TA	RT (12, vac), 60 (1, vac)	–	57
	H_4dobdc	$[Fe_2(dobdc)(DMF)_{2]}$	Fe-MOF-74	SE,^{f} TA	160 (48, vac)	PXRD, TGA	167
	H_4olz	$[Fe_2(olz)(solvent)_2]$	$[Fe_2(olz)]$	SE,^{c,f} TA	120 (vac)	PXRD, TGA	310

Table 2 *(continued)*

				Formation of OMS			
OMS	Ligand	MOF-formula with solvent ligands (without pore solvent)	MOF-acronym	Removal strategies	Temp.[°C] (Time [h], vac)	Verification methods	Ref.
Co	$\mathrm{H_2bbta}$	$\mathrm{[Co_2Cl_2(bbta)(H_2O)_2]}$	MAF-X27-Cl	SE,[f,g] TA	100 (12, vac)	PXRD, TGA	182 and 184
	$\mathrm{H_2bdc}$ L = 4,5-Bis[4(4-pyridyl)phenyl]1-ethyl-1*H*-imidazole)	$\mathrm{[Co_3L(CH_3OH)_{0.5}(H_2O)_{0.5}(bdc)_{2.5}(OAc)]}$	$\mathrm{[Co_3(L)(bdc)_{2.5}(OAc)]}$	TA	70 (2)	PXRD, TGA	99
	$\mathrm{H_2btdd}$	$\mathrm{[Co_2Cl_2(btdd)(H_2O)_2]}$	$\mathrm{[Co_2Cl_2(btdd)]}$	SE,[f] TA	100 (vac)	PXRD, TGA	83
	$\mathrm{H_3btt}$	$\mathrm{Co_3[(Co_4Cl)_3(btt)_8(MeOH)_{12}]_2}$	Co-btt	SE,[f] TA	135 (24, vac)	FTIR, PXRD, TGA	155
	$\mathrm{H_3tatb}$	$\mathrm{2H_3O^+\ [Co_4O(tatb)(H_2O)_4]_{8/3}}$	PCN-9(Co)	SE[b,f]	RT (12, vac), 60 (1, vac)	PXRD	57
	$\mathrm{H_3tzpa}$	$\mathrm{[Co_2(tzpa)(OH)(H_2O)_2]}$	$\mathrm{[Co_2(tzpa)(\mu_3{-}OH)]}$	SE,[f] TA	220 (vac)	PXRD, TGA, FTIR	181
	$\mathrm{H_4dobdc}$	$\mathrm{[Co_2(dobdc)(H_2O)_2]}$	Co-MOF-74	SE,[f] TA	200 (vac)	SCXRD, TGA	70 and 173
	$\mathrm{H_4olz}$	$\mathrm{[Co_2(olz)(solvent)_2]}$	$\mathrm{[Co_2(olz)]}$	SE,[c,f] TA	180 (12, vac)	PXRD, TGA	310
	$\mathrm{H_8tdcppy}$	$\mathrm{[Co_3(\mu_3\text{-}O)(tdcppy)_6(solvent)_3]}$	$\mathrm{[Co_3(\mu_3\text{-}O)(tdcppy)_6]}$	SE,[f] TA	65 (12, vac)	PXRD, TGA	67
Ni	$\mathrm{H_2bdc}$ Hna	$\mathrm{[(Ni_2(H_2O)_2)_{1.5}(Ni_3OH)_2(bdc)_6(na)_6]}$	–	SE,[b,c] TA	100 (vac)	PXRD, TGA	58
	$\mathrm{H_2btdd}$	$\mathrm{[Ni_2Cl_2(btdd)(H_2O)_2]}$	$\mathrm{[Ni_2Cl_2(btdd)]}$	SE,[f] TA	100 (vac)	PXRD, TGA	83
	$\mathrm{H_4dobdc}$	$\mathrm{[Ni_2(dobdc)(H_2O)_2]}$	Ni-MOF-74	SE,[f] TA TA CA PA	200 120 (1, vac) – 167 (30 min)	NMR, PXRD, TGA	70, 101–105,174 and 326
	$\mathrm{H_4olz}$	$\mathrm{[Ni_2(olz)(solvent)_2]}$	$\mathrm{[Ni_2(olz)]}$	SE,[c,f] TA	180 (12, vac)	PXRD, TGA	310
	$\mathrm{H_2sip}$	$\mathrm{[NaNi_3(OH)(sip)_2]}$	–	TA	300–350 (vac)	PXRD, TGA	59
Cu	$\mathrm{H_2bdc}$	$\mathrm{[Cu_2(bdc)_2(DMF)_2]}$	Cu-bdc/MOF-2	SE[f], TA CA	60 (12), 120 (vac) –	FTIR, SEM, NMR, PXRD	98 and 101 – 104
	$\mathrm{H_2dmcapz}$	$\mathrm{[Cu_2(dmcapz)_2(H_2O)]}$	$\mathrm{[Cu_2(dmcapz)_2]}$	SE[g], TA	150 (7, vac), –196 (vac)	PXRD, TGA	100
	$\mathrm{H_2sp5\text{-}BF_4}$	[Cu-sp5-MeOH]	[Cu-sp5]	TA	120 (15, vac)	PXRD, TGA	332
	$\mathrm{H_3btc}$	$\mathrm{[Cu_3(btc)_2(H_2O)_2]}$	HKUST-1/MOF-199	SE,[a,f,g] TA CA PA	RT (24, vac), 70 (1-2); 100 (12, vac), 170–280; 120–150 (vac) 150 (10, vac) – 125 (30 min)	DSC, FTIR, NMR, PXRD, TGA, SEM	93, 101–105, 190, 111, 313 and 334

Table 2 *(continued)*

OMS	Ligand	MOF-formula with solvent ligands (without pore solvent)	MOF-acronym	Formation of OMS Removal strategies	 Temp.[°C] (Time [h], vac)	Verification methods	Ref.
Co	H_2bbta	$[Co_2Cl_2(bbta)(H_2O)_2]$	MAF-X27-Cl	SE,^{f,g} TA	100 (12, vac)	PXRD, TGA	182 and 184
	H_2bdc L = 4,5-Bis[4(4-pyridyl)phenyl]1-ethyl-1*H*-imidazole)	$[Co_3L(CH_3OH)_{0.5}(H_2O)_{0.5}(bdc)_{2.5}(OAc)]$	$[Co_3(L)(bdc)_{2.5}(OAc)]$	TA	70 (2)	PXRD, TGA	99
	H_2btdd	$[Co_2Cl_2(btdd)(H_2O)_2]$	$[Co_2Cl_2(btdd)]$	SE,^{f} TA	100 (vac)	PXRD, TGA	83
	H_3btt	$Co_3[(Co_4Cl)_3(btt)_8(MeOH)_{12}]_2$	Co-btt	SE,^{f} TA	135 (24, vac)	FTIR, PXRD, TGA	155
	H_3tatb	$2H_3O^+ [Co_4O(tatb)(H_2O)_4]_{8/3}$	PCN-9(Co)	SE^{b,f}	RT (12, vac), 60 (1, vac)	PXRD	57
	H_3tzpa	$[Co_2(tzpa)(OH)(H_2O)_2]$	$[Co_2(tzpa)(\mu_3{-}OH)]$	SE,^{f} TA	220 (vac)	PXRD, TGA, FTIR	181
	H_4dobdc	$[Co_2(dobdc)(H_2O)_2]$	Co-MOF-74	SE,^{f} TA	200 (vac)	SCXRD, TGA	70 and 173
	H_4olz	$[Co_2(olz)(solvent)_2]$	$[Co_2(olz)]$	SE,^{c,f} TA	180 (12, vac)	PXRD, TGA	310
	$H_8tdcppy$	$[Co_3(\mu_3\text{-}O)(tdcppy)_6(solvent)_3]$	$[Co_3(\mu_3\text{-}O)(tdcppy)_6]$	SE,^{f} TA	65 (12, vac)	PXRD, TGA	67
Ni	H_2bdc Hna	$[(Ni_2(H_2O)_2)_{1.5}(Ni_3OH)_2(bdc)_6(na)_6]$	–	SE,^{b,c} TA	100 (vac)	PXRD, TGA	58
	H_2btdd	$[Ni_2Cl_2(btdd)(H_2O)_2]$	$[Ni_2Cl_2(btdd)]$	SE,^{f} TA	100 (vac)	PXRD, TGA	83
	H_4dobdc	$[Ni_2(dobdc)(H_2O)_2]$	Ni-MOF-74	SE,^{f} TA TA CA PA	200 120 (1, vac) – 167 (30 min)	NMR, PXRD, TGA	70, 101–105,174 and 326
	H_4olz	$[Ni_2(olz)(solvent)_2]$	$[Ni_2(olz)]$	SE,^{c,f} TA	180 (12, vac)	PXRD, TGA	310
	H_2sip	$[NaNi_3(OH)(sip)_2]$	–	TA	300–350 (vac)	PXRD, TGA	59
Cu	H_2bdc	$[Cu_2(bdc)_2(DMF)_2]$	Cu-bdc/MOF-2	SE^{f}, TA CA	60 (12), 120 (vac) –	FTIR, SEM, NMR, PXRD	98 and 101 – 104
	$H_2dmcapz$	$[Cu_2(dmcapz)_2(H_2O)]$	$[Cu_2(dmcapz)_2]$	SE^{g}, TA	150 (7, vac), –196 (vac)	PXRD, TGA	100
	$H_2sp5\text{-}BF_4$	[Cu-sp5-MeOH]	[Cu-sp5]	TA	120 (15, vac)	PXRD, TGA	332
	H_3btc	$[Cu_3(btc)_2(H_2O)_2]$	HKUST-1/MOF-199	SE,^{a,f,g} TA CA PA	RT (24, vac), 70 (1-2); 100 (12, vac), 170–280; 120–150 (vac) 150 (10, vac) – 125 (30 min)	DSC, FTIR, NMR, PXRD, TGA, SEM	93, 101–105, 190, 111, 313 and 334

Table 2 *(continued)*

				Formation of OMS			
OMS	Ligand	MOF-formula with solvent ligands (without pore solvent)	MOF-acronym	Removal strategies	Temp.[°C] (Time [h], vac)	Verification methods	Ref.
Cu	H_3btt	$HCu[(Cu_4Cl)_3(btt)_8(H_2O)_{12}]$	Cu-btt	SE,^{f} TA	120 (24, vac)	FTIR, PXRD, TGA	158
	H_3btt_{ri}	$H_3[(Cu_4Cl)_3(btt_{ri})_8(DMF)_{12}]$	Cu-btt_{ri}	SE,^{f} TA	180 (12, vac); RT (3, vac), 180 (3, vac)	PXRD, TGA	278, 287, 288 and 300
	H_3L = [1,1´:4´,1´´-terphenyl]-3,4´´,5-tricarboxylic acid	$[Cu_2(L)_2(HCOO)_2(H_2O)_2]$ $[Cu_6(L)_4(H_2O)_6]$	PCP-31; PCP-32	SE,^{a} TA	RT (6), 60 (6), 120 (24, vac)	PXRD	119
	H_3tzi	$[Cu_6O(tzi)_3(H_2O)_9(NO_3)]$	–	SE,^{e} TA	RT (vac), 85 (6, vac)	PXRD	60
	H_4adip	$[Cu_2(adip)(H_2O)_2]$	PCN-14	SE,^{b,f} TA	RT (12, vac), 120 (4, vac)	PXRD, TGA	121
	H_4aobtc	$[Cu_2(abtc)(H_2O)_2]$	PCN-10(Cu)	SE,^{b,f} TA	RT (12, vac), 120 (4, vac)	PXRD, TGA	63
	H_4bptc	$[Cu_2(bptc)(H_2O)_2]$	MOF-505/ NOTT-100	SE,^{a} TA	RT (15, vac); 70 (15, vac); 120 (12, vac)	PXRD, TGA	86 and 87
	H_4dobdc	$[Cu_2(dobdc)(DMF)_2]$	Cu-MOF-74	SE,^{d} TA CA	70 (vac), 150-225 (5, vac) –	NMR, PXRD	101–104 and 157
	H_4L = 4′,4‴-(pyridine-3,5-diyl)bis([1,1′-biphenyl]-3,5-dicarboxylic acid)	$[Cu_2(C_{33}H_{17}NO_8)(H_2O)_{0.65}]$	MFM-170	SE,^{a} TA	423 (24, vac)	PXRD, TGA	122
	H_4mbdpb	$[Cu_6(mbdpb)_3(H_2O)_6]$	NJFU-3	SE,^{c,f} TA	90(20, vac)	PXRD	118
	H_4mdip	$[Cu_6(C_s\text{-}mdip)_2(C_{2v}\text{-}mdip)(H_2O)_6]$	PCN-12(Cu)	SE,^{b,f} TA	RT (12, vac), 150 (4, vac)	PXRD, TGA	117
	H_4sbtc	$[Cu_2(sbtc)(H_2O)_2]$	PCN-11(Cu)	SE,^{b,f} TA	RT (12, vac), 120 (4, vac)	PXRD, TGA	63
	H_5n	$[Cu_2(n)(H_2O)_2]$	NEM-4	SE,^{f} TA	90 (12, vac)	NMR, PXRD	110
	H_6bhb	$[Cu_3(bhb)(H_2O)_3]$	UTSA-20	SE,^{a} TA	120 (24, vac)	PXRD	177 and 360
	H_6tdpat	$[Cu_3(tdpat)(H_2O)_3]$	Cu-tdpat	SE,^{f} TA	120 (24, vac); 120 (10, vac)	PXRD, TGA	333 and 334
	$H_6L = C_{54}H_{30}O_{12}$	$[Cu_3(C_{54}H_{24}O_{12})(H_2O)_3]$	NOTT-116/PCN-68	SE,^{a} TA	RT (vac), 100 (12, vac)	PXRD, TGA	62 and 87

Table 2 *(continued)*

OMS	Ligand	MOF-formula with solvent ligands (without pore solvent)	MOF-acronym	Formation of OMS Removal strategies	 Temp.[°C] (Time [h], vac)	Verification methods	Ref.
Cu	H_6L = H_6btat	$[Cu_3(L)(H_2O)_3)]$	NOTT-112/ MFM-112a	SE,[a] TA	115 (16, vac)	PXRD, TGA	61, 62 and 120
	H_4L = tetracarboxylic acid ligands with different functionalities at the aromatic core	$[Cu_2(L)(H_2O)_2]$	NOTT-101/ ZJU-24; NOTT-102/ MFM-102; -103; -105; -106; -107	SE,[a] TA	140 (20, vac)	PXRD, TGA	87 and 312
Zn	H_3btc	$[Zn_2(btc)(NO_3)(EtOH)_3]$	MOF-4	TA	RT (48, vac), 72 (16, vac)	–	32 and 33
	H_4dobdc	$[Zn_2(dobdc)(DMF)_2]$	Zn-MOF-74	PA	145 (30 min)	PXRD	105, 173 and 340
	H_4olz	$[Zn_2(olz)(solvent)_2]$	$[Zn_2(olz)]$	SE,[c,f] TA	100 (12, vac	PXRD, TGA	310
Cd	H_3btt	$Cd_3[(Cd_4Cl)_3(btt)_8(MeOH)_{12}]_2$	Cd-btt	SE,[f] TA	135 (24, vac	FTIR, PXRD, TGA	155
	H_4dobdc	$[Cd_2(dobdc)(H_2O)_2]$	Cd-MOF-74	SE,[f] TA	100 (18, vac)	FTIR, PXRD, TGA	176
Eu	H_3btc	$[Eu(btc)(H_2O)]$	[Eu-btc]	TA	140 (24, vac)	TGA	180

[a] Solvent exchange (SE) with acetone. [b] SE with DCM. [c] SE with DMF. [d] SE: solvent not given. [e] SE with ethanol. [f] SE with methanol. [g] SE with water. For a deciphering of the used acronyms such as HKUST, MIL, UiO, NJU, etc. see abbreviations at the end of this review.

In activated HKUST-1 the presence and co-existence of Cu^{1+} and Cu^{2+} was observed through the spectroscopic investigation of CO_2, CO or NO adsorbates (see in the application Section 4). Apparently, the oxidation state of copper can be reduced from Cu^{2+} and Cu^{1+} at higher temperature (approx. 473 K), for example by redox treatments, using vacuum and/or reducing gases at different sample temperatures.[127,131–133]

Other Cu MOFs that have been investigated for open metal sites are MOF-505 and MOF-2 ($[Cu_2(bdc)_2(DMF)_2]$).[86,98,134] Yaghi *et al.*[86] reported on the Cu-MOF MOF-505, which is isoreticular to HKUST-1 with the 3,3′,5,5′-biphenyltetracarboxylic acid (H_4bptc) ligand. Accordingly, the as-synthesized MOF-505 was activated by soaking in fresh acetone three times for 24 h each (72 h total) to remove the DMF molecules from the pores. After that, the acetone-containing material was carefully evacuated at <1 x 10^{-6} bar in three steps to remove the coordinated water molecules. In the first step, the solid kept at room temperature loses 42 wt% over 15 h and changes its color from blue-green to light blue. In the second step, at 70 °C for 15 h, the weight decrease continues (5.3 wt%), and the color changes to dark blue. In the third step, the solid, kept at 120 °C for 12 h, loses 4.7 wt% and changes its color to purple. Subsequently, the nitrogen uptake of MOF-505 increased over the three different activation steps. The nitrogen uptake in step I increased from 278 mg g^{-1} to 386 mg g^{-1} in step II, with a final increase to 526 mg g^{-1} in step III. The authors analyzed the stability of the framework under SE conditions using powder X-ray diffraction patterns and thermogravimetric analysis. They reported that the X-ray diffraction patterns of the simulated, as-synthesized, and acetone-exchanged scenarios showed nearly the same pattern and the PXRD of the desolvated material showed a decrease in the intensities and broader reflections with an additional broader reflection at around 7° 2-theta. The thermogravimetric analysis showed a weight loss of 30.8% below 250 °C, which agrees with the calculated value of 30.5% from the liberation of 2.5 acetone and three water molecules per Cu_2bptc formula unit. Furthermore, they explained that the removal of non-coordinated DMF/water molecules and coordinated water molecules have two positive effects, due to a decrease of sample mass and an increase of available micropore volume and specific surface area, on the H_2 adsorption capacity. The OMS enhance the hydrogen-framework (SBU) interaction. The authors also reported that MOF-505 has a high hydrogen uptake capacity due to the availability of open metal sites. The hydrogen uptake, which is 14.1 mg g^{-1} (1.41 wt%) after the first activation step, increased to 19.7 mg g^{-1} (1.97 wt%) in the second step, and finally to 24.7 mg g^{-1} (2.47 wt%) after complete dehydration in the third step.[86]

Liu *et al.*[98] reported on the Cu-bdc MOF MOF-2 as a heterogeneous interfacial catalyst for a sustainable Suzuki coupling reaction. For this, the open Cu sites were grafted with pyridyl-salicylimine (Py-SI) to get Cu-bdc/Py-SI, and then palladium(II) chloride was added to produce Pd@Cu-bdc/Py-SI MOF. To remove the coordinated DMF solvent molecules, the SE and TA method was used. The as-synthesized Cu-bdc was washed one time with DMF, then with hot methanol (70 °C) for 4 h, filtered, dried at 60 °C overnight, and activated at 120 °C under vacuum. The DMF-characteristic IR band at 1663 cm^{-1} had disappeared after activation.[98] Guo *et al.*[110] investigated the Cu-MOF NEM-4 with open Cu^{2+} sites in hydrocarbon storage and separation. Before measuring the gas sorption, NEM-4 was activated by the SE method using methanol and under dynamic vacuum at 90 °C for 12 h. Hereby, the color of NEM-4 changed from pale blue to dark blue, similar to the situation of other Cu-MOFs in which open sites can be generated.[110]

The d^4-Cr^{2+} ion (high-spin) also shows the Jahn–Teller effect and typically exhibits a tetragonally distorted-octahedral or square-planar coordination environment. For example, $[Cr_3(btc)_2]$ was activated by SE with methanol and dried under vacuum at 160 °C for 48 h. The fully activated framework exhibits a short Cr–Cr distance of 2.06(2) Å within the paddle-wheel SBU, which is typically interpreted as a quadruple bond.[134] Consequently the Cr^{2+} ion has a decreased Lewis acidity.[135]

Dinuclear distorted SBUs. For Mn^{2+} the octahedral coordination is typical. Since the high-spin d^5-Mn^{2+} ion has no crystal field stabilization energy, different geometries are possible depending on the coordinated ligands.[136] Employing 5-(pyridin-3-yl)isophthalic acid (H_2pyip) as a bifunctional trigonal linker in a solvothermal reaction with $MnCl_2·4H_2O$ leads to the construction of $[Mn_2(pyip)_2DMF]·DMF·MeOH$ (NJU-Bai33; Nanjing University) including dinuclear distorted $[Mn_2(COO)_4N_2]$ SBUs.[137] As shown in Fig. 8, two crystallographically independent Mn^{2+} ions (Mn1 and Mn2) are present in the $[Mn_2(COO)_4N_2]$ SBU. The Mn1 coordination consists of five carboxylate moieties and one N atom from different linkers. The coordination environment of Mn2 is completed by an oxygen atom from DMF. Based on the thermogravimetric analysis the removal of the coordinated DMF molecules was achieved after SE with acetone followed by TA at 110 °C for 10 h under vacuum.[137]

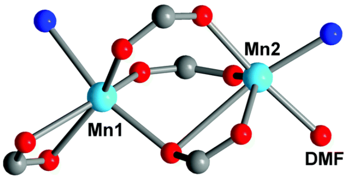

Fig. 8 Ball and stick presentation of the distorted $[Mn_2(COO)_4N_2(DMF)]$ cluster. Crystal structure information from ref. 137 (CSD-Refcode GASTIG).

In 2012, Kitagawa *et al.*100 reported on the Cu-MOF $[Cu_2(dmcapz)_2(H_2O)]·DMF_{1.5}$, obtained from CuX_2 (X = Cl, NO_3) salts with 3,5-dimethyl-4-carboxypyrazole (H_2dmcapz). This compound consists of a dinuclear SBU were the Cu^{2+} ions are surrounded by two N-donor atoms from two pyrazolate groups and by two carboxylate groups in a bidentate coordination mode each from different linkers. Further, the Cu^{2+} ions are bridged by a μ_2-OH_2 water ligand achieving a distorted square-pyramidal geometry (Fig. 9). The presence of bridging water molecules in a MOF SBU is unusual.[100]

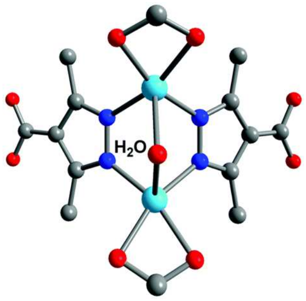

Fig. 9 SBU of $[Cu_2(dmcapz)_2(H_2O)]$. Crystal structure information from ref. 100 (CSD-Refcode ZECKID).

To obtain open metal sites they used a reversed combination of TA and SE method and described a stepwise removal. In the first step, the as-synthesized material $[Cu_2(dmcapz)_2(H_2O)]\cdot DMF_{1.5}$ was evacuated at 120 °C for 7 h under high vacuum. The dark-blue TGA curve of $[Cu_2(dmcapz)_2(H_2O)]\cdot DMF_{1.5}$ in Fig. 10, left shows a weight loss of 30% at around 100 °C, which stands for the removal of the DMF guest molecules and the aqua bridge, and a weight loss between 270 and 300 °C, due to framework decomposition.

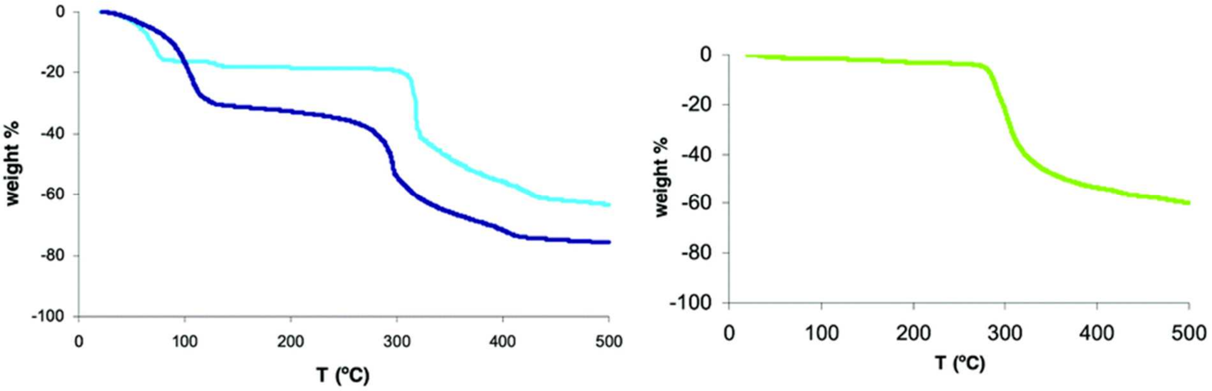

Fig. 10 Left: Thermogravimetric analyses of $[Cu_2(dmcapz)_2(H_2O)]\cdot DMF_{1.5}$, (dark-blue), $[Cu_2(dmcapz)_2(H_2O)]\cdot H_2O_{4.5}$ (pale blue) and right: of $[Cu_2(dmcapz)_2]$ (green). Reproduced from ref. 100 with permission of Wiley-VCH Verlag GmbH & Co. KGaA, Weinheim, copyright 2012.

Then the sky blue $[Cu_2(dmcapz)_2(H_2O)]\cdot DMF_{0.9}$ was soaked in water for 24 h to remove remaining DMF solvent molecules together with impurities of unreacted ligand or $CuCl_2$. In the next step, the water-exchanged pale blue $[Cu_2(dmcapz)_2(H_2O)]\cdot H_2O_{4.5}$ was evacuated at 150 °C for 7 h under high vacuum. The pale blue TGA curve of $[Cu_2(dmcapz)_2(H_2O)]\cdot H_2O_{4.5}$ in Fig. 10 shows a weight loss of 15% at around 80 °C, which means a loss of water guest molecules (calculated 16.1%), a small weight loss at around 120 °C, due to the loss of one water molecule per $[Cu_2(dmcapz)_2]$ unit (experimental 3.8, calculated 4.3%) and a weight loss above 300 °C because of framework decomposition. The water removal is accompanied by a color change from pale blue to dark blue for which is akin to the color change in HKUST-1.[31] Therefore, the color change was also evidence to the loss of the water molecules coordinated to the Cu centers. The coordination number of the Cu atoms should have decreased from five (distorted square-pyramidal geometry) to four (distorted square planar), albeit it can be noted that no structural proof on the material [Cu_2(dmcapz)$_2$] was provided. The obtained dark-blue activated network [Cu_2(dmcapz)$_2$], returned its color to pale-blue within a few minutes under ambient moisture. Activated [Cu_2(dmcapz)$_2$] adsorbed ambient moisture and returned into [Cu_2(dmcapz)$_2$(H_2O)]·$H_2O_{4.5}$. If after the final activation step, [Cu_2(dmcapz)$_2$] was cooled to liquid-nitrogen temperature (77 K, under He atmosphere) a forest green (proven porous) material [Cu_2(dmcapz)$_2$], was obtained which was highly air- and moisture-stable at RT. The color change from dark blue to forest green at 77 K was interpreted to reflect a further change in the coordination of the metal centers. The authors assume a small twist of the dmcapz ligands concomitant with this change, so that a distortion from the initial square-planar geometry occurs to a distorted-tetrahedral coordination in [Cu_2(dmcapz)$_2$]. The higher hydrophobicity of the forest-green material compared with the dark-blue one seen as due to the structural reorganization which took place during the freezing process. To return forest-green [Cu_2(dmcapz)$_2$] into [Cu_2(dmcapz)$_2$(H_2O)]·$H_2O_{4.5}$, the former had to be soaked in deionized H_2O. The thermal stability of forest-green [Cu_2(dmcapz)$_2$] was followed by TGA (Fig. 10) with the green TGA curve indicating a fully activated material.[100]

Differences in the PXRDs at various temperature reflected the structural changes at the activation step from [Cu_2(dmcapz)$_2$(H_2O)]·$DMF_{1.5}$ to [Cu_2(dmcapz)$_2$]. From PXRD it was deduced that the μ_2-OH_2 bridge molecule is removed between 90 and 110 °C.[100]

Trinuclear SBUs. The solvothermal reaction of $Co(OAc)_2$ and 1,4-H_2bdc with the addition of imidazole as co-ligan (L = 4,5-bis[4(4-pyridyl)phenyl]1-ethyl-1*H*-imidazole), yielded a red-purple 3D-framework [$Co_3L(CH_3OH)_{0.5}(H_2O)_{0.5}(bdc)_{2.5}$(OAc)] solvent, which consists of Co_3-hourglass-like SBUs (Fig. 11).[99]

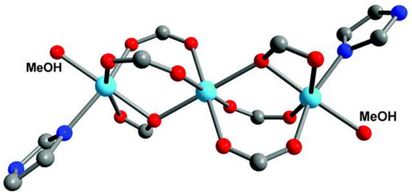

Fig. 11 Representation of the trinuclear Co^{2+} SBU in [Co_3(L)(bdc)$_{2.5}$]. Crystal structure information from ref. 99 (CSD-Refcode YUZRES).

The desolvated form [Co_3(L)(bdc)$_{2.5}$] with open Co^{2+} sites, was generated by heating at 70 °C for 2 h. During the activation, one of the six-coordinated {CoO_5N} chromophores changed to a coordinatively unsaturated five-coordinated one {CoO_4N}. For the other three types of Co^{2+} centers, no coordination-mode change was observed. After removing the coordinated methanol molecules, the solvent accessible void volume in [$Co_3L(bdc)_{2.5}(OAc)$] solvent increased to 1307 $Å^3$, that is to 41% of the total unit cell volume of 3181 $Å^3$. To regenerate [$Co_3L(CH_3OH)(bdc)_{2.5}(OAc)$] solvent without losing the single crystallinity, the activated form was soaked in methanol at room temperature for one day. Simulated and measured X-ray diffraction patterns were positively matched to further support the reversible methanol substitution-triggered single-crystal to single-crystal transformation. The thermogravimetric analysis of [$Co_3L(CH_3OH)_{0.5}(H_2O)_{0.5}(bdc)_{2.5}(OAc)$] solvent showed a weight loss of 4.8% at 150 °C, which indicates the removal of the MeOH/H_2O molecules. Based on TGA the desolvated OMS-containing Co^{2+}-MOF was stable up to 350 °C.[9]

It has to be noted that the coordination chemistry of Co^{2+} is a special case with its easy and reversible octahedral to tetrahedral transition. When two labile solvent ligands are present, then upon their removal the octahedral Co^{2+} environment change to a tetrahedral Co^{2+} geometry, which can be identified through the concomitant color change from pink (octahedral) to blue (tetrahedral).[116] However, this well-known transition does not form OMS. Therefore, examples of such Co-MOFs were not included here as OMS-MOFs. It is also known that Co^{2+} forms low-spin compounds with strong-field ligands, which are often planar.

Open Cr^{3+}, Fe^{3+}, Sc^{3+}, $V^{3+/4+}$ and site MOFs with trinuclear $M_3O(CO_2)_6$ SBUs have been investigated in the 3D terephthalate (bdc) based structures MIL-101(Cr) and MIL-101(V) and in the trimesate (btc) based network MIL-100(Cr) (MIL = Materiaux de l'Institute Lavoisier). These MIL frameworks have the empirical formulae [$M_3(O)X(bdc_3/btc_2)(H_2O)_2$] (M= Cr^{3+}, Fe^{3+}, Sc^{3+}, $V^{3+/4+}$; X = OH^- or F^-).[112,113,138–142] Both MIL-100 and MIL-101 consist of three μ_3-oxido vertex-sharing M^{3+} octahedra, which are interconnected by bdc^{2-} or btc^{3-} ligands.[12] The trinuclear SBU [$M_3(\mu_3\text{-}O)(F/OH)(O_2C^-)6(H2O)2$] in MIL-101 and MIL-100 compounds has two terminal aqua ligands at two of the three octahedral M^{3+} ions (Fig. 12).

Fig. 12 Representation of the trinuclear SBU in MIL-101 and MIL-100 structures (pale blue metal atom = Cr^{3+}, Fe^{3+} or V^{3+}). Crystal structure information from ref. 149 (CSD-Refcode CIGXIA).

The octahedral environment of the third metal atom is achieved through the coordination of an anionic ligand (OH^- or F^-), depending on the synthesis.[113,143–149]

In 2018, Mohsenzad *et al.*[112] reported on $MoO(O_2)_2$@En/MIL-100(Cr) as a new bifunctional Mo/Cr-MOF catalyst for selective thioether oxidation. To generate open metal sites, MIL-100(Cr) was activated in hot DMF at 110 °C, or in ethanol at 60 °C, or in water at 90 °C for 4 h, then it was dried at room temperature (for 16 h) and under vacuum between 120 and 140 °C for 12 h.[138] By comparison, MIL-100(Fe) was activated in hot water at 80 °C for 5 hours and then in hot ethanol at 60 °C for 3 h. After drying at 100 °C (overnight) and under vacuum the two aqua ligands were removed to form open Fe^{3+} sites (see dehydration, Fig. 13).

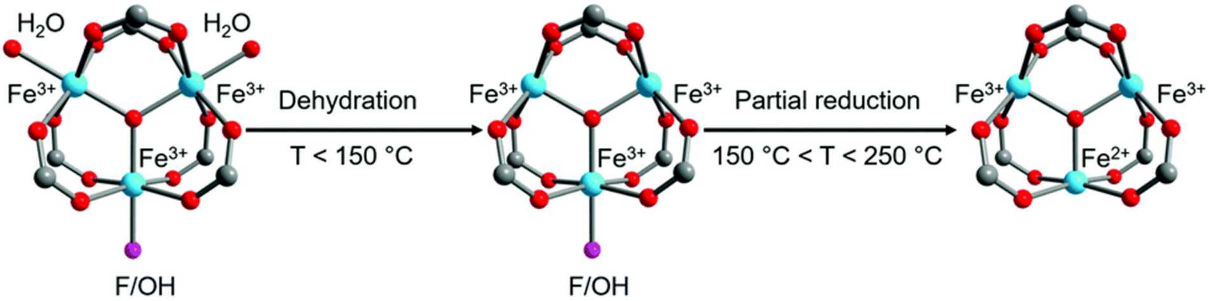

Fig. 13 Formation of open Fe^{3+} sites and Fe^{2+} site in an octahedral iron trimer of MIL-100(Fe) by dehydration and partial reduction through the removal of the anionic ligand (● $=OH^-$ or F^-). Crystal structure information from ref. 149 (CSD-Refcode CIGXIA). Adapted from ref. 142 with permission of Wiley-VCH Verlag GmbH & Co. KGaA, Weinheim, copyright 2010.

When the sample was dried above 150 °C (12 h) and under vacuum increasing amounts of Fe^{2+} were observed by Mößbauer spectroscopy which reach 14 mol(Fe)% at 260 °C degassing for 90 h. The formation of Fe(II) is due to the removal of the anionic ligands OH^- or F^- (see partial reduction, Fig. 13).[142]

Several groups reported on MIL-101(Cr) for its catalysts, gas sorption, postsynthetic modification *etc*. In order to obtain OMS in activated MIL-101(Cr) the material is typically heated at 150 °C under vacuum for one day (24 h).[113,143–154]

Tetranuclear SBUs. A series of isostructural tetrazolate MOFs with the chemical formula $M_3[(M_4Cl)_3(btt)_8(solvent)_{12}]_2$, named M-btt ($Cr^{2+}$, Mn^{2+}, Fe^{2+}, Cu^{2+}; btt^{3-} = 1,3,5-benzenetristetrazolate) have been discussed in accordance to the presence of a high density of OMS.[155–158] A representative structure of the SBU in M-btt is given in Fig. 14. In general, these SBUs consist of chloride-centered square-planar $[M_4Cl]^{7+}$ units, which are connected by eight triangular btt^{3-} bridging ligands.

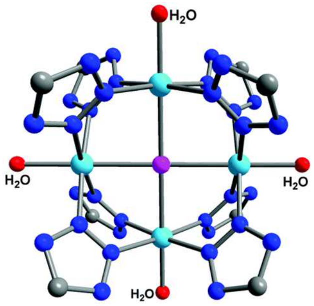

Fig. 14 Representation of the tetranuclear SBU in Fe-btt, where the axial Fe^{2+} sites are coordinated by water molecules. Crystal structure information from ref. 157 (CSD-Refcode GAGQAI).

The sixth coordination site on each M^{2+} ion is terminated by aqua ligands. These terminal aqua ligands can be removed through SE followed by TA to achieve OMS, verified with PXRD and TGA.[157–160] For example, Fe-btt, $Fe_3[(Fe_4Cl)_3(btt)_8(MeOH)_{12}]_2$, was washed with methanol and activated by heating at 135 °C for 24 h under a dynamic vacuum. Cr-btt, $Cr_3[(Cr_4Cl)_3(btt)_8(DMF)_{12}]_2$, was activated by soaking in fresh DMF, then washed with methanol and finally heating at 150 °C overnight under a dynamic vacuum. Cu-btt, $HCu[(Cu_4Cl)_3(btt)_8(H_2O)_{12}]$, was activated by a complete exchange of DMF for methanol and heating at 120 °C for approx. 24 h under reduced pressure. Mn-btt, $Mn_3[(Mn_4Cl)_3(btt)_8(MeOH)_{12}]_2$, was washed with DMF and methanol several times and activated at 150 °C for 2 h under dynamic vacuum.[157–160]

However, Queen *et al.*[156] showed that upon CO_2 loading a rapid drop in the isosteric heat of adsorption in Fe- and Mn-btt occurs, because some of the primary metal adsorption sites are still blocked by solvent molecules. Based on Rietveld refinement of the neutron diffraction data, the authors explained that the activated OMS M-btt frameworks showed that 23% (Cr), 65% (Fe) and 17% (Cu) of the metal sites (as potential OMS) were still occupied by coordinated solvent. For identically activated M-btt, the order for the amount of available OMS is Cu ≈ Cr > Fe > Mn. In this study the M-btt MOFs had been activated by the sequence soaking in DMF at 393 K for 24 h, decanting, soaking three times in (fresh) methanol at 343 K for 24 h, filtration, and heating under dynamic vacuum (< 10 mbar) at 433 K for 24 h.[156]

Also, earlier *in situ* studies of D_2 adsorption yielded a significant number of metal sites in these MOFs that are still blocked by solvent molecules which had not been removed by normal activation procedures.[157,160] We note that these works clearly demonstrate that quantitative OMS generation cannot be taken for granted by ‟standard" activation protocols. It must be noted that more studies are needed to quantify the formed OMS.[157,160]

Hexanuclear SBUs. The class of UiO (University in Oslo) 3D frameworks consist of hexanuclear $[Zr_6(\mu_3\text{-}O_4)(\mu_3\text{-}OH)_4]$ clusters with eight-coordinated square-antiprismatic zirconium ions (Fig. 15, left).

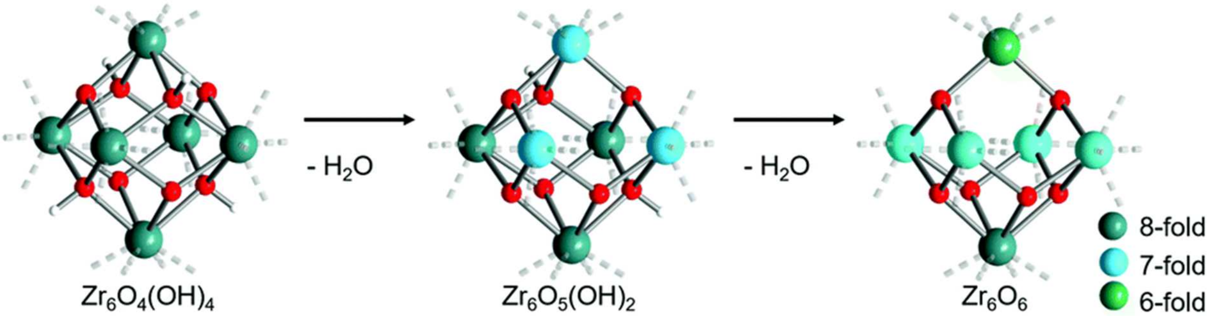

Fig. 15 Zr_6-SBU in UiO-MOFs without the carboxylate groups (for clarity) and a schematic two-step water-removal from the bridging OH^- and O^{2-} groups through TA under vacuum. The formed water consists of OH^- and H^+ from another OH^- group (transformed to O^{2-}). The different colors represent the coordination of the Zr atoms, with dark cyan = 8-fold, cyan = 7-fold and green = 6-fold coordination. Adapted from ref. 162 with permission from The Royal Society of Chemistry, copyright 2018. Crystal structure information from ref. 165 (CSD-Refcode RUBTAK02). For illustration purpose, the hydrogen atoms have been added manually with the ‘‘Add hydrogen atoms’’ function implemented in Mercury.[166]

The prototypical UiO-66 has the formula unit $[Zr_6O_4(OH)_4(btc)_6]$.[161] The synthesis of open Zr^{4+} sites can be described with a gradual removal of two water molecules upon TA (Fig. 15). The loss of the first water molecule leads to a reduction in coordination number from eight to seven of three Zr^{4+} ions within the cluster. The lost water molecules originate from and are composed of a μ_3-OH group together with the H-atom of another μ_3-OH group. The removal of the second water molecule lowers the coordination number of two more Zr^{4+} ions to seven and one Zr^{4+} from seven to six.[105,114,162–164] Lamberti *et al.*[165] reported on a study of the hydroxylated and dehydroxylated forms of UiO-66. They used the TA method to remove the solvent molecules from the ordered $[Zr_6O_4(OH)_4]$ cluster and to generate a distorted Zr_6O_6 cluster. Based on the thermogravimetric analysis the loss of two water molecules per $[Zr_6O_4(OH)_4]$ cluster were obtained after heating above 250 °C (300 °C). IR data confirmed the full removal of OH groups and EXAFS (extended X-ray absorption fine structure) confirmed the loss of about one oxygen atom in the first coordination sphere of the Zr atoms.[165]

Gao *et al.*[114] reported also on the dehydration of UiO-66. They explained that the dehydrated UiO-66 with open Lewis-acid sites is a heterogeneous and size-selective catalyst for cyanosilylation reaction of aldehydes with trimethylsilylcyanide. To obtain the dehydrated UiO-66 with OMS Zr^{4+}, hydrous UiO-66 was calcinated at 300 °C for only two hours.[114]

In 2018, Speybroeck *et al.*[162] reported on the intrinsic dynamic nature of UiO-66. The structural deformation of UiO-66 can be explained through defect formation or removal of coordinated molecules. In their work UiO-66 was dehydrated between 523 and 573 K.[162]

Infinite rod-shaped SBUs. The ligand *para*-2,5-dioxido-1,4- benzenedicarboxylate ($dobdc^{4-}$) with the metals Mg^{2+}, Mn^{2+}, Fe^{2+}, Co^{2+}, Ni^{2+}, Cu^{2+}, Zn^{2+} and Cd^{2+} leads to the formation of the isostructural series M-MOF-74, $[M_2(p\text{-dobdc})(\text{solvent})_2]$ (also known as CPO-27-M, solvent = H_2O or DMF) which have infinite rod-shaped SBUs.[167–176] Also the ligand

4,6-dioxido-1,3-benzene-dicarboxylate (*m*-dobdc^{4-}) leads to the same topology in [M_2(*m*-dobdc)(solvent)$_2$] as a structural isomer to the M-MOF-74 series.[88] In M-MOF-74, edge connected {MO_6} octahedra infinite linked rod shape SBUs with one coordinated water molecule per metal center (Fig. 16).

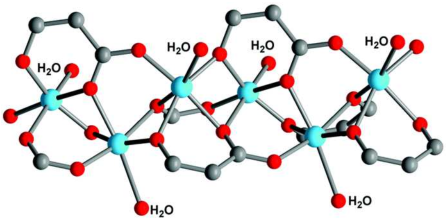

Fig. 16 Representation of the SBU in M-MOF-74 (left; M = Mg^{2+}, Mn^{2+}, Fe^{2+}, Co^{2+}, Ni^{2+}, Cu^{2+} and Zn^{2+}), with the labelled aqua ligands. Crystal structure information from ref. 179 (CSD-Refcode ORIVUI).

The coordinated water or DMF molecule completes the octahedral coordination environment of each metal center. The bridging linkers then combine these parallel SBUs to give hexagonal, one-dimensional channels.

The OMS of Mg^{2+}, Mn^{2+}, Fe^{2+}, Co^{2+}, Ni^{2+}, Cu^{2+} and Zn^{2+} sites in the M-MOF-74 series can be generated by using SE followed by TA. Through desolvation of the coordinated solvent molecule the metal center converts to a distorted square pyramidal coordination environment with the OMS pointing into the channel.[70,88,101–105] The originally six-coordinated metal ions d^7-Co^{2+} (high spin) and d^9-Cu^{2+} feature the Jahn–Teller distortion. It should be noted that the pseudo-octahedral coordination environment of Co^{2+} and Cu^{2+} show an elongation along the axial bonds and this allows for an easier removal of the axially coordinated solvent molecule. At the same time the Jahn–Teller effect, impedes the approach and strong binding of molecules on the open metal site.[70,177]

Moreover, Moon *et al.*[178] reported on [M_2(dobdc)(EG)$_2$] with coordinated ethylene glycol molecules (EG). To generate open Mg^{2+}, Co^{2+} and Ni^{2+} sites, the single crystals were soaked in anhydrous methanol and heated up to 200 °C. Based on single-crystal X-ray analysis (SCXRD) the coordinated and free EG molecules were replaced with methanol and based on the thermogravimetric analysis the coordinated methanol molecule was completely removed up to 250 °C.

Lobkovsky *et al.*[180] reported an Eu^{3+} MOF also with an infinite rod-shaped SBU, in which the OMS can be generated for the sensing of small molecules. [Eu(btc)(H_2O)] is isostructural with MOF-76 and was achieved in a solvothermal reaction $Eu(NO_3)_3 \cdot 6H_2O$ and H_3btc in a solvent mixture of DMF, ethanol, and water.[35] As shown in Fig. 17 the rod-shaped SBU consists of Eu^{3+} ions coordinated by six carboxylate oxygen atoms from the btc^{3-} linker and an oxygen atom from one water molecule in a seventh site.

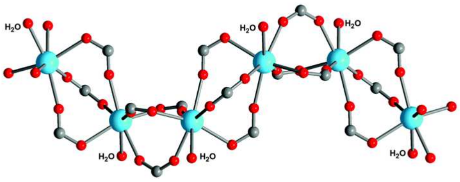

Fig. 17 Representation of the SBU in [Eu(btc)(H_2O)]. Crystal structure information from ref. 180 (CSD-Refcode OFEREX).

The as-synthesized [Eu(btc)(H_2O)]·1.5H_2O was activated at 140 °C under vacuum for one day and the removal of the free and Eu-bound water molecules was assessed by TGA where the water molecules were removed in the temperature range of 25 to 150 °C.[179]

The solvothermal reaction of Co(NO_3)$_2$·6H_2O with a T-shaped tetrazolyl-carboxyl ligand H_3tzpa (5-(4-(tetrazol-5-yl)phenyl)isophthalic acid) leads to the formation of the MOF [Co_2(tzpa)(OH)(H_2O)$_2$]·DMF based on infinite ribbon-like SBUs.[181] Which can be thought of being constructed from edge-sharing $Co_3(N_4C)_3(\mu_3\text{-OH})$-metallacycles. As shown in Fig. 18, two of the three Co atoms have two aqua ligands each. The removal of these coordinated water molecules was achieved through SE with methanol followed by TA at 220 °C under vacuum, to yield the solvent-free framework [Co_2(tzpa)(μ_3-OH)].[181]

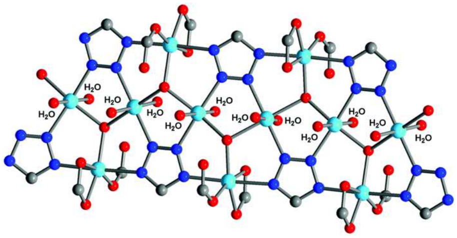

Fig. 18 Infinite ribbon-like SBU in [Co_2(tzpa)(OH)(H_2O)$_2$]. Crystal structure information from ref. 181 (CSD-Refcode SINTAN).

The group of Dincă *et al.*[83] demonstrated that the replacement of carboxylate moieties with triazolate ligands leads to the formation of networks with similar topology to the architecture of M-MOF-74. The solvothermal reaction of a bisbenzotriazole ligand, bis(1*H*-1,2,3-triazolo[4,5-*b*],[4′,5′-*i*])dibenzo[1,4]dioxin (H_2btdd) with hydrated Mn^{2+}, Co^{2+} and Ni^{2+} chlorides leads to the formation of the three isostructural MOFs, [Mn_2Cl_2(btdd)(H_2O)$_2$], [Co_2Cl_2(btdd)(H_2O)$_2$] and [Ni_2Cl_2(btdd)(H_2O)$_2$]. The octahedral coordination environment of the metal center was built by the coordination of three N-donor atoms from different btdd^{2-} linkers, two bridging chloride ions and one terminal water molecule pointing into the channel (Fig. 19).

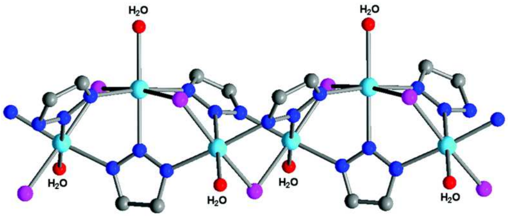

Fig. 19 Representation of the infinite rod-shaped SBU in [M_2Cl_2(btdd)(H_2O)$_2$]. Crystal structure information from ref. 83 (CSD-Refcode OVUNIE).

The authors used Soxhlet extraction with methanol to remove the solvent molecules in the as-synthesized materials and then continued with TA (100 °C under dynamic vacuum) to create open Mn^{2+}, Co^{2+} and Ni^{2+} sites. They explained that upon activation, the color changed from red to green [Co_2Cl_2(btdd)] and from white to lime-green [Ni_2Cl_2(btdd)], due to the change in the metal-ion coordination number from six to five, while [Mn_2Cl_2(btdd)] remained off-white.[83] The MAF-X27 (M = Co^{2+}) and MAF-X25 (M = Mn^{2+}) MOFs with the 1*H*,5*H*-benzene(1,2-*d*:4,5-d′)bistriazole (H_2bbta) ligand have the same SBU as [M_2Cl_2(btdd)] (*cf.* Fig. 19).[182–184]

Open metal sites can be also obtained by using a so-called urothermal synthesis.[185] Hereby, various urea derivatives were used as solvents, which can be bound reversible to the metal sites, act as porogen, apparently aid in the crystallization and can be removed by SE to generate porosity and potential OMS. For example, the Y^{3+} sites in as-synthesized crystals in [Y_2(bdc)$_3$(e-urea)$_2$(H_2O)$_2$] are eight-coordinate, of which there are two urea solvent molecules for potential OMS.[185]

2.II Chemical activation

Chemical activation (CA) is a variant of ‘‘solvent exchange and removal by thermal activation’’ aims to allow for the final solvent removal at room temperature (RT), that is, without additional heating.

It can be noted that supercritical drying with CO_2 (scCO_2) would also belong to CA, since a stronger coordinating solvent together with the pore solvent would be replaced by CO_2 which is subsequently removed at or below RT. The supercritical carbon dioxide activation, which is performed by exchanging acetone or ethanol molecules, corresponds to the CA with halogenated solvents (see below), but is a much ‘‘greener’’ route, due to the use of the non-halogenated green solvent CO_2.[186,187] Upon CO_2 removal no (or little) surface tension or cavitation effects are expected – different to the removal of more strongly coordinating solvents. Freeze-drying is another solvent removal process, where the products are dried at temperatures below the freezing point of the solvent. This process has a direct solid-to-gas phase transition (sublimation), without the liquid phase.[188] Thus, both CA (including scCO_2 drying) and freeze-drying aim to prevent the framework collapse in the case of less-stable MOF structures. The only examples of the use of $scCO_2$ in connection with OMS reported a case with framework collapse.[189,190] Cases where $scCO_2$ or freeze-drying were used for the simple solvent removal from the pores, without dedicated OMS formation, are of course numerous.[191-194]

The mild CA by chlorinated solvents was described in detail for the activation of HKUST-1, but was also reported for MOF-2 and examples of M-MOF-74.[101–103] Jeong *et al.*[101–104] reported the CA route by treatment with halogenated solvents, like dichloromethane (DCM), without using extra thermal energy to remove the introduced halogenated solvent molecules in HKUST-1, MOF-2, M-MOF-74 (M = Cu, Ni). In contrast to the conventional TA route which is performed by applying heat energy to above room temperature and vacuum (possibly after SE), the CA proceeds by soaking the MOFs in halogenated solvents several times at room temperature and in a moisture-free argon-charged glove box.[101–103]

Fig. 20 shows schematically the CA route in ways of direct and multiple coordination exchange.

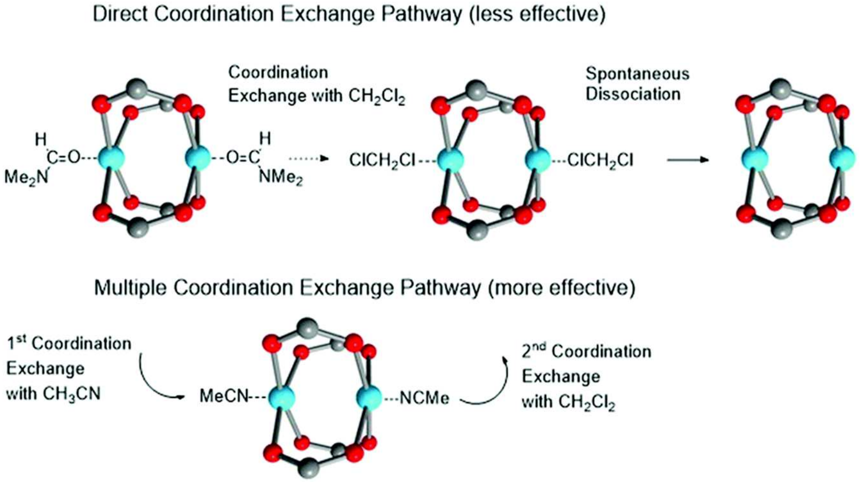

Fig. 20 Schematic illustration of the direct coordination exchange way for the CA of HKUST-1 by DCM (CH_2Cl_2) (top) and the multiple coordination exchange way by MeCN and DCM (bottom). Crystal structure information from ref. 128 (CSD-Refcode DIHVIB01). Reproduced from ref. 104 with permission from The Royal Society of Chemistry, copyright 2018.

The first step of the direct coordination exchange way is the exchange of DMF with DCM, and the second step is the spontaneous dissociation of the very weakly coordinated DCM at RT. As a variant, the multiple coordination exchange way proceeds by first exchanging the bound low-volatile DMF solvent with a more volatile one, such as MeCN, MeOH or EtOH followed by the final exchange with DCM.[101–104]

HKUST-1 was used as a proof of principle for the CA methodology. After synthesis, an activated solvent-free sample of HKUST-1 was prepared and loaded with DMF to prove the removal of the low-volatile DMF solvent through this method. The DMF coordinated and loaded HKUST-1 was soaked 30 times in DCM (30 x 10 min, RT) (direct exchange pathway, Fig. 20). The subsequent solution NMR analysis of the digested HKUST-1 showed no more signal of

DMF (Fig. 21). Alternatively, the DMF-coordinated and -loaded HKUST-1 was soaked in MeOH, EtOH or MeCN (several times x 10 min, RT). Then the obtained MeOH, EtOH or MeCN coordinated HKUST-1 was soaked 30 times in DCM (30 x 10 min, RT) (multiple exchange pathway, Fig. 20). Again, the solution NMR analysis revealed the complete solvent removal (Fig. 21). Thereby, it is also shown that methanol, ethanol or acetonitrile can be removed by multiple soaking with DCM.[101–104]

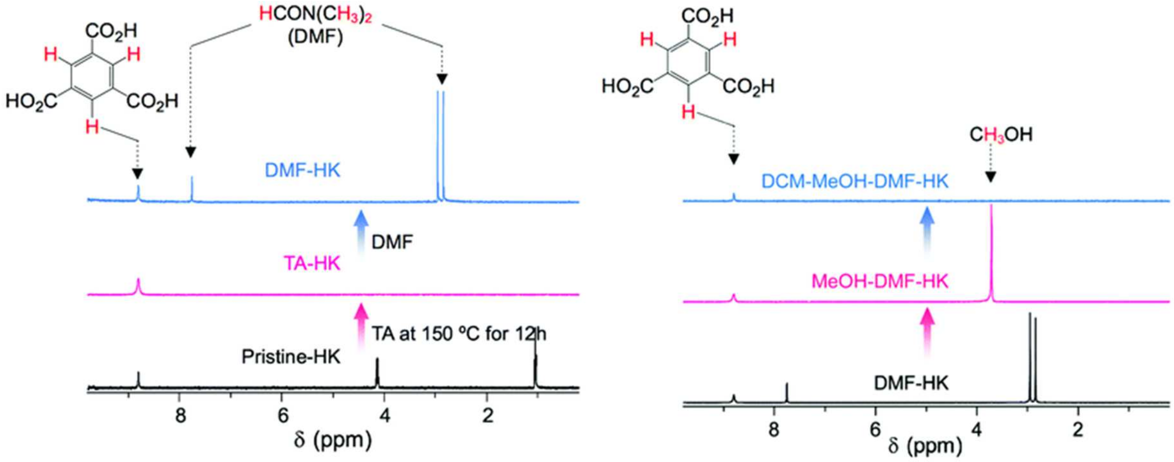

Fig. 21 Solution 1H NMR spectra after HKUST-1 (HK) digestion of DMF-loaded HK before and after initial solvent treatment with MeOH and after final solvent treatment with DCM (CH_2Cl_2). Left: Reproduced from ref. 102 with permission from the American Chemical Society, copyright 2017. Right: Reproduced from ref. 104 with permission from The Royal Society of Chemistry, copyright 2018

2.III Photothermal activation

In comparison to the above methods of solvent exchange and removal and chemical activation, which are performed by using solvents (and heat energy), the photothermal activation (PA) proceeds by only irradiation of the solid MOF sample. In 2018, Maspoch *et al.*[105] reported on this one-step activation method for MOFs by using UV-vis irradiation of 300–650 nm. The authors suggested that the light-to-heat conversion has significant potential in evaporation processes because of the local nature of the heat generated, thereby minimizing heat diffusion and energy loss. Under direct irradiation the MOFs experience a significant temperature increase (to 120–220 °C) in a few minutes (≤ 30 min) at atmospheric pressure, so that solvent molecules can be removed, and open metal sites can be generated. The MOFs exhibit absorption bands in the range 300–650 nm. The authors also pointed out that the MOF-to-light guide distance, ‘‘the distance of lamp to sample’’, is an important factor that can influence the PA of MOFs. The author used several verification methods, such as PXRD, N_2 sorption, UV-vis spectroscopy to analyze the successful activation.[105]

Evaluation of the activation parameters for HKUST-1, showed that the light distance and concomitant irradiance with the resulting temperature are crucial. A shorter distance induced a higher temperature. For example, when HKUST-1 was directly irradiated at 3 cm (2650 mW cm^{-2}, 5 min, ~250 °C), it turned amorphous and nonporous, and when it was irradiated at 5 cm (900 mW cm^{-2}, 5 min, ~ 187 °C), it remained crystalline and porous. Furthermore, they reported that the BET surface area increased from 1209 m^2 g^{-1} (7 cm, 500 mW cm^{-2}, 5 min), over 1583 (7 cm, 500 mW cm^{-2}, 30 min) to 1819 m^2 g^{-1} (5 cm, 900 mW cm^{-2}, 30 min). In comparison, the BET surface area of the conventionally activated HKUST-1 (through SE and TA) was between 1450 to 1800 m^2 g^{-1}.[105]

Fig. 22 shows that the color of the HKUST-1 powder changed from pale blue to dark blue (deep purple) after irradiation with the UV-vis lamp.

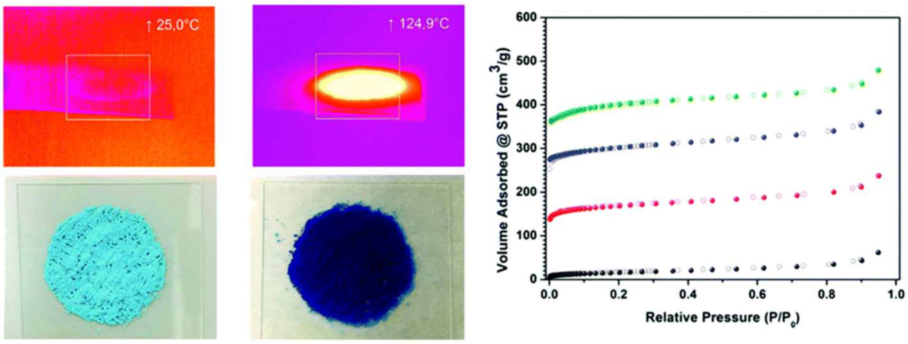

Fig. 22 Left, top: IR camera pictures of HKUST-1 before (left) and during UV-vis irradiation (right). Left, bottom: Pictures of HKUST-1 powder before (sky blue) and after (dark blue) irradiation. Right: N_2 sorption isotherms of HKUST-1. Black: as-synthesized sample. Red: thermal activated sample (120 °C, 30 min, S_{BET} = 655 m^2 g^{-1}), blue: photothermal activated sample (5 min, 500 mW cm^{-2}, S_{BET} = 1209 m^2 g^{-1}) and green (30 min, 500 mW cm^{-2}, S_{BET} = 1583 m^2 g^{-1}). Reproduced from ref. 105 with permission from the American Chemical Society, copyright 2018.

The color change signaled the loss of the water molecules coordinated to the Cu^{2+} paddle-wheel clusters. The authors explained that the solid-state UV-vis spectrum of HKUST-1 showed a broad absorption band at 720 nm attributed to the d–d transition of the Cu^{2+} ion. The contribution of this absorption band was further studied by irradiating HKUST-1 in wavelength ranges of 320–390 nm (UV) and of 390–500 nm (visible). As expected, in both cases, lower temperatures (40 and 60 °C, respectively) were reached, demonstrating that the irradiation wavelengths close to the absorption maximum contributes significantly to the photothermal effect.[105] Using this PA process, Maspoch and co-workers[105] activated also Zn/Ni/Mg-MOF-74, by following conditions, Zn: 145 °C, 30 min; Ni: 167 °C, 30 min; and Mg: 136 °C, 30 min. Also, UiO-66, by these conditions: 57 °C, 30 min.

2.IV Quantifying OMS

The techniques gas or vapor adsorption, probe molecule infrared spectroscopy and temperature-programmed desorption (TPD) were used to quantify the relative amount (percentage) of Lewis acid sites or OMS in MOFs.[195,196]

OMS should be the primary adsorption site for suitable adsorbate molecules, such as H_2O, H_2, CO_2 and CO with significantly higher heats of adsorption than for the remaining pore walls. Thus, if the completed adsorption of such gas or vapor molecules to OMS identifies themselves through a step in the adsorption isotherm before adsorption continues at the pore walls, then the absolute gas uptake allows to quantify the amount of OMS in the given sample mass. Also, the step in the heat of adsorption curve versus the amount adsorbed can be used to quantify the OMS. Examples are H_2 isosteric heat of adsorption (Q_{st}) curves plotted against H_2 adsorbed/metal (see Section 4, H_2 sorption and Fig. 35, 37, 38 and 39, left). The isosteric heat of adsorption of H_2 is usually obtained using the Clausius–Clapeyron relation from H_2 isotherm data at 77 and 87 K which are fitted with appropriate isotherm equation, *e.g.*, a dual-site Langmuir–Freundlich equation or a trisite Langmuir equation.[88]

IR spectroscopy quantifies OMS through the increasing or decreasing absorbance of bands of adsorbed or desorbed probe molecules at the metal atoms. Used probe molecules are for example water, pyridine, deuterated acetonitrile, acetone and CO.[195,197,198]

TPD can identify the type and amount of Lewis-acid sites through the chemisorption of a chosen molecular probe at a low temperature followed by measuring the rate of its desorption as the temperature increases.[195] TPD of ammonia[11,199–204] and nitrogen oxide (NO)205 were, for example, used to probe Lewis-acid sites. It has been pointed out, however, that the use of ammonia TPD in estimating MOF OMS densities presents two major drawbacks: First, the temperature range for desorption from different types of acid sites can often overlap, making peak deconvolution a necessary step in quantifying these different acid sites. Second, the temperatures required to desorb strong basic probe molecules such as ammonia may exceed the MOF thermal stability limit.[206] The methods of vapor adsorption and probe molecule IR spectroscopy are briefly explained with the following illustrative examples. Bollini *et al.*[206] used the quantity of irreversibly water adsorbed at room temperature on MIL-100(Cr) to measure the OMS density under a given set of activation conditions. Given the chemical binding of water molecules in the first coordination sphere of the metal as aqua ligands, it was assumed that adsorption of water onto open-metal sites at room temperature is irreversible under not too harsh activation condition. The type V adsorption isotherms of water onto the MOF exhibits three distinct steep regions (Fig. 23).

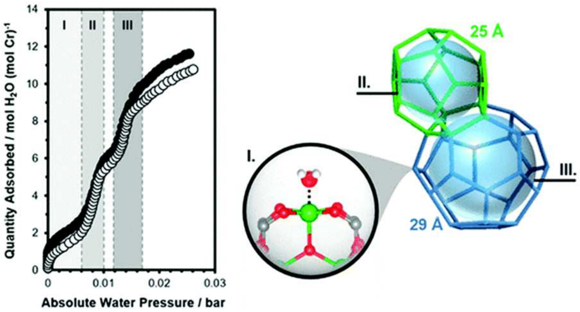

Fig. 23 H_2O adsorption isotherm (at 296 K) of MIL-100(Cr) evacuated ($P \approx 6.7 \times 10^{-5}$ bar) at 523 K for 6 h (●) and the repeat adsorption isotherm obtained immediately after evacuation for 12 h at the analysis temperature (○). Schematic representing the sequential adsorption of water onto the open Cr sites (I), filling of the smaller (25 Å) mesopores (II), and filling of the larger (29 Å) mesopores (II). Reproduced from ref. 206 with permission from the American Chemical Society, copyright 2020.

Region I lies between approximately 0 and 1 x 10^{-4} bar and the water uptake corresponds roughly to 1 mol of water per mole chromium and the authors suggested that adsorption in this region of the isotherm may occur exclusively on open chromium sites (obtained when activated at 523 K).

The calculated open-metal site count close to a value of 1 mol H_2O per mol Cr was interpreted in that 523 K is a sufficiently high temperature under vacuum to render the vast majority (if not all) of the chromium in the MIL-100(Cr) material under investigation as open-metal chromium.[206] However, we note that an irreversible water uptake of 1 mol H_2O (mol Cr)$^{-1}$ cannot be rationalized with the empirical formula $[Cr_3(O)X(btc_2)(H_2O)_2]$ (X = OH^- or F^-) of MIL-100(Cr) which has only 2 mol H_2O (3 mol Cr)$^{-1}$ or 0.66 mol H_2O (mol Cr)$^{-1}$.[141]

Still, increasing the activation temperature in MIL-100(Cr) from 303 to 523 K (at a given vacuum and time) clearly showed an increasing fraction of OMS (Fig. 24, left).[206]

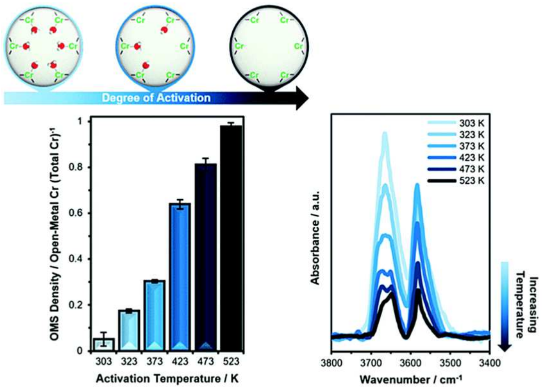

Fig. 24 Left: Estimated fraction of open Cr sites in MIL-100(Cr) as a function of activation temperature, determined using difference isotherms with H2O as an adsorbate. Right: IR spectra of MIL-100(Cr) activated under vacuum (P = 8–11 x 10^{-5} bar) for 1 h at increasing temperature. Reproduced from ref. 206 with permission from the American Chemical Society, copyright 2020.

In parallel, the relative infrared absorbance of hydroxyl vibrations was used for the quantification of OMS with increasing temperature. Aqua ligands at chromium in MIL-100(Cr) gave bands at 3672 and 3649 cm^{-1}. The areas for the aqua-ligand hydroxyl vibrations decrease upon activation between 303–523 K. The relative quantity of remaining coordinated water species was estimated by comparing the total area of the v(OH) bands at 3672 and 3649 cm^{-1} for each activation temperature to that at 303 K, which in turn gave an estimate for the fraction of coordinated water removed (Fig. 24, right). We note that the equation for the estimation should be $H_2O\cdot\cdot\cdot Cr$ retained = area $(H_2O\cdot\cdot\cdot Cr)_{T=x}$/area $(H_2O\cdot\cdot\cdot Cr)_{T=303K}$ or $H_2O\cdot\cdot\cdot Cr$ removed = 1 – area $(H_2O\cdot\cdot\cdot Cr)_{T=x}$/area $(H_2O\cdot\cdot\cdot Cr)_{T = 303\ K}$ where x is the temperature at which MIL-100(Cr) has been evacuated at for 1 h.[206]

3. Computational studies

The focus of MOF synthesis lies on the design of MOFs with binding sites that are tuned to the adsorption of a preferred guest molecule. MOFs with OMS contain such stronger binding sites which lead to an increased interaction with different sorbate molecules (see Section 4), compared to MOFs where the metal sites are fully occupied. The knowledge, how various OMS interact with the guest molecules opens access to new materials that can be tailored to a desired property.[207] It should be noted, however, that these interactions cannot easily be deduced from experiments. Computational studies can help in these cases and are a main foundation for studying and predicting sorption and separation properties in MOFs.

For the computational description of MOFs, a variety of different approaches exist, which differ in computational demand and accuracy.[208] Force-field methods form a cost-efficient way to reproduce structural properties of periodic MOFs and, depending on their parametrization, allow for a fairly accurate prediction of geometry parameters. Simulations using standard force fields, however, often fail in reproducing the interaction of the sorbate molecules and OMS.[171,209–211] Here, an adjustment of those parameters which include adsorbate/OMS interactions is necessary to obtain a quantitative prediction of adsorption isotherms. Force fields derived from quantum mechanical (QM) calculations allow for a much better description of the interaction between guest molecules and OMS.[171,211] Thermodynamic data, as *e.g.* adsorption isotherms, is accessible through Grand-Canonical Monte Carlo (GCMC) simulations based on classical and QM-improved force fields.[212–219]

Density-functional theory (DFT) calculations have been most widely applied to predict the electrostatic interactions between the adsorbate molecules with OMS. The accuracy of the DFT method, however, depends on the employed exchange correlation functional.[220] Generally, most of the exchange–correlation functionals that neglect dispersion effects fail in describing the adsorbate/OMS interaction energy.[221,222] Here, pure generalized gradient approximation (GGA) functionals (*e.g.* PBE) and hybrid functionals (B3LYP, ωB97X)[211,220,222,223] mostly underestimate the dispersive interaction, while local density approximation (LDA) functionals[222] overestimate them, due to their inability to describe long-range electron correlation, which is responsible for van der Waals (vdW) or London dispersion forces.[221,223–228]

The inclusion of dispersion corrections has been proven to be crucial for improving the accuracy of the calculated results. To capture weak interactions and improve the accuracy in simulations, the implementation of vdW density and dispersion corrected functionals have been proposed.[70] These can be used in combination with the standard exchange–correlation functionals.

An approach to describe the dispersion forces by vdW empirical corrections has been introduced by Grimme *et al*. and the associated corrections are denoted as "-D" functionals.[224] Depending on the level of dispersion correction, the extended functionals are referred to as -D1,[229] -D2[224] and -D3.[230] Quantum mechanics (QM) methods based on *ab initio* wave function methods such as the Møller–Plesset Second-Order (MP2) level of theory and the coupled cluster (CC) approach have also been applied to study the gas adsorption on OMS.[222,231] In order to improve the accuracy of adsorption energies, a promising approach was found in combined QM/QM and QM/MM methods.[221,222,232,233]

Nachtigall *et al*. showed that improved results can be achieved by employing a combined DFT-*ab initio* DFT/CC computational method.[232] Here, periodic DFT calculations with the PBE exchange correlation functional were employed to model the periodic crystal, while a subset of the structure (*i.e*. an embedded cluster) was described with the coupled cluster (CC) method including singles and doubles with perturbative triples (CCSD(T)).

Gas adsorption on OMS has been simulated for various gases using Grand-canonical Monte Carlo, DFT and *ab initio* methods of electronic structure. These studies have been employed to determine various sorption sites within the MOFs and to elucidate the role of the OMS related to the electronic interactions with different guest molecules. Using cluster models of HKUST-1 and a highly accurate coupled-cluster singles doubles (CCSD) approach, Rubeš *et al*. predicted that the OMS/adsorbate interactions can be classified into dispersion-driven interactions (CH_4), electrostatic and dispersion interactions (H_2, N_2, and CO_2), and the interaction with a partially covalent (dative) bonding character (CO).[221]

In this part, we consider computations on OMS-MOFs with gas and vapor adsorbates.[221] Hereby, we focus on the accuracy of the selected computational methods referring to the binding enthalpies in comparison to experimental data. It should be noted that some authors give the calculated binding energies (ΔE) as electronic energies. These cannot be directly compared with the experimental heats of adsorption (Q_{st}, ΔH_{ads}). To achieve a comparable value, the calculated electronic binding energies need to be adjusted by adding finite temperature and zero-point energy (ZPE) effects to approach the binding enthalpy

(ΔH).[70,222,223,234,235] However, both the predicted ΔE and ΔH results provide information on how the adsorbate/OMS interaction can be tuned by metal substitution, thereby producing novel promising adsorbents for a particular adsorbate.

Computational adsorption of H_2 on OMS

In 2014, Space *et al*. performed GCMC simulations of H2 adsorption in Mg-MOF-74 using the three-site Darkrim– Levesque (DL)[236] model (model 1) and the five-site charge–quadrupole Belof Stern Space (BSS)[237] model (model 2).[238] Both models include charge-quadrupole interactions, but no explicit terms to describe polarizability. Compared to the experimentally obtained H_2 sorption isotherm for Mg-MOF-74 at lower pressures (< 10 kPa), these models show a significantly lower H_2 uptake and do not reproduce the sharp increase at lower pressures (Fig. 25, left). This and the calculated initial isosteric heats of adsorption of – 6.5 kJ mol^{-1} and –6.0 kJ mol^{-1} indicate that these models do not capture the sorption on Mg^{2+} sites (Fig. 25, right). The total energy in these simulations was dominated by van der Waals contributions, hence sorption at open metal sites was not detected.[238]

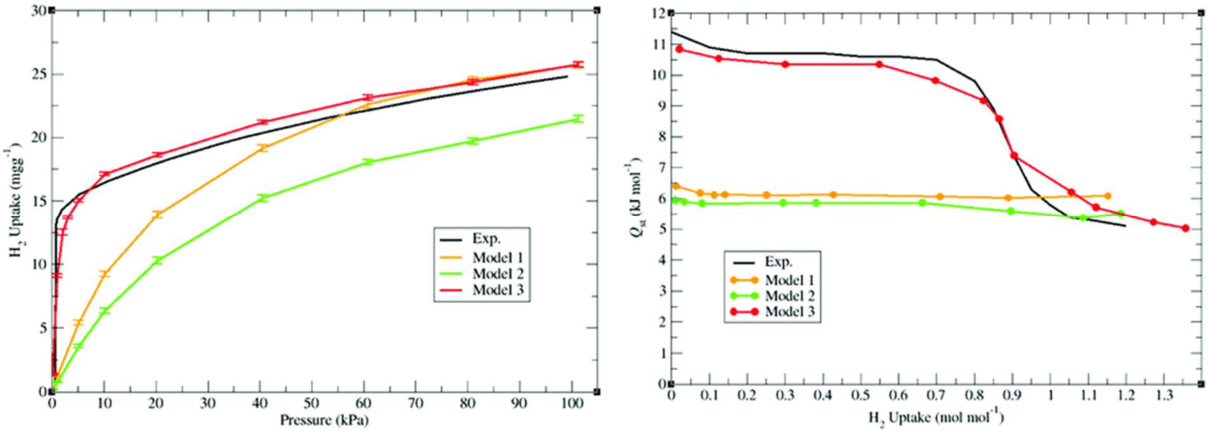

Fig. 25 Left: Low-pressure H_2 sorption isotherms at 77 K. Right: Isosteric heats of adsorption, Q_{st}, for H_2 in Mg-MOF-74 for experiment (black) and simulation using models 1 (orange), 2, (green), and 3 (red). Reproduced from ref. 238 with permission from the American Chemical Society, copyright 2014.

Space *et al*. showed that the BSSP model[237] (model 3) which includes explicit many-body polarization interactions, proves most suitable for an accurate reproduction of the experimental H_2 sorption isotherms and the resulting Q_{st} values for M-MOF-74 and the **rht** type MOFs, PCN-61 and NOTT-112.[238–240] In NOTT-112, two distinct environments for the Cu^{2+} metal sites within the paddle-wheel SBU were determined.[240] There are Cu^{2+} ions which face the cuboctahedral cage of the network and Cu^{2+} ions which are directed towards the linker. Simulations using the BSSP model indicated that the Cu^{2+} ions which face to the cuboctahedral cage of the network have a higher partial positive charge. Hence, these Cu^{2+} ions represent the main H_2 sorption sites.[240] For Mg-MOF-74, the BSSP model produces an isotherm with a sharp increase at lower pressures (< 5 kPa), which is also seen in the experiment (Fig. 25, left).[238]

Also, the calculated value for the heat of adsorption (–10.9 kJ mol^{-1}) is very close to the experiment (–11.4 kJ mol^{-1}), indicating the sorption of H_2 molecules on the Mg^{2+} OMS (Fig. 25, right and Table S2 in ESI†). Furthermore, a Mg^{2+}–H_2 center distance of 2.60 Å was calculated using the radial distribution function. Space *et al.* pointed out that this distance is an indication that the H_2 molecules are not directly coordinated to the open Mg^{2+} site, but rather are physisorbed around the site. In this regard, there is no direct interaction between the H_2 molecule and the open Mg^{2+} site. In comparison, no peak in this region was found with the models which lack explicit polarization. Here, the nearest interaction distance was found at 3.20 Å, indicating that the largest amount of H_2 molecules adsorbs in the area of the linker.[238]

One year later, the same group applied the BSSP model to the corresponding M-MOF-74 analogs with the metals Ni^{2+}, Co^{2+}, and Zn^{2+}.[177] The highest initial Q^0_{st} value of –14.0 kJ mol^{-1} was calculated for Ni-MOF-74, followed by Co-MOF-74 with a Q^0_{st} value of –12.4 kJ mol^{-1}, then for Zn-MOF-74, with the lowest Q^0_{st} value for these MOFs at around –8.7 kJ mol^{-1}. This GCMC-calculated Q^0_{st} values are in good agreement with the experimental results (see Table 3). Also, the inverse sigmoidal shape in the isosteric heat of adsorption, which then remains constant at higher loadings, could be reproduced for Ni-MOF-74 > Co-MOF-74 > Mg-MOF-74. This indicates that the OMS are already fully occupied at lower loadings and there is a large difference in the sorption energetics between the open metal sites and the secondary adsorption sites, which were observed in the proximity of the neighboring metal-coordinated oxygen atoms. On the contrary, the experimental shape of the heat of adsorption for Zn-MOF-74 decreases only weakly with increasing loading, which is also reflected by the GCMC simulation. This behavior suggests that the energy for H_2 adsorption at the metal atoms is similar to the adsorption energy within the channels. Furthermore, a correlation between the H_2–M^{2+} distance and the Q^0_{st} values for the corresponding MOFs was found.[177]

The lowest Q_{st} value for H_2 was discovered in Cu-MOF-74. Space *et al.* performed electronic structure calculations for Cu-MOF-74 to investigate the reason for the low H_2 sorption ability and low isosteric heat of adsorption value in comparison to the M-MOF-74 analogs.[241] The results of this study indicate a lower positive partial charge for Cu-MOF-74, compared to the other transition metals, due to the Jahn–Teller effect. This leads to steric strains in the crystal structure and consequently to a weaker interaction of the open Cu^{2+} site and the H_2 molecule. GCMC calculations of H_2 sorption isotherms at 77 K and 87 K revealed a nearly constant Q_{st} value of –6.5 kJ mol^{-1} in Cu-MOF-74, which indicates similar energies for H_2 adsorbed onto the open Cu^{2+} sites and the secondary sites (defined as the oxido groups of the dobdc^{4-} ligands).[241]

Table 3 Experimental isosteric heats of adsorption of CO_2 and H_2 in OMS-MOFs

		$-Q_{st}^0$ [kJ/mol]
OMS	MOF	H_2
Zr	UiO-66-NH_2[164]	7.0[284]
	$Mg(acac)_2$@UiO-66-NH_2	7.9; 8.2[284]
	$Ni(acac)_2$@UiO-66-NH_2	9.3[284]
Cr	$[Cr_3(btc)_2]$	7.4[135,159]
	MIL-100	6.3[55]
	MIL-101	10.0[55]
Mn	PCN-9	8.7[56,57]
Fe	PCN-9	6.4[56,57]
Co	PCN-9	10.1[57,336]
Ni	$[Ni_2(H_2O)_2)_{1.5}(Ni_3OH)_2(bdc)_6(na)_6]$	6.7[58]
	$[NaNi_3(OH)(sip)_2]$	10.4[59]
Cu	Cu-btt_{ri}	10.5[300]
	$[Cu_6O(tzi)_3(H_2O)_9(NO_3)]$	9.5[60]
	HKUST-1	4.5[313]
	MOF-505/NOTT-100	6.1[87,312]
	NJFU-3	6.27[118]
	NOTT-101	5.34[312]
	NOTT-102	~5.20[312]
	NOTT-103	5.71[312]
	NOTT-105	5.77[312]
	NOTT-106	6.34[312]
	NOTT-107	6.70[312]
	NOTT-112	5.64[61,62,87,240]
	NOTT-116/PCN-68	6.7[62,87]
	PCN-10	~7[63]
	PCN-11	~7[63]
	PCP-31	7.6[119]
	PCP-32	6.0[119]
Zn	$[Zn_3(\mu_3\text{-}OH)(H_2O)]_4(L)(L\text{-}H_2)_2]$ L = tetrakis{3,5-bis[(4-carboxyl)phenyl]phenyl}methane	6.8[64]
In	In-*soc* MOF	6.5[65]

MOF	OMS	$-Q_{st}^0$ [kJ/mol]	
		CO_2	H_2
M-MOF-74 $[M_2(p\text{-dobdc})]$	Mg	47.0[52]	10.3[308]
		45.0[69]	10.6[309]
		44.0[178]	10.9[89]
		43.5[70]	
		42.0[220,378]	
		39.0[71]	
	Mn	31.9[220]	8.5[89]
		31.7[70]	8.8[88,89,309]
		28.0[378]	
	Fe	30.0[351]	9.5-10.0[89]
		33.2[70]	9.7[88,309]
	Co	37.0[52]	10.7[309]
		34.5[220]	10.8[88]
		34.4[178]	11.5[89]
		33.6[70]	

Table 3 *(continued)*

MOF	OMS	$-Q_{st}^0$ [kJ/mol]	
		CO_2	H_2
	Ni	41.0[52]	11.9[88]
		38.8[178]	12.9[309]
		38.7[220]	13.5[89]
		38.6[70]	
	Cu	22.1[70]	6.1[89]
	Zn	30.6[220]	8.3[241]
		30.0[69]	8.5[309]
		26.8[70]	8.8[89]
[M_2(*m*-dobdc)]	Mn		10.3[88]
	Fe		11.1[88]
	Co		11.5[88]
	Ni		12.3[88]
[M_2(dobpdc)]	Mg		10.7[309]
	Mn		8.7[309]
	Fe		10.0[309]
	Co		11.3[309]
	Ni		12.0[309]
	Zn		8.4[309]
[M_2(olz)]	Mg		10.8[310]
	Fe		10.9[310]
	Co		11.4[310]
	Ni		12.1[310]
	Zn		7.3[310]
M-btt	Cr	36.7[156]	10.0[159]
	Mn	45.6[156]	10.1[157–160]
	Fe	51.2[156]	11.91[57,158]
	Cu	30.7[156]	9.5[157–159]

The result that the open Cu^{2+} sites and the secondary adsorption sites are equally energetic in H_2 adsorption was supported by Dietzel *et al.*[89] This group has shown that the H_2 sorption properties can also be reproduced using DFT at the PBE level with and without dispersion corrections. In general, calculations at the pure DFT level exhibit an even weaker binding energy for the open Cu^{2+} site than for the secondary adsorption sites. If dispersion effects were included, a marginally stronger binding energy on the Cu^{2+} site than on the secondary adsorption sites was found. In summary, there is a decrease in the difference of the H_2 adsorption energy of the open metal site and the secondary adsorption sites according the following order $Ni^{2+} > Co^{2+} > Mg^{2+} > Fe^{2+} > Zn^{2+} \sim Mn^{2+} > Cu^{2+}$.[89]

For the DFT-simulation of H_2-bonding in MOFs, the range-separated, dispersion-corrected ωB97X-D functional has proven to be a suitable and accurate model.[242] In addition to thermochemistry and kinetics, it captures covalent and non-covalent interactions. Long *et al.* predicted differences in electronic structure at the open metal sites of M-MOF-74 ([M_2(*p*-dobdc)]) and [M_2(*m*-dobdc)] with the use of DFT calculations including the ωB97X-D functional.[88] While both frameworks have approximately the same surface area, their H_2

adsorption ability is different. For example, it was found that the open Ni^{2+} sites show stronger interaction with H_2 molecules in [Ni_2(*m*-dobdc)] compared to Ni-MOF-74. The binding strength in the M–H_2 system was examined by energy decomposition analysis (EDA). The advantage of using EDA calculations is that the interpretable physical components are considered individually. Otherwise, when comparing absolute energy differences, a single number is used to describe the H_2 bond strength. Based on absolutely localized molecular orbitals (ALMOs), the EDA was used to break down the entire binding energies into frozen energy, polarization and charge transfer components.[243] In the *p*-dobdc^{4-} linker MOFs in M-MOF-74, the H_2 binds in a linear end-on geometry while in the *m*-dobdc^{4-} MOFs the H_2 molecule is oriented bent end-on in the direction of the oxygen atom of the linker.[88]

DFT calculations with the PBE functional were performed for MOF-505.[244] Here, several localizations and orientations of the H_2 molecule were investigated around the paddle-wheel cluster. The strongest adsorption energy of –13.44 kJ mol^{-1} was calculated when the H_2 molecule was located perpendicularly in the direction of the open Cu^{2+} site.

Computational adsorption of CO_2 on OMS

Computational investigations applying DFT and GCMC methods predicted several adsorption sites for CO_2 in OMS-MOFs that result in different adsorption enthalpies. To study the interaction energy for CO_2 in relation to the different OMS, various computational approaches were used. At low coverage, the CO_2 molecules preferentially adsorb on the OMS.[155,232,234,245,246] Therefore, we will limit our discussion to the results achieved for the low-pressure regime.

Space *et al.* performed GCMC simulation studies to evaluate the sorption mechanism of CO_2 on open Cu^{2+} sites and to determine the heat of adsorption for CO_2 in UTSA-20.[210] For the CO_2 sorption simulation, three different potentials were used which are briefly described below: First, the non-polarizable TraPPe potential (transferable potentials for phase equilibria),[247] which is suitable for the description of explicit repulsion/ dispersion as well as electrostatic interactions. It includes Lennard-Jones parameters and point partial charges at the atomic sites. Second, the five-site CO_2-PHAST-model[248] (PHAST = potentials with high accuracy, speed, and transferability), which determines bulk pressure–density data and potential energy curves for CO_2 dimers. And third, the analogous CO_2-PHAST*- model,[248] where the * stands for the inclusion of explicit polarization. With the inclusion of this parameter, explicit many-body polarization interactions are obtained which are important for the simulation in heterogeneous media with strongly charged and polar sites. It has been shown that the use of the TraPPe model is not suitable for the simulation of CO_2/OMS, as it does not detect the loading at the open Cu^{2+} sites and revealed significantly higher CO_2 uptakes compared to the experiment.

The CO_2-PHAST- and CO_2-PHAST*-models are in better agreement, albeit slightly higher uptakes were received. However, the CO_2-PHAST model fails due to the lack of induced dipole parameters, as it detects only a weak proportion of CO_2 molecules near the Cu^{2+} sites. Using the CO_2-PHAST*-model, it was found that the inclusion of explicit many body polarization interactions makes an important contribution to capturing the sorption on the open Cu^{2+} sites. The heat of adsorption revealed an almost constant value as a function of loading in the range of -30 kJ mol^{-1}, calculated with TraPPE, CO_2-PHAST, and CO_2-PHAST* potentials, which is close to the experimental adsorption enthalpy of -29.0 kJ mol^{-1} at lowest loading.[232] A constant value of the heat of adsorption with increasing CO_2 loading can be attributed to the fact that the OMS and the adsorption sites within the pore have similar energies. This would also explain why the values for the heat of adsorption received from TraPPE and CO_2-PHAST are close to those of the CO_2-PHAST* model, even if they do not reproduce the CO_2/Cu^{2+} interaction.[210]

For M-MOF-74, DFT-D studies revealed that the adsorbed CO_2 molecule is end-on coordinated on the OMS and possesses an angular $M\cdot\cdot\cdot O{=}C{=}O$ orientation.[234,249] An orientation towards the linker was assigned to a secondary vdW interaction between the CO_2 molecule and the adjacent oxygen atom of the carboxylate group from the linker.[234,245] Here, Wang *et al*. confirmed that the CO_2 adsorption onto OMS has contributions from the Lewis acid and base interaction between O_{CO2} and the metal ion as well as from the interaction between C_{CO2} and the carboxylate oxygen in the square plane of the metal ion.[234] Based on various transition metals, Snurr *et al*. found an explanation for the relative CO_2 binding strengths in the effective charge of the metal atom.[222] The authors confirmed that a strong positive potential on the metal cation and a strong negative potential around the coordinated carboxylate oxygen atoms cause the angular geometry of the $Mg^{2+}\cdots O{=}C{=}O$ complex. Thus, due to the quadrupole moment of CO_2, there is a lateral interaction between the CO_2 molecule and the oxygen atom from the carboxylate group of the linker.[222]

DFT calculations including Grimme-dispersion (*e.g*. PBE-D2, PBE-D3, B3LYP-D, B3LYP-D*, ωB97X-D) were employed, with the intention of reproducing experimental heat of adsorption for CO_2 in OMS-MOFs.[171,220,223,249] Compared to the standard PBE functional, the Grimme D2 and D3 dispersion corrected PBE functional gives more accurate binding energies.[171,250] However, Siepmann *et al*. stated that PBE-D3 underestimates the magnitude of the experimental heats of adsorption for CO_2 in M-MOF-74 with a mean unsigned percentage error of 8.4%.[171] Smit *et al*. gave a percent deviation of ~6% for the PBE-D3 functional and a slightly smaller deviation of 4.4% for PBE-D2.[223] Bordiga *et al*.[249] achieved a ΔH^0 value of -37.9 kJ mol^{-1} for Mg-MOF-74 using the B3LYP-D* functional, which is somewhat underestimated compared to the experimental data (-39 to -47 kJ mol^{-1}).[52,69–71,178,222] Likewise, an improved value of -44.9 kJ mol^{-1} for Mg-MOF-74 was obtained with the ωB97X-D method.[220] Both, the ωB97X-D and the B3LYP-D functional, however, deliver underestimated

ΔH values for MIL-101(Cr) (–29.2 kJ mol^{-1} and –30.8 kJ mol^{-1} compared to the experimental enthalpy at zero coverage of about –44 kJ mol^{-1}).[220,251]

One of the latest computational studies by Yang *et al*. used DFT-D2 methodology to investigate CO_2 adsorption properties of several MOFs built from Cu^{2+} paddle-wheel units.[252] Since the investigated MOFs consist of the same paddle-wheel cluster but differ in the carboxylate ligands, the calculations were performed on a selected Cu^{2+} paddle-wheel cluster model derived from HKUST-1. The development of a combination of Coulomb potentials and vdW interactions (with Morse potential parameters derived from quantum calculations) was required to describe the interaction in the considered system. The DFT-D2 computed interaction energy for CO_2 of –21.2 kJ mol^{-1} is underestimated compared to the experimental Q^0_{st} value of – 29.0 kJ mol^{-1} (see Table 3).[232,252]

In addition to the Grimme approach, further adjustments of the standard exchange–correlation functionals were pursued by Lundqvist *et al.*[253] The authors include a nonlocal term to capture long-range interactions such as vdW-forces (vdW-DF functional). A second generation of this approach has been proposed, employing both, a semi-local exchange functional (PW86)[254] and a large-N asymptote gradient correction (vdW-DF2), where N refers to the number of electrons.[255] DF functionals such as optB88-vdW and optB86b-vdW were used to calculate the binding energies for CO_2 in M-MOF-74.[223] However, Smit *et al*. found that these functionals overestimate the experimental values by ~8 kJ mol^{-1}.[223]

Sayós *et al*. showed for Mg-MOF-74, that the calculated vdW-DF2 zero-coverage adsorption energy at 298 K for CO_2 adsorbed at the open Mg^{2+} sites (–47.9 kJ mol^{-1}) is in good agreement with the experimental result (–45 kJ mol^{-1}).[178,246]

Brown *et al*. indicated that the CO_2 adsorption ability is determined by the bond strength of the CO_2 molecule on the OMS.[70] The authors obtained the binding energies using the dispersion-correlation functional vdW-DF2+*U*. The inclusion of the Hubbard-like parameter *U* that relates single particle potentials to the magnetic and orbitals parameters was recommended to localize the d-states of the transition metals.

The CO_2 binding enthalpies ΔH (at loadings of 0.167 CO_2 per M^{2+}), which were obtained by including quantum zero-point energies (ZPEs) and finite-temperature thermal energies (TEs) at the level of a harmonic approximation, suggested the trend Mg^{2+} (–40.9 kJ mol^{-1}) > Ni^{2+} (– 37.3 kJ mol^{-1}) > Fe^{2+} (–34.1 kJ mol^{-1}) > Mn^{2+} (–33.9 kJ mol^{-1}) > Co^{2+} (–33.8 kJ mol^{-1}) > Zn^{2+} (–30.2 kJ mol^{-1}) > Cu^{2+} (–27.1 kJ mol^{-1}). Here, the calculated values differed slightly from the experimental data (giving the trend Mg^{2+} (–43.5 kJ mol^{-1}) > Ni^{2+} (–38.6 kJ mol^{-1}) > Co^{2+} (– 33.6 kJ mol^{-1}) > Fe^{2+} (–33.2 kJ mol^{-1}) > Mn^{2+} (–31.7 kJ mol^{-1}) > Zn^{2+} (–26.8 kJ mol^{-1}) > Cu^{2+} (–22.1 kJ mol^{-1})) and showed a deviating isosteric heat of adsorption for Mn^{2+}, Fe^{2+}, Co^{2+} and Zn^{2+}.[70]

In general, within the M-MOF-74-series, the largest affinity for CO_2 from computational studies was found for Mg-MOF-74, which agrees to the experimental data (see also Section 4, CO_2 adsorption).

The higher CO_2 uptake ability for Mg^{2+} in comparison to transition metals in the M-MOF-74 series could also be detected with the use of non-polarizable force fields derived from DFT calculations including periodic boundary conditions.[256] The calculated probability density plots for Mg-MOF-74 showed a lower mobility of the adsorbed CO_2 molecules as well as less obvious secondary adsorption sites (adjacent to the primary site) than in both Co- and Zn-MOF-74 (Fig. 26).

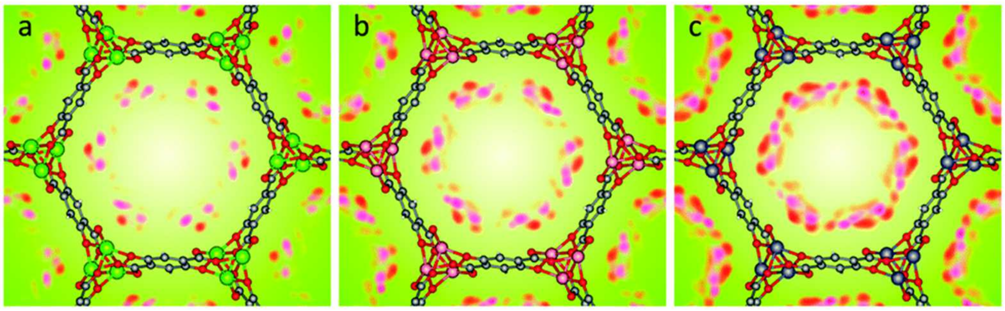

Fig. 26 Probability density plots obtained with a DFT-derived force field for CO_2 in (a) Mg-, (b) Co-, and (c) Zn-MOF-74, at 100 K. Orange dots indicate the density of the oxygen atoms in CO_2, whereas magenta dots correspond to the density of the carbon atoms. Darker colors refer to a higher probability of finding a guest at those positions. Each colored sphere corresponds to the following atoms: C, gray; O, red; H, white; Mg, lime green; Co, pink; Zn, slate. Reproduced from ref. 256 with permission from the American Chemical Society, copyright 2016. Direct link: http://pubs.acs.org/doi/10.1021/acs.jpcc.6b03393.

This lower mobility was attributed to the fact that Mg-MOF-74 has a large energetic difference between open metal and secondary adsorption sites. Therefore, all OMS are occupied first. Comparatively, in Co-MOF-74 and Zn-MOF-74 the secondary adsorption sites are more occupied, as here the computed binding energies of OMS and secondary adsorption sites are almost similar.[256] In further work, Smit *et al*. stated that in addition to the electrostatic interaction, the binding strength between CO_2 and the OMS is influenced by the hybridization between the metal d_{z2} orbital and a lone pair on CO_2. For Mn^{2+} through Co^{2+}, the d_{z2} orbital is singly occupied, while in Cu^{2+} and Zn^{2+} this orbital is doubly occupied, and the binding strength decreases.[223]

The lowest binding enthalpy within the M-MOF-74 series was found for Cu^{2+} and was related to the fact that the elongation along the axial ligand oxygen atom impedes the approach of CO_2 towards the Cu^{2+} site.

Brown *et al*. showed that the $M\cdot\cdot\cdot O(CO_2)$ distance correlates with the M–CO_2 binding strength, *i.e*. longer distances decrease the binding energy, albeit their vdW-DF2 calculated distances were overestimated compared to experimental data.[70]

Smit *et al*. furthermore found that for OMS-MOFs the vdWDF2 functional overestimated the bond distances, resulting in a slightly higher binding energy ($\Delta E = \pm 1.3$ kJ mol^{-1}) compared to the experimental value. Therefore, the rev-vdW-DF2 has been applied to improve the geometries.[223] By using this functional the binding energy was overestimated by only 0.4 kJ mol^{-1}.

Queen *et al*. confirmed that the inclusion of vdW dispersion correlations in DFT calculations quantitatively support the structural features associated with the OMS as binding sites for CO_2.[156] The authors performed periodic DFT calculations using the dispersion corrected rev-vdW-DF2+*U* functional to study the CO_2 binding interaction in the M-btt (M = Cr^{2+}, Fe^{2+} and Cu^{2+}) series.

In this M-btt series, the primary adsorption sites were found at the OMS and secondary adsorption sites were above the $[M_4Cl]^{7-}$ cluster, arising through the interaction of the CO_2 molecule with the tetrazolate rings of the linker (Fig. 27).

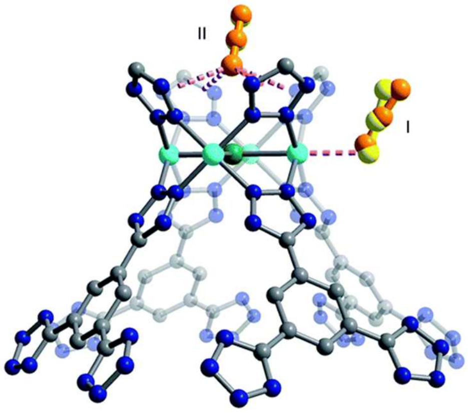

Fig. 27 Structure of Cu-btt showing the primary CO_2 adsorption site I (at right) and secondary site II (at top), as identified by DFT calculations (yellow ball-and-stick representations) and by *in situ* powder neutron diffraction (orange ball-and-stick representations). Cyan, grey, blue, and green spheres represent Cu, C, N, and Cl atoms, respectively; hydrogen atoms are omitted for clarity. Reproduced from ref. 156 with permission from The Royal Society of Chemistry, copyright 2018. (*cf*. to Fig. 47 for the experimental adsorption sites from Rietveld refinement).

An insight into the adsorptive behavior of the isostructural M-btt MOFs was provided by comparison of the DFT derived CO_2 binding energies for sites I (open metal site) and II (adsorption site above the $[M_4Cl]^{7-}$ cluster).[156] While the bond strength at site I depends mainly on the metal identity, the bond strength at site II is independent of the metal and is almost identical for the investigated species. The highest theoretical binding enthalpy on the primary site I was calculated for Fe-btt (as –51.7 kJ mol^{-1}), followed by Cr-btt (–36.6 kJ mol^{-1}) and then Cu-btt (–29.4 kJ mol^{-1}). These values are in very good agreement with the experimental isosteric heats of adsorption determined at zero coverage (see Table 3). The higher binding energy for Fe-btt was related to the shorter calculated Fe–O(CO_2) distance of 2.301 Å in comparison to the Jahn–Teller-elongated distances for Cu(II)· · ·O(CO_2) (2.567 Å) and

Cr(II)· · ·O(CO_2) (2.625 Å). A shorter binding distance is normally correlated with a higher binding energy, hence the shorter Cu· · ·O distance with lower binding energy is somewhat counter-intuitive. The smaller Cu· · ·O than Cr· · ·O distance can be explained by the shorter ionic radii of Cu^{2+} and Cr^{2+}.[156] The lower Cu· · ·O binding may result from the stronger electronic repulsion of the doubly-occupied d_{z2} orbital in d^9-Cu^{2+} relative to the singly-occupied d_{z2} orbital in d^4-Cr^{2+}(high-spin).

Snurr *et al*. showed that calculations at the MP2-level give improved values for the binding energies compared to pure DFT methods.[222] For the M-MOF-74 series a more refined description of the binding energies for CO_2 molecules adsorbed at OMS was obtained with the use of relaxed structures obtained from B3LYP in combination with single point energies calculated at the MP2 level (Table S1 in ESI†).[222]

For HKUST-1, the most favorable orientation of the CO_2 molecule is linear and tilted away from the Cu–Cu axis of the paddle wheel SBU.[232] Here, Nachtigall *et al*. suggested that the interaction of CO_2 with Cu^{2+} is modulated by the additional electrostatic interaction with the hydrogen of the trimesic acid and the Cu^{2+} cation of the adjacent paddle-wheel SBU, as well as by the dispersion interaction with organic linkers (Fig. 28).

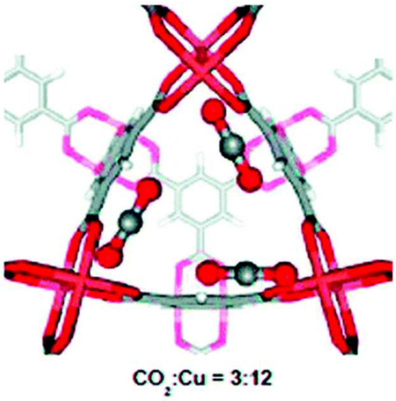

Fig. 28 Structure of the CO_2 adsorption complexes on the Cu^{2+} site for CO_2/Cu coverage of 3: 12. Reproduced from ref. 232 with permission from the American Chemical Society, copyright 2011.

Using the DFT/CC method for HKUST-1, an interaction energy of –28.2 kJ mol^{-1} was calculated at low coverage with one CO_2 molecule per Cu^{2+} site, which is consistent with the findings by Rubeš *et al*. using the same method.[221,232] Nachtigall *et al*. added that at a coverage of three CO_2 molecules per 12 Cu^{2+} centers (3 : 12 coverage), the CO_2 molecules are not statistically distributed over the Cu^{2+} sites but are preferably adsorbed at the adjacent three Cu^{2+} sites within the triangular-shaped small cage forming one small opening (Fig. 28).[232] Here, an increased interaction energy of –35.9 kJ mol^{-1} for the third CO_2 molecule was calculated, because of an additional stabilization due to the T-shaped interaction of adjacent CO_2 molecules (as was also found in M-MOF-74, *cf*. Fig. 41b).

Computational adsorption of CO on OMS

The influence of open metal sites on the CO adsorption was investigated with periodic DFT and cluster models including various levels of correlation.[221,257–260]

Georgiev *et al*. applied cluster and periodic DFT calculations at the PBE level to study the CO adsorption at open Cu^{2+} sites in Cu-MOF-74 (Fig. 29).[73]

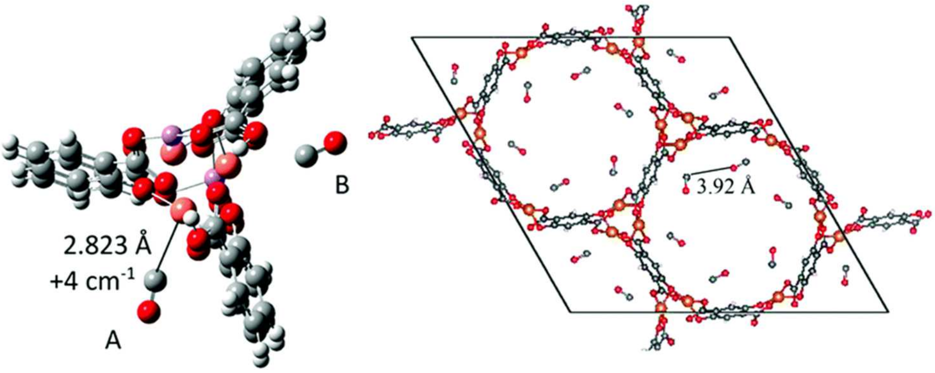

Fig. 29 Left: 92-atom cluster of Cu-MOF-74, with one CO molecule adsorbed at the open Cu^{2+} site, A, and a second CO molecule, B, adsorbed at the nearest Cu^{2+} adjacent site, which appears in the adjacent pore channel. Right: Periodic model of the Cu-MOF-74 structure. Reproduced from ref. 73 with permission from the American Chemical Society, copyright 2018.

Both models revealed a weak CO binding at the Cu^{2+} sites, which was mainly attributed to dispersive interactions. The calculated binding energies of -23.4 kJ mol^{-1} with the periodic model and -17.8 kJ mol^{-1} with the cluster model were in the range of the adsorption enthalpy of -20 kJ mol^{-1} obtained *via* variable-temperature IR (VTIR) experiments.[73]

DFT calculations for CO and the transition metal atoms Mg^{2+}, Co^{2+} and Ni^{2+} in M-MOF-74 revealed that Ni^{2+} and Co^{2+} interact stronger with CO molecules than Mg^{2+} sites, as expected from the established d-orbital bonding models of CO to transition metals and the lack of π-back-bonding from main-group metals (Fig. 30).[178]

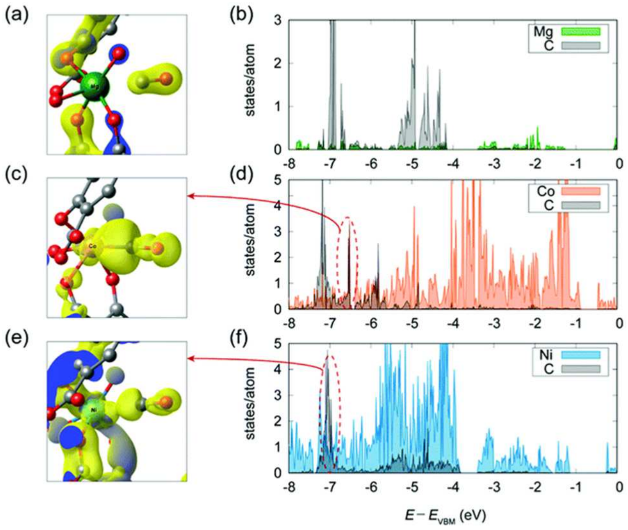

Fig. 30 Electronic properties calculated using DFT for CO adsorbed in (a and b) Mg-MOF-74, (c and d) Co-MOF-74 (e and f) Ni-MOF-74. Left: Isosurface of total charge density and right: partial density of states (PDOS). The partial charge densities in (c) and (e) were obtained from the states indicated by the red dashed ellipse. Reproduced from ref. 178 with permission from the American Chemical Society, copyright 2019.

The electron transfer from the open Ni^{2+} and Co^{2+} sites to the antibonding π-orbitals of Cos was confirmed. As needed for stable M-CO interactions, the open Co^{2+} and Ni^{2+} sites enter into strong π-back-bonding with CO *via* electron transfer from the d-orbitals of the transition metal to the π*-antibonding molecular orbitals of CO. The main-group metal Mg^{2+} cannot participate in such an electron transfer or orbital overlap with CO because of its lack of valence electrons (see also Section 4, CO adsorption).

Periodic DFT-D calculations at the B3LYP-D* level of theory were applied to calculate the heats of adsorption of CO on M-MOF-74 Mg^{2+}, Ni^{2+} and Zn^{2+} at 298 K.[245,249] The simulations at the B3LYP + D* level predicted heats of adsorption ΔH (Ni^{2+}, –41.9 kJ mol^{-1}; Mg^{2+}, –30 kJ mol^{-1}; Zn^{2+}, –24.8 kJ mol^{-1}) which underestimate the experimental data (Ni^{2+}, –59.7 kJ mol^{-1}; Mg^{2+}, – 38.3 kJ mol^{-1}).[178,245,249] Sauer *et al*. showed that the hybrid MP2:B3LYP + D* method gives improved results, although the obtained values still deviate from the experiment (Ni^{2+}, – 50.3 kJ mol^{-1}; Mg^{2+}, –41.2 kJ mol^{-1}; Zn^{2+}, –39.8 kJ mol^{-1}).

Computational adsorption of C_2H_2 on OMS

Wang *et al*. predicted that the strong C_2H_2 interaction with open OMS in the M-MOF-74 series is caused by the σ-donor/ π-acceptor bonding between of C_2H_2 and suitable transition metal atoms, as established in organometallic chemistry.[234]

Fröba *et al*. pointed out the need for inclusion of a parameter adjustment based on *ab initio* calculations to describe the interaction of guest molecules with the OMS.[209] To account for electrostatic interactions between the sorbate and the OMS, point charges for the MOF were derived by fitting them to the DFT-PBE calculated electrostatic potential. This method revealed for HKUST-1 an isosteric heat of adsorption of –30 kJ mol^{-1} for C_2H_2 at low coverage, which deviates slightly from the experimental Q^0_{st} value (–30.4 to –39.0 kJ mol^{-1}).[209,261,262]

Li *et al*. performed GCMC simulations and DFT calculations to study the C_2H_2 adsorption in a series of Cu^{2+} paddle-wheel MOFs, such as MOF-505, Nju-Bai12, PCN-46, ZJU-40 and NOTT-X (X = 101, 102, 103, 106, 108).[263] It was found that OMS, organic ligands and the functionalization of the ligands make an important contribution in promoting C_2H_2 storage capacity and the separation of C_2H_2 over CH_4 and CO_2 below 2 bar. Quantum-mechanical calculations were used to capture the interactions of C_2H_2 with the OMS. The corresponding terms were produced by fitting the DFT energy surface. Optimization of the ground state geometries was performed employing GGA exchange implemented with PBE. In all Cu^{2+} paddle-wheel MOFs, three adsorption sites for C_2H_2 were found (Fig. 31, left). These sites are referred to the open Cu^{2+} site (site I), the basket site, where three paddle-wheel clusters and three ligands form a basket (site II) and the sites which are mostly near the aromatic rings of the linker (site III). The basket site II was found to be the most preferred adsorption site for C_2H_2. For this basket-pocket site higher binding energies (–34.0 to –41.1 kJ mol^{-1}) than for site I (–33.7 to –29.9 kJ mol^{-1}) and for site III (–14.3 to –33.4 kJ mol^{-1}) were calculated using DFT (Fig. 31, right).[263]

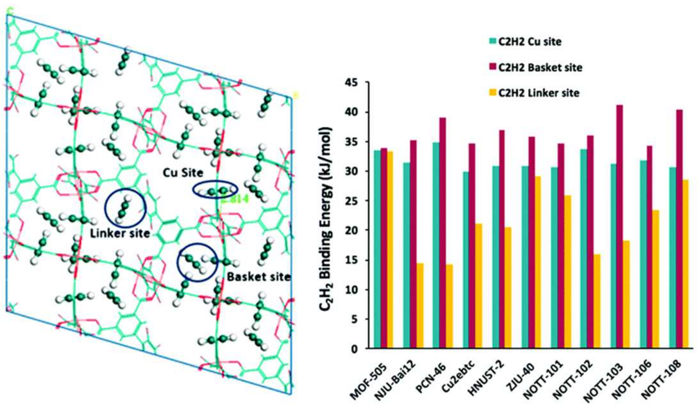

Fig. 31 Left: DFT optimized binding positions of C_2H_2 molecules in NOTT-108. Right: DFT calculated C_2H_2 binding energies for OMS (blue), basket pocket sites (red), and linker sites (yellow). Reproduced from ref. 263 permission from the American Chemical Society, copyright 2017.

Computational adsorption of CH_4 on OMS

Computational studies for the CH4 adsorption behavior in the paddle-wheel MOFs $[M_3(btc)_2]$ (M = Cu^{2+}, Cr^{2+}) and PCN-14 indicate that the OMS are not the preferred adsorption sites for CH_4.[212,264,265]

Cavalcante *et al*. classified the Cu^{2+} sites in PCN-14 as weak methane adsorption sites.[265] GCMC simulated adsorption isotherms performed for HKUST-1 and PCN-14 at 150 K revealed an occupation of CH_4 at the open Cu^{2+} sites (1.67 and 0.05 bar). At 290 K over a pressure range of 0.01–35 bar no adsorption on these sites could be determined theoretically. Likewise, GCMC calculations show no energy barriers between weak and strong adsorption sites in PCN-14, allowing open Cu^{2+} sites to direct the CH_4 molecules to the neighboring adsorption sites. After all, it was reasoned that multiple adsorption sites and efficient linking between them can explain the high methane uptake in PCN-14.[265]

Brown *et al*. stated that, consequently, the strength of the CH_4 binding at the OMS in HKUST-1 and $[Cr_3(btc)_2]$ is caused by intermolecular interactions with adjacent CH_4 molecules adsorbed at the windows of the octahedral cages (primary sites) instead of an electronic interaction with the metal center.[264] The values for the binding enthalpy for the open Cu^{2+} site in HKUST-1 was calculated to be –9.4 kJ mol^{-1} using the DFTvdW- DF2+*U* method. Comparatively, a significantly higher value for the binding enthalpies at the windows of HKUST-1 (– 21.8 kJ mol^{-1}) and $[Cr_3(btc)_2]$ (–21.5 kJ mol^{-1}) was calculated. The authors noted that the DFT calculations for $[Cr_3(btc)_2]$ fail to capture the multireference character of the Cr–Cr bond in the singlet ground state, and they argued that the detection of bond enthalpies at the open Cr^{2+} site is therefore unreliable. Furthermore, these simulations revealed no difference in the adsorption behavior of HKUST-1 and $[Cr_3(btc)_2]$, for the interaction with the respective OMS.[264] The type of the metal cation affects the adsorption mechanism only very little and the strong binding is due to a combination of structural features that are identical in both $[M_3(btc)_2]$ materials together with $CH_4\cdots CH_4$ vdW interactions. Hence, the uptake values for HKUST-1 and $[Cr_3(btc)_2]$ are similar.[264]

Düren *et al*. used DFT/CC-PES simulations to derive the favorable adsorption sites in HKUST-1.[212] With the intention to eliminate the ambiguity and inaccuracy that results from generic force fields, they applied a potential energy surface (PES) calculated by a hybrid DFT/*ab initio* method (DFT/CC) in the GCMC simulations. Here, the DFT/CC corrections were performed using PBE with the AVQZ basis set and CCSD(T)/CBS (complete basis set limit) calculations. The authors noted that simulation of CH_4 adsorption isotherms at 77 K and 87 K using the UFF-based GCMC method is not suitable to capture the CH_4 adsorption on the OMS. Instead, DFT/CC-PES simulations capture the shape of the experimental adsorption isotherm and the CH_4 adsorption sites including the OMS. This study revealed a population in the centers of the small pores at low CH_4 loading, followed by adsorption on the center of the windows to the small cavities and only at higher loading an occupancy of the OMS was observed.[212] According to the DFT/CC-PES, an occupancy of 96% was determined on the OMS, corresponding to 46.25 of the 48 OMS being occupied by CH_4. Also, the simulated distance between the CH_4 molecules and the open Cu^{2+} site of 3.097 Å agrees well with the experimental value (3.075 Å).

Furthermore, the fluid framework potential energy derived with DFT/CC-PES yields an interaction with the OMS, while this effect was not captured by the PES derived from the UFF force field.[212]

Separation

Independent of the open metal source, computational studies using DFT-derived non-polarizable force fields for the adsorption of dry $N_2/CO_2/CH_4$ gas mixtures reproduce for the whole M-MOF-74 series a higher CO_2 adsorption over CH_4 and N_2, with almost no N_2 adsorbed under natural gas purification conditions.[256] Smit *et al.* developed DFT-derived non-polarizable force fields to study the adsorption properties of the gas mixture CO_2/H_2O in M-MOF-74 considering the H_2O sensitivity of these frameworks. The use of this method allowed for a forecast how fast a CO_2 uptake will decrease in the presence of water. It could be detected that the CO_2 uptake decreases with increasing H_2O bonding energy. Thus, in Mg-MOF-74, with the highest DFT binding energy for H_2O (–66.9 kJ mol^{-1}), the H_2O uptake is greater than for CO_2, even when the mole fraction of H_2O in the gas mixture is only 0.1% at 313 K and 0.15 bar. In contrast, in Zn-MOF-74, with the weakest DFT-calculated H_2O binding energy (–46.3 kJ mol^{-1}), the H_2O uptake surpasses the CO_2 uptake only when the mole fraction of H_2O is above 2% (at 313 K and 0.15 bar). Thus, Zn-MOF-74 can tolerate the presence of 20-times more H_2O than Mg-MOF-74. The latter will be useless for carbon capture as most flue gases contain significantly more than 2% H_2O. The values for the other M-MOF-74 analogues lie in a range between 0.1% and 2%. Consequently, none of the M-MOF-74 frameworks will be applicable for CO_2 adsorption from moist gas streams.[256]

In summary, theoretical methods are used to calculate adsorption isotherms, heats of adsorption, binding geometries of adsorbates at the MOF surface *etc*. With adequate description of adsorbate-adsorbent interactions, quantum mechanical calculations of potential energy surfaces are able to reproduce experimental binding enthalpies. At the DFT-level, the inclusion of van der Waals interactions is crucial. The best results compared to the experiment are obtained through a combination of dispersion corrected DFT and high-level *ab initio* methods, as *e.g.* DFT-D and coupled cluster (CC) methods including complete basis set extrapolation. It is possible to achieve agreement between computational and experimental Q^0_{st} values for the heat of adsorption within 1–2 kJ mol^{-1} (Tables S1–S3 in ESI†). The deviation of 1–2 kJ mol^{-1} is within the experimental error, even if such Q^0_{st} values are unjustified reported with a decimal digit.[266–268]

4. Open metal site applications

“Application” can mean different things. In basic research it could be already considered an “application” that OMS allow for the defined post-synthetic modification of a different linker at the metal site. Further, the formation of an OMS is also the prerequisite for the “binding” of weakly coordinating adsorbates such as CO_2, H_2 *etc*. As outlined in the computational Section 3, these gas molecules bind most strongly to the OMS which forms the basis of “applying” OMS-MOFs for high gas uptake and separation (see below). At the same time, the structure elucidation of the binding mode of these adsorbed gas molecules in OMS-MOFs is also “applied” in structural studies.

In addition, we note that the following “applications” of OMS-MOFs (or MOFs at large) in gas sorption, catalysis and sensing are “potential applications”, which are suggested from lab experiments and which have not yet been commercialized.

Noteworthy, this section only collects “applications” in connection with verified OMS formation and does not refer to work which only claims OMS effects.

Post functionalization of OMS in MOFs

By definition, post-functionalization refers to a chemical modification of the MOF after its synthesis. We emphasize again that the structure of the MOF should be preserved upon functionalization, which needs to be verified *e.g.* by powder X-ray diffraction, FT-IR spectroscopy and gas sorption experiments after the reaction.[12]

The general and basic strategy found in the literature for post-functionalization of OMS is a ligand coordination to the OMS. This ligand coordination is also named “grafting”[98,269,270] in the literature. Also the term “amination” is used,[271,272] when an amine ligand is coordinated to the OMS. The term “extended hook”273 is found for bifunctional ligands, like ethylenediamine, where one end is anchored to the open metal sites on the framework and the other end is available as an additional functionality in the pore, for example to capture metal ions or clusters at the centers of the channels.[12,98,113,143,146,148,182,269–286]

Using post-functionalization *via* grafting a ligand to the open metal sites in MOFs can improve their performance in various applications, for example increase the gas uptake or catalytic activity. It should be evident that the quantification of the amount of grafted ligands to OMS is essential and can be carried out, for example, by MOF digestion and NMR analysis.

We note that the post-functionalization by ligand-coordination or -grafting to metal sites does not necessarily need to proceed *via* a proven or prepared OMS intermediate. A simple ligand exchange where the solvent–ligand at the metal atom in the MOF framework is replaced by the new (functional) ligand will also achieve this type of post-functionalization. If this ligand exchange proceeds through a more dissociative mechanism, that is, by the existing ligand dissociating first, then OMS will be a short-lived intermediate. However, ligand replacement in coordination chemistry can also occur *via* an associate mechanism through expansion of the coordination number.

In this section we will only discuss post-functionalization by ligand-coordination or -grafting which occurred *via* a verified OMS intermediate.

Post-functionalization of open Cr^{3+} sites

Kim *et al.*[143] reported on the post-functionalized MIL-101(Cr) compounds, CMIL-1 and CMIL-2, where the chiral pyridyl modified organocatalytic L-proline ligands L1 [(*S*)-*N*-(pyridin--3-yl)-pyrrolidine-2-carboxamide] and L2 [(*S*)-*N*-(pyridin-4-yl)-pyrrolidine-2-carboxamide] were coordinated to the open Cr^{3+} sites. The CMIL compounds showed catalytic activities in asymmetric aldol reactions and by comparison with the chiral ligands alone a much higher enantioselectivity. For the post-functionalization, the activated MOF and the new ligand were mixed together in anhydrous chloroform and refluxed under N_2 atmosphere for 24 h. The structure of MIL-101(Cr) did not change after grafting with the chiral ligands based on PXRD. The success of the grafting was based on FT-IR spectroscopy which showed characteristic bands of C=O at 1558 and 1695 cm^{-1}, and N–H stretching bands at 3189 and 3220 cm^{-1}, and on elemental analysis which suggested that ~1.8 chiral ligands per formula unit were incorporated inside the pores of CMILs. The BET surface area decreased from 3850 (for MIL-101(Cr)) to 1420 (for CMIL-1) and to 1375 $m^2\ g^{-1}$ (for CMIL-2), due to the incorporation of the organic molecules inside the pores.143 Along the same lines, Ren *et al.*[113] grafted the chiral pyridyl modified L-proline derivative [(*S*)-1-formyl-*N*-(pyridin-3-yl)pyrrolidine-2-carboxamide] to the open Cr^{3+} sites of the MIL-101(Cr) framework. They used the same methods as Kim *et al.*,[143] to check the successful introduction of the ligand. The elemental analysis results indicated that 1.45 chiral ligands per formula unit are incorporated inside the pores of CMIL-101 and the BET surface area decreased from 2963 to 1258 $m^2\ g^{-1}$, due to of the immobilization of organic molecules inside the pores (Fig. 32).[113]

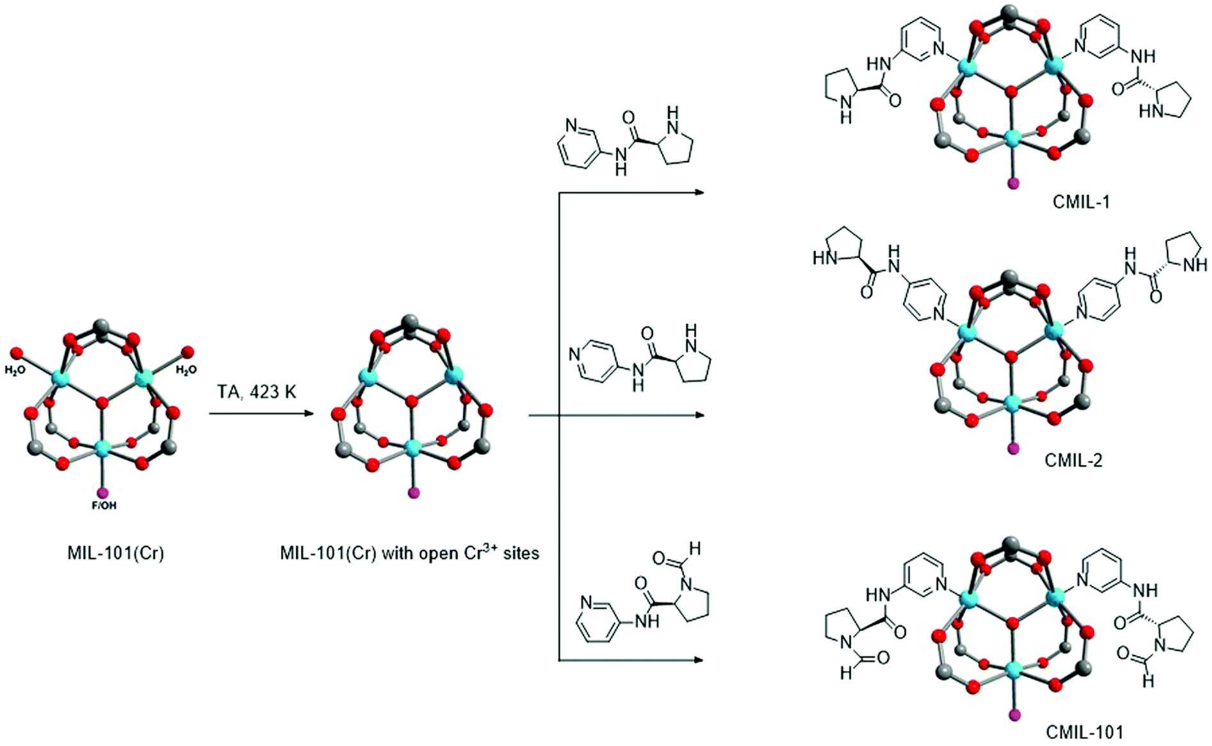

Fig. 32 Activation and post-modification with chiral ligands of MIL-101(Cr). Crystal structure information from ref. 149 (CSD-Refcode CIGXIA). Adapted from ref. 113 with permission of Elsevier BV., copyright 2017 and from ref. 143 with permission from the American Chemical Society, copyright 2009.

Furthermore, Jhung *et al.*[269] reported on MIL-101(Cr) with or without modification for the adsorptive removal of the artificial sweeteners saccharin, acesulfame and cyclamate. For the post-modification of MIL-101(Cr), the activated MIL and melamine or urea was mixed together in toluene solvent and refluxed for 12 hours. Under these conditions and low basicity, the amino groups of melamine or urea were grafted onto the open Cr^{3+} sites. FT-IR spectroscopy showed characteristic bands of N–H bending, C–N stretching, and N–H wagging at 1608 and 1265/1211 cm^{-1}, and 707 cm^{-1} and the BET surface area decreased from 3030 (for MIL-101(Cr)) to 1970 (for urea MIL-101) and to 1350 $m^2\ g^{-1}$ (for melamine MIL-101), indicating the successful introduction of urea and melamine into MIL-101(Cr). It must be noted that the study did not quantify the amount of grafting.[269]

Moreover, Janiak *et al.*[138] grafted several glycols ethylene glycols and ethylenediamine onto MIL-100(Cr) and quantified the amount of grafting, by using solution NMR spectroscopy. The ^{1}H-NMR spectra showed signals of the deprotonated and deuterium exchanged ligand $C_6H_3(COO^-)_3$, (btc^{3-}) and the grafted reagents (Fig. 33) and the integration gave ranges of grafted glycols and amine in MIL-100(Cr) from 1.28 to 1.88 molar equivalents for each $[Cr_3(\mu_3\text{-}O)(F,OH)(btc)_2]$ formula unit.[138]

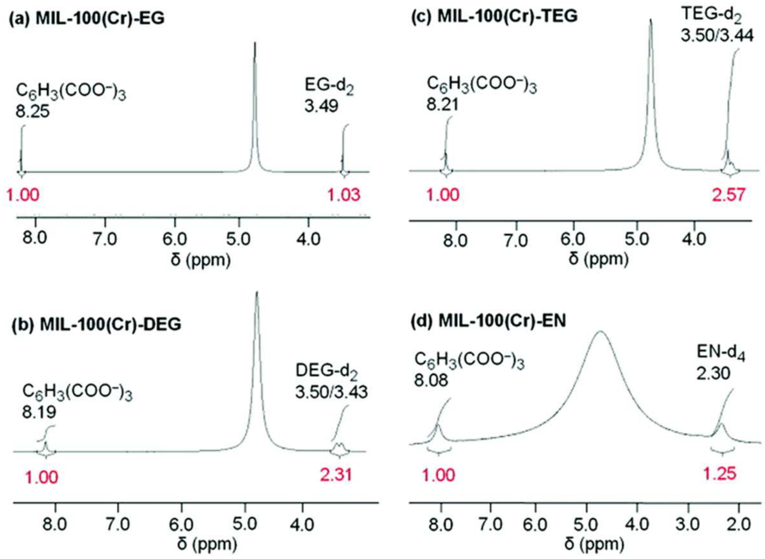

Fig. 33 ^{1}H NMR spectra (200 MHz) of modified MIL-101(Cr) after dissolution in D_2O/NaOD (EG = ethylene glycol, DEG = diethylene glycol, TEG = triethylene glycol, EN = ethylenediamine). Reproduced from ref. 138 with permission of Elsevier BV., copyright 2015.

Post-functionalization of open Cu^{2+} sites

Liu *et al.*[98] reported on the grafting with pyridyl-salicylimine (Py-SI) to open metal sites in Cu-bdc MOF MOF-2 by stirring the ligand and activated Cu-bdc in dry toluene. Afterwards, a solution of $PdCl_2$, toluene and DMF was added to Cu-bdc/Py-SI to obtain a Pd@Cu-bdc/Py-SI catalyst for Suzuki coupling (Fig. 34).

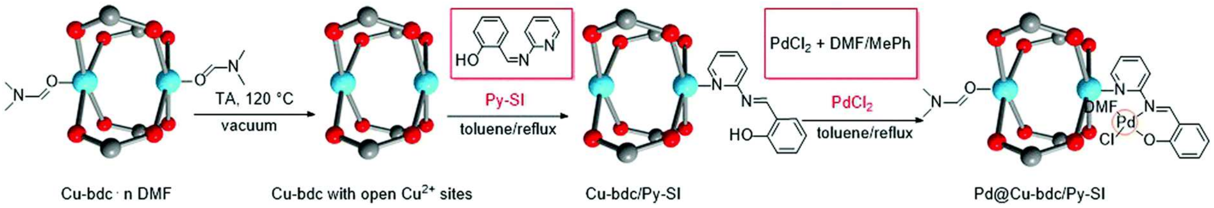

Fig. 34 Activation and grafting of $[Cu_2(bdc)_2(DMF)_2]$ with pyridyl-salicylimine (Py-SI). Crystal structure information from ref. 128 (CSD-Refcode DIHVIB01). Adapted from ref. 98 with permission of Elsevier Inc., copyright 2016.

They based the successful grafting on SEM-EDX quantification of Cl, Pd, and N. To enhance the CO_2 capture in $H_3[(Cu_4Cl)_3(bttri)_8]$ Long *et al.*[278] grafted *N,N'*-dimethylethylenediamine (mmen) to the Cu sites to yield $H_3[(Cu_4Cl)_3(bttri)_8(mmen)_{12}]$.[287,288] However, half of the Cu-OMS were not grafted at all, as the grafting was successful only at the large pores. The grafted material did not collapse and retained the original structure according to PXRD. From N_2 sorption measurement the BET surface area decreased from 1770 $m^2\ g^{-1}$ to 870 $m^2\ g^{-1}$.[278] Rosseinsky *et al.*[274] described the binding of secondary amines to the coordination sites on the

Cu^{2+} paddle-wheel MOF HKUST-1. The modified HKUST-1 was then exposed to NO to form a coordinated *N*-diazenium diolates (NONOates).[274]

Gas sorption

Gas adsorption, including harmful gases is an issue of constant interest in MOF chemistry.[79,289] The amount and affinity of the adsorbed gas depends on adsorbent (MOF) binding sites, surface area, porosity, temperature, pressure and the polarity of the adsorbate (gas).290 MOFs have been widely studied with respect to the selective adsorption and separation of gases such as H_2, CO_2, CO, NO, C_2H_2, CH_4 and SO_2.[291,292] Open metal sites and large surface area in MOFs are two important parameters for adsorption capacity and efficiency. Stable MOFs with accessible open metal sites have a higher gas affinity and binding energy compared to the same MOF without OMS.[293] The somewhat higher porosity of OMS-MOFs also leads to a higher gas uptake. Gas adsorption to OMS is typically reflected in a steeper rise of the adsorption isotherm and a higher (negative) heat of adsorption (Q^0_{st}) at low loading compared to the same non-OMS MOF.[220] Such a steep rise and high Q^0_{st} reflects the affinity, that is preferential binding of the gas molecules to the free metal site. We note that the comparison of adsorption capacity or gas uptake values at $p/p_0 = 1$ or 1 bar absolute pressure is less meaningful since these values are largely determined by pore volume.[67,251]

In connection with gas sorption studies on OMS-MOFs, experimental high-resolution[70,155]/powder neutron diffraction[70,159,228,294–296] studies, synchrotron X-ray diffraction analysis[155,178,297,298] and near sites edge X-ray adsorption fine structure (NEXAFS)[299] spectroscopy were performed to obtain structural information of MOFs with OMS and to derive insight into the role of the OMS on the MOF–adsorbate interactions.[300]

One must admit that single crystal X-ray studies which require sizeable and good quality single crystals are seldom available for OMS-MOFs with adsorbates (see below for examples). We note that often MOF structures, *e.g.*, for HKUST-1, are reported with no solvent–ligand at the metal atom. Usually, the electron density which is associated with this solvent ligand then has not been refined or has been removed by the Squeeze option in the refinement procedure.[301-303] The knowledge about the interaction and dynamics between the OMS and adsorbate molecules is crucial for the design of frameworks with efficient gas capture possibilities. However, it is evident that in order to study OMS–adsorbate interactions by experimental structure methods, a fully activated sample without remaining coordinated solvent ligands on the metal atom is highly advantageous to induce and have only the adsorbate bound to the metal atoms.[155]

H_2 adsorption

In the early but superseded realm of hydrogen storage in MOFs metal–organic frameworks with open metal sites were seen as an important class for hydrogen sorption. The X-ray and neutron diffraction studies showed that OMS are the understandable primary location for adsorbed H_2 molecules. For OMS only the low pressure H_2 adsorption is relevant. Due to the good hydrogen affinity, they can slightly increase the H_2 uptake capacity and improve the isosteric heat of adsorption at low coverage (Q^0_{st}). However, due to the still relatively weak interactions with H_2, MOFs were not able not meet the gravimetric and volumetric storage targets.[86–88,91,304–306]

The most investigated series of metal–organic frameworks is the M-MOF-74 family consisting of, *e.g.*, [M_2(*p*-dobdc)], [M_2(*m*-dobdc)], [M_2(dobpdc)], and [M_2(olz)], which possess a high concentration of OMS, which can interact more strongly with the H_2 molecules. The isosteric heats of H_2 adsorption in [M_2(*p*-dobdc)] (M = Mg^{2+}, Mn^{2+}, Fe^{2+}, Co^{2+}, Ni^{2+}, Cu^{2+}, Zn^{2+}) indicated initial stronger binding sites and lower enthalpies of adsorption upon increasing adsorption. From the quantitative assessment of H_2 uptake a change in adsorption isotherm shape occurs upon reaching approx. one equivalent of H_2 per metal site. The isosteric heat dropped from about 8–13 kJ mol^{-1} (depending on the metal, see Fig. 35) to a lower value of about 5– 6 kJ mol^{-1} after saturation of the stronger binding sites at a loading of ~0.8 molecule H_2 per metal.[88,89,91,307–309]

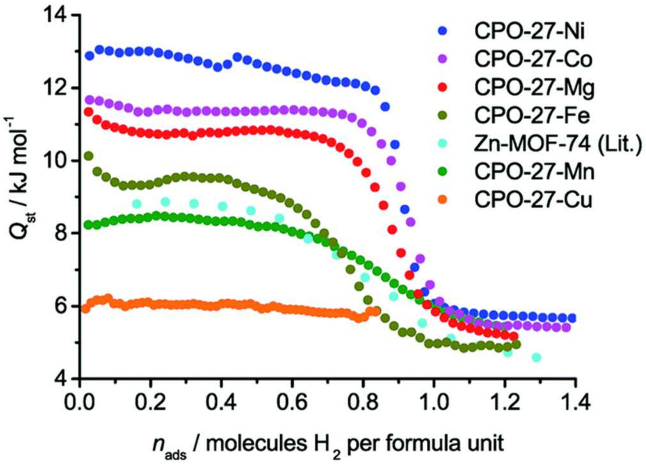

Fig. 35 Maximum H_2 isosteric heat of adsorption ($Q_{st,max}$) curves for M-MOF-74 (M = Mg, Mn, Fe, Co, Ni, Cu, Zn) (denoted in the figure as M-CPO-27). For M-MOF-74 a formula unit of [M(C4HO3)] was used here. Reproduced from ref. 89 with permission from The Royal Society of Chemistry, copyright 2015.

It can be noted that conversely the loading of ~0.8mol H_2 per mol metal may represent a quantification of the amount of formed OMS if the alternative of missing-metal defects or pore blocking can be excluded. Based on neutron diffraction the presence of primary strong H_2/D_2 binding sites and several additional weaker binding sites was elucidated for M-MOF-74.

Neutron diffraction studies with M-MOF-74 revealed metal-to-D_2 distances for the primary binding site of 2.20(1)–3.03 Å with $Ni^{2+} < Co^{2+} < Mg^{2+}$ o $Fe^{2+} < Zn^{2+} < Mn^{2+} < Cu^{2+}$ (Fig. 36).

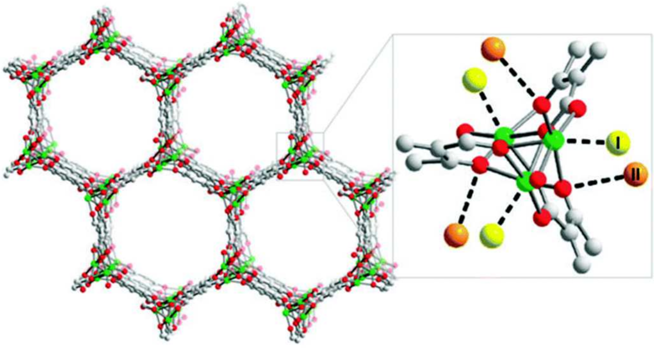

Fig. 36 View of the crystal structure of Mg-MOF-74 in the [001] direction. Atom color scheme: Mg green; C gray; O red. D_2 binding sites were determined by neutron diffraction: site I yellow; site II orange. Reproduced from ref. 308 with permission from The Royal Society of Chemistry, copyright 2011.

The metal-to-D_2 bond distances correlate with the adsorption enthalpies, with ordering as $Cu^{2+} < Mn^{2+} \sim Zn^{2+} < Fe^{2+} < Mg^{2+} < Co^{2+} < Ni^{2+}$.[307,308]

In isoreticular MOFs the Q^0_{st} ordering is $Mn^{2+} < Fe^{2+} < Co^{2+} < Ni^{2+}$ which is inversely proportional to the ionic radius of the metal ions which steadily drops from (high spin) Mn^{2+} to Ni^{2+} (Fig. 37).[88,310]

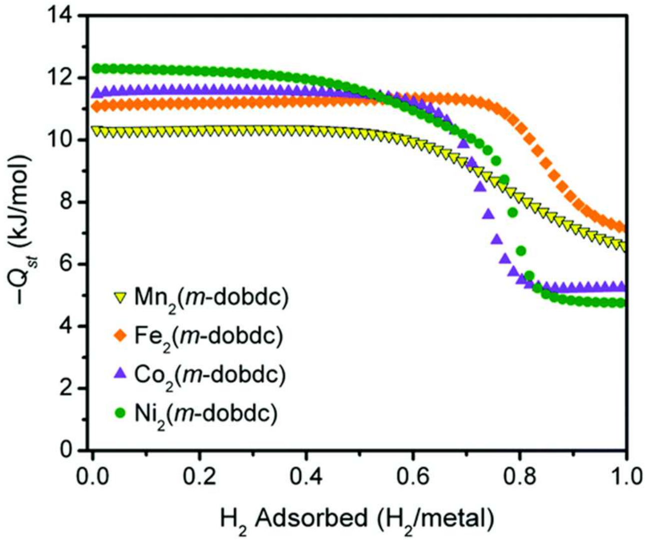

Fig. 37 H_2 isosteric heat of adsorption curves for [M_2(*m*-dobdc)] (M = Mn, Fe, Co, Ni). Reproduced from ref. 88 with permission from the American Chemical Society, copyright 2014.

As noted above for Fig. 35, the inflection points in Fig. 37 from ~0.75 H_2/M in [Co_2(*m*-dobdc)] to ~0.85 H_2/M in [Fe_2(*m*-dobdc)], may be interpretation as the fraction of OMS generated and available for H_2 binding. The inflection points are similar to the H_2-isosteric heat values for the M-MOF-74 series shown in Fig. 35.[88]

In case of [M_2(dobpdc)] the isosteric heat curve had the inflection point only for [Mn_2(dobpdc)] and [Co_2(dobpdc)] at an H_2 loading of one molecule per mol metal while for M = Mg^{2+}, Fe^{2+}, Ni^{2+}, Zn^{2+} the inflection point is at a lower loading than 1 eq. of H_2/M, as defects or intergrowth of crystallites may block some of the channels or the OMS are not quantitatively formed (Fig. 38).

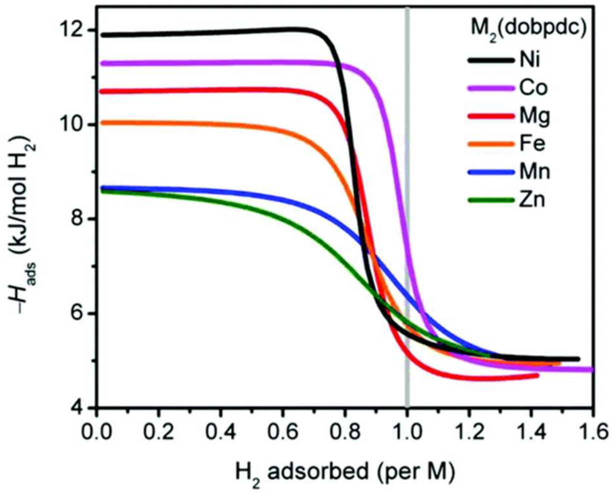

Fig. 38 H_2 isosteric heats of adsorption curves for [M_2(dobpdc)] (M = Mg, Mn, Fe, Co, Ni, Zn). Reproduced from ref. 309 with permission from the American Chemical Society, copyright 2016.

This can explain why Ni-MOF-74 displayed a higher H_2 uptake capacity at pressures up to approx. 300 mbar (at 77 K) than [Ni_2(dobpdc)]. While at the same time, [Ni_2(dobpdc)] showed a higher gravimetric density of OMS (6.42 *vs.* 5.16 mmol g^{-1}) and a higher low-coverage isosteric heat. Noteworthy also Zn^{2+} showed the lowest value, due to its $3d^{10}$ electron configuration.[309]

The charge density at the metal sites and thus the H_2 binding enthalpies could be enhanced by replacing the linker *p*-dobdc^{4-} with *m*-dobdc^{4-}, thereby going from the M-MOF-74 to [M_2(*m*-dobdc)] (M = Mn^2+, Fe^{2+}, Co^{2+}, Ni^{2+}) (Table 3). The stronger interaction between H_2 and the metal centers in the latter is evidenced by shorter M–H_2 contacts based on the results from powder neutron diffraction, inelastic spectroscopy and IR spectroscopy experiments.[88]

The MOFs, [M_2(olz)] (M = Mg^{2+}, Fe^{2+}, Co^{2+}, Ni^{2+}, olz^{2-} = olsalazinate), exhibit the same SBU and ligand coordinating functionality as [M_2(*p*-dobdc)].[310] The isosteric heats od adsorption values for [M_2(olz)] are very similar to [M_2(*m*-dobdc)] and [M_2(dobpdc)] (Fig. 39, left).[310]

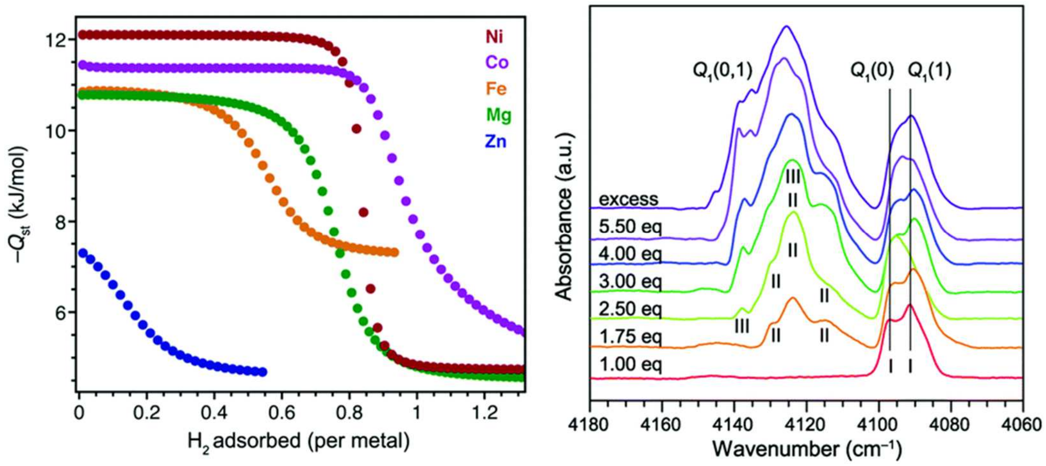

Fig. 39 Left: H_2 isosteric heat of adsorption curves for [M_2(olz)] (M = Mg, Fe, Co, Ni, Zn). Right: IR absorption of H_2 in [Mg_2(olz)] performed at 15 K. The equivalents (eq.) refer to the number of H_2 molecules per Mg^{2+}, and the spectral features corresponding to the distinct sites observed are denoted with Roman numerals. Q(0) refers to *para*-H_2 and Q(1) to *ortho*-H_2 modes. The IR spectra indicate that H_2 is adsorbed at multiple sites as a function of loading. Reproduced from ref. 310 with permission from the American Chemical Society, copyright 2016.

The inflection points in the isosteric heat plot of Fig. 39, left indicate the amount of available OMS. For [Co_2(olz)] the inflection point at 'H_2 adsorbed/metal' of about 1 shows near complete preceding activation and Co–OMS availability. The MOF [Ni_2(olz)] and [Mg_2(olz)] still have the inflection point at about 85% and 70% 'H_2 adsorbed/metal', respectively. A significant lower inflection point, *i.e.* OMS availability of about 0.6 'H_2 adsorbed/metal' is seen for [Fe_2(olz)], which was explained with the milder activation conditions employed for this compound. *In situ* IR spectroscopy was used to determine the nature of the [Mg_2/Ni_2(olz)] interaction with H_2. To follow the binding of H_2 at the OMS the characteristic red-shift of the H–H stretching frequency can be used. IR spectra (Fig. 39, right) showed a doublet (4097 and 4091 cm^{-1}) at a loading of one H_2 per metal. The authors described that these are the pure vibrational modes of ortho-H_2 and para-H_2 bound to the OMS for 1 eq. H_2/M.[310]

The curves of H_2 isosteric heats of adsorption *versus* the amount of H_2 adsorbed/metal in Fig. 35, 37, 38 and 39, left allow to estimate the amount of available OMS. Thereby it can be assumed that '/metal' means total molar metal amount based on the sample mass and idealized formula unit. The isosteric heat of adsorption of H_2 data can be obtained from low-pressure H_2 isotherms at two different temperatures, *e.g.* 77 and 87 K using the Clausius-Clapeyron relation.

The H_2 amount at which the isosteric heat decreases (the inflection point), can be taken as an indicator for the amount and the accessibility of the OMS. If the inflection point is at 'H_2 adsorbed/metal' ≈1 then the framework was probably fully activated and all OMS were accessible to H_2. If the inflection point in the isosteric heat curve is at 'H_2 adsorbed/metal' <1, then part of the OMS is not accessible to H_2. This could be due incomplete activation that is incomplete solvent removal or missing-metal (or other) defects or pore-blocking in the channels which renders the metal sites inaccessible to gas molecules.

M-btt (M = Cr^{2+}, Mn2+, Fe2+, Cu2+) was one of the first OMS MOF series which was studied for hydrogen storage (Table 3).[157–160,311] As noted above Fe-btt exhibits a higher isosteric heat of adsorption compared to Mn-btt, due to the smaller radius for Fe^{2+} (higher charge-to-radius ratio), giving a more polarizing binding site at the Fe ion.[309,311] Powder neutron diffraction of D2-loaded Cr-btt[159] suggested only moderately strong Cr^{2+}–D_2 interactions from the rather long Cr–D_2 distance. However, the isosteric heat at low coverage was higher for Cr-btt compared to $[Cr_3(btc)_2]$[135] (Table 3). $[Cr_3(btc)_2]$, with the same paddle-wheel SBU as HKUST-1. It was suggested that the Cr≣Cr quadropole bond decreases the Lewis acidity of the Cr^{2+} centers.[157-160,311]

Paddle-wheel MOFs, like HKUST-1, NOTT-X, PCN-10, -11 with OMS feature in general comparatively low Q^0_{st} values of less than –7 kJ mol^{-1} (Table 3). It should be noted that tor Cu^{2+} in HKUST-1 and related MOFs its Jahn–Teller effect provides no strong driving force for coordination of gas molecules at the Cu^{2+} site.[135]

Accordingly, the series of NOTT-X (X = 100–107) MOFs with the paddle-wheel SBU showed isosteric heats of adsorption at low coverage in the range of 5.20 to 6.70 kJ mol^{-1} (Table 3) and the enthalpy of H_2 binding is influenced by pore size and the presence of additional aromatic rings not the OMS.[312]

Still, the paddle-wheel OMS-MOFs have a higher hydrogen affinity at low pressures in comparison to MOFs without OMS. The isosteric heat of adsorption in HKUST-1 (– 4.5 kJ mol^{-1}, Table 3) is higher than in MOF-5 (–3.8 kJ mol^{-1}), due to the steep rise in the adsorption isotherm.[313]

In summary, open metal sites MOFs with M= Mg, Mn, Fe, Co, Ni are the most promising candidates for hydrogen sorption at low pressures, due to the higher enthalpy of adsorption of H_2 at these metal ions (isosteric heat of adsorption from about –10 to –13.5 kJ mol^{-1}). The isosteric heat of H_2 adsorption to the MOF pore wall is only around –3.8 kJ mol^{-1}.[313]

CO_2 adsorption

The interaction between CO_2 and OMS is generally more than 30 kJ mol^{-1}, giving a high CO_2 uptake at low relative pressure.[67,251,314] The binding affinity between the OMS and the CO_2 adsorbate is correlated with electrostatic interactions (CO_2 has a quadrupole moment).[315] The isostructural frameworks M-MOF-74 (M = Mg^{2+}, Mn^{2+}, Fe^{2+}, Co^{2+}, Ni^{2+}, Cu^{2+}, Zn^{2+}) have been extensively studied for their high performance in CO_2 storage.[52,70,316–319] Since these frameworks can be synthesized with different metals, they reflect both the role of each metal and the degree of Lewis acid interaction between the metal center and the CO_2 molecules. In particular, the presence of the stronger CO_2–OMS binding and a high density of OMS within the framework led to large CO_2 uptakes and makes this MOF group an interesting candidate for CO_2 adsorption.[52,97] Especially at low pressures (0.1–0.2 bar), which is the pressure region of interest in flue gas separation, these OMS-MOFs show high CO_2 uptakes.[55]

Kortrigh *et al*. applied 'near sites edge X-ray absorption fine structure' (NEXAFS) spectroscopy measurements at the Mg K-edge to study the interactions of Mg-MOF-74 with CO_2 molecules at open Mg^{2+} sites.[299] The authors associated the square pyramidal geometry at the open Mg^{2+} site with the appearance of a pre-edge peak in the Mg K-edge spectrum. A reduction in the intensity of this pre-edge feature, accompanied by a slight blue shift and an increase in intensity of the strongest major edge feature upon adsorption of CO_2, is interpreted as a recovery of the octahedral geometry around the Mg^{2+} cation with CO_2 coordination. This interpretation of the experimental results was supported with DFT calculations.[299]

Yildirim *et al*. showed by neutron powder diffraction measurements for the example of Mg-MOF-74, that the OMS in the M-MOF-74 series represent the primary adsorption sites.[228] Subsequently, the occupation of other CO_2 adsorption sites within the framework was later authenticated by neutron diffraction experiments and synchrotron X-ray diffraction measurements and was further supported by *in situ* ^{13}C NMR measurements.[70,178,294,320]

As is shown in Fig. 40 the CO_2 molecule assumes a bent end-on configuration when binding to metal atoms, as was detected for OMS in M-MOF-74 (Mg^{2+}, Mn^{2+}, Fe^{2+}, Co^{2+}, Cu^{2+}, Zn^{2+}) *via* powder neutron diffraction experiments.[70]

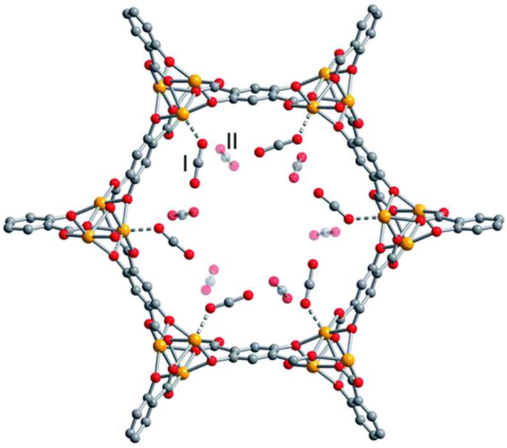

Fig. 40 View of a single channel in Fe-MOF-74 that is loaded with 1.5 CO_2 per iron(II) site. From the powder neutron diffraction data, there are two apparent CO_2 sites labelled as I and II in order of decreasing binding strength. Orange, grey, and red spheres represent Fe, C, and O atoms, respectively. Reproduced from ref. 70 with permission from The Royal Society of Chemistry, copyright 2014.

Moon *et al*. performed single-crystal X-ray diffraction experiments with CO_2 adsorbed single crystals of Mg-, Co- and Ni- MOF-74, to obtain insight into the CO_2 adsorption sites at the atomic level.[178] Also, two non-independent adsorption sites within the framework were found, which were assigned to the OMS (site A) and a secondary adsorption site between two OMS (site B) (Fig. 41).[178]

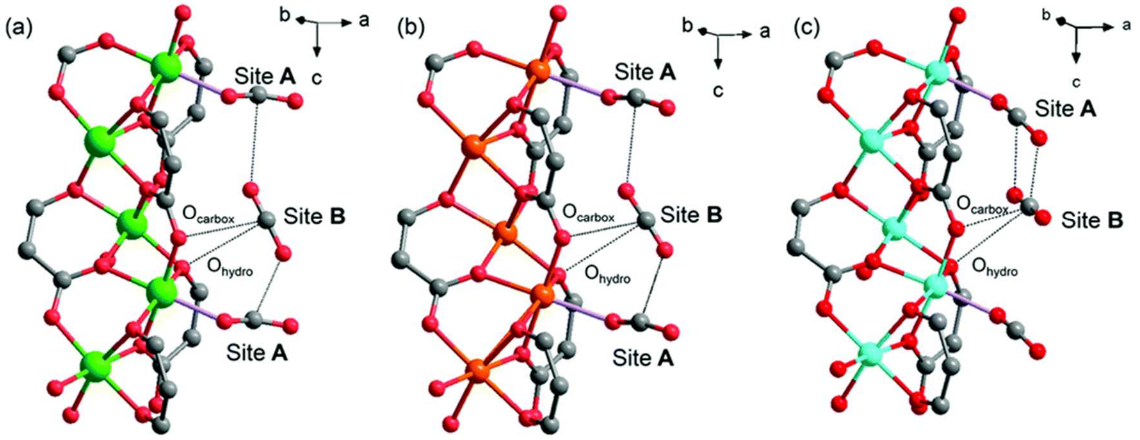

Fig. 41 Single-crystal X-ray structure of CO_2-adsorbed (a) Mg-MOF-74, (b) Co-MOF-74, and (c) Ni-MOF-74. Reproduced from ref. 178 with permission from the American Chemical Society, copyright 2019.

According to CO_2 adsorption isotherms at 298 K, the CO_2 capacity of Mg-, Co- and Ni-MOF-74 are 0.81, 1.30 and 1.67 mol mol^{-1}, respectively, at 0.1 bar.[178] The experimental obtained Q^0_{st} values for CO_2 at OMS in the M-MOF-74 series are in the range from –39.0 to 47.0 kJ mol^{-1} for Mg^{2+} to –22.1 kJ mol^{-1} for Cu^{2+} following the order Mg^{2+} > Ni^{2+} > Co^{2+} ~ Fe^{2+} > Mn^{2+} > Zn^{2+} > Cu^{2+}.[52,70,71,222,297]

Adsorption of CO_2 at the OMS should also be reflected in the observation of an M–O(CO_2) 'bond' distance. Findings from single-crystal X-ray diffraction revealed short M–O(CO_2) bond distances, (Mg^{2+}–O(CO_2), 2.13(2) Å; Co^{2+}–O(CO_2), 2.27(2) Å; Ni^{2+}–O(CO_2), 2.08(6) Å), indicating the strong affinity for CO_2 molecules.[178] Single-crystal X-ray diffraction data for Mg- and Co-MOF-74 show interactions, of each O(CO_2) atom in site B with the C(CO_2) atom in site A, resulting in a T-shaped arrangement of adjacent CO_2 molecules (Fig. 41a and b). For the CO_2 molecule adsorbed on Ni-MOf-74, a slipped-parallel geometry was indicated (Fig. 41c).[178]

The values for the M–O(CO_2) distances determined *via* high-resolution powder neutron diffraction experiments were Mg^{2+}–O(CO_2), 2.27(1) Å; Co^{2+}–O(CO_2), 2.23(9) Å; Ni^{2+}–O(CO_2), 2.29(3) Å (taken at a temperature of 10 K) and differ only slightly from the single-crystal X-ray diffraction values.[70] The elongated M–O(CO_2) distances found for Mn^{2+} (2.51(3) Å), Cu^{2+} (2.86(3) Å) and Zn^{2+} (2.43(4) Å) analogues reflect their lower isosteric heats of adsorption. For Mn^{2+} this has been explained by its larger ionic radius.[70] It can be noted that for Cu^{2+} its Jahn-Teller effect together with an overall lower effective ionic charge of the Cu^{2+} ion provide no strong driving force for coordination of CO_2 molecule at the apical Cu^{2+} site in Cu-MOF-74.[297]

It has been shown that the adsorption capacity of CO_2 can vary depending on the metal species. Semilogarithmic plots of the adsorption isotherms depict a two-step adsorption, indicating a sequential occupation of the adsorption sites.[222,297,320,321] The first step at low loadings was assigned to the adsorption on the OMS (site A in Fig. 41).[297] Depending on the metal species, it occurs at increasing pressure in the order $Mg^{2+} < Ni^{2+} < Co^{2+} < Mn^{2+} < Zn^{2+} << Cu^{2+}$. At higher pressures the occupation of the secondary adsorption sites (site B in Fig. 41) occurs with the same metal order.[297]

A significantly lower Q^0_{st} value of –22.1 kJ mol^{-1} and a nearly linear uptake for CO_2 is evidence that there is no decisive preference for adsorbing CO_2 at the apical Cu^{2+} OMS or in the pores (Fig. 42).[70]

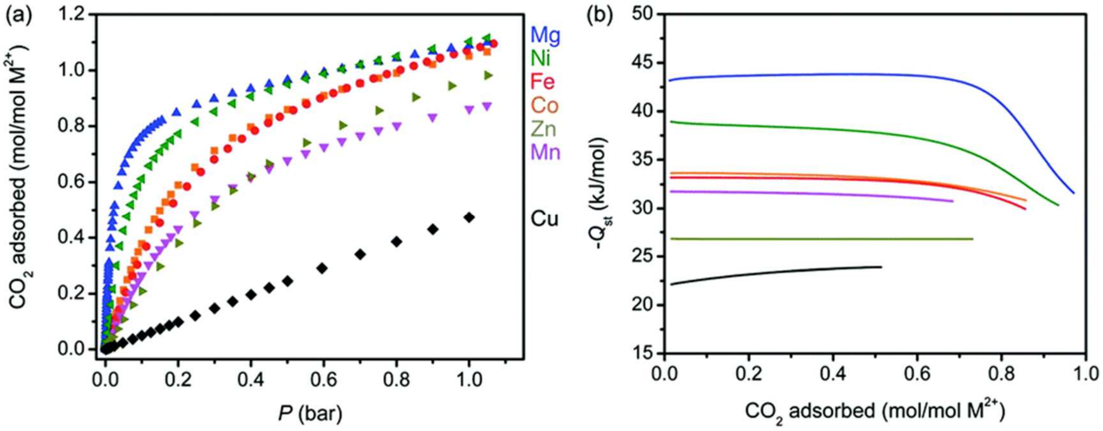

Fig. 42 Excess CO_2 adsorption isotherms for the M-MOF-74 series at 298 K. (b) Low coverage Q_{st} determined from CO_2 adsorption isotherms collected at 298, 308, and 318 K. Reproduced from ref. 70 with permission from The Royal Society of Chemistry, copyright 2014.

Further, the Cu–O–C(CO_2) angle was estimated to be 1211, while the M–O–C(CO_2) angles of the M-MOF-74 analogs are in the range of 145–1501.[297] The small bond angle for Cu-MOF-74 together with the weaker Cu–O interaction, indicates a strong influence of van der Waals interactions between CO_2 and the adjacent pore wall of the dobdc^{4-} ligand.

The structure and dynamics of CO_2 molecules adsorbed to OMS were also examined by IR spectroscopy for the M-MOF series.[322–325] Schmidt *et al*. observed *via* diffuse reflectance IR spectroscopy, that Mg-MOF-74 induces a blue shift in the asymmetric stretching vibration (v_3 mode) of CO_2 adsorbed at the metal site, while the transition metal analogues cause a redshift (Fig. 43).[322]

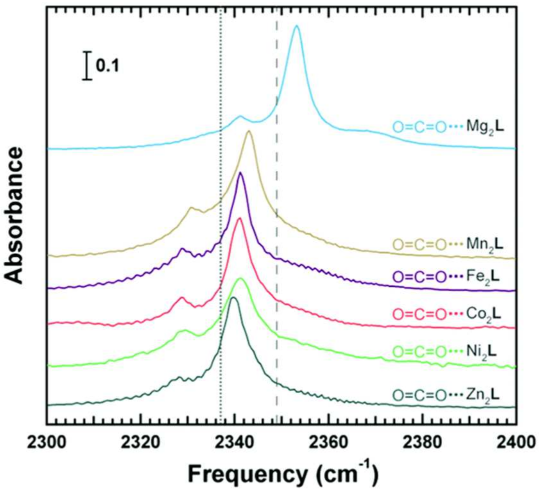

Fig. 43 Diffuse reflectance IR spectra of adsorbed CO_2 M-MOF-74 (M = Mg, Mn, Fe, Co, Zn) at 293 K. The dashed line at 2349 cm^{-1} marks the gas phase CO_2 v_3 frequency and the dotted line at 2337 cm^{-1} marks the much weaker band involving the n3 transition of CO_2 in the first excited v_2 level. Reproduced from ref. 322 with permission from the American Chemical Society, copyright 2015.

While the bonding to transitional metals occurs by electrostatic and charge transfer effects, the bonding to Mg^{2+} is almost exclusively due to electrostatic effects. Complete cancellation of contributions from the opposite local modes give rise to the observed frequency shift. This observation was explained by the absence of d-valence electrons in Mg^{2+}, so that no back bonding (electron donation to the CO_2 π* orbital) is possible.[322]

The dependency of the adsorption strength on the temperature in Mg-MOF-74 was investigated by Long *et al*.[326] Mg-MOF-74 shows an initial steep CO_2 uptake at low pressures which is characteristic for high CO_2 affinity. Huang *et al*. performed variable-temperature (VT) ^{17}O solid-state NMR spectroscopy (SSNMR) from 150 K to 403 K, to characterize the CO_2 adsorption capacity of MOFs as a function of the metal–CO_2 bond strength.[327] The authors stated that the CO_2 molecule is attached in a minimum energy configuration to the OMS, with a temperature-dependent angle Mg–O–C(CO_2) of ca. 120–130° (Fig. 44).

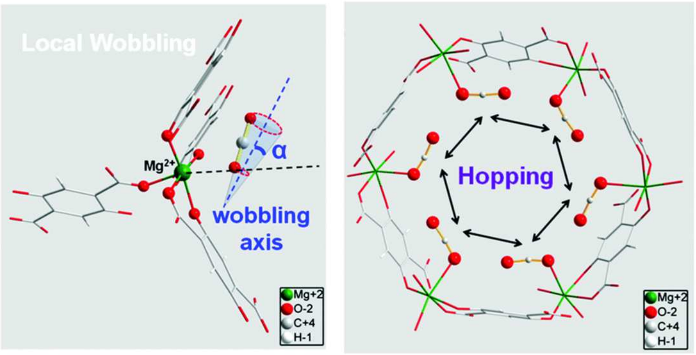

Fig. 44 Demonstration of the motion of adsorbed CO_2 molecules in Mg-MOF-74. For the adsorbed CO_2 two distinct motions were found: (left) localized wobbling, with precession of CO_2 around an angle a about the wobbling axis defined by its minimum energy configuration

with respect to Mg; and (right) nonlocalized 6-fold hopping of adsorbed CO_2 between OMS. Reproduced from ref. 327 with permission from the American Chemical Society, copyright 2014.

Variable temperature ^{17}O SSNMR line shapes were interpreted by a wobbling of CO_2 about its axis and a hopping between different adsorption sites (Fig. 44). A reduced mobility of the CO_2 molecules at low temperatures leads to an increased interaction with the OMS and *vice versa*. With increasing temperature to about 403 K wobbling increases and remains in the fast motion regime (107 Hz), indicating that CO_2 moves through a larger space. On the other hand, the hopping angle decreases with increasing temperature, which was attributed to be a result of enhanced CO_2 motion along the length of the channels.

In HKUST-1 two primary adsorption sites were revealed by the Fourier difference maps.[228] One adsorption site is associated to the open Cu^{2+} site and the other is associated to "the small cage window site, where the CO_2 sits in the four triangular-shaped openings into the small octahedral cage." Neutron diffraction measurement on the CO_2 adsorption in HKUST-1, for two different CO_2 loadings (1.07 and 1.47 CO_2/Cu), revealed that most CO_2 molecules prefer to adsorb on the open Cu^{2+} sites at low CO_2 concentration. The preferred adsorption on the OMS was associated with the higher electrostatic interaction between the OMS and the CO_2 quadrupole moment compared to an otherwise near vdW interaction between the organic framework walls and CO_2. Only with increased CO_2 loading, adsorption on the center of the small octahedral cage and the corner of the large cuboctahedral cage, was observed.[228]

Nachtigall *et al*. calculated the heat of adsorption from the CO_2 adsorption isotherm at 303 K of approx. –29 kJ mol^{-1} at low coverage. A slightly increase of heat of adsorption to approx. – 32 kJ mol^{-1} was observed with higher loading (>8 mmol g^{-1}).[232]

Supported by DFT calculations, this behavior was explained as follows: The CO_2 molecules adsorb onto Cu^{2+} sites at low coverage. The adsorbed CO_2 molecules are tilted towards adjacent Cu^{2+} site, which leads to maximized lateral CO_2–CO_2 interactions. With increasing coverage (up to CO_2/Cu = 20 : 12, CO_2) the occupation takes place in the cage windows of small cages. Here, the CO_2 molecules in cage window sites are stabilized through lateral interactions with the CO_2 adsorbed at the Cu^{2+} site. At even higher coverages, CO_2 molecules adsorb in the center of small cages and in large cages. The increasing adsorption enthalpies which were found in the high-coverage regime, were attributed to lateral interactions between these molecules and those already adsorbed in Cu^{2+} sites and cage windows sites.[232]

For MIL-100(Cr), the isosteric heat of adsorption Q^0_{st} of –58 kJ mol^{-1} was calculated from CO_2 adsorption isotherms at 273, 298, and 323 K at low coverage.[328] Usually, the value for the heat of adsorption can be obtained from adsorption isotherms at two different temperatures by applying the Clausius–Clapeyron equation.[329] From variable-temperature infrared (VTIR) spectroscopy standard adsorption enthalpies for CO_2 can be obtained from analysis of IR spectra recorded over a temperature range while simultaneously measuring the equilibrium pressure inside a closed IR cell.[140] This study, revealed the following heats of adsorption for MIL-100(Cr) (–63 kJ mol^{-1}), MIL-100(V) (–54 kJ mol^{-1}) and MIL-100(Sc) (–48 kJ mol^{-1}).[140]

In comparison Férey *et al*. reported an adsorption enthalpy of –62 kJ mol^{-1} for MIL-100(Cr) from CO_2 adsorption isotherms coupled with microcalorimetric experiments, that is in good agreement with the value delivered form VTIR spectroscopy analysis.[251]

The asymmetric stretching vibration (v_3 mode) of free CO_2 (2349 cm^{-1}) remains essentially invariant upon adsorption of CO_2 in for MIL-100(Cr) (2349 cm^{-1}), MIL-100(V) (2348 cm^{-1}) and MIL-100(Sc) (2352 cm^{-1}).[140] However, Palomino *et al*. did not take the vibration of free CO_2 as a reference but the value of 2341 cm^{-1} for carbon dioxide confined in the pores of silicalite.[330] Relative to this value of 2341 cm^{-1} the above blue-shifted values near 2350 cm^{-1} were interpreted as being due to a CO_2 adsorption onto open Cr^{3+}, V^{3+} and Sc^{3+} sites.[140]

Also, Férey *et al*. associated the strong v_3-CO_2 band at 2351 cm^{-1} forMIL-100(Cr) after CO_2 adsorption with the formation of CO_2-coordinated species on the Lewis acid sites ($O{=}C{=}O\cdot\cdot\cdot Cr^{3+}$).[251] In addition, a weak band was observed at 1271 cm^{-1}, which is assigned to the 2v2 overtone in Fermi resonance with the v_1 mode near 1370 cm^{-1} and which is infrared-inactive for the free CO_2 molecule. It was also noted that CO_2 adsorption on MIL-100(Cr) with the aqua ligands still present on the Lewis acid sites did not exhibit the 2351 cm^{-1} band.[251]

Microcalorimetric experiments for MIL-100(Fe) were also performed, to investigate the energetics of interactions between iron sites and CO_2 during gravimetric measurements of adsorption.[142]

Here, the heat of adsorption of CO_2 for MIL-100(Fe), lies in the range of –25 kJ mol^{-1} and – 30 kJ mol^{-1}, for the sample (activated at 100 °C) where only Fe^{3+} sites are present and – 35 kJ mol^{-1} for the partially reduced sample (activated at 250 °C) where Fe^{3+}/Fe^{2+} are present (see solvent removal strategies).[142]

The most recent computational studies through a periodic quantum mechanical hybrid HF/DFT approach of MIL-100(M^{3+}) structures with Cr^{3+} and Fe^{3+}, revealed that Cr^{3+} interacts strongly with the CO_2 molecule showing a short Cr^{3+}–(CO_2) distance (2.35 Å).[331] This was explained by the high electrostatic potential and the role of partly occupied d-orbitals (Fig. 45).

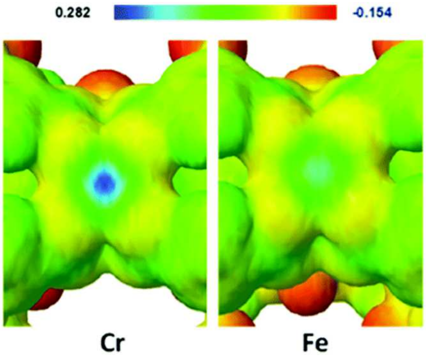

Fig. 45 Electrostatic potential of MIL-100 around the open Cr^{3+} and Fe^{3+} site. Reproduced from ref. 331 with permission from the American Chemical Society, copyright 2019.

In comparison Fe^{3+} shows a longer Fe–O(CO_2) distance (2.46 Å) and a smaller electrostatic potential thus leading to a weaker interaction energy.

Low-pressure adsorption isotherms on M-btt (M = Cr^{2+}, Mn^{2+}, Fe^{2+}, Cu^{2+}), at 298 K exhibit a steep initial rise, which is characteristic for the presence of highly polarizing adsorption sites (Fig. 46).[156]

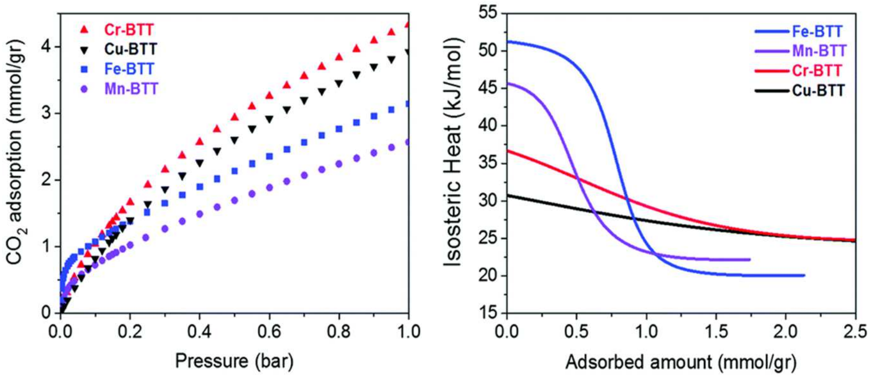

Fig. 46 Left: Excess CO_2 adsorption isotherms for M-btt (M = Cr^{2+}, Mn^{2+}, Fe^{2+}, Cu^{2+}) at 298 K. Right: Isosteric heats of adsorption, Q_{st}, plotted as a function of CO_2 loading. Reproduced from ref. 156 with permission from The Royal Society of Chemistry, copyright 2018.

The steepest rise in the adoption isotherm was observed for Fe-btt, indicating a stronger interaction with CO_2 in comparison to its analogues. The calculated isosteric heats of adsorption at zero coverage were in the range of –51.2 kJ mol^{-1} to –30.7 kJ mol^{-1}, following the order $Fe^{2+} > Mn^{2+} > Cr^{2+} > Cu^{2+}$. Queen *et al*. showed, that the M–CO_2 adsorption strength is reflected in the increase in the bond distance range from 2.36(3) Å for Fe-btt to 2.60(3) Å for Cu-btt.[156]

Also, structural investigations *via* high-resolution powder neutron diffraction experiments of M-btt reveal the expected preferred adsorption of the guest molecules on the OMS (Fig. 47).

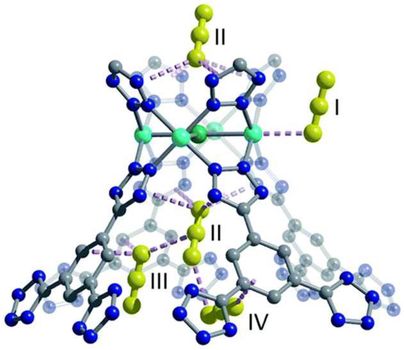

Fig. 47 View of the four different CO_2 adsorption sites within the MOFs Cu-btt as determined from Rietveld analysis of high-resolution powder neutron diffraction data. Cyan, grey, blue, and green spheres represent Cu, C, N, and Cl atoms, respectively, and yellow ball-and-stick models represent CO_2. Reproduced from ref. 156 with permission from The Royal Society of Chemistry, copyright 2018 (*cf*. to Fig. 27 for the adsorption sites identified by DFT calculations).

However, it was pointed out[156] that Mn-btt is not suitable for these *in situ* diffraction experiments, as 83% of the OMS remained coordinated by methanol solvent molecules after activation (based on a previous X-ray analysis).[160]

In [Cu_2(dmcapz)] a steep uptake of 2.3 mmol g^{-1} was investigated at lower pressure, corresponding to the adsorption of one molecule CO_2 at each dinuclear Cu_2 unit.[100]

Furthermore, it has been shown, that the Cu^{2+} paddle-wheel MOFs Cu-tdpat and Cu-Sp5, with both OMS and Lewis basic sites (LBS) within the linker, display an improved CO_2 adsorption capacity. The adsorption enthalpy at zero loading of –42.2 kJ mol^{-1} for Cu-tdpat and – 43.1 kJ mol^{-1} for Cu-Sp5 was calculated from the CO_2 sorption data.[332] Feng *et al*. noted that these higher than expected (see above) adsorption enthalpies for Cu-tdpat and Cu-Sp5 are not only caused by the interaction with the open Cu^{2+} site, but also influenced by further adsorption sites (LBS and phenyl rings) as was investigated with room-temperature IR absorption measurements.[333]

Zhu *et al*. found that in the framework of [Co_2(tzpa)(μ_3-OH)], the existence of accessible OMS, μ_3-OH groups, and uncoordinated carboxylate O sites, cause strong affinity towards CO_2.[181]

CO adsorption

MOFs with OMS have been proven to show a high heat of adsorption for CO at zero loading. In the literature the dipole moment of CO is sometimes invoked to explain the CO interaction with the metal at the OMS. We note however, that the dipole of CO is only 0.10 Debye with the negative end at the carbon atom. Instead and as can be expected from well-established metal-carbonyl chemistry, CO is an excellent ligand with strong covalent interaction to transition-metal atoms. When complete occupancy of the OMS has been achieved the dispersive forces between CO molecules and the organic pore walls of the network become effective. This leads to a decrease in the adsorption enthalpy. Based on the experimentally determined heat of adsorption for the M-MOF-74 series, it was found that the CO affinity for the OMS follows the order $Ni^{2+} > Co^{2+} \gg Mg^{2+} > Cu^{2+}$, indicating strong interaction of Ni^{2+} and Co^{2+} for CO molecules.[73,178]

The heat of adsorption values for CO in M-MOF-74 reflect the influence of the metal atom on the CO affinity. Moon *et al*. found the strongest affinity to CO for Ni^{2+}, reaching a Q^0_{st} value of –59.7 kJ mol^{-1}, followed by Co^{2+} with –55.5 kJ mol^{-1} and Mg^{2+} with a significantly lower value of –38.3 kJ mol^{-1} at 298 K (the lower value was explained due the lack of d-valence electrons in Mg^{2+} see above).[178] FT-IR analysis revealed stretching vibrations of CO bound to Co^{2+} at 2160 cm^{-1} and to Ni^{2+} at 2170 cm^{-1}, which compared with free CO at 2143 cm^{-1} would indicate only a σ-donor bond from CO to the metal with no metal-to-CO back-bonding. No CO vibration was observed for Mg-MOF-74.[178]

It is noted that in comparison to the valence band for free CO at 2143 cm^{-1} the above higher wavenumbers indicate an only very weak M-to-CO back bonding, due to the relatively high metal 2+ oxidation state. CO is known to prefer to bind to metal atoms in low oxidation state (0 or even negative) as in neutral metal carbonyls or negative carbonyl metallates.[23,24]

To obtain insight into the CO adsorption sites at the atomic level, Moon *et al*. performed Single-crystal X-ray diffraction experiments with CO-adsorbed single crystals of Mg-, Co- and Ni-MOF-74. The CO molecules were bound to unsaturated transition metal centers with Co^{2+}/Ni^{2+}–CO bond distances of 2.151(2) and 2.147(3) Å, respectively, as seen before in metal carbonyls. As expected the $Mg^{2+}\cdots CO$ distance for the nonclassical main-group metal-carbonyl bond is much longer with 2.420(2) Å. Additional adsorbed CO molecules (at site B) show only van der Waals interactions to the metal-bound CO molecules at site A (Fig. 48).[178]

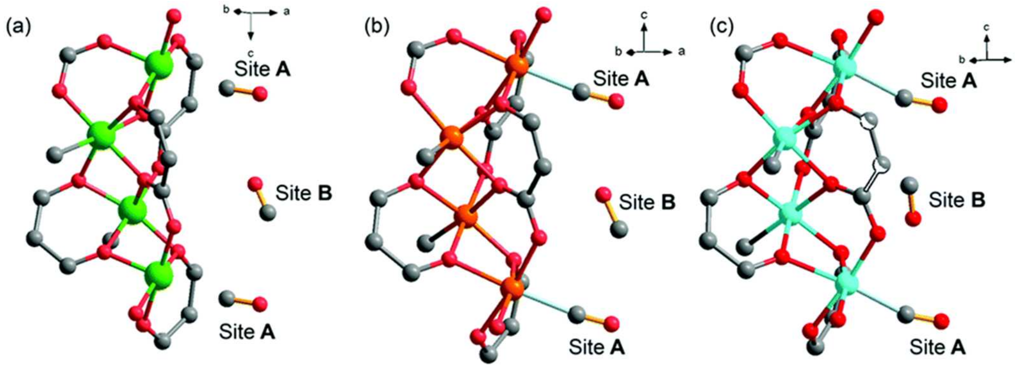

Fig. 48 Single-crystal X-ray crystal structure of CO-adsorbed (a) Mg-MOF-74, (b) Co-MOF-74, and (c) Ni-MOF-74. Reproduced from ref. 178 with permission from the American Chemical Society, copyright 2019.

For Cu-MOF-74, an even low adsorption enthalpy of approx. –20 kJ mol^{-1} was indicated by variable temperature IR experiments.[73] Georgiev *et al*. observed the formation of carbonyls with the participation of Cu^{2+} sites, by the appearance of intense IR bands at 2153–2149 cm^{-1}.

It was found that with low coverage, the carbonyl band dominates at 2153 cm^{-1}, which converts into a band at 2150 cm^{-1} with increased coverage. With further coverage increase, the band is additionally and gradually redshifted. We note that this comparatively high wavenumber for the CO vibrations suggests very weak interactions with the Cu^{2+} adsorption site. Further a band at 2136 cm^{-1} was referred to physically adsorbed CO. Also, a small fraction of the copper ions was found in the Cu^{+} state, indicated by the weak IR band at 2120 cm^{-1}. Indeed, this band is the only one with remarkable stability towards outgassing.

The authors assumed, that the relatively constant intensity of this band indicates that the respective Cu^{+} sites are formed on specific structures, most probably at the external MOF surface.[73]

Kitagawa *et al*. noted accordingly, that despite the presence of open Cu^{2+} sites in [Cu_2(dmcapz)], the CO adsorption at 195 K is negligible for this compound.[100]

Lueking *et al*. performed *in situ* FTIR measurements on the paddle-wheel MOFs HKUST-1 and Cu-tdpat. FITR spectroscopy was able to detect interaction between CO and Cu^{2+} sites in HKUST-1.[334] Here, in 0.34 bar CO at 150 K, the CO vibration was observed at 2169 cm^{-1}. It should be evident that the high wavenumber signals again a non-classical metal carbonyl with a weak $Cu^{2+}\cdot\cdot\cdot CO$ bond due to the non-existing π-back bonding (Fig. 49).

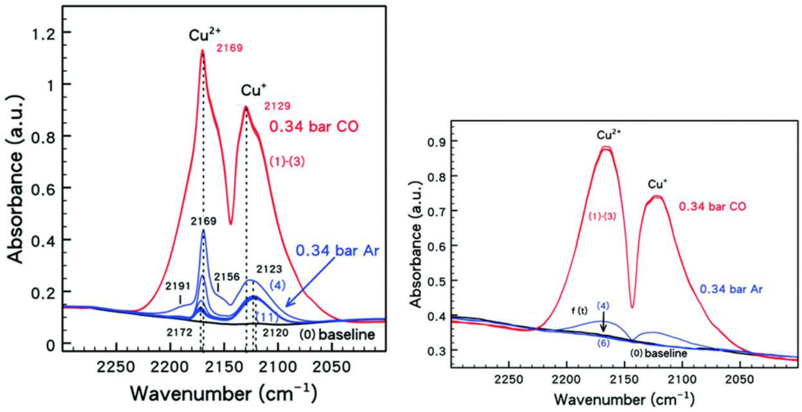

Fig. 49 Left: FTIR spectra of HKUST-1 at 150 K in 0.34 bar CO (1–3), and after 0.34 bar Ar purging to remove physisorbed CO (4–11). Right: FTIR spectra of Cu-tdpat at 150 K in excess CO exposure (1–3) and after Ar purging to remove gas phase CO (4–6). Reproduced from ref. 334 with permission from the Owner Societies, copyright 2015.

Furthermore, CO vibrations at 2120 cm^{-1} were found, which were assigned to interactions of CO with Cu^{+}. After Ar purging, broad shoulders at 2156 cm^{-1} and 2191 cm^{-1} disappeared as excess CO was removed, while modes at 2172 cm^{-1} and 2120 cm^{-1} remained in the spectra. Also, the blue-shift from 2169 cm^{-1} to 2172 cm^{-1} in the CO–Cu^{2+} mode with removal of gaseous CO was attributed to a decrease in the number of CO interacting with the Cu^{2+}.

At the same time, the CO spectra of Cu-tdpat revealed no remaining Cu-adsorption after Ar purging for CO removal, despite the similar axial Cu^{2+} adsorption site as in HKUST-1.

Further investigations *via* temperature programmed desorption (TPD) measurements, showed a virtually identical profile of CO adsorbed to Cu-tdpat and HKUST-1, suggesting that CO adsorbs more strongly to the open metal site. Also, it was found that the amount of CO adsorbed at the axial Cu^{2+} sites of Cu-tdpat exceeds that of HKUST-1 up to temperatures above 150 K.[334] Gumma *et al*. examined the effect of the CO polarity and the electrostatic CO-OMS interactions on CO-loading in MIL-101(Cr) and HKUST-1, from CO adsorption measurements.[335] Low-pressure CO adsorption at 283 K revealed a high adsorption enthalpy of -48.2 kJ mol^{-1} for MIL-101(Cr) at zero loading. Despite the presence of open Cu^{2+} sites in HKUST-1, a comparatively weaker adsorption enthalpy of -23.4 kJ mol^{-1} was found at similar loading. The adsorption enthalpy decreases at an increased loading of about 6 mmol g^{-1} to $- 17.4$ kJ mol^{-1}. The authors justified the higher adsorption enthalpy in MIl-101(Cr), with a stronger electrostatic contribution between Cr^{3+} and CO. The authors also suggested, that the Cu^{2+} cations in HKUST-1 are not fully accessible, because the coordinated solvent molecules from the synthesis were not completely removed.[335]

Férey *et al*. studied the interaction behavior of MIL-100(Fe) and CO in dependence of the activation conditions, (see above coordinated solvent removal strategies).[142] *In situ* IR spectroscopic analysis using CO as a probe allowed both the oxidation states of iron and the amount of OMS to be quantified. At room temperature, CO does not interact strongly with Fe^{3+} sites (weak band at 2190 cm^{-1}). An increase in the activation temperature leads to partial Fe^{3+} reduction to Fe^{2+} and to the appearance of two new bands at 2182 and 2173 cm^1 (that are still observed after desorption under vacuum). In the case, where only open Fe^{3+} sites are present the heat of adsorption is -39 kJ mol^{-1}. For the partially reduced sample, where both, open Fe^{2+} and Fe^{3+} sites are present the value of the heat of adsorption increases to about $- 51$ kJ mol^{-1}. IR measurements revealed, that the higher value confirms the slightly stronger interaction of Fe^{2+} cations with CO over that of Fe^{3+} cations. Here, the weak interaction between the Fe^{3+} cations and CO are coincident with the weak band at 2190 cm^{-1}. The appearance of two CO valence bands at 2182 and 2173 cm^1, was assigned to the adsorption on the open Fe^{2+}.[142]

NO adsorption

Open metal sites MOFs were applied for the specific nitric oxide (NO) adsorption and storage in view of the known good ligating properties of nitrosyl towards transition metal atoms. MOF have been investigated to store and to release NO, *e.g.* by exposure to water in connection to its pharmaceutical effect. NO is a biological signaling molecule, and is used *in vitro* and *in vivo* for anti-bacterial, anti-thrombotic and wound healing applications. MOFs are envisioned for the storage, delivery and biological activity of NO for these in healthcare applications. In part, this NO delivery is achieved on exposure of the MOF to moisture.[74,90]

The interaction of the NO with the open Cu^{2+} sites in HKUST-1 and with the Ni^{2+} and Co^{2+} sites in M-MOF-74 was reported by Morris *et al.*[90,336,337] They compared the NO sorption data of the three OMS-MOFs with MIL-53(Al/Cr) MOFs without OMS. Thereby, HKUST-1 (~3 mmol NO per g) and M-MOF-74 (M = Co, Ni; ~7 mmol NO per g) adsorbed high amounts of NO at RT in comparison to MIL-53 (<1 mmol g^{-1}). Moreover, the MOFs HKUST-1 and M-MOF-74 showed also large, and MIL-53 a small hysteresis on desorption of NO (Fig. 50).[90]

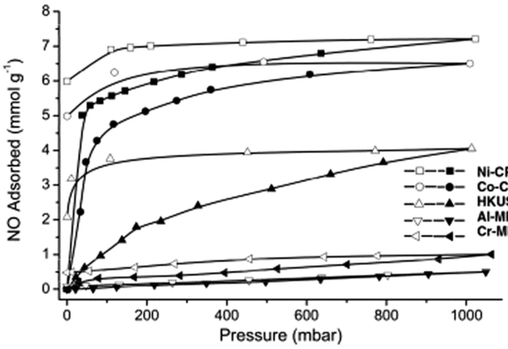

Fig. 50 The NO sorption isotherms of HKUST-1, M-MOF-74 (M = Ni, Co) (denoted in the figure as Ni/Co-CPO-27) and M-MIL-53 (M = Al; Cr) at RT. Reproduced from ref. 90 with permission of Elsevier Inc., copyright 2009.

The large hysteresis indicated the expected ligand binding of NO to OMS. HKUST-1 released only 1 µmol NO per g out of the ~3 mmol NO per g which underscore the NO chemisorption in this MOF. About 2.21 mmol g^{-1} is not desorbed when the NO pressure is reduced to almost zero.[90] This corresponds to ~1 NO per dicopper SBU in HKUST-1.[133,337]

In HKUST-1 Cu1+ sites can be formed *via* TA or photoreduction (see Section 2). The reduced open Cu^{1+} sites in HKUST-1 interact more strongly with NO in the presence of water, compared to the interaction of the higher oxidation state (Cu^{2+}) with NO.[338,339]

The nature of this Cu–NO interactions was investigated by XPS and NEXAFS with the latter showing a decrease of the intensity of the Cu^{1+} peak and an increase of the area of the Cu^{2+} peak with the introduction of NO (Fig. 51).

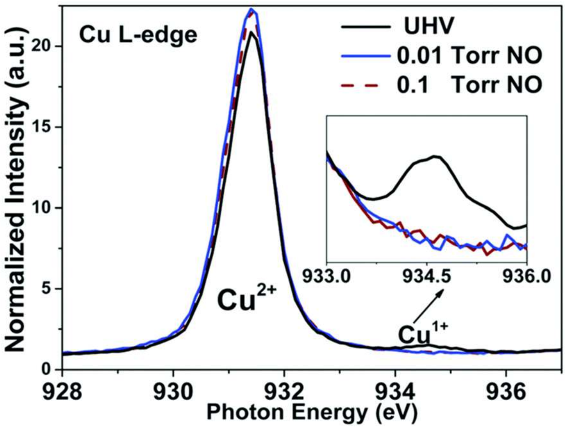

Fig. 51 Cu L-edge NEXAFS image in UHV and as a function of NO pressure in HKUST-1. Reproduced from ref. 338 with permission from The Royal Society of Chemistry, copyright 2014.

This suggest that Cu^{1+} was oxidized by NO to form Cu^{2+}–NO^{-}. The reformed Cu^{2+} centers are then different (due to the bound NO) than the pristine Cu^{2+} in HKUST-1.[338,339] Zn-MOF-74[340] adsorbed approx. 5 mmol NO per g.[336] Hartmann and his co-workers341 investigated the spectroscopic properties of NO adsorbed in M-MOF-74 (M = Co^{2+}, Ni^{2+}), by using low-temperature electron paramagnetic resonance (EPR) and IR spectroscopy. IR spectra showed the stretching frequency of NO (1878 cm^{-1} for free NO) for Ni-NO at 1838 cm^{-1} and for Co–NO adducts at 1797 cm^{-1}. These two bands were retained upon desorption at RT due to the good ligating action of NO with Co and Ni, again as expected from the good ligating action of NO towards transition metals.[341]

C_2H_2 sorption

Safe and efficient storage and separation of acetylene (C_2H_2) is a major challenge. Since highly reactive acetylenes explode at room temperature above a pressure of 2 atm, the industrial focus is on the development of low-pressure acetylene storage and separation methods.[342] MOFs provide an alternative solution for storing and depositing C_2H_2 at low pressures.[343] Especially MOFs with OMS could make an important contribution to C_2H_2 storage technology.[261,262,344–351]

OMS–MOFs show high values for the isosteric heats of adsorption for C_2H_2, from approx. – 30.4 to –39.0 kJ mol^{-1} for HKUST-1, –41.0 kJ mol^{-1} for Mg-MOF-74, –45.0 kJ mol^{-1} for Co-MOF-74 to –45.0 to –46.5 kJ mol^{-1} for Fe-MOF-74 with the highest Q^0_{st} value.[209,261,262,351] Comparatively, the C_2H_2 adsorption enthalpies for MOFs without OMS such as MIL-53, MOF-5 and ZIF-8 are in the range of approx. –13 to –20 kJ mol^{-1}.[262]

Compared to non-OMS MOFs, Chen *et al*. attributed the Q^0_{st} value for HKUST-1 to the interaction of the Cu^{2+}–OMS with C_2H_2. The authors established the preferred interaction site between deuterated acetylene molecules and Cu^{2+} by neutron powder diffraction studies.

Rietveld refinement of the neutron diffraction data revealed, that at a 0.62 C_2D_2 per Cu loading acetylene is adsorbed entirely at an open Cu^{2+} site. A linear orientation of the C_2H_2 molecule parallel to the O–Cu–O axis was found, with a Cu–C bonding distance of 2.62 Å. Adsorption at the entrance window of a small cage (cage window site), was found at an increased loading of 1.5 C_2D_2 per Cu. The authors concluded that these primary and secondary adsorption sites together cause the relatively high acetylene uptake of 201 $cm^3\ g^{-1}$ C_2H_2 for HKUST-1 at RT and 1 atm.[262]

CH_4 adsorption

CH_4 has technical relevance as the main component of natural gas. Increasing the storage capacity in a given volume or at a given pressure by adsorption in a (cheap and stable) porous material would be highly attractive. Referring to this, MOFs have been extensively studied and have been proven to be promising materials for methane storage.[352–357] A promising approach to increase the methane storage capacity was seen in the design of MOFs with suitable pore sizes and a high density of open metal sites, which can more strongly interact with CH_4 than the organic pore walls.[358–360]

In previous studies authors claim an influence of OMS in connection with increased adsorption capacity of CH_4.[361] Within the M-MOF-74 series, it was found that Ni-MOF-74 exhibits the highest Q^0_{st} at low CH_4 loading and adsorbs the largest amount of CH_4. According to neutron diffraction experiments, the OMS were identified as primary CH4 adsorption sites (Fig. 52).[294] Physisorption of CH4 on the OMS in Mg-MOF-74, was confirmed using neutron diffraction experiments with the experimental Mg· · ·C distance of 3.4 Å. This distance is only slightly smaller than the experimental C· · ·C distance of 3.45 Å for CH_4 adsorbed on a graphite surface. In Mg-MOF-74 the neighboring methane molecules on sites I and II have a C· · ·C distance of ~3.73 Å, only slightly smaller than that in solid methane, suggesting that the adsorbed CH_4 molecules on site II has similar weak interactions with both the framework (mainly the C and O atoms on the organic linker) and the CH_4 molecules on site I (Fig. 52).[294]

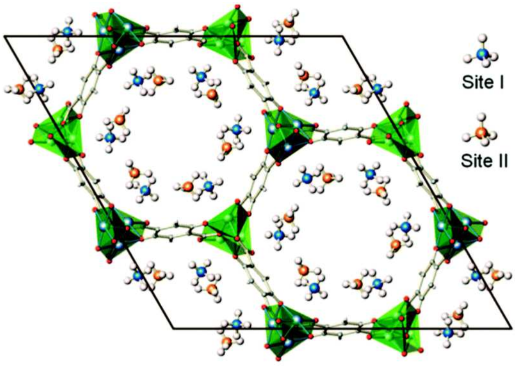

Fig. 52 Projection of the unit cell of Mg-MOF-74 with CH_4 adsorbed on site I and site II, as determined from neutron diffraction. Note that each metal ion is in contact to one methane

molecule. Reproduced from ref. 294 with permission from the American Chemical Society, copyright 2009.

However, also in this work, the heats of adsorption for M-MOF-74 (Mg^{2+}, Mn^{2+}, Co^{2+}, Ni^{2+}, Zn^{2+}), delivered from CH_4 adsorption isotherms (at 270, 280, and 298 K), are in the range of approx. -18.3 kJ mol^{-1} to -20.2 kJ mol^{-1}, with little variation with the metal and no variation with CH_4 loading (Fig. 53, left).[294]

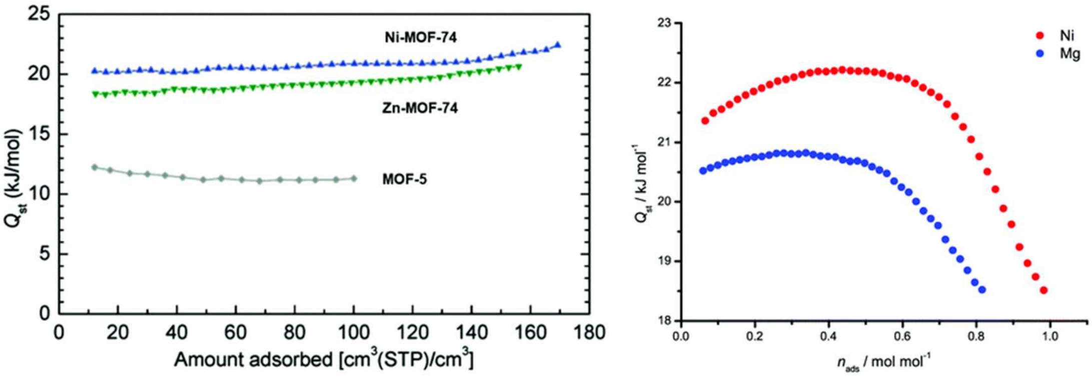

Fig. 53 Left: The experimental Q_{st} of Ni-MOF-74 and Zn-MOF-74, delivered from CH_4 adsorption isotherms at 270, 280, and 298 K. The Q_{st} of Mg-MOF-74, Mn-MOF-74, and Co-MOF-74 fall between the two curves and, thus, are not shown for clarity. The Q_{st} of MOF-5 are plotted for comparison. Reproduced from ref. 294 with permission from the American Chemical Society, copyright 2009. Right: Isosteric heat of adsorption of CH_4 in Ni-MOF-74 (red) and Mg-MOF-74 (blue) as a function of loading, calculated from the isotherms at 179 and 283 K. Reproduced from ref. 321 with permission from The Royal Society of Chemistry, copyright 2009.

It must be noted that the absence of higher Q^0_{st} values at low loading speaks against an effect or significant interaction with OMS.

At the same time, the authors added, that in the case of methane, the M· · ·C distance is largely constrained by the CH_4 geometry (a steric effect) and thus varies very little among different metals. This makes the CH_4 binding strength nearly independent of the open metal species. Therefore, we conclude that different from other adsorbates with dipole or quadrupole moment, CH_4 interacts only very weakly with OMS and not much stronger than with the organic pore walls.

Different to the finding of Yildirim *et al*., where the methane heat of adsorption was almost constant for the whole loading range, Blom *et al*. highlighted a decrease from -20 to -22 kJ mol^{-1} to approx. -18.5 kJ mol^{-1} upon full occupancy for both Ni-MOF-74 and Mg-MOF-74 (Fig. 53, right). The heat of adsorption was calculated from the isotherms at 179 K and 283 K.[321]

Zhou *et al*. predicted for the paddle-wheel MOFs, HKUST-1, PCN-11 and PCN-14, that direct binding of a methane molecule to any Cu^{2+} site should be possible at room temperature and

35 bar, but this would then represent only a fraction of the total storage capacity in these MOFs.[358] The adsorption enthalpy for UTSA-20 from CH_4 adsorption isotherms at 200 K, 240 K, 270 K, and 300 K, was calculated to be –17.7 kJ mol^{-1} at zero coverage.[360] We note that it was not elucidated further if OMS had an influence on the heat of adsorption and if the heat of adsorption decreased after OMS coverage. The experimental determined heats of adsorption of –17.1(5) kJ mol^{-1} for HKUST-1 and –17.5(5) kJ mol^{-1} for $[Cr_3(btc)_2]$, from CH_4 adsorption isotherms at room temperature and 35 bar are in a similar range.[264] In this experimental work, Brown *et al*. found for $[M_3(btc)_2]$ (M = Cu^{2+}, Cr^{2+}), that at CD_4 loadings of 0.4, 0.7, the primary adsorption sites are around and within the small octahedral cage of the network and these adsorptions sites are favored over the open Cu^{2+} and Cr^{2+} sites, as assessed by situ neutron powder diffraction measurements. Additional nuclear density in the octahedral cages and at the OMS was discovered, both for HKUST-1 and for $[Cr_3(btc)_2]$ at an increased loading (1.5 CD_4 per metal atom).[264]

SO_2 adsorption

Sulfur dioxide (SO_2) is an acidic and toxic gas in the atmosphere, which originates from both natural and anthropogenic source. The burning of fossil fuels and industrial processes contribute to the anthropogenic emissions. Although flue gas desulfurization (FGD) is in large parts (85–95%) carried out with established lime-stone absorption,[362,363] up to 150–450 ppm of residual SO_2 are emitted to the atmosphere, contributing a large part to the 80 Mt of worldwide anthropogenic SO_2 emissions from energy related sources in 2015.[364] New materials and processes to enhance FGD are desirable.[365–367] Open metal sites can act as sites for SO_2 adsorption.[368,369] In 2008, Yaghi *et al.*[79] reported on the dynamic adsorption capacity of *e.g.* HKUST-1 and Zn-MOF-74, which are potential OMS-MOFs. The adsorption of SO_2 to open Cu^{2+} sites was reported for the paddle-wheel MOF MFM-170.[122] *In situ* synchrotron single-crystal X-ray diffraction experiments show the SO_2 coordination to OMS within a MOF for the first time. The preferred SO_2 adsorption site was found on a three-fold rotational axis in the triangular window of metal–organic cuboctahedra. The open Cu^{2+} sites represent the secondary adsorption sites, where the SO_2 molecule binds to the open Cu^{2+} site in an end-on mode [O(SO_2)–Cu = 2.28(10) Å] with an occupancy of 0.67 (Fig. 54).

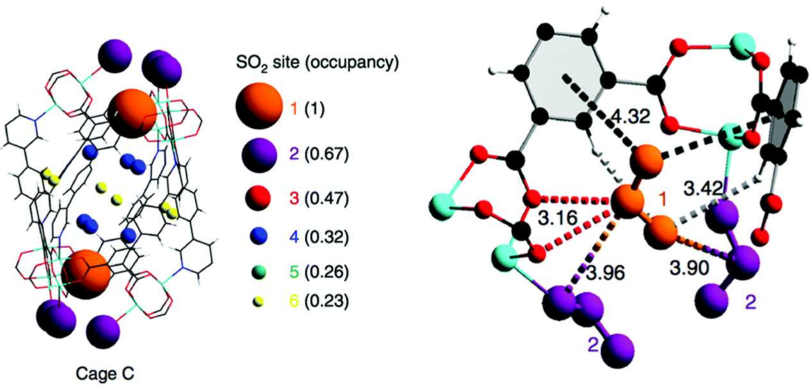

Fig. 54 Positions of SO_2 molecules in MFM-170 from in situ single-crystal X-ray diffraction. Left: Packing of SO_2 within cage C. Right: Intermolecular interactions between adsorbed SO_2 molecules and MFM-170 framework atoms. Single-colored dashed lines represent distances between adsorbed SO_2 molecules and framework atoms: red (O), blue (N), light grey (H), black (phenyl ring centroid). Dual-colored dashed lines represent intermolecular interactions between crystallographically distinct SO_2 molecules. Reproduced from ref. 122 with permission of Springer Nature, copyright 2019.

The authors showed *via* controlled desorption of SO_2 from MFM-170 that the open Cu^{2+} site is the most thermodynamically favored site. The diffraction data was collected under a dynamic vacuum at 298 K and desorption of SO_2 left the last adsorbate as the Cu^{2+}-bound SO_2 with an occupancy of 0.09. This suggests that the Cu^{2+} site is the thermodynamically strongest binding site, but (due to the Jahn–Teller effect) is still weak so that it is almost entirely desorbed on reduction of pressure.[122]

Separation

The separation of CO_2 from coal-gas exhaust gases and CH_4 from natural gas feeds is of great industrial importance. The selective adsorption or permeation of CO_2 is investigated in the context of CO_2 (“carbon”) capture and sequestration,[315,370–373] or the CO_2 removal from natural gas (“natural gas sweetening”, natural gas upgrading by removal of CO_2).[374–376] MOFs with OMS provide a distinct affinity for H_2, CO_2, CO, NO, and C_2H_2 due to specific OMS–adsorbate interactions. This was also evident from some of the earlier discussed theoretical studies. The presence of OMS in MOFs is a promising approach to enhance the CO_2 separation from gas mixtures with N_2 and CH_4 because of the high CO_2 adsorption energy to OMS (see above). The (calculated) adsorption enthalpy for CH_4 is about half the value for CO_2 and (see Tables S1 and S3 in ESI†). This explains the high selectivity of CO_2 over CH_4. OMS-MOFs can be used as solid adsorbents for selectively removing CO_2 (due to its large quadrupole moment and great polarizability) from dry gas mixtures with N_2 or CH_4.[71,178,321,332,333,377]

Single-crystal X-ray diffraction analysis and breakthrough experiments have been performed to investigate the role of OMS on the CO_2/CO or CO_2/CH_4 gas separation process.[178,378]

It has been shown that especially Mg-MOF-74 possesses high selectivity for CO_2 over CO and CH_4, since the main-group metal Mg^{2+} has no strong preference for CO (see above).[71,178] In breakthrough experiments with Mg-MOF-74 and a CO_2/CO gas mixture a longer breakthrough time for CO_2 than for CO was found, resulting in a high separation ability of CO_2 over CO.[178]
Furthermore, Mg-MOF-74 exhibits a high selectivity of CO_2 over CH_4.[71] Yaghi *et al*. showed that when Mg-MOF-74 is exposed to a gas mixture of CO_2/CH_4 in a ratio of 1 : 5, it only adsorbs CO_2. Breakthrough data revealed an CO_2 uptake of 8.9 wt% corresponding to 0.44 molecules of CO_2 per Mg^{2+} site before breakthrough. In comparison, for Zn-MOF-74, a CO_2 uptake of only 0.35 wt% was obtained under the same conditions.[71]

Schröder *et al*. have recently reported the coordination of SO_2 to open Cu^{2+} sites in MFM-170. MFM-170 provides high selectivity for SO_2.[122] The authors calculated the selectivity for equimolar mixtures of SO_2/CO_2, SO_2/N_2, SO_2/CO and SO_2/CH_4 from single-component isotherms at 298 K and 1 bar. Based on ideal adsorbed solution theory (IAST), high selectivity was proposed for SO_2/N_2 (944), followed by SO2/CH4 (260), SO_2/CO (203) and SO_2/CO_2 (35).[122]

A high adsorption capacity of OMS-MOFs was predicted for both CO_2 and C_2H_2, hence resulting in low C_2H_2/CO_2 selectivity (see the theoretical sections above).[209,234,351] Since the adsorption enthalpy of C_2H_2 is close to the one of CO_2 and the (calculated) adsorption enthalpy for CH_4 is about half (see Tables S1 and S3 in ESI†) this leads to an also high selectivity of C_2H_2 over CH_4. Calero *et al*. noted, that among the OMS-MOFs Fe-MOF-74 shows the largest adsorption selectivity values for both C_2H_2/CH_4 and C_2H_2/CO_2 gas mixtures at 298 K and low pressure.[351]

Catalysis and photocatalysis

The utilization of heterogeneous MOF catalysts can offer a number of advantages over homogeneous metal catalysts, including easy separation, efficient recycling, minimization of metal traces in the product, and improved handling and process control. MOF catalysts also aim to exploit porosity and chemical tunability for reaction selectivity.[32,39] There are several strategies to implement catalytic activity in the MOFs structure. Catalytic sites can be incorporated into the bridging ligands or postsynthetically grafted onto the linker or the metal SBU of the MOF. Often MOF catalysts try to use their OMS as catalytically active centers. After formation, the OMS will act as a Lewis acid, and it will be available to accept electron density from any donor molecule that can be present.[379]

We note that there is a myriad of literature on MOF catalysis claiming the influence of OMS without proof. We did not include and will not comment this work here but have limited the noted work to cases with proven OMS effects. Such examples describing the use of MOF catalysts containing OMS have been published, with uses in the cyanosilylation of carbonyl compounds[380] or of benzaldehyde or acetone,[125] the Mukaiyama aldol condensation,[381] the organophosphorous ester hydrolysis,[382] the cycloaddition with propylene epoxide and other small substrates,[383] the isomerization of a-pinene oxide[384] or of glucose,[385] the conversion of citronellal into isopulegol,[384] as well as for the oxidation of alcohols[39,91] or various organic substrates[99] or for selective hydrogenations[38,153] and in photocatalysis.[386]

In 1994, Fujita *et al.*[387] demonstrated for the first time the utility of a 2D MOF $[Cd(4,4'\text{-}bpy)_2(NO_3)_2]$, (bpy = bipyridine) as a heterogeneous Lewis acid catalyst, which promoted the cyanosilylation of aldehydes with shape selectivity. Kaskel *et al.*[125] showed that the open Cu^{2+} sites in HKUST-1 could catalyze the cyanosilylation of benzaldehyde or acetone. De Vos *et al.*[384] reported that activated HKUST-1 is a highly selective Lewis acid catalyst for the isomerization of a-pinene oxide to campholenic aldehyde, the cyclization of citronellal to isopulegol, and the rearrangement of α-bromoacetals due to its free Cu^{2+} coordination sites. Long *et al.*[381] described Mn-btt for the cyanosilylation of aromatic aldehydes with good conversion for small substrates and also substrate-size selectivity. Mn-btt can also be used to catalyze the Mukaiyama aldol reaction. The Lewis acid Cu^{2+} sites in the paddle-wheel MOF $[Cu_2[(C_{20}H_{12}N_2O_2)(COO)_4]]$, with accessible acylamide groups[383] is a heterogeneous catalyst for carbon fixation *via* catalytic conversion of CO_2.

The OMS MOF MIL-101(Cr) was reported by Kaskel *et al.*[380] for the cyanosilylation of carbonyl compounds. The authors demonstrated that MIL-101(Cr) with open Cr^{3+} sites possess a higher Lewis acidity to yield a more active catalyst for the cyanosilylation reaction, in comparison to HKUST-1. OMS MIL-101(Cr) showed a high yield of 98.5% at 313 K after 3 h, and the catalytic sites were immune to unwanted reduction by benzaldehyde.

Li *et al.*[39] generated a Pd/MIL-101(Cr) catalyst for the liquid phase aerobic oxidation of various alcohols and analyzed the effect of OMS of the MOF-support on the reactivity of Pd nanoparticles for the alcohol oxidation. It was observed that after ethylenediamine grafting on the open Cr^{3+} sites the catalytic Pd activity was suppressed. The oxidation of cinnamyl alcohol indicated results that range from <3/98 to 99/99 (conv./sel%) in the order MIL-101(Cr) < 0.35% Pd/En-MIL-101(Cr) < 0.35% Pd/MIL- 101(Cr). Accordingly, the use of 0.35% Pd/MIL-101 gave a complete conversion of cinnamyl alcohol to cinnamyl aldehyde within 0.5 h at 80 °C, while the amine grafted sample 0.35% Pd/En-MIL-101 showed only 45% yield of cinnamyl aldehyde within 3 h. After addition of a small amount of base additives (*e.g.* NaOH) to the system the activity increased (95% conversion of alcohol within 3 h). It can be deduced that the open Cr^{3+} sites play an imported role in the alcohol oxidation related to a promoting effect observed in MIL-101-supported metal nanoparticles for the conversions of aromatics.[388,389]

The MOFs TMU-10 and 12 with open Co^{2+} sites were studied by Morsali *et al.*[390] for the oxidative desulfurization reaction of a model oil, which was prepared by dissolving dibenzothiophene (DBT) in n-hexane. The Lewis acidic Co^{2+} sites in these structures successfully completed the quantitative desulfurization process after 6 h.

Kitagawa *et al.*[385] investigated the potential of MIL-101(Cr) derivatives for glucose isomerisation. In comparison to Amberlyst-15, a strongly acidic ion-exchange resin, MIL-100 and MIL-101 showed higher catalytic activity. Here, the catalytic activity can be modulated through the Lewis-acidity of the OMS by modification of the organic ligands with functional groups, like $–NH_2$, $–(CH_3)_2$, $–NO_2$ and $–SO_3H$. Electron donating $–NH_2$ and $–(CH_3)_2$ groups on the aromatic ring of the terephthalate, decrease the Lewis acidity of open Cr^{3+} sites and increase the electron density. Whereas electron-accepting $–NO_2$ and $–SO_3H$ groups increase the Lewis acidity of OMS and decrease the electron density. The authors described also that MIL-100 and MIL-101 have though the same Lewis acidity, but different production yields of fructose, due to the differences in window size of the mesopores. MIL-101(Cr)–SO_3H provided a high conversion of glucose and selectively produced fructose.

Hatton *et al.*[382] investigated the modification of MIL-101(Cr) with dialkylaminopyridines (DAAP) for the hydrolytic degradation of organophosphorus esters such as diethyl-4-nitrophenyl phosphate (paraoxon). Different supernucleophilic DAAP ligands were coordinatively attaching onto part of the OMS of MIL-101. The authors showed, that the catalytic activity of the DAAP modified MIL-101(Cr) was higher than activated MIL-101(Cr). Furthermore, the synergistic activation of the substrate by the Lewis acid Cr^{3+} sites and the electron-rich nucleophiles (DAAP) gave a Lewis acid–Lewis base activation mechanism. For the selective semihydrogenation Luo *et al.* and coworkers[38] reported on Pd@Zn-MOF-74, which showed a high styrene selectivity of 92% at full conversion with a turnover frequency of 98.1 h^{-1} – compared to the selectivity of the Lindlar catalyst with 56%. The origin of ultrahigh selectivity, as proposed by DFT calculation, is due to a coordination of the C≡C bond of phenylacetylene to the open Zn(II) site.[38]

MIL-101(Fe) was studied for the photocatalytic CO_2 reaction by Li *et al.*[386] The authors demonstrated with *in situ* FT-IR studies that the open Fe sites are the photocatalytically active sites for this reaction. The adsorption of CO_2 directly onto the metal center activates the substrate for the photocatalytic CO_2 reduction reaction.

Morsali *et al.*[391] have reported the mixed-metal MOFs with open Cd sites for phenol degradation from aqueous solutions under UV and/or visible light irradiation. The authors compared the four TMU MOFs, $[Zn(oba)(4\text{-}bpdh)_{0.5}]$, $[Cd_{0.15}Zn_{0.85}(oba)(4\text{-}bpdh)_{0.5}]$, $[Cd_{0.3}Zn_{0.7}(oba)(4\text{-}bpdh)_{0.5}]$ and [Cd(oba)(4-bpdh)]. The mixed metal-based MOFs with 15 and 30% Cd were photocatalytically more active than the just Cd or Zn containing MOF.

Hong *et al.*[111] explained that the activation temperature had an important effect on the catalytic activity for CO oxidation because more open metal sites available in HKUST-1 gave a higher

CO activity, the catalytic activity then increased in the order HKUST-1-553 K < 443 K < 473 K < 503 K < 523 K.

Sensing

Chemical materials for highly selective and sensitive detection of analytes in the gas and liquid phase are competitively investigated for applications in industrial processes, chemical threat detection, medical diagnostics, food quality control, occupational safety and environmental monitoring. Thereby Lewis acidic or basic sites in the ligands or OMS play an important role through their interactions with guest molecules for the selective recognition. Often luminescent MOFs (LMOFs) are utilized as sensor through the quenching or enhancement of their luminescence by the analyte. Mesoporous LMOFs allow also the sensing of larger molecules such as biologically active species.[392]

A few examples of porous MOFs with open metal sites have been investigated for their sensing properties. Morsali *et al.*[393] showed the potential of open Zn^{2+} sites in activated TMU-41, $[Zn_2(bdc)_{1.5}(L)]$ (L = pyridine 4-carboxylate) for the selective and recyclable luminescent sensing of MnO_4^-, $Cr_2O_7^{2-}$ and CrO_4^{2-}. Lobkovsky *et al.*[180] showed that the luminescent MOF $[Eu(btc)(H_2O)]$ after removal of the solvent molecules contained open Eu^{3+} sites, which could act as a highly selective sensor for small molecules, such as dimethyl formamide, acetone, and ethanol. For more practical use weakly coordinated 1-propanol molecules on the Eu^{3+} sites were replaced by DMF and acetone to gradually increase and decrease the fluorescence intensity, respectively.

The lanthanide MOF $[Eu_2(\mu_2\text{-pzdc})(\mu_4\text{-pzdc})(\mu_2\text{-ox})(H_2O)_4]$ (H_2pzdc = 2,5-pyrazinedicarboxylic acid, H_2ox = oxalic acid) was reported by Guillou *et al.*[394] for the recognition and sensing of acetone. After removal of the solvent molecules the MOF exhibited a high quenching effect with acetone.

Chen *et al.*[395] reported on the near infrared (NIR) luminescent Yb-MOF $[Yb(bpt)(H_2O)(DMF)_{1.5}(H_2O)_{1.25}]$ (bpt = biphenyl-3,4,5-tricarboxylate) for the sensing of small molecules. Activated [Yb(bpt)] showed typical NIR emission from the $^2F_{5/2}$ - $^2F_{7/2}$ transition of Yb^{3+} at 980 nm, when excited at 326 nm. In comparison to [Eu(btc)] the luminescence intensity of [Yb(bpt)] indicated even higher enhancing and quenching effects with DMF and acetone.

Dincă *et al.*[41] described the interaction of NH_3 with $[Zn_2(tcpe)]$ (tcpe = tetrakis(4-carboxyphenyl)ethylene) and $[Mg(H_2dhbdc)]$ (H_2dhbdc^{2-} = 2,5-dihyroxybenzene-1,4-dicarboxylate), which caused fluorescence shifts and turn-on luminescence responses over potential interferents such as water, methanol, amines, and other gases. The exposure of activated $[Zn_2(tcpe)]$ to ammonia, triethylamine, ethylenediamine, *N,N*-diethylformamide and water vapors shifted its emission maximum by up to 23 nm at room temperature. At 100 °C ammonia exposure led to a shift of the emission maximum from 487 to 511 nm, thus revealing a good selectivity for NH_3 detection. Based on *in situ* IR studies the authors verified the binding of NH_3 to the open Mg^{2+} sites in $[Mg(H_2dhbdc)]$.

4. Conclusions

The as-synthesized MOF will have initially all metal ions in its SBU in their fully coordinatively saturated state. This is themost stable metal coordination environment according to the usual metal coordination number, which is typically six (octahedral) or four (tetrahedral) for most 3d transition metal ions. Open metal sites in MOFs (OMS-MOFs) can be obtained by the removal of an initial labile terminal ligand, which may typically be a solvent molecule, from its coordinating metal atom. The procedure for this ligand removal with OMS generation is usually solvent exchange and removal, which may be generally termed “activation” and can be further differentiated into thermal, chemical or photothermal activation. Seldom noted, but definitely more important, is the at least partial reduction of the metal at the OMS upon its formation, as was already observed for HKUST-1 with Cu^{2+} to Cu^{1+} and MIL-100 with Fe^{3+} to Fe^{2+}; but such a reduction may also occur in many other OMS-MOFs.

OMS are often invoked but it is important to prove the presence of OMS by suitable analytical methods, such as NMR, TGA, FT-IR in connection with gas sorption studies. It is just becoming apparent that quantitative OMS generation cannot be taken for granted by ‘‘standard’’ activation protocols. Few studies have so far addressed the issue of OMS quantification and more such studies are needed to quantify the formed OMS. The current characterization techniques for the detection and quantification of Lewis-acid sites in MOFs are gas or vapor adsorption, probe-molecule infrared spectroscopy and temperature-programmed desorption (TPD). The techniques are versatile but their application in OMS research remains limited. Most of the OMS work simply did not address the quantities of OMS formed. Also, further improvement and additional techniques are warranted. The NH_3-TPD technique, for example, has the limitation in quantifying OMS in the presence of Brønsted acid sites.

In MOF structures any change to the metal ions in the metal SBU must ensure the integrity of the network. Importantly, the MOF structure must not collapse, and their crystallinity and porosity should be preserved, that is, a labile terminal ligand should be removed without damage to the framework. Retention of the framework integrity is usually verified by PXRD. It is the strength of theory that OMS can be easily studied regarding their electronic effects on the interactions with substrate molecules. The theory-based knowledge, how OMS interact with the guest molecules is needed along the experimental work for understanding the properties of OMS-MOFs. We note, however, that without additional parametrization, standard force fields are barely able to deliver accurate thermodynamic data. More accurate values for binding enthalpies are obtained through quantum mechanical calculation of potential energy surfaces, preferably using periodic boundaries. At the DFT-level, the inclusion of van der Waals interactions is crucial. The most accurate approach involves a combination of dispersion corrected DFT and high-level *ab initio* methods, as *e.g.* DFT-D and coupled cluster (CC) methods including complete basis set extrapolation. Theoretical studies support that OMS interactions with gaseous adsorbates are dispersion-driven for CH_4, involve electrostatic and dispersion for H_2, N_2, and CO_2, and contain a partially covalent (dative) bonding character with CO and C_2H_2.

The presence of OMS in the MOF causes enhanced interactions between the metal site and guest molecules. OMS are the primary adsorption sites for H_2, CO_2, CO, NO and C_2H_2 giving high heats of adsorption (Q_{st}). OMS are, however, not the primary adsorption site for CH_4 and possibly SO_2. The formation of an OMS is also the prerequisite for the "metal-binding" of weakly coordinating adsorbates such as CO_2 and H_2. Gas sorption studies on OMS-MOFs in connection with high-resolution/powder neutron diffraction studies, powder synchrotron X-ray diffraction analysis and near sites edge X-ray adsorption fine structure (NEXAFS) spectroscopy yielded structural information and insight into the role of the OMS on the MOF-adsorbate interactions.

The defined synthesis of OMS in MOFs is the basis for targeted functionalization through grafting, the coordination of weakly binding species and increased (supramolecular) interactions with guest molecules. The enhanced interactions can be highly effective on the MOF performance in the potential applications gas sorption and separation, catalysis and sensing. For example, MOFs with OMS are among the most promising solid adsorbents for selectively removing CO_2 from dry gas mixtures and have been described as highly active Lewis-acid catalysts.

Abbreviations

Ligands arranged alphabetically without protic H atoms

H_4abtc	3,3′,5,5′-Azobenzene-tetracarboxylic acid
H_4adip	5-Aminodiacetic isophthalic
H_4aobtc	Azoxybenzene-2,2′,3,3′-tetracarboxylic acid
H_2bbta	1*H*,5*H*-Benzene(1,2-*d*:4,5-*d*′)bistriazole
H_2bdc	Benzene-1,4-dicarboxylic acid/terephthalic acid
H_2bdc-NH_2	2-Aminoterephthalic acid
H_6bhb	3,3′,3″,5,5′,5″-Benzene-1,3,5-triylhexabenzoic acid
H_6btat	5,5′,5″-(Benzene-1,3,5-triyltris(anthracene-10,9-diyl))triisophthalic acid
4-bpdh	2,5-Bis(4-pyridyl)-3,4-diaza-2,4-hexadiene
H_3bpt	Biphenyl-3,4′,5-tricarboxylic acid
H_4bptc	1,1′-biphenyl-2,2′,6,6′-tetracarboxylic acid

H_3btc	Benzene-1,3,5-tricarboxylic acid/Trimesic acid
H_2btdd	Bis-(1*H*-1,2,3-triazolo-[4,5-*b*],[4′,5′-*i*])dibenzo-[1,4]-dioxine
H_3btt	5,5′,5″-(1,3,5-Phenylene)tris(1*H*-tetrazole)
H_3bttri	1,3,5-Tris(1*H*-1,2,3-triazol-5-yl)benzene
H_2dmcapz	3,5-Dimethyl-4-carboxypyrazole
H_4dobpdc	4,4′-Dioxidobiphenyl-3,3′-dicarboxylate
H_4(*p*-dobdc)	*para*-2,5-Dihydroxyterephthalic acid
H_4mbdpb	5-Methoxyl-1,3-bis(3,5-dicarboxylphenyl)benzene
H_4mdip	5,5′-Methylenediisophthalate
H_4(*m*-dobdc)	*meta*-4,6-Dioxido-1,3-benzene-dicarboxylate
H_5n	2,5-Di(3,5-dicarboxylphenyl)-nicotinic acid
Hna	Nicotinic acid
H_2oba	4,4′-Oxybis(benzoic acid)
H_4olz	Olsalazine acid
H_2ox	Oxalic acid
H_2pyip	5-(Pyridin-3-yl)isophthalic acid
H_2pzdc	2,5-Pyrazinedicarboxylic acid
H_4sbtc	5-Sulfonyl-1,2,4-benzenetricarboxylic acid
H_2sip	5-Sulfoisophthalate
H_2sp_5-BF_4	1,3-Bis(4-carboxyphenyl)-4,5-dihydro-1*H*-imidazol-3-ium tetrafluoroborate
H_3tatb	4,4′,4″-*s*-Triazine-2,4,6-triyltribenzoate
H_4tcpe	Tetrakis(4-carboxyphenyl)ethylene
H_8tdcppy	1,3,6,8-Tetra(3,5-dicarboxyphenyl)pyrene
H_6tdpat	2,4,6-Tris(3,5-dicarboxylphenylamino)-1,3,5-triazine
H_3tzi	5-Tetrazolylisophthalic acid
H_3tzpa	5-(4-(Tetrazol-5-yl)phenyl)isophthalic acid
approx.	Approximately
BET	Brunauer–Emmett–Teller
BSS	Belof Stern Space
CA	Chemical activation
CAS	Confirmation of Acceptance for Studies
CC	Coupled cluster
CCDC	Cambridge crystallographic data center
CCSD	Coupled cluster singles and doubles
CCSD(T)	Coupled cluster singles, doubles with perturbative triples
CPO	Coordination polymer of Oslo

CSD	Cambridge structural database
CUS	Coordinatively unsaturated site(s)
D_2O/NaOD	Deuterium oxide/sodium deuteroxide solution
DCM	Dichloromethane
DFT	Density functional theory
DMF	*N,N*-Dimethylformamide
DSC	Differential scanning calorimetry
EDA	Energy decomposition analysis
EDX	Energy dispersive X-ray spectroscopy
EtOH	Ethanol
eq.	Equivalent
EXAFS	Extended X-ray absorption fine structure
FT-IR	Fourier transform infrared spectroscopy
GCMC	Grand Canonical Monte Carlo
HKUST	Hong Kong University of Science and Technology
IR	Infrared spectroscopy
MeCN	Acetonitrile
MeOH	Methanol
MIL	Materiaux de l'Institute Lavoisier
MOF(s)	Metal–organic framework(s)
NEXAFS	Near Edge X-ray Absorption Fine Structure
NMR	Nuclear magnetic resonance
NJFU	Nanjing Forestry University
NJU	Nanjing University
NONOates	N-Diazenium dialates
NOTT	University of Nottingham
OCS	Open coordination site(s)
OMS	Open metal site(s)
PA	Photothermal activation
PES	Potential energy surface
PBE	Perdew–Burke–Ernzernhof
PCN	Porous coordination network
PHAST(*)	Potentials with high accuracy, speed, and transferability; the * stands for the inclusion of the explicit polarization
PDOS	Partial density of states
P-XRD	Powder X-ray diffraction
Py-SI	Pyridyl-salicylimine

QM/MM	Combined quantum mechanical and molecular mechanical method
rht	Rhombicuboctahedral and trigonal, topology term
S_{BET}	Surface area
SBU	Secondary building unit
$scCO_2$	Supercritical carbon dioxide
SCXRD	Single crystal X-ray diffraction
SE	Solvent exchange
SEM	Scanning electron microscope
SEM-EDX	Scanning Electron Microscopy/Energy Dispersive X-Ray Spectroscopy
soc	Square octahedral, topology term
TA	Thermal activation
TGA	Thermogravimetric analysis
TraPPe	Transferable Potentials for Phase Equilibria force Field
UiO	University in Oslo
UFF	Universal Force Field
UTSA	University of Texas at San Antonio
UV-Vis spectroscopy	Ultraviolet-visible spectroscopy
vdW	van der Waals
XPS	X-ray photoelectron spectroscopy
ZJU	Zhejiang University

Conflicts of interest

The authors declare no competing financial interest.

Acknowledgements

The authors gratefully acknowledge the financial support of the German Research Foundation (Deutsche Forschungsgemeinschaft, DFG) under grant no. Ja466/40-1 and project no. 396890929/GRK 2482.

References

1 S. R. Batten, N. R. Champness, X.-M. Chen, J. Garcia-Martinez, S. Kitagawa, L. Öhrström, M. O’Keeffe, M. P. Suh and J. Reedijk, *Pure Appl. Chem.*, 2013, **85**, 1715−1724.

2 S. R. Batten, N. R. Champness, X.-M. Chen, J. Garcia-Martinez, S. Kitagawa, L. Öhrström, M. O'Keeffe, M. P. Suh and J. Reedijk, *CrystEngComm*, 2012, **14**, 3001−3004.

3 M. E. Davis, *Nature,* 2002, **417**, 813−821.

4 Z. Ma, T. Kyotani, Z. Liu, O. Terasaki and A. Tomita, *Chem. Mater.*, 2001, **13**, 4413−4415.

5 C. Janiak and J. K. Vieth, *New J. Chem.*, 2010, **34**, 2366−2388.

6 V. Safarifard, S. Rodríguez-Hermida, V. Guillerm, I. Imaz, M. Bigdeli, A. Azhdari Tehrani, J. Juanhuix, A. Morsali, M. E. Casco and J. Silvestre-Albero, *Cryst. Growth Des.*, 2016, **16**, 6016−6023.

7 J. Dechnik, J. Gascon, C. J. Doonan, C. Janiak and C. J. Sumby, *Angew. Chem. Int. Ed.*, 2017, **56**, 9292−9310.

8 B. Li, H.-M. Wen, W. Zhou and B. Chen, *J. Phys. Chem. Lett.*, 2014, **5**, 3468−3479.

9 P. Serra-Crespo, E. V. Ramos-Fernandez, J. Gascon and F. Kapteijn, *Chem. Mater.*, 2011, **23**, 2565−2572.

10 J. Y. Lee, O. K. Farha, J. Roberts, K. A. Scheidt, S. T. Nguyen and J. T. Hupp, *Chem. Soc. Rev.*, 2009, **38**, 1450−1459.

11 Y.-B. Huang, J. Liang, X.-S. Wang and R. Cao, *Chem. Soc. Rev.*, 2017, **46**, 126−157.

12 A. Herbst and C. Janiak, *CrystEngComm*, 2017, **19**, 4092−4117.

13 K. Berijani and A. Morsali, *J. Catal.*, 2019, **378**, 28−35.

14 M. Bagheri, M. Y. Masoomi and A. Morsali, *ACS Catal.*, 2017, **7**, 6949−6956.

15 M. Bagheri, M. Y. Masoomi and A. Morsali, *Sens. Actuators B,* 2017, **243**, 353−360.

16 P. Horcajada, R. Gref, T. Baati, P. K. Allan, G. Maurin, P. Couvreur, G. Férey, R. E. Morris and C. Serre, *Chem. Rev.*, 2012, **112**, 1232−1268.

17 Z.-G. Gu, D.-J. Li, C. Zheng, Y. Kang, C. Wöll and J. Zhang, *Angew. Chem. Int. Ed.*, 2017, **56**, 6853−6858.

18 F. Jeremias, D. Fröhlich, C. Janiak and S. K. Henninger, *New J. Chem.*, 2014, **38**, 1846−1852.

19 M. F. de Lange, K. J. Verouden, T. J. Vlugt, J. Gascon and F. Kapteijn, *Chem. Rev.*, 2015, **115**, 12205−12250.

20 D. Fröhlich, E. Pantatosaki, P.D. Kolokathis, K. Markey, H. Reinsch, M. Baumgartner, M. A. van der Veen, D. E. De Vos, N. Stock and G. K. Papadopoulos, *J. Mater. Chem. A*, 2016, **4**, 11859−11869.

21 H. Kummer, F. Jeremias, A. Warlo, G. Füldner, D. Fröhlich, C. Janiak, R. Gläser and S. K. Henninger, *Ind. Eng. Chem. Res.*, 2017, **56**, 8393−8398.

22 J. E. Huheey, E. A. Keiter and R. L. Keiter, *Inorganische Chemistry: Principles of Structure und* Reactivity, Harper Collines, New York, 4th edn, 1993.

23 C. Elschenbroich, *Organometallic*, Wiley-VCH Verlag GmbH & Co. KGaA, Weinheim, 3rd edn, 2006.

24 C. Janiak, H.-J. Meyer, D. Gudat and R. Alsfasser, *Riedel: Moderne Anorganische Chemie*, Walter de Gruyter GmbH & Co. KG Berlin/Boston, 4th edn, 2012.

25 L. Beyer and J. A. Cornejo, *Koordinationschemie: Gundlagen – Synthesen – Anwendungen*, Vieweg + Teubner Verlag, Spinger Fachmedien Wiesbaden, 2012.

26 M. Bosch, M. Zhang and H.-C. Zhou, *Adv. Chem.*, 2014, **2014**, 182327.

27 M. C. Das, S. Xiang, Z. Zhang and B. Chen*, Angew. Chem. Int. Ed.*, 2011, **50**, 10510−10520.

28 M. Y. Masoomi, A. Morsali, A. Dhakshinamoorthy and H. Garcia, *Angew. Chem. Int. Ed.*, 2019, **58**, 15188−15205.

29 S.-i. Noro, S. Kitagawa, M. Yamashita and T. Wada, *Chem. Commun*., 2002, 222−223

30 Z. Zhang, S. Xiang, K. Hong, Madhab, C. Das, H. D. Arman, M. Garcia, J. U. Mondal, K. M. Thomas, B. Chen, *Inorg. Chem*., 2012, **51**, 4947−4953.

31 S. S. Y. Chui, S. M. F. Lo, J. P. H. Charmant, A. G. Orpen and I. D. Williams, *Science*, 1999, **283**, 1148−1150.

32 M. Eddaoudi, H. Li and O. Yaghi, *J. Am. Chem. Soc.*, 2000, **122**, 1391−1397.

33 O. M. Yaghi, C. E. Davis, G. Li and H. Li, *J. Am. Chem. Soc.*, 1997, **119**, 2861−2868.

34 M. Eddaoudi, D. B. Moler, H. Li, B. Chen, T. M. Reineke, M. O´Keefe and, O. M. Yaghi, *Acc. Chem. Res.*, 2001, **34**, 319−330.

35 N. L. Rosi, J. Kim, M. Eddaoudi, B. Chen, M. O’Keeffe and O. M. Yaghi, *J. Am. Chem. Soc.*, 2005, **127**, 1504−1518.

36 J. W. Yoon, H. Chang, S.-J. Lee, Y. K. Hwang, D.-Y. Hong, S.-K. Lee, J. S. Lee, S. Jang, T.-U. Yoon, K. Kwac, Y. Jung, R. S. Pillai, F. Faucher, A. Vimont, M. Daturi, G. Férey, C. Serre, G. Maurin, Y.-S. Bae and J.-S. Chang, *Nat. Mater.*, 2017, **16**, 526−531.

37 L. Alaerts, M. Maes, M. A. van der Veen, P. A. Jacobs and D. E. De Vos, *Phys. Chem. Chem. Phys*., 2009, **11**, 2903−2911.

38 H. Q. Wu, L. Huang, J. Q. Li, A. M. Zheng, Y. Tao, L. X. Yang, W. H. Yin and F. Luo, *Inorg. Chem.*, 2018, **57**, 12444−12447.

39 G. Chen, S. Wu, H. Liu, H. Jiang and Y. Li, *Green Chem.*, 2013, **15**, 230−235.

40 A. Verma, K. Tomar and P. K. Bharadwaj, *Inorg. Chem*., 2017, **56**, 13629−13633.

41 N. B. Shustova, A. F. Cozzolino, S. Reineke, M. Baldo and M. Dincă, *J. Am. Chem. Soc.*, 2013, **135**, 13326−13329.

42 A. R. Kulkarni and D. S. Sholl, *J. Phys. Chem. C*, 2016, **120**, 23044−23054.

43 A. Luna-Triguero, J. M. Vicent-Luna, P. Gómez-Álvarez and S. Calero, *J. Phys. Chem. C*, 2017, **121**, 3126−3132.

44 A. Luna-Triguero, J. M. Vicent-Luna, A. Poursaeidesfahani, T. J. H. Vlugt, R. Sánchez-de-Armas, P. Gómez-Álvarez and S. Calero, *ACS Appl. Mater. Interfaces*, 2018, **10**, 16911−16917.

45 Y.-S. Bae, C. Y. Lee, K. C. Kim, O. K. Farha, P. Nickias, J. T. Hupp, S. B. T. Nguyen and R. Q. Snurr, *Angew. Chem. Int. Ed.*, 2012, **51**, 1857−1860.

46 J. Duan, M. Higuchi, J. Zheng, S.-i. Noro, I-Y. Chang, K. Hyeon-Deuk, S. Mathew, S. Kusaka, E. Sivaniah, R. Matsuda, S. Sakaki and S. Kitagawa, *J. Am. Chem. Soc.*, 2017, **139**, 11576−11583.

47 Z. Liu, L. Lv, Y. He and Y. Feng, *CrystEngComm*, 2017, **19**, 2795−2801.

48 J.-W. Zhang, M.-C. Hu, S.-N. Li, Y.-C. Jiang, P. Qu and Q.-G. Zhai, *Chem. Commun.*, 2018, **54**, 2012−2015.

49 J.-W. Zhang, M.-C. Hu, S.-N. Li, Y.-C. Jiang and Q.-G. Zhai, *Chem. – Eur. J.*, 2017, **23**, 6693−6700.

50 H. He, D.-Y. Zhang, F. Guo and F. Sun, *Inorg. Chem.*, 2018, **57**, 7314−7320.

51 H. Kim and Y. Jung, *J. Phys. Chem., Lett.*, 2014, **5**, 440−446.

52 S. R. Caskey, A. G. Wong-Foy and A. J. Matzger, *J. Am. Chem. Soc.*, 2008, **130**, 10870−10871.

53 H. Oh, I. Savchenko, A. Mavrandonakis, T. Heine and M. Hirscher, *ACS Nano*, 2014, **8**, 761−770.

54 C.-X. Chen, S.-P. Zheng, Z.-W. Wei, C.-C. Cao, H.-P. Wang, D. Wang, J.-J. Jiang, D. Fenske and C.-Y. Su, *Chem. – Eur. J.*, 2017, **23**, 4060−4064.

55 M. Latroche, S. Suble, C. Serre, C. Mellot-Draznieks, P. L. Llewellyn, J.-H. Lee, J.-S. Chang, S. H. Jhung and G. Ferey, *Angew. Chem. Int. Ed.*, 2006, **45**, 8227−8231.

56 S. Ma and H.-C. Zhou, *J. Am. Chem. Soc.*, 2006, **128**, 11734−11735.

57 S. Ma, D. Yuan, J.-S. Chang and H.-C. Zhou, *Inorg. Chem.*, 2009, **48**, 5398−5402.

58 G.-J. Ren, Z. Chang, J. Xu, Z. Hu, Y.-Q. Liu, Y.-L. Xu and X.-H. Bu, *Chem. Commun.*, 2016, **52**, 2079−2082.

59 P. M. Forster, J. Eckert, B. D. Heiken, J. B. Parise, J. W. Yoon, S. H. Jhung, J.-S. Chang and A. K. Cheetham, *J. Am. Chem. Soc.*, 2006, **128**, 16846−16850.

60 F. Nouar, J. F. Eubank, T. Bousquet, L. Wojtas, M. J. Zaworotko and M. Eddaoudi, *J. Am. Chem. Soc.*, 2008, **130**, 1833−1835.

61 Y. Yan, X. Lin, S. Yang, A. J. Blake, A. Dailly, N. R. Champness, P. Hubberstey and M. Schröder, *Chem. Commun.*, 2009, 1025−1027.

62 Y. Yan, I. Telepeni, S. Yang, X. Lin, W. Kockelmann, A. Dailly, A. J. Blake, W. Lewis, G. S. Walker, D. R. Allan, S. A. Barnett, N. R. Champness and M. Schröder, *J. Am. Chem. Soc.*, 2010, **132**, 4092−4094.

63 X.-S. Wang, S. Ma, K. Rauch, J. M. Simmons, D. Yuan, X. Wang, T. Yildirim, W. C. Cole, J. J. López, A. de Meijere and H.-C. Zhou, *Chem. Mater.*, 2008, **20**, 3145−3152.

64 D. Liu, H. Wu, S. Wang, Z. Xie, J. Li and W. Lin, *Chem. Sci.*, 2012, **3**, 3032−3037.

65 T. Pham, K. A. Forrest, A. Hogan, B. Tudor, K. McLaughlin, J. L. Belof, J. Eckert and B. Space, *Cryst. Growth Des.*, 2015, **15**, 1460−1471.

66 G. Y. Yoo, W. R. Lee, H. Jo, J. Park, J. H. Song, K. S. Lim, D. Moon, H. Jung, J. Lim, S. S. Han, Y. Jung and C. S. Hong, *Chem. – Eur. J.*, 2016, **22**, 7444−7451.

67 W.-Y. Gao, S. Palakurty, L. Wojtas, Y.-S. Chen and S. Ma, *Inorg. Chem. Front.*, 2015, **2**, 369−372.

68 A. Masala, J. G. Vitillo, G. Mondino, C. A. Grande, R. Blom, M. Manzoli, M. Marshall and Silvia Bordiga, *ACS Appl. Mater. Interfaces*, 2017, **9**, 455−463.

69 J. M. Simmons, H. Wu, W. Zhou and T. Yildirim, *Energy Environ. Sci.*, 2011, **4**, 2177−2185.

70 W. L. Queen, M. R. Hudson, E. D. Bloch, J. A. Mason, M. I. Gonzalez, J. S. Lee, D. Gygi, J. D. Howe, K. Lee, T. A. Darwish, M. James, V. K. Peterson, S. J. Teat, B. Smit, J. B. Neaton, J. R. Long and C. M. Brown, *Chem. Sci.*, 2014, **5**, 4569−4581.

71 D. Britt, H. Furukawa, B. Wang, T. G. Glover and O. M. Yaghi, *Proc. Natl. Acad. Sci. U. S. A.*, 2009, **106**, 20637−20640.

72 P. Verma, R. Maurice and D. G. Truhlar, *J. Phys. Chem. C*, 2015, **119**, 28499−28511.

73 N. Drenchev, M. H. Rosnes, P. D. C. Dietzel, A. Albinati, K. Hadjiivanov and P. A. Georgiev, *J. Phys. Chem. C*, 2018, **122**, 17238−17249.

74 A. H. Khan, K. Peikert, F. Hoffmann, M. Fröba and M. Bertmer, *J. Phys. Chem. C*, 2019, **123**, 4299−4307.

75 J. Yang, B. Du, J. Liu, R. Krishna, F. Zhang, W. Zhou and Y. Wang, J. Li and B. Chen, *Chem. Commun.*, 2018, 54, 14061−14064.

76 J. Pang, F. Jiang, M. Wu, C. Liu, K. Su, W. Lu, D. Yuan and M. Hong, *Nat. Commun.*, 2015, **6**, 7575.

77 C. Song, J. Jiao, Q. Lin, H. Liu and Y. He, *Dalton Trans.*, 2016, **45**, 4563−4569.

78 S. Xiang, W. Zhou, Z. Zhang, M. A. Green, Y. Liu and B. Chen, *Angew. Chem. Int. Ed.*, 2010, **49**, 4615−4618.

79 D. Britt, D. Tranchemontagne and O. M. Yaghi, *Proc. Natl. Acad. Sci. U. S. A.*, 2008, **105**, 11623–11627.

80 Y. He, W. Zhou, T. Yildirim and B. Chen, *Energy Environ. Sci.*, 2013, **6**, 2735−2744.

81 H. S. Koh, M. K. Rana, A. G. Wong-Foy and D. J. Siegel, *J. Phys. Chem. C*, 2015, **119**, 13451−13458.

82 M. Jorge, M. Fischer, J. R. B. Gomes, C. Siquet, J. C. Santos and A. E. Rodrigues, *Ind. Eng. Chem. Res.*, 2014, **53**, 15475−15487.

83 A. J. Rieth, Y. Tulchinsky and M. Dincă, *J. Am. Chem. Soc.*, 2016, **138**, 9401−9404.

84 Y.-Han Shih, K.-Y. Wang, B. Singco, C.-H. Lin and H.-Y. Huang, *Langmuir*, 2016, **32**, 11465−11473.

85 M. H. Weston, W. Morris, P. W. Siu, W. J. Hoover, D. Cho, R. K. Richardson and O. K. Farha, *Inorg. Chem.*, 2015, **54**, 8162−8164.

86 B. Chen, N. W. Ockwig, A. R. Millward, D. S. Contreras and O. M. Yaghi, *Angew. Chem. Int. Ed.*, 2005, **44**, 4745−4749.

87 Y. Yan, S. Yang, A. J. Blake and M. Schröder, *Acc. Chem. Res.*, 2014, **47**, 296−307.

88 M. T. Kapelewski, S. J. Geier, M. R. Hudson, D. Stück, J. A. Mason, J. N. Nelson, D. J. Xiao, Z. Hulvey, E. Gilmour, S. A. FitzGerald, M. Head-Gordon, C. M. Brown and J. R. Long, *J. Am. Chem. Soc.*, 2014, **136**, 12119−12129.

89 M. H. Rosnes, M. Opitz, M. Frontzek, W. Lohstroh, J. Peter Embs, P. A. Georgiev and P. D. C. Dietzel, *J. Mater. Chem. A*, 2015, **3**, 4827−4839.

90 N. J. Hinks, A. C. McKinlay, B. Xiao, P. S. Wheatley and R. E. Morris, *Microporous Mesoporous Mater.*, 2010, **129**, 330−334.

91 J. L. C. Rowsell and O. M. Yaghi, *J. Am. Chem. Soc.*, 2006, **128**, 1304−1315.

92 J. J. Goings, S. M. Ohlsen, K. M. Blaisdell and D. P. Schofield, *J. Phys. Chem. A*, 2014, **118**, 7411−7417.

93 J. Bentley, G. S. Foo, M. Rungta, N. Sangar, C. Sievers, D. S. Sholl and S. Nair, *Ind. Eng. Chem. Res.*, 2016, **55**, 5043−5053.

94 Z. R. Herm, E. D. Bloch and J. R. Long, *Chem. Mater.*, 2014, **26**, 323−338.

95 S. M. Chavan, G. C. Shearer, E. Bloch and S. Bordiga, *ChemPhysChem*, 2012, **13**, 445−448.

96 U. Böhme, B. Barth, C. Paula, A. Kuhnt, W. Schwieger, A. Mundstock, J. r. Caro and M. Hartmann, *Langmuir*, 2013, **29**, 8592−8600.

97 A. Ö. Yazaydın, R. Q. Snurr, T.-H. Park, K. Koh, J. Liu, M. D. LeVan, A. I. Benin, P. Jakubczak, M. Lanuza, D. B. Galloway, J. J. Low and R. R. Willis, *J. Am. Chem. Soc.*, 2009, **131**, 18198−18199.

98 S. Rostamnia, H. Alamgholiloo and X. Liu, *J. Colloid Interface Sci.*, 2016, **469**, 310−317.

99 J.-C. Wang, F.-W. Ding, J.-P. Ma, Q.-K. Liu, J.-Y. Cheng and Y.-B. Dong, *Inorg. Chem.*, 2015, **54**, 10865−10872.

100 E. Q. Procopio, T. Fukushima, E. Barea, J. A. R. Navarro, S. Horike and S. Kitagawa, *Chem. – Eur. J.*, 2012, **18**, 13117−13125.

101 H. K. Kim, W. S. Yun, M.-B. Kim, J. Y. Kim, Y.-Y. Bae, J. Lee and N. C. Jeong, *J. Am. Chem. Soc.*, 2015, **137**, 10009−10015.

102 J. Bae, J. S. Choi, S. Hwang, W. S. Yun, D. Song, J. Lee and N. C. Jeong, *ACS Appl. Mater. Interfaces*, 2017, **9**, 24743−24752.

103 J. S. Choi, J. Bae, E. J. Lee and N. C. Jeong, *Inorg. Chem.*, 2018, **57**, 5225−5231.

104 J. Bae, E. J. Lee and N. C. Jeong, *Chem. Commun.*, 2018, **54**, 6458−6471.

105 J. Espín, L. Garzón-Tovar, A. Carné-Sánchez, I. Imaz and D. Maspoch, *ACS Appl. Mater. Interfaces*, 2018, **10**, 9555−9562.

106 C.-D. Wu and M. Zhao, *Adv. Mater.*, 2017, **29**, 1605446.

107 R. Kitaura, G. Onoyama, H. Sakamoto, R. Matsuda, S.-i. Noro and S. Kitagawa, *Angew. Chem. Int. Ed.*, 2004, **43**, 2684−2687.

108 D.-M. Chen, J.-Y. Tian, C.-S. Liu and M. Du*, Chem. Commun*., 2016, **52**, 8413−8416.

109 S. Rostamnia, H. Alamgholiloo, M. Jafari, R. Rookhosh and A. R. Abbasi, *Appl. Organometal. Chem*., 2016, **30**, 954−958.

110 X. Liu, W. Fan, M. Zhang, G. Li, H. Liu, D. Sun, L. Zhao and H. Zhu and W. Guo, *Mater. Chem. Front*., 2018, **2**, 1146−1154.

111 Q. Wenge, W. Yu, L. Chuanqiang, Z. Zongcheng, Z. Xuehong, Z. Guizhen, W. Rui and H. Hong, *Chin. J. Catal*., 2012, **33**, 986−992.

112 S. Rostamnia and F. Mohsenzad, *Mol. Catal.*, 2018, **445**, 12−20.

113 J. Chen, X. Chen, Z. Zhang, Z. Bao, H. Xing, Q. Yang and Q. Ren, *Mol. Catal.*, 2018, **445**, 163−169.

114 F.-G. Xi, Y. Yang, H. Liu, H.-F. Yao and E.-Q. Gao, *RSC Adv*., 2015, **5**, 79216-79223.

115 M. Vandichel, J. Hajek, F. Vermoortele, M. Waroquier, D. E. De Vos and V. Van Speybroeck, *CrystEngComm*., 2015, **17**, 395−406.

116 S. Nagarkar and S. K. Ghosh, *J. Chem. Sci*., 2015, **127**, 627−633.

117 X.-S. Wang, S. Ma, P. M. Forster, D. Yuan, J. Eckert, J. J. López, B. J. Murphy, J. B. Parise and H.-C. Zhou, *Angew. Chem. Int. Ed*., 2008, **47**, 7263−7266.

118 L. Du, Z. Lu, L. Xu and J. Zhang, *RSC Adv.*, 2017, **7**, 21268−21272

119 H. Lyu, Q. Zhang, Y. Wang and J. Duan, *Dalton Trans*., 2018, **47**, 4424−4427.

120 Y. Yan, D. I. Kolokolov, I. da Silva, A. G. Stepanov, A. J. Blake, A. Dailly, P. Manuel, C. C. Tang, S. Yang and M. Schröder, *J. Am. Chem. Soc*., 2017, **139**, 13349−13360.

121 S. Ma, D. Sun, J. M. Simmons, C. D. Collier, D. Yuan and H.-C. Zhou, *J. Am. Chem. Soc.*, 2008, **130**, 1012−1016.

122 G. L. Smith, J. E. Eyley, X. Han, X. Zhang, J. Li, N. M. Jacques, H. G. W. Godfrey, S. P. Argent, L. J. McCormick McPherson, S. J. Teat, Y. Cheng, M. D. Frogley, G. Cinque, S. J. Day, C. C. Tang, T. L. Easun, S. Rudić, A. J. Ramirez-Cuesta, S. Yang and M. Schröder, *Nat. Mater*., 2019, **18**, 1358−1365.

123 Z. Wei, W. Lu, H.-L. Jiang and H.-C. Zhou, *Inorg. Chem*., 2013, **52**, 1164−1166.

124 M. V. Veidis, G. H. Schreiber, T. E. Gough and G. J. Palenik, *J. Am. Chem. Soc*., 1969, **91**, 1859−1860.

125 K. Schlichte, T. Kratzke and S. Kaskel, *Microporous Mesoporous Mater*., 2004, **73**, 81−88.

126 A. A. Talin, A. Centrone, A. C. Ford, M. E. Forster, V. Stavila, P. Haney, R. A. Kinney, V. Szalai, F. El Gabaly, H. P. Yoon, F. Léonard and M. D. Allendorf, *Science*, 2014, **342**, 66−69.

127 C. Prestipino, L Regli, J. G. Vitillo, F. Bonino, A. Damin, C. Lamberti, A. Zecchina, P. L. Solari, K. O. Kongshaug and S. Bordiga, *Chem. Mater.*, 2006, **18**, 1337−1346.

128 A. A. Yakovenko, J. H. Reibenspies, N. Bhuvanesh and H.-C. Zhou, *J. Appl. Crystallogr.*, 2013, **46**, 346−353.

129 R. S. Kumar, S. S. Kumar and M. A. Kulandainathan, *Microporous Mesoporous Mater.*, 2013, **168**, 57−64.

130 Y. D. Liu, J. Kim, W.-S. Ahn and H. J. Choi, *Chem. Commun.*, 2012, **48**, 5635−5637.

131 J. Szanyi, M. Daturi, G. Clet, D. R. Baer and C. H. F. Peden, *Phys. Chem. Chem. Phys.*, 2012, **14**, 4383−4390.

132 C. Chen, T. Wu, D. Yang, P. Zhang, H. Liu, Y. Yang, G. Yang and B. Han, *Chem. Commun.*, 2018, **54**, 5984−5987.

133 S. Bordiga, L. Regli, F. Bonino, E. Groppo, C. Lamberti, B. Xiao, P. S. Wheatly, R. E. Morris and A. Zecchina, *Phys. Chem. Chem. Phys.*, 2007, **9**, 2676−2685.

134 L. J. Murray, M. Dincă, J. Yano, S. Chavan, S. Bordiga, C. M. Brown and J. R. Long, *J. Am. Chem. Soc.*, 2010, **132**, 7856−7857.

135 K. Sumida, J.-H. Her, M. Dincă, L. J. Murray, J. M. Schloss, C. J. Pierce, B. A. Thompson, S. A. FitzGerald, C. M. Brown and J. R. Long, *J. Phys. Chem. C*, 2011, **115**, 8414−8421.

136 M. Soo Lah and H. Chun, *Inorg. Chem.*, 1997, **36**, 1782−1785.

137 J. Jiang, Q. Wang, M. Zhang and J. Bai, *Cryst. Growth Des.*, 2017, **17**, 2223−2227.

138 M. Wickenheisser, F. Jeremias, S. K. Henninger and C. Janiak, *Inorg. Chim. Acta.*, 2013, **407**, 145−152.

139 J. Yang, Y. Wang, L. Li, Z. Zhang and J. Li, *J. Colloid Interface Sci.*, 2015, **456**, 197−205.

140 C. P. Cabello, P. Rumori and G. T. Palomino, *Microporous Mesoporous Mater.*, 2014, **190**, 234−239.

141 J. W. Yoon, H. Chang, S.-J. Lee, Y. K. Hwang, D.-Y. Hong, S.-K. Lee, J. S. Lee, S. Jang, T.-U. Yoon, K. Kwac, Y. Jung, R. S. Pillai, F. Faucher, A. Vimont, M. Daturi, G. Férey, C. Serre, G. Maurin, Y.-S. Bae and J.-S. Chang, *Nature Mater.*, 2017, **16**, 526−532.

142 J. W. Yoon, Y.-K. Seo, Y. K. Hwang, J.-S. Chang, H. Leclerc, S. Wuttke, P. Bazin, A. Vimont, M. Daturi, E. Bloch, P. L. Llewellyn, C. Serre, P. Horcajada, J.-M. Grenèche, A. E. Rodrigues and G. Férey, *Angew. Chem. Int. Ed.*, 2010, **49,** 5949−5952.

143 M. Banerjee, S. Das, M. Yoon, H. J. Choi, M. H. Hyun, S. M. Park, G. Seo and K. Kim, *J. Am. Chem. Soc.*, 2009, **131**, 7524−7525.

144 D.-Y. Hong, Y. K. Hwang, C. Serre, G. Férey and J.-S. Chang, *Adv. Funct. Mater.*, 2009, **19**, 1537−1552.

145 S. Bhattacharjee, C. Chen and W.-S. Ahn, *RSC Adv.*, 2014, **4**, 52500−52525.

146 S. M. Cohen, *Chem. Rev.*, 2012, **112**, 970–1000.

147 Q. Yang, Q. Xu and H. L. Jiang, *Chem. Soc. Rev.*, 2017, **46**, 4774−4808.

148 A. Herbst, A. Khutia and C. Janiak, *Inorg. Chem.*, 2014, **53**, 7319−7333.

149 P. Horcajada, S. Surblé, C. Serre, D.-Y. Hong, Y.-K. Seo, J.-S. Chang, J.-M. Grenèche, I. Margiolaki and G. Férey, *Chem. Commun.*, 2007, 2820–2822.

150 H. R. Moon, D.-W. Lim and M. P. Suh, *Chem. Soc. Rev.*, 2013, **42**, 1807−1824.

151 A. Dhakshinamoorthy and H. Garcia, *Chem. Soc. Rev.*, 2012, **41**, 5262−5284.

152 F. Schröder and R. A. Fischer, *Top. Curr. Chem.*, 2010, **293**, 77−113.

153 M. T. Zhao, K. Yuan, Y. Wang, G. D. Li, J. Guo, L. Gu, W. P. Hu, H. J. Zhao and Z. Y. Tang, *Nature*, 2016, **539**, 76−80.

154 H. Pan, X. Li, D. Zhang, Y. Guan and P. Wu, *J. Mol. Catal. A: Chem.*, 2013, **377**, 108−114.

155 S. Biswas, M. Maes, A. Dhakshinamoorthy, M. Feyand, D. E. De Vos, H. Garcia and N. Stock, *J. Mater. Chem.*, 2012, **22**, 10200−10209.

156 M. Asgari, S. Jawahery, E, D. Bloch, M. R. Hudson, R. Flacau, B, Vlaisavljevich, J. R. Long, C. M. Brown and W. L. Queen, *Chem. Sci.*, 2018, **9**, 4579−4588.

157 K. Sumida, S. Horike, S. S. Kaye, Z. R. Herm, W. L. Queen, C. M. Brown, F. Grandjean, G. J. Long, A. Dailly and J. R. Long, *Chem. Sci.*, 2010, **1**, 184−191.

158 M. Dincă, W. S. Han, Y. Liu, A. Dailly, C. M. Brown and J. R. Long, *Angew. Chem. Int. Ed.*, 2007, **46**, 1419−1422.

159 E. D. Bloch, W. L. Queen, M. R. Hudson, J. A. Mason, D. J. Xiao, L. J. Murray, R. Flacau, C. M. Brown and J. R. Long, *Angew. Chem. Int. Ed.*, 2016, **55**, 8605−8609.

160 M. Dincă, A. Dailly, Y. Liu, C. M. Brown, D. A. Neumann and J. R. Long, *J. Am. Chem. Soc.*, 2006, **128**, 16876−16883.

161 J. H. Cavka, S. Jakobsen, U. Olsbye, N. Guillou, C. Lamberti, S. Bordiga and K. P. Lillerud, *J. Am. Chem. Soc.*, 2008, **130**, 13850−13851.

162 J. Hajek, C. Caratelli, R. Demuynck, K. De Wispelaere, L. Vanduyfhuys, M. Waroquier and V. Van Speybroeck, *Chem. Sci.*, 2018, **9**, 2723−2732.

163 G. C. Shearer, S. Forselv, S. Chavan, S. Bordiga, K. Mathisen, M. Bjørgen, S. Svelle and K. P. Lillerud, *Top Catal.*, 2013, **56**, 770−782.

164 P. M. Schoenecker, C. G. Carson, H. Jasuja, C. J. J. Flemming and K. S. Walton, *Ind. Eng. Chem. Res.*, 2012, **51**, 6513−6519.

165 L. Valenzano, B. Civalleri, S. Chavan, S. Bordiga, M. H. Nilsen, S. Jakobsen, K. P. Lillerud and C. Lamberti, *Chem. Mater.*, 2011, **23**, 1700−1718.

166 C. F. Macrae, I. J. Bruno, J. A. Chisholm, P. R. Edgington, P. McCabe, E. Pidcock, L. Rodriguez-Monge, R. Taylor, J. van de Streek and P. A. Wood, *J. Appl. Crystallogr.*, 2008, **41**, 466−470.

167 E. D. Bloch, L. J. Murray, W. L. Queen, S. Chavan, S. N. Maximoff, J. P. Bigi, R. Krishna, V. K. Peterson, F. Grandjean, O Gary J. Long, B. Smit, S. Bordiga, C. M. Brown and J. R. Long, *J. Am. Chem. Soc.*, 2011, **133**, 14814−14822.

168 M. H. Rosnes, D. Sheptyakov, A. Franz, M. Frontzek, P. D. C. Dietzel and P. A. Georgiev, *Phys. Chem. Chem. Phys.*, 2017, **19**, 26346−26357.

169 M. Märcza, R. E. Johnsen, P. D.C. Dietzel and H. Fjellvåg, *Microporous Mesoporous Mater.*, 2012, **157**, 62−74.

170 K. Lee, J. D. Howe, L.-C. Lin, B. Smit and J. B. Neaton, *Chem. Mat.*, 2015, **27**, 668−678.

171 E. Haldoupis, J. Borycz, H. Shi, K. D. Vogiatzis, P. Bai, W. L. Queen, L. Gagliardi and J. I. Siepmann, *J. Phys. Chem. C*, 2015, **119**, 16058−16071.

172 P. D. C. Dietzel, R. Blom and H. Fjellvåg, *Eur. J. Inorg. Chem.*, 2008, 3624−3632.

173 P. C. Dietzel, Y. Morita, R. Blom and H. Fjellvåg, *Angew. Chem. Int. Ed.*, 2005, **44**, 6354−6358.

174 F. Bonino, S. Chavan, J. G. Vitillo, E. Groppo, G. Agostini, C. Lamberti, P. D. C. Dietzel, C. Prestipino and S. Bordiga, *Chem. Mater.*, 2008, **20**, 4957−4968.

175 R. Sanz, F. Martínez, G. Orcajo, L. Wojtas and D. Briones, *Dalton Trans.*, 2013, **42**, 2392−2398.

176 M. Díaz-García and M. Sánchez-Sánchez, *Microporous Mesoporous Mater.*, 2014, **190**, 248−254.

177 T. Pham, K. A. Forrest, R. Banerjee, G. Orcajo, J. Eckert and B. Space, *J. Phys. Chem. C*, 2015, **119**, 1078−1090.

178 H. Kim, M. Sohail, K. Yim, Y. C. Park, D. H. Chun, H. J. Kim, S. O. Han and J.-H. Moon, *ACS Appl. Mater. Interfaces*, 2019, **11**, 7014−7021.

179 W. Wong-Ng, J. A. Kaduk, H. Wu and M. Suchomel, *Powder Diffr.*, 2012, **27**, 256−262.

180 B. Chen, Y. Yang, F. Zapata, G. Lin, G. Qian and E. B. Lobkovsky, *Adv. Mater.*, 2007, **19**, 1693−1696.

181 H.-H. Wang, L. Hou, Y.-Z. Li, C.-Y. Jiang, Y.-Y. Wang and Z. Zhu, *ACS Appl. Mater. Interfaces*, 2017, **9**, 17969−17976.

182 X.-F. Lu, P.-Q. Liao, J.-W. Wang, J.-X. Wu, X.-W. Chen, C.-T. He, J.-P. Zhang, G.-R. Li and X.-M. Chen, *J. Am. Chem. Soc.*, 2016, **138**, 8336–8339.

183 P.-Q. Liao, X.-Y. Li, J. Bai, C.-T. He, D.-D. Zhou, W.-X. Zhang, J.-P. Zhang and X.-M. Chen, *Chem. – Eur. J.*, 2014, **20**, 11303−11307.

184 P.-Q. Liao, H. Chen, D.-D. Zhou, S.-Y. Liu, C.-T. He, Z. Rui, H. Ji, J.-P. Zhang and X.-M. Chen, *Energy Environ. Sci.*, 2015, **8**, 1011−1016.

185 J. Zhang, J. T. Bu, S. Chen, T. Wu, S. Zheng, Y. Chen, R. A. Nieto, P. Feng and X. Bu, *Angew. Chem.*, 2010, **122**, 9060−9063.

186 http://www.incaweb.org/transit/iupacgcdir/overview.htm; retrieved February 2019.

187 H. Reinsch, *Eur. J. Inorg. Chem.*, 2016, 4290−4299.

188 L. Ma, A. Jin, Z. Xie and W. Lin, *Angew. Chem. Int. Ed.*, 2009, **48**, 9905−9908.

189 S. Barman, H. Furukawa, O. Blacque, K. Venkatesan, O. M. Yaghi, G.-X. Jin and H. Berke, *Chem. Commun.*, 2011, **47**, 11882−11884.

190 K. M. Patil, S. G. Telfer, S. C. Moratti, O. T. Qazvini and L. R. Hanton, *CrystEngComm.*, 2017, **19**, 7236−7243.

191 E. Hastürk, C. Schlüsener, J. Quadbach, A. Schmitz and C. Janiak, *Mircoporous Mesoporous Mater.*, 2019, **280**, 277−287.

192 N. Sahiner and S. Demirci, *React. Funct. Polym.*, 2016, **105**, 60−65.

193 N. Sahiner and S. Demirci, *J. Appl. Polym. Sci.*, 2016, **133**, 44137-1−44139-9.

194 X. Liu, S. Zhang, Y. Xing, S. Wang, P. Yang and H. Li, *New J. Chem.*, 2016, **40**, 9679−9683.

195 Z. Hu and D. Zhao, *CrystEngComm*, 2017, **19**, 4066−4081.

196 J. Jiang and O. M. Yaghi, *Chem. Rev.*, 2015, **115**, 6966−6997.

197 E. Pérez-Mayoral, Z. Musilová, B. Gil, B. Marszalek, M. Položij, P. Nachtigall and J. Čejka, *Dalton Trans.*, 2012, **41**, 4036−4044.

198 A. Vimont, H. Leclerc, F. Maugé, M. Daturi, J.-C. Lavalley, S. Surblé, C. Serre and G. Férey, *J. Phys. Chem. C*, 2007, **111**, 383–388.

199 C. V. Hidalgo, H. Itoh, T. Hattori, M. Niwa and Y. Murakami, *J. Catal.*, 1984, **85**, 362−369.

200 G. Centi, S. Perathoner, F. Trifiro, A. Aboukais, C. F. Aissi and M. Guelton, *J. Phys. Chem.*, 1992, **96**, 2617−2629.

201 F. Lónyi and J. Valyon, *Microporous Mesoporous Mater.*, 2001, **47**, 293−301.

202 D.-W. Kim, H.-G. Kim and D.-H. Cho, *Catal. Commun.*, 2016, **73**, 69−73.

203 A. H. Valekar. K.-H. Cho, S. K. Chitale, D.-Y. Hong, G.-Y. Cha, U.-H. Lee, D. W. Hwang, C. Serre, J.-S. Chang, and Y. K. Hwang, *Green Chem.*, 2016, **18**, 4542−4552.

204 J. Kim, S.-N. Kim, H.-G. Jang, G. Seo and W.-S. Ahn, *Appl. Catal. A*, 2013, **453**, 175−180.

205 H. Jiang, Q. Wang, H. Wang, Y. Chen and M. Zhang, *ACS Appl. Mater. Interfaces*, 2016, **8**, 26817−26826.

206 J. N. Hall and P. Bollini, *Langmuir*, 2020, **36**, 1345−1356.

207 R. Poloni, K. Lee, R. F. Berger, B. Smit and J. B. Neaton, *J. Phys. Chem. Lett.*, 2014, **5**, 861−865.

208 M. Fischer, J. R. B. Gomes and M. Jorge, *Mol. Simul.*, 2014, **40**, 537−556.

209 M. Fischer, F. Hoffmann and M. Fröba, *ChemPhysChem*, 2010, **11**, 2220−2229.

210 T. Pham, K. A. Forrest, D. M. Franz, Z. Guo, B. Chen and B. Space, *Phys. Chem. Chem. Phys.*, 2017, **19**, 18587−18602.

211 J. Borycz, L.-C. Lin, E. D. Bloch, J. Kim, A. L. Dzubak, R. Maurice, D. Semrouni, K. Lee, B. Smit and L. Gagliardi, *J. Phys. Chem. C*, 2014, **118**, 12230−12240.

212 L. Chen, L. Grajciar, P. Nachtigall and T. Düren, *J. Phys. Chem. C*, 2011, **115**, 23074−23080.

213 B. Sun, S. Kayal and A. Chakraborty, *Energy*, 2014, **76**, 419−427.

214 K. S. Walton, A. R. Millward, D. Dubbeldam, H. Frost, J. J. Low, O. M. Yaghi and R. Q. Snurr, *J. Am. Chem. Soc.*, 2008, **130**, 406−407.

215 L. Chen, C. A. Morrison and T. Düren, *J. Phys. Chem. C*, 2012, **116**, 18899−18909.

216 S. Chen, Y. Shi and B. Gu, *AIChE J.*, 2018, **64**, 1383-1388.

217 T. Pham, K. A. Forrest and B. Space, *Phys. Chem. Chem. Phys.*, 2016, **18**, 21421−21430.

218 A. Kundu, K. Sillar and J. Sauer, *J. Phys. Chem. Lett.*, 2017, **8**, 2713−2718.

219 E. O. Fetisov, M. S. Shah, J. R. Long, M. Tsapatsis and J. I. Siepmann, *Chem. Commun.*, 2018, **54**, 10816−10819.

220 K. Yu, K. Kiesling and J. R. Schmidt, *J. Phys. Chem. C*, 2012, **116**, 20480−20488.

221 L. Grajciar, P. Nachtigall, O. Bludský and M. Rubeš, *J. Chem. Theory Comput.*, 2015, **11**, 230−238.

222 D. Yu, A. O. Yazaydin, J. R. Lane, P. D. C. Dietzel and R. Q. Snurr, *Chem. Sci.*, 2013, **4**, 3544−3556.

223 B. Vlaisavljevich, J. Huck, Z. Hulvey, K. Lee, J. A. Mason, J. B. Neaton, J. R. Long, C. M. Brown, D. Alfè, A. Michaelides and B. Smit, *J. Phys. Chem. A*, 2017, **121**, 4139−4151.

224 S. Grimme, *J. Comput. Chem.*, 2006, **27**, 1787−1799.

225 C. Zhou, L. Cao, S. Wei, Q. Zhang and L. Chen, *Comput. Theor. Chem.*, 2011, **976**, 153−160.

226 S. Kristyán and P. Pulay, *Chem. Phys. Lett.*, 1994, **229**, 175−180.

227 M. K. Rana, H. S. Koh, J. Hwang and D. J. Siegel, *J. Phys. Chem. C*, 2012, **116**, 16957−16968.

228 H. Wu, J. M. Simmons, G. Srinivas, W. Zhou and T. Yildirim, *J. Phys. Chem. Lett.*, 2010, **1**, 1946−1951.

229 S. Grimme, *J. Comput. Chem.*, 2004, **25**, 1463−1473

230 S. Grimme, J. Antony, S. Ehrlich and H. Krieg, *J. Chem. Phys.*, 2010, **132**, 154104.

231 M. S. Gordon, Q. A. Smith, P. Xu and L. V. Slipchenko, *Annu. Rev. Phys. Chem.*, 2013, **64**, 553−578.

232 L. Grajciar, A. D. Wiersum, P. L. Llewellyn, J.-S. Chang and P. Nachtigall, *J. Phys. Chem. C*, 2011, **115**, 17925−17933.

233 A. L. Barnes, D. Bykov, D. I. Lyakh and T. P. Straatsma, *J. Phys. Chem. A*, 2019, **123**, 8734−8743.

234 X.-J. Hou, P. He, H. Li and X. Wang, *J. Phys. Chem. C*, 2013, **117**, 2824−2834.

235 K. Sillar, A. Kundu and J. Sauer, *J. Phys. Chem. C*, 2017, **121**, 12789−12799.

236 F. Darkrim and D. Levesque, *J. Chem. Phys.*, 1998, **109**, 4981.

237 J. L. Belof, A. C. Stern and B. Space, *J. Chem. Theory Comput.*, 2008, **4**, 1332−1337.

238 T. Pham, K. A. Forrest, K. McLaughlin, J. Eckert and B. Space, *J. Phys. Chem. C*, 2014, **118**, 22683−22690.

239 K. A. Forrest, T. Pham, K. McLaughlin, J. L. Belof, A. C. Stern, M. J. Zaworotko and B. Space, *J. Phys. Chem. C*, 2012, **116**, 15538−15549.

240 D. Franz, K. A. Forrest, T. Pham and B. Space, *Cryst. Growth Des.*, 2016, **16**, 6024−6032.

241 T. Pham, K. A. Forrest, J. Eckert and B. Space, *Cryst. Growth Des.*, 2016, **16**, 867−874.

242 J.-D. Chai and M. Head-Gordon, *Phys. Chem. Chem. Phys.*, 2008, **10**, 6615−6620.

243 R. Z. Khaliullin, E. A. Cobar, R. C. Lochan, A. T. Bell and M. J. Head- Gordon, *Phys. Chem. A*, 2007, **111**, 8753−8765.

244 Q. Yang and C. Zhong, *J. Phys. Chem. B*, 2006, **110**, 655−658.

245 L. Valenzano, B. Civalleri, K. Sillar and J. Sauer, *J. Phys. Chem. C*, 2011, **115**, 21777−21784.

246 G. Alonso, D. Bahamon, F. Keshavarz, X. Giménez, P. Gamallo and R. Sayós, *J. Phys. Chem. C*, 2018, **122**, 3945−3957.

247 J. J. Potoff and J. I. Siepmann, *AIChE J.*, 2001, **47**, 1676−1682.

248 A. L. Mullen, T. Pham, K. A. Forrest, C. R. Cioce, K. McLaughlin and B. Space, *J. Chem. Theory Comput.*, 2013, **9**, 5421−5429.

249 L. Valenzano, B. Civalleri, S. Chavan, G. T. Palomino, C. O. Arean and S. Bordiga, *J. Phys. Chem. C*, 2010, **114**, 11185−11191.

250 J. Park, H. Kim, S. S. Han and Y. Jung, *J. Phys. Chem. Lett.*, 2012, **3**, 826−829.

251 P. L. Llewellyn, S. Bourrelly, C. Serre, A. Vimont, M. Daturi, L. Hamon, G. De Weireld, J.-S. Chang, D.-Y. Hong, Y. K. Hwang, S. H. Jhung and G. Férey, *Langmuir*, 2008, **24**, 7245−7250.

252 C. Zhang, L. Wang, G. Maurin and Q. Yang, *AIChE J.*, 2018, **64**, 4089−4096.

253 M. Dion, H. Rydberg, E. Schröder, D. C. Langreth and B. I. Lundqvist, *Phys. Rev. Lett.*, 2004, **92**, 246401.

254 J. P. Perdew and Y. Wang, *Phys. Rev. B: Condens. Matter Mater. Phys.*, 1986, **33**, 8800−8802.

255 K. Lee, É. D. Murray, L. Kong. B. I. Lundqvist and D. C. Langreth, *Phys. Rev. B: Condens. Matter Mater. Phys.*, 2010, **82**, 081101.

256 R. Mercado, B. Vlaisavljevich, L.-C. Lin, K. Lee, Y. Lee, J. A. Mason, D. J. Xiao, M. I. Gonzalez, M.T. Kapelewski, J. B. Neaton and B. Smit, *J. Phys. Chem. C*, 2016, **120**, 12590−12604.

257 Y. Hijikata, S. Sakaki, *Inorg. Chem.*, 2014, **53**, 2417−2426.

258 W. You, Y. Liu, J. D. Howe and D. S. Sholl, *J. Phys. Chem. C*, 2018, **122**, 8960−8966.

259 L. Ding and A. Ö. Yazaydin, *J. Phys. Chem. C*, 2012, **116**, 22987−22991.

260 L. Valenzano, J.G. Vitillo, S. Chavan, B. Civalleri, F. Bonino, S. Bordiga and C. Lamberti, *Catal. Today*, 2012, **182**, 67−79.

261 Y. He, R. Krishna and B. Chen, *Energy Environ. Sci.*, 2012, **5**, 9107−9120.

262 S. Xiang, W. Zhou, J. M. Gallegos, Y. Liu and B. Chen, *J. Am. Chem. Soc.*, 2009, **131**, 12415−12419.

263 Y. Ji, L. Ding, Y. Cheng, H. Zhou, S. Yang, F. Li and Y. Li, *J. Phys. Chem. C*, 2017, **121**, 24104−24113.

264 Z. Hulvey, B. Vlaisavljevich, J. A. Mason, E. Tsivion, T. P. Dougherty, E. D. Bloch, M. Head-Gordon, B. Smit, J. R. Long, and C. M. Brown, *J. Am. Chem. Soc.*, 2015, **137**, 10816−10825.

265 S. M. P. Lucena, P. G. M. Mileo, P. F. G. Silvino and C. L. Cavalcante, *J. Am. Chem. Soc.*, 2011, **133**, 19282−19285.

266 F. Jeremias, A. Khutia, S. K. Henninger and C. Janiak, *J. Mater. Chem.*, 2012, **22**, 10148−10151.

267 F. Jeremias, V. Lozan, S. K. Henninger and C. Janiak, *Dalton Trans.* 2013, **42**, 15967−15973.

268 F. Jeremias, D. Fröhlich, C. Janiak and S. K. Henninger, *RSC Adv.*, 2014, **4**, 24073−24082.

269 P. W. Seo, N. A. Khan, Z. Hasan and S. H. Jhung, *ACS Appl. Mater. Interfaces*, 2016, **8**, 29799−29807.

270 V. Pentyala, P. Davydovskaya, M. Ade, R. Pohle and G. Urban, *Sens. Actuators B*, 2016, **225**, 363−368.

271 N. Wang, A. Mundstock, Y. Liu, A. Huang and J. Caro, *Chem. Eng. Sci.*, 2015, **124**, 27−36.

272 J. S. Yeon, W. R. Lee, N. W. Kim, H. Jo, H. Lee, J. H. Song, K. S. Lim, D. W. Kang, J. G. Seo, D. Moon, B. Wiers and C. S. Hong, *J. Mater. Chem. A*, 2015, **3**, 19177−19185.

273 S.-T. Zheng, X. Zhao, S. Lau, A. Fuhr, P. Feng and X. Bu, *J. Am. Chem. Soc.*, 2013, **135**, 10270−10273.

274 M. J. Ingleson, R. Heck, J. A. Gould and M. J. Rosseinsky, *Inorg. Chem*., 2009, **48**, 9986−9988.

275 S. Zhao, J. Mei, H. Xu, W. Liu, Z. Qu, Y. Cui and N. Yan, *J. Hazard. Mater.*, 2018, **35**1, 301−307.

276 S. N. Kim, S.-T. Yang, J. Kim, J.-E. Park and W.-S. Ahn, *CrystEngComm.*, 2012, **14**, 4142−4147.

277 M. Xu, S. Yuan, X.-Y. Chen, Y.-J. Chang, G. Day, Z.-Y. Gu and H.-C. Zhou, *J. Am. Chem. Soc.*, 2017, **139**, 8312−8319.

278 T. M. McDonald, D. M. D’Alessandro, R. Krishna and J. R. Long, *Chem. Sci.*, 2011, **2**, 2022−2028.

279 N. Al-Janabi, H. Deng, J. Borges, X. Liu, A. Garforth, F. R. Siperstein and X. Fan, *Ind. Eng. Chem. Res.*, 2016, **55**, 7941−7949.

280 X. Du, R. Fan, L. Qiang, K. Xing, H. Ye, X. Ran, Y. Song, P. Wang and Y. Yang, *ACS Appl. Mater. Interfaces*, 2017, **9**, 28939−28948.

281 B. M. Wiers, M.-L. Foo, N. P. Balsara and J. R. Long, *J. Am. Chem. Soc.*, 2011, **133**, 14522−14525.

282 H. Wang, J. Xu, D.-S. Zhang, Q. Chen, R.-M. Wen, Z. Chang and X.-H. Bu, *Angew. Chem. Int. Ed.*, 2015, **54**, 5966−5970.

283 D. Denysenko, M. Grzywa, J. Jelic, K. Reuter and D. Volkmer, *Angew. Chem. Int. Ed.*, 2014, **53**, 5832−5836.

284 E. Žunkovič, M. Mazaj, G. Mali, M. Rangus, T. Devic, C. Serre and N. Z. Logara, *J. Solid State Chem.*, 2015, **225**, 209−215.

285 Z. Wang and S. M. Cohen, *Chem. Soc. Rev.*, 2009, **38**, 1315−1329.

286 K. K. Tanabe and S. M. Cohen, *Chem. Soc. Rev.*, 2011, **40**, 498−519.

287 Z. R. Herm, J. A. Swisher, B. Smit, R. Krishna and J. R. Long, *J. Am. Chem. Soc.*, 2011, **133**, 5664−5667.

288 A. Demessence, D. M. D´Alessandro, M. L. Foo and J. R. Long, *J. Am. Chem. Soc.*, 2009, **131**, 8784−8786.

289 K. C. Kim, *J. Organomet. Chem.*, 2018, **854**, 94−105.

290 H. Frost, T. Düren and R. Q. Snurr, *J. Phys. Chem. B*, 2006, **110**, 9565−9570.

291 J.-R. Li, R. J. Kuppler and H.-C. Zhou, *Chem. Soc. Rev.*, 2009, **38**, 1477−1504.

292 A. Ö. Yazaydin, A. I. Benin, S. A. Faheem, P. Jakubczak, J. J. Low, R. R. Willis and R. Q. Snurr, *Chem. Mater.*, 2009, **21**, 1425−1430.

293 E. J. García, J. P. S. Mowat, P. A. Wright, J. Pérez-Pellitero, C. Jallut and G. D. Pirngruber, *J. Phys. Chem. C*, 2012, **116**, 26636−26648.

294 H. Wu, W. Zhou and T. Yildirim, *J. Am. Chem. Soc.*, 2009, **131**, 4995−5000.

295 W. L. Queen, C. M. Brown, D. K. Britt, P. Zajdel, M. R. Hudson and O. M. Yaghi, *J. Phys. Chem. C*, 2011, **115**, 24915−24919.

296 J. Getzschmann, I. Senkovska, D. Wallacher, M. Tovar, D. Fairen-Jimenez, T. Düren, J. M. van Baten, R. Krishna and S. Kaskel, *Microporous Mesoporous Mater.*, 2010, **136**, 50−58.

297 B. Pato-Doldán, M. H. Rosnes and P. D. C. Dietzel, *ChemSusChem*, 2017, **10**, 1710−1719.

298 M. I. Gonzalez, J. A. Mason, E. D. Bloch, S. J. Teat, K. J. Gagnon, G. Y. Morrison, W. L. Queen and J. R. Long, *Chem. Sci.*, 2017, **8**, 4387−4398.

299 W. S. Drisdell, R. Poloni, T. M. McDonald, J. R. Long, B. Smit, J. B. Neaton, D. Prendergast and J. B. Kortright, *J. Am. Chem. Soc.*, 2013, **135**, 18183−18190.

300 M. Asgari, R. Semino, P. Schouwink, I. Kochetygov, O. Trukhina, J. D. Tarver, S. Bulut, S. Yang, C. M. Brown, M. Ceriotti and W. L. Queen, *Eur. J. Inorg. Chem.*, 2019, 1147−1154.

301 A. L. Spek, Structure Validation in Chemical Crystallography, *Acta Crystallogr., Sect. B: Struct. Sci.*, 2009, **65**, 148−155.

302 R. B. Getman, Y.-S. Bae, C. E. Wilmer and R. Q. Snurr, *Chem. Rev.*, 2012, **112**, 703−723.

303 S. O. Odoh, C. J. Cramer, D. G. Truhlar and L. Gagliardi, *Chem. Rev.*, 2015, **115**, 6051−6111.

304 M. Paik Suh, H. J. Park, T. K. Prasad and D.-W. Lim, *Chem. Rev.*, 2012, **112**, 782−835.

305 H. W. Langmi, J. Ren, B. North, M. Mathe and D. Bessarabov, *Electrochim. Acta*, 2014, **128**, 368−392.

306 V. K. Peterson, Y. Liu, C. M. Brown and C. J. Kepert, *J. Am. Chem. Soc.*, 2006, **128**, 15578−15579.

307 P. D. C. Dietzel, B. Panella, M. Hirscher, R. Blom and H. Fjellva, *Chem. Commun.*, 2006, **2006**, 959−961.

308 K. Sumida, C. M. Brown, Z. R. Herm, S. Chavan, S. Bordiga and J. R. Long, *Chem. Commun.*, 2011, **47**, 1157−1159.

309 D. Gygi, E. D. Bloch, J. A. Mason, M. R. Hudson, M. I. Gonzalez, R. L. Siegelman, T. A. Darwish, W. L. Queen, C. M. Brown and J. R. Long, *Chem. Mater.*, 2016, **28**, 1128−1138.

310 D. J. Levine, T. Runčevski, M. T. Kapelewski, B. K. Keitz, J. Oktawiec, D. A. Reed, J. A. Mason, H. Z. H. Jiang, K. A. Colwell, C. M. Legendre, S. A. FitzGerald and J. R. Long, *J. Am. Chem. Soc.*, 2016, **138**, 10143−10150.

311 K. Sumida, D. Stück, L. Mino, J.-D. Chai, E. D. Bloch, O. Zavorotynska, L. J. Murray, M. Dincă, S. Chavan, S. Bordiga, M. Head-Gordon and J. R. Long, *J. Am. Chem. Soc.*, 2013, **135**, 1083−1091.

312 X. Lin, I. Telepeni, A. J. Blake, A. Dailly, C. M. Brown, J. M. Simmons, M. Zoppi, G. S. Walker, K. M. Thomas, T. J. Mays, P. Hubberstey, N. R. Champness and M. Schröder, *J. Am. Chem. Soc.*, 2009, **131**, 2159−2171.

313 B. Panella, M. Hirscher, H. Pütter and U. Müller, *Adv. Funct. Mater.*, 2006, **16**, 520−524.

314 C. Chen, Y.-R. Lee and W.-S. Ahn, *J. Nanosci. Nanotechnol.*, 2016, **16**, 4291−4301.

315 Z. Zhang, Y. Zhao, Q. Gong, Z. Li and J. Li, *Chem. C*ommun., 2013, **49**, 653−661.

316 L.-C. Lin, J. Kim, X. Kong, E. Scott, T. M. McDonald, J. R. Long, J. A. Reimer and B. Smit, *Angew. Chem. Int. Ed.*, 2013, **52**, 4410−4413

317 C. Chen, X. Feng, Q. Zhu, R. Dong, R. Yang, Y. Cheng, C. He and *Inorg. Chem.*, 2019, **58**, 2717−2728.

318 P. D. C. Dietzel, R. E. Johnsen, H. Fjellvåg, S. Bordiga, E. Groppo, S. Chavan and R. Blom, *Chem. Commun.*, 2008, **2008**, 5125−5127.

319 R. M. Marti, J. D. Howe, C. R. Morelock, M. S. Conradi, K. S. Walton, D. S. Sholl and S. E. Hayes, *J. Phys. Chem. C*, 2017, **121**, 25778−25787.

320 X. Kong, E. Scott, W. Ding, J. A. Mason, J. R. Long and J. A. Reimer, *J. Am. Chem. Soc.*, 2012, **134**, 14341−14344.

321 P. D. C. Dietzel, V. Besikiotis and R. Blom, *J. Mater. Chem.*, 2009, **19**, 7362−7370.

322 S. A. FitzGerald, J. M. Schloss, C. J. Pierce, B. Thompson, J. L. C. Rowsell, K. Yu and J. R. Schmidt, *J. Phys. Chem. C*, 2015, **119**, 5293−5300.

323 J. G. Vitillo and G. Ricchiardi, *J. Phys. Chem. C*, 2017, **121**, 22762−22772.

324 Y. Yao, N. Nijem, J. Li, Y. J. Chabal, D. C. Langreth and T. Thonhauser, *Phys. Rev. B: Condens. Matter Mater. Phys*, 2012, **85**, 064302.

325 N. Nijem, P. Canepa, L. Z. Kong, H. H. Wu, J. Li, T. Thonhauser and Y. J. Chabal, *J. Phys.: Condens. Matter*, 2012, **24**, 424203.

326 J. A. Mason, K. Sumida, Z. R. Herm, R. Krishna and J. R. Long, *En*ergy Environ. Sci., 2011, **4**, 3030−3040.

327 W. D. Wang, B. E. G. Lucier, V. V. Terskikh, W. Wang and Y. Huang, *J. Phys. Chem. Lett.*, 2014, **5**, 3360−3365.

328 J. Yang, H. Bai, F. Zhang, J. Liu, J. Winarta, Y. Wang and B. Mu, *J. Chem. Eng. Data*, 2019, J*. Chem. Eng. Data*, 2019, **64**, 5814−5823.

329 J. Moellmer, A. Moeller, F. Dreisbach, R. Glaeser and R. Staudt, *Microporous Mesoporous Mater.*, 2011, **138**, 140−148.

330 B. Bonelli, B. Civalleri, B. Fubini, P. Ugliengo, C. O. Areán and E. Garrone, *J. Phys. Chem. B*, 2000, **104**, 10978−10988.

331 M. D'Amore, B. Civalleri, I. J. Bush, E. Albanese and M. Ferrabone, *J. Phys. Chem. C*, 2019, **123**, 28677−28687.

332 I. Kochetygov, S. Bulut, M. Asgari and W. L. Queen, *Dalton Trans.*, 2018, **47**, 10527−10535.

333 B. Li, Z. Zhang, Y. Li, K. Yao, Y. Zhu, Z. Deng, F. Yang, X. Zhou, G. Li, H. Wu, N. Nijem, Y. J. Chabal, Z. Lai, Y. Han, Z. Shi, S. Feng and J. Li, *Angew. Chem. Int. Ed.*, 2012, **51**, 1412−1415.

334 C.-Y. Wang, P. Ray, Q. Gong, Y. Zhao, J. Li and A. D. Lueking, *Phys. Chem. Chem. Phys.*, 2015, **17**, 26766−26776.

335 P. Chowdhury, S. Mekala, Frieder Dreisbach and S. Gumma, *Microporous Mesoporous Mater.*, 2012, **152**, 246−252.

336 A. C. McKinlay, B. Xiao, D. S. Wragg, P. S. Wheatley, I. L. Megson and R. E. Morris, *J. Am. Chem. Soc.*, 2008, **130**, 10440−10444.

337 B. Xiao, P. S. Wheatley, X. Zhao, A. J. Fletcher, S. Fox, A. G. Rossi, I. L. Megson, S. Bordiga, L. Regli, K. M. Thomas and R. E. Morris, *J. Am. Chem. Soc.*, 2007, **129**, 1203−1209.

338 N. Nijem, H. Bluhm, M. L. Ng, M. Kunz, S. R. Leone and M. K. Gilles, *Chem. Commun.*, 2014, **50**, 10144−10147.

339 M. Todaro, G. Buscarino, L. Sciortino, A. Alessi, F. Messina, M. Taddei, M. Ranocchiari, M. Cannas and F. M. Gelardi, *J. Phys. Chem. C*, 2016, **120**, 12879−12889

340 P. D. C. Dietzel, R. E. Johnson, R. Blom and H. Fjellvag, *Chem. – Eur. J.*, 2008, **14**, 2389−2397.

341 B. Barth, M. Mendt, A. Pöppl and M. Hartmann, *Microporous Mesoporous Mater.*, 2015, **216**, 97−110.

342 R. Matsuda, R. Kitaura, S. Kitagawa, Y. Kubota, R. V. Belosludov, T. C. Kobayashi, H. Sakamoto, T. Chiba, M. Takata, Y. Kawazoe and Y. Mita, *Nature*, 2005, **436**, 238−241.

343 X. Rao, J. Cai, J. Yu, Y. He, C. Wu, W. Zhou, T. Yildirim, B. Chen and G. Qian, *Chem. Commun.*, 2013, **49**, 6719−6721.

344 Z. Zhang, S. Xiang and B. Chen, *CrystEngComm*, 2011, **13**, 5983−5992.

345 L. Zhang, K. Jiang, Y. Li, D. Zhao, Y. Yang, Y. Cui, B. Chen, and G. Qian, *Cryst. Growth Des.*, 2017, **17**, 2319−2322.

346 T. Xia, J. Cai, H. Wang, X. Duan, Y. Cui, Y. Yang and G. Qian, *Microporous Mesoporous Mater.*, 2015, **215**, 109−115.

347 C. Song, J. Hu, Y. Ling, Y. Feng, D.-L. Chen, and Y. He, *Dalton Trans.*, 2015, **44**, 14823−14829.

348 X. Duana, Y. Heb, Y. Cuia, Y. Yanga, R. Krishna, B. Chen, and G. Qian, *RSC Adv.*, 2014, **4**, 23058−23063.

349 X. Duan, Y. Zhou, R. Lv, B. Yu, H. Chen, Z. Ji, Y. Cui, Y. Yang and G. Qian, *J. Solid State Chem.*, 2018, **260**, 31−33.

350 L. Zhang, C. Zou, M. Zhao, K. Jiang, R. Lin, Y. He, C.-D. Wu, Y. Cui, B. Chen and G. Qian, *Cryst. Growth Des.*, 2016, **16**, 7194−7197.

351 A. Luna-Triguero, J. M. Vicent-Luna, R. M. Madero-Castro, P. Gómez-Álvarez and S. Calero, *ACS Appl. Mater. Interfaces*, 2019, **11**, 31499−31507.

352 A. A. Fomkin, A. Y. Tsivadze, O. E. Aksyutin, A. G. Ishkov, A. A. Pribylov, A.V. Shkolin, I. E. Men'shchikov, K. V. Romanov, R. V. Teterevlev, U. Müller, L. Arnold and M. Piontek, *Prot. Met. Phys. Chem. Surf.*, 2018, **54**, 347−353.

353 M. K. Taylor, T. Runčevski, J. Oktawiec, M.I. Gonzalez, R.L. Siegelman, J.A. Mason, J. Ye, C.M. Brown and J. R. Long, *J. Am. Chem. Soc.*, 2016, **138**, 15019−15026.

354 F. Gándara, H. Furukawa, S. Lee and O.M. Yaghi, *J. Am. Chem. Soc.*, 2014, **136**, 5271−5274.

355 Y. Peng, V. Krungleviciute, I. Eryazici, J.T. Hupp, O.K. Farha and T. Yildirim, *J. Am. Chem. Soc.*, 2013, **135**, 11887−11894.

356 M. Zhang, W. Zhou, T. Pham, K.A. Forrest, W. Liu, Y. He, H. Wu, T. Yildirim, B. Chen and B. Space, *Angew. Chem. Int. Ed.*, 2017, **56**, 11426−11430.

357 Y. He, W. Zhou, G. Qian and B. Chen, *Chem. Soc. Rev.*, 2014, **43**, 5657−5678.

358 H. Wu, J. M. Simmons, Y. Liu, C. M. Brown, X.-S. Wang, S. Ma, V. K. Peterson, P. D. Southon, C. J. Kepert, H.-C. Zhou, T. Yildirim and W. Zhou, *Chem. Eur. – J.*, 2010, **16**, 5205−5214.

359 V. J. Witherspoon, R. Mercado, E. Braun, A. Mace, J. Bachman, J. R. Long, B. Blümich, B. Smit and J. A. Reimer, *J. Phys. Chem. C*, 2019, **123**, 12286−12295.

360 Z. Guo, H. Wu, G. Srinivas, Y. Zhou, S. Xiang, Z. Chen, Y. Yang, W. Zhou, M. O'Keeffe and B. Chen, *Angew. Chem. Int. Ed.*, 2011, **50**, 3178−3181.

361 W. Zhou, *Chem. Rec.*, 2010, **10**, 200.

362 J.-Y. Lee, T. C. Keener and Y. J. J. Yang, *Air Waste Manage. Assoc.*, 2012, **59**, 725−732.

363 R. K. Srivastava and W. J. Jozewicz, *Air Waste Manage. Assoc*. 2011, **51**, 1676−1688.

364 International Energy Agency, World Energy Outlook 2016, IEA Publications: Paris, 2016.

365 Y. Zhang, P. Zhang, W. Yu, J. Zhang, J. Huang, J. Wang, M. Xu, Q. Deng, Z. Zeng and S. Deng, *ACS Appl. Mater. Interfaces*, 2019, **11**, 10680−10688.

366 B. Brandt, A. Nuhnen, M. Lange, J. Möllmer, O. Weingart and C. Janiak, *ACS Appl. Mater. Interfaces*, 2019, **11**, 17350−17358.

367 D. Dietrich, C. Licht, A. Nuhnen, S.-P. Höfert, L. De Laporte and C. Janiak, *ACS Appl. Mater. Interfaces*, 2019, **11**, 19654−19667.

368 T. G. Glover, G. W. Peterson, B. J. Schindler, D. Britt and O. M. Yaghi, *Chem. Eng. Sci.*, 2011, **66**, 163−170.

369 J. B. DeCoste, T. J. Demasky, M. J. Katz, O. K. Farha and J. T. A. Hupp, *New J. Chem.*, 2015, **39**, 2396−2399.

370 K. Sumida, D. L. Rogow, J. A. Mason, T. M. McDonald, E. D. Bloch, Z. R. Herm, T.-H. Bae and J. R. Long, *Chem. Rev.*, 2012, **112**, 724−781.

371 J. Liu, P. K. Thallapally, B. P. McGrail, D. R. Brown and J. Liu, *Chem. Soc. Rev.*, 2012, **41**, 2308−2322.

372 J.-R. Li Y. Ma, M.-C. McCarthy, J. Sculley, J. Yu, H.-K. Jeong, P. B. Balbuena and H.-C. Zhou, *Coord. Chem. Rev.*, 2011, **225**, 1791−1823.

373 X. Lu, D. Jin, S. Wei, Z. Wang, C. An and W. Guo, *J. Mater. Chem*. A, 2015, **3**, 12118−12132.

374 Z. Y Yeo, T.L. Chew, P. W. Zhu, A. R. Mohamed and S.-P. Chai, *J. Nat. Gas Chem.*, 2012, **21**, 282−298.

375 A. K. Datta and P. K. Sen, *J. Membr. Sci.*, 2006, 283, 291−300.

376 B. Seoane, J. Coronas, I. Gascon, M. E. Benavides, O. Karvan, J. Caro, F. Kapteijn and J. Gascon, *Chem. Soc. Rev.*, 2015, **44**, 2421−2454

377 S. Nandi, R. Maity, D. Chakraborty, H. Ballav and R. Vaidhyanathan, *Inorg. Chem.*, 2018, **57**, 5267−5272.

378 P. Mishra, S. Edubilli, B. Mandal and S. Gumma, *J. P*hys. Chem. *C*, 2014, **118**, 6847−6855.

379 J. N. Hall and P. Bollini, *React. Chem. Eng.*, 2019, **4**, 207−222.

380 A. Henschel, K. Gedrich, R. Kraehnert and S. Kaskel, *Chem. Commun.*, 2008, 4192−4194.

381 S. Horike, M. Dincă, K. Tamaki and J. R. Long, *J. Am. Chem. Soc.*, 2008, **130**, 5854−5855.

382 S. Wang, L. Bromberg, H. Schreuder-Gibson and T.A. Hatton, *ACS Appl. Mater. Interfaces*, 2013, **5**, 1269−1278.

383 P.-Z. Li, X.-J. Wang, J. Liu, H.S. Phang, Y. Li and Y. Zhao, *Chem. Mater.*, 2017, **29**, 9256−9261.

384 L. Alaerts, E. Ségiun, H. Poelman, F. Thibault-Starzyk, P. A. Jacobs and D. E. De Vos, *Chem. – Eur. J.*, 2006, **12**, 7353−7363

385 G. Akiyama, R. Matsuda, H. Sato and S. Kitagawa, *Chem. Asian J.*, 2014, **9**, 2772−2777.

386 D. Wang, R. Huang, W. Liu, D. Sun and Z. Li, *ACS Cata*l., 2014, **4**, 4254−4260.

387 M. Fujita, Y. J. Kwon, S. Washizu and K. Ogura, *J. Am. Chem. Soc.*, 1994, **116**, 1151−1152.

388 H. Liu, Y. W. Li, H. Jiang, C. Vargas and R. Luque, *Chem. Commun.*, 2012, **48**, 8431−8433.

389 H. Liu, Y. W. Li, R. Luque and H. Jiang, *Adv. Synth. Catal.*, 2011, **353**, 3107−3113.

390 M. Y. Masoomi, M. Bagheri and A. Morsali, *Inorg. Chem.*, 2015, **54**, 11269−11275.

391 M. Y. Masoomi, M. Bagheri, A. Morsali and P. C. Junk, *Inorg. Chem. Front.*, 2016, **3**, 944−951.

392 T. Rasheed and F. Nabeel, *Coord. Chem. Rev.*, 2019, **401**, 213065.

393 N. Abdollahi and A. Morsali, *Anal. Chim. Acta*, 2019, **1064**, 119−125.

394 D. Ma, W. Wang, Y. Li, J. Li, C. Daiguebonne, G. Calvez, O. Guillou, *CrystEngComm*, 2010, **12**, 4372−4377.

395 Z. Guo, H. Xu, S. Su, J. Cai, S. Dang, S. Xiang, G. Qian, H. Zhang, M. O´Keeffe and B. Chen, *Chem. Commun.*, 2011, **47**, 5551−5553.

The article is reproduced from Ref. 116 with permission from the The Royal Society of Chemistry 2020.

Coordinatively Unsaturated Metal Sites (Open Metal Sites) in Metal-Organic Frameworks: Design and Applications†

Ülkü Kökçam-Demir,[§a] Anna Goldman,[§a] Leili Esrafili,[b] Maniya Gharib,[b] Ali Morsali[§b,*]
Oliver Weingart[c] and Christoph Janiak[§a,*]

[a] Institut für Anorganische Chemie und Strukturchemie, Heinrich-Heine-Universität Düsseldorf, D-40204 Düsseldorf Germany. Email: janiak@hhu.de

[b] *Department of Chemistry, Faculty of Sciences, Tarbiat Modares University, P.O. Box 14115-175, Tehran, Islamic Republic of Iran. Email: morsali_a@modares.ac.ir*

[c] *Institut für Theoretische Chemie und Computerchemie, Heinrich-Heine-Universität Düsseldorf, D-40204 Düsseldorf Germany. Email: Oliver.Weingart@hhu.de*

† § These authors contributed equally.

E-mail addresses: Uelkue.Koekcam@hhu.de, Anna.Goldman@hhu.de, leiliesrafili@gmail.com, mania.gha1990@gmail.com, morsali_a@modares.ac.ir; Oliver.Weingart@hhu.de, janiak@hhu.de.

Table S1 Calculated binding energies –ΔE and isosteric heats of adsorption (–ΔH, –Q_{st}) values for CO_2 in relation to the different OMS, using computational methods in comparison to –Q_{st}^0 values from experimental studies.

MOF	M-MOF-74								HKUST-1
OMS	**Mg**	**Cr**	**Mn**	**Fe**	**Co**	**Ni**	**Cu**	**Zn**	**Cu**
Exp.	39.0-47.0[1,2,3,4,6,17]	/	31.7-31.9[6,17]	33.2-34.3[6,17]	33.6-37.0[3,4,6,17]	38.6-41.0[3,4,6,17]	22.1-24.0[6,17]	26.8-30.6[1,6,17]	29.0[5]
MP2	40.5[6]		30.3[6]	24.2[6]	29.7[6]	31.2[6]	16.2[6]	29.7[6]	
LDA	54.3[6] (51.2)[7]		38.4[6]	38.1[6]	42.5[6] (36.6)[7]	43.1[6]	31.0[6]	40.2[6]	(30.6)[7] 32.78
GGA-PW91	23.9[6]		13.3[6]	9.4[6]	10.6[6]	12.5[6]	6.0[6]	12.6[6]	
GGA-PBE	(20.2)[7]				(8.3)[7]	(8.8)[7]			(9.4)[7]
Hybrid-GGA B3LYP	23.9[6] 27.1[9]		12.1[6]	4.5[6]	7.06	11.6[6]	3.5[6]	11.8[6]	
DFT-D2	(39.7)[7]				(29.0)[7]	(30.6)[7]			(18.5)[7]
PBE-D2	40.5[10]		33.8[10]	33.9[10]	33.7[10]	36.9[10]	27.1[10]	30.5[10]	21.0[11]
PBE-D3	39.7[10]		34.6[10] 32.4[12]	34.5[10]	33.9[10] 29.5[12]	36.7[10] 32.3[12]	28.0[10] 21.5[12]	31.8[10]	21.0[11]
PBE-D3 BJ	40.5[10]		35.5[10]	35.3[10]	34.5[10]	37.4[10]	27.8[10]	31.0[10]	
B3LYP-D*	(37.9)[13,14]					(35.5)[14]		(31.7)[14]	
ωB97X-D	(44.9)[9]								
optB88-vdW	(52.8)[7] 53.1[10]	46.2[10]		46.5[10]	(39.9)[7] 46.7[10]	(43.1)[7] 51.0[10]	37.9[10]	41.6[10]	
optB86b-vdW	52.510 (53.9)[7]	45.9[10]		46.1[10]	46.6[10] (40.4)[7]	50.7[10] (45.6)[7]	37.5[10]	41.3[10]	28.0[11] (25.4)[7]
vdW-DF	(40.5)[15]								
PBE-vdW	(58.3)[15]								
optPBE-vdW	(57.2)[7]				(43.7)[7]	(46.6)[7]			(27.7)[7]
revPBE-vdW	(47.3)[7]				(37.2)[7]	(37.8)[7]			(23.3)[7]
rPW86-vdW	(46.2)[7]				(32.5)[7]	(34.5)[7]			(21.5)[7]
vdW-DF2	(37.4)[15] (44.7)[16]	38.1[10]		38.1[10]	37.7[10]	41.5[10]	30.9[10]	34.0[10]	22.0[11]
vdW-DF2 + U	(40.9)[17] (41.0)[29]		(33.9)[17] (27.0)[29]	(34.1)[17] (34.0)[29]	(33.8)[17] (34.0)[29]	(37.3)[17] (34.0)[29]	(27.1)[17] (37.0)[29]	(30.2)[17] (27.0)[29]	(30.0)[29]
rev-vdW-DF2	43.6[10]		37.0[10]	37.3[10]	37.4[10]	41.3[10]	28.2[10]	32.1[10]	
B3LYP+D*/MP2	(42.7)[14]					(40.5)[14]		(39.0)[14]	
DFT/CC									28.0[11]
QM/MM DFT/MP2	48.2[6]		37.2[6]	32.2[6]	37.0[6]	39.1[6]	23.9[6]	37.0[6]	
GCMC PHAST*									30[18]
MOF	**M-btt**								
Exp.		36.7[19]		51.2[19]			30.7[19]		
vdW-DF+ U		(36.6)[19]		(51.7)[19]			(29.4)[19]		

Table S2 Calculated –ΔE and (–ΔH, $-Q_{st}$) values for H_2 in relation to the different OMS, using computational methods in comparison to $-Q_{st}^0$ from experimental studies.

MOF	M-MOF-74							
OMS	**Mg**	**Cr**	**Mn**	**Fe**	**Co**	**Ni**	**Cu**	**Zn**
Exp.	10.1-10.7[20,24]		8.8[21,24]	9.7[21]	10.7[21,24]	12.9-13.5[22,23,24]	6.1[28]	8.5-8.8[24,25]
DL	(6.5)[20]							
BSS	(6.0)[20]							
BSSP	(10.9)[20]				(12.4)[26]	(14.0)[26]	(6.5)[27]	(8.7)[26]
LDA	24.8[24]		22.4[24]		35.6[24]	39.0[24]		22.0[24]
GGA-PBE	12.4[24]		11.1[24]		12.8[24]	15.0[24]		10.5[24]
PBE+D			13.9[28]				11.3[28]	
vdW-DF2	(10.0)[29]	(6.0)[29]	(8.0)[29]	(9.0)[29]	(9.0)[29]	(10.0)[29]	(6.0)[29]	(8.0)[29]
MOF	**MOF-505**							
Exp.							6.1[24,]30	
PBE							13.4[31]	

Table S3 Calculated –ΔE and (–ΔH, –Q_{st}) values for C_2H_2, CO, CH_4 in relation to the different OMS, using computational methods in comparison to –Q_{st}^0 from experimental studies.

C_2H_2									
MOF	**M-MOF-74**								
OMS	**Mg**	**Cr**	**Mn**	**Fe**	**Co**	**Ni**	**Cu**	**Zn**	
Exp.	41.0[32]			45.0-46.5[32,33]	45.0[32]				30.4-39.0[32,34]
DFT-PBE									(30.0)[35]
vdW-DF2	(38.0)[29]	(31.0)[29]	(38.0)[29]	(37.0)[29]	(36.0)[29]	(37.0)[29]	(20.0)[29]	(35.0)29	
				Cu-paddle-wheel-MOFs					
MOF	**MOF-505**	**PCN-46**	**NJU-Bai12**	**ZJU-40**	**NOT-101**	**NOT-102**	**NOT-103**	**NOT-106**	**NOT-108**
Exp.	24.7[38,36]			34.5[38,37]	37.1[38,36]	22.0[38,37]	30.8[38,36]		
GCMC	(27.7)[38]	(24.1)[38]	(22.9)[38]	(23.9)[38]	(23.8)[38]	(24.7)[38]	(23.3)[38]	(25.5)[38]	(26.2)[38]
PBE	33.6[38]	34.8[38]	31.4[38]	30.8[38]	30.7[38]	33.7[38]	31.2[38]	31.8[38]	30.8[38]
CO									
MOF					**M-MOF-74**				
OMS	**Mg**	**Cr**	**Mn**	**Fe**	**Co**	**Ni**	**Cu**	**Zn**	
Exp.	38.0[3]				55.5[3]	59.7[3]			
B3LYP-D*	(30.0)[14]					(41.9)[14]		(24.8)[14]	
vdW-DF2	(35.0)[29]	(20.0)[29]	(29.0)[29]	(30.0)[29]	(30.0)[29]	(34.0)[29]	(16.0)[29]	(25.0)[29]	
B3LYP+D*/MP2	(41.2)[14]					(50.3)[14]		(39.8)	
MOF	**MIL-101**								
Exp.									
ωB97X-D		(37.4)[9]							
CH_4									
MOF					**M-MOF-74**				
Exp.	18.2[6]		18.2[6]		19.2[6]	19.0[6]		18.3[39]	
vdW-DF2+U	(19.0)[29]	(14.0)[29]	(19.0)[29]	(19.0)[29]	(18.0)[29]	(19.0)[29]	(14.0)[29]	(19.0)[29]	
MOF					**HKUST-1**				
DFT/CC-PES							13.23[40]		

1 J. M. Simmons, H. Wu, W. Zhou and T. Yildirim, *Energy Environ. Sci.*, 2011, **4**, 2177−2185.

2 D. Britt, H. Furukawa, B. Wang, T. G. Glover and O. M. Yaghi, *PNAS*, 2009, **106**, 20637−20640.

3 H. Kim, M. Sohail, K. Yim, Y. C. Park, D. H. Chun, H. J. Kim, S. O. Han and J.-H. Moon, *ACS Appl. Mater. Interfaces*, 2019, **11**, 7014−7021.

4 S. R. Caskey, A. G. Wong-Foy and A. J. Matzger, *J. Am. Chem. Soc.*, 2008, **130**, 10870−10871.

5 L. Grajciar, A. D. Wiersum, P. L. Llewellyn, J.-S. Chang and P. Nachtigall, *J. Phys. Chem. C*, 2011, **115**, 17925−17933.

6 D. Yu, A. O. Yazaydin, J. R. Lane, P. D. C. Dietzel and R. Q. Snurr, *Chem. Sci.*, 2013, **4**, 3544−3556.

7 M. K. Rana, H. S. Koh, J. Hwang and D. J. Siegel, *J. Phys. Chem. C*, 2012, **116**, 16957−16968.

8 H. Wu, J. M. Simmons, G. Srinivas, W. Zhou and T. Yildirim, *J. Phys. Chem. Lett.*, 2010, **1**, 1946−1951.

9 K. Yu, K. Kiesling and J. R. Schmidt, *J. Phys. Chem. C*, 2012, **116**, 20480−20488.

10 B. Vlaisavljevich, J. Huck, Z. Hulvey, K. Lee, J. A. Mason, J. B. Neaton, J. R. Long, C. M. Brown, D. Alfè, A. Michaelides and B. Smit, *J. Phys. Chem. A*, 2017, **12**1, 4139−4151.

11 L. Grajciar, P. Nachtigall, O. Bludský and M. Rubeš, *J. Chem. Theory Comput.*, 2015, **11**, 230−238.

12 E. Haldoupis, J. Borycz, H. Shi, K. D. Vogiatzis, P. Bai, W. L. Queen, L. Gagliardi and J. I. Siepmann, *J. Phys. Chem. C*, 2015, **119**, 16058−16071.

13 L. Valenzano, B. Civalleri, S. Chavan, G. T. Palomino, C. O. Arean and S. Bordiga, *J. Phys. Chem. C*, 2010, **114**, 11185−11191.

14 L. Valenzano, B. Civalleri, K. Sillar and J. Sauer, *J. Phys. Chem. C,* 2011, **115**, 21777−21784.

15 R. Poloni, B. Smit and J. B. Neaton, *J. Phys. Chem. A*, 2012, **116**, 4957−4964.

16 G. Alonso, D. Bahamon, F. Keshavarz, X. Giménez, P. Gamallo and R. Sayós, *J. Phys. Chem. C*, 2018, **122**, 3945−3957.

17 W. L. Queen, M. R. Hudson, E. D. Bloch, J. A. Mason, M. I. Gonzalez, J. S. Lee, D. Gygi, J. D. Howe, K. Lee, T. A. Darwish, M. James, V. K. Peterson, S. J. Teat, B. Smit, J. B. Neaton, J. R. Long and C. M. Brown, *Chem. Sci.*, 2014, **5**, 4569−4581.

18 T. Pham, K. A. Forrest, D. M. Franz, Z. Guo, B. Chen and B. Space, *Phys. Chem. Chem. Phys.*, 2017, **19**, 18587−18602.

19 M. Asgari, S. Jawahery, E, D. Bloch, M. R. Hudson, R. Flacau, B. Vlaisavljevich, J. R. Long, C. M. Brown and W. L. Queen, *Chem. Sci.*, 2018, **9**, 4579−4588.

20 T. Pham, K. A. Forrest, K. McLaughlin, J. Eckert and B. Space, *J. Phys. Chem. C*, 2014, **118**, 22683−22690.

21 D. Gygi, E. D. Bloch, J. A. Mason, M. R. Hudson, M. I. Gonzalez, R. L. Siegelman, T. A. Darwish, W. L. Queen, C. M. Brown and J. R. Long, *Chem. Mater.*, 2016, **28**, 1128−1138.

22 P. D. C. Dietzel, P. A. Georgiev, J. Eckert, R. Blom, T. Strassle and T. Unruh, Chem. Commun., 2010, **46**, 4962−4964.

23 J. G. Vitillo, L. Regli, S. Chavan, G. Ricchiardi, G. Spoto, P. D. C. Dietzel, S. Bordiga, and A. Zecchina, *J. Am. Chem. Soc.*, 2008, **130**, 8386−8396.

24 W. Zhou, H. Wu and T. Yildirim, *J. Am. Chem. Soc.*, 2008, **130**, 15268−15269.

25 Y. Liu, H. Kabbour, C. M. Brown, D. A. Neumann and C. C. Ahn, *Langmuir*, 2008, **24**, 4772−4777.

26 T. Pham, K. A. Forrest, R. Banerjee, G. Orcajo, J. Eckert and B. Space, *J. Phys. Chem. C*, 2015, **119**, 1078−1090.

27 T. Pham, K. A. Forrest, J. Eckert and B. Space, *Cryst. Growth Des.*, 2016, **16**, 867−874.

28 M. H. Rosnes, M. Opitz, M. Frontzek, W. Lohstroh, J. Peter Embs, P. A. Georgiev and P. D. C. Dietzel, J. *Mater. Chem. A*, 2015, **3**, 4827−4839.

29 K. Lee, J. D. Howe, L.-C. Lin, B. Smit and J. B. Neaton, Chem. Mat., 2015, **27**, 668−678.

30 Y. Yan, X. Lin, S. Yang, A. J. Blake, A. Dailly, N. R. Champness, P. Hubberstey and M. Schröder, *Chem. Commun.*, 2009, 1025−1027.

31 Q. Yang and C. Zhong, *J. Phys. Chem. B*, 2006, **110**, 655−658.

32 Y. He, R. Krishna and B. Chen, *Energy Environ. Sci.*, 2012, **5**, 9107−9120.

33 A. Luna-Triguero, J. M. Vicent-Luna, R. M. Madero-Castro, P. Gómez-Álvarez and S. Calero, *ACS Appl. Mater. Interfaces*, 2019, **11**, 31499−31507.

34 S. Xiang, W. Zhou, J. M. Gallegos, Y. Liu and B. Chen, *J. Am. Chem. Soc.*, 2009, **131**, 12415−12419.

35 M. Fischer, F. Hoffmann and M. Fröba, *ChemPhysChem*, 2010, **11**, 2220−2229.

36 Y He, B. Li, M. O’Keeffe and B. Chen, *Chem. Soc. Rev.*, 2014, **43**, 5618−5656.

37 H.-M. Wen, H. Wang, B. Li, Y. Cui, H. Wang and G. Qian, *Inorg. Chem.*, 2016, **55**, 7214−7218.

38 Y. Ji, L. Ding, Y. Cheng, H. Zhou, S. Yang, F. Li and Y. Li, *J. Phys. Chem. C*, 2017, **121**, 24104−24113.

39 H. Wu, W. Zhou and T. Yildirim, *J. am. Chem. Soc.*, 2009, **131**, 4995−5000.

40 L. Chen, L. Grajciar, P. Nachtigall and T. Düren, *J. Phys. Chem. C*, 2011, **115**, 23074−23080.

3.2. Two-dimensional Cobalt-Carboxylate Framework with Hourglass Trinuclear $Co_3(COO)_6(DMA)_3$ Secondary Building Unit

Anna Goldman,[a] Katharina Nardin,[a] Simon-Patrick Höfert,[a] Simon Millan[a] and Christoph Janiak*[a], *Z. Anorg. Allg. Chem.*, 2018, **644**, 1387–1392. DOI: 10.1002/zaac.201800330; SHORT COMMUNICATION

Das folgende Paper beinhaltet die Synthese und die Kristallstruktur eines 2D-Cobaltnetzwerkes mit der Zusammensetzung $[Co_3(bdc)_3(DMA)_3]\cdot DMA$ (bdc^{2-} = Benzol-1,4-Dicarboxylat, DMA = *N,N*-Dimethylacetamid), das über eine durch ionische Flüssigkeit (IL) unterstützte Solvothermalreaktion erhalten wurde. Einkristalle von $[Co_3(BDC)_3(DMA)_3]\cdot DMA$ wurden durch die Reaktion von $Co(BF_4)_2\cdot 6H_2O$ und H_2bdc in einer Mischung der ionischen Flüssigkeit 1-Butyl-3-methylimidazoliumtetrafluoroborat [BMIm] $[BF_4]$ mit DMA als Lösungsmittel bei 160 °C erhalten. Zusätzlich wurde Tetrafluoroborsäure HBF_4 als Modulator hinzugegeben, um eine langsame Kristallisation aufgrund der Protonierung des bdc^{2-} Liganden zu gewährleisten. Die erhaltene Struktur besteht aus sanduhrförmigen $\{Co_3(COO)_6(DMA)_3\}$ SBUs und liegt in einer **hxl**-Topologie vor. Im Vergleich zu anderen zuvor berichteten Co-BDC Sanduhr-SBUs konnte eine neue Koordinationssequenz Co_{oct}-Co_{oct}-$Co_{sq\text{-}pyr}$ erreicht werden. Die Anwesenheit der IL war grundlegend für die Bildung gut geformter und großer Kristalle. In Abwesenheit der IL, unter ansonsten identischen Bedingungen konnten nur sehr kleine, nicht identifizierbare Kristalle erhalten werden. Des Weiteren konnte die IL in der Lösungsmittelmischung eine SBU-Änderung an bekannten Strukturtypen induzieren um eine neue Co_3-Sanduhrkonfiguration zu erhalten. Auch DMA spielte eine entscheidende Rolle bei der Konstruktion der 2D-Struktur durch die Koordination an die terminalen Cobaltatome der dreikernigen SBU.

Eigenanteile an der Veröffentlichung:

- Konzeption des Projektes auf Basis einer ausgiebigen Literaturrecherche in Zusammenarbeit mit Herrn Dr. Simon Millan.
- Darstellung und Verschriftlichung der Ergebnisse in Form einer wissenschaftlichen Veröffentlichung.
- Frau Katharina Nardin war während ihrer Masterarbeit an der Implementierung und Synthese von $[Co_3(bdc)_3(DMA)_3]\cdot DMA$ beteiligt.
- Herr Simon-Patrick Höfert führte die Aufnahme und Strukturverfeinerung durch.
- Überarbeitung, finale Abstimmung des Manuskripts und der Revision in Zusammenarbeit erfolgte mit Herrn Prof. Dr. Christoph Janiak.

The work presented in this chapter has been published in:

Two-dimensional Cobalt-Carboxylate Framework with Hourglass Trinuclear $Co_3(COO)_6(DMA)_3$ Secondary Building Unit

Anna Goldman,[a] Katharina Nardin,[a] Simon-Patrick Höfert,[a] Simon Millan[a] and Christoph Janiak*[a], *Z. Anorg. Allg. Chem.*, 2018, **644**, 1387–1392. DOI: 10.1002/zaac.201800330; SHORT COMMUNICATION

Dedicated to Professor Bernt Krebs on the Occasion of his 80th Birthday

The article is reproduced from Ref. 117 with permission from WILEY-VCH Verlag GmbH & Co. KGaA, Weinheim 2018.

Abstract

The two-dimensional (2D) cobalt-carboxylate framework of the hxl type with the formula $[Co_3(bdc)_3(DMA)_3]\cdot DMA$ was synthesized in a mixture of the ionic liquid 1-butyl-3-methylimidazolium tetrafluoroborate [BMIm][BF_4], HBF_4 and *N,N*-dimethylacetamide (DMA) *via* solvothermal reaction. The structure of $[Co_3(bdc)_3(DMA)_3]\cdot DMA$ (bdc^{2-} = benzene-1,4-dicarboxylate) consists of an hourglass trinuclear secondary building unit (SBU) with the first octahedral (oct)-octahedral and square-pyramidal (sq-pyr) coordinated cobalt atoms in the sequence Co_{oct}–Co_{oct}–$Co_{sq\text{-}pyr}$ with terminally coordinated DMA molecules. These SBUs are bridged by six bdc^{2-} ligands into a two-dimensional layered structure.

Introduction

Metal-organic frameworks (MOFs) are typically composed of multinuclear secondary building units (SBUs) as metal containing nodes and bridging organic linkers.[1,2] The design of the SBUs is influenced by the coordination arrangement of the metal sources and the orientation of the bridging donor atoms in organic linkers. Depending on the synthetic conditions, SBUs with a different arrangement and connectivity may be formed for a given metal.[3] Terephthalate (benzene-1,4-dicarboxylate, bdc^{2-}) is a common ligand used in prototypical MOFs such as MOF-5, MIL-53, and MIL-101.[4–8] The construction of MOFs composed of cobalt carboxylate SBUs is difficult to predict as the coordination number and arrangement of cobalt(II) can range from four (tetrahedral) to six (octahedral). For example, cobalt exhibits tetrahedral coordination in the Co-MOF-5-analog, square-pyramidal coordination in paddlewheel based MOFs, chains of corner-sharing CoO_6 octahedra in Co-MOF-71 and clusters of higher nuclearity.[9–14]

To the best of our knowledge ten crystallographically different hourglass-like $Co_3(COO)_6$-SBUs with the bdc^{2-} ligand are known until now, including $[Co_3(bdc)_3(DMA)_3]\cdot DMA$ reported in this work, highlighting the complexity of the cobalt coordination chemistry (Figure 1).[15–23]

The main difference lies in the local coordination environment of the cobalt atoms. In general the central cobalt atom of the trinuclear $Co_3(COO)_6$ cluster is coordinated to six oxygen atoms from different carboxylate ligands. Depending on the synthetic conditions the terminal cobalt atoms can be coordinated to solvent molecules like dimethylformamide (DMF), neutral N-donor ligands (*e.g.* pyridine), or they are fully ligated by the terephthalate linkers, to form different coordination environments. If the terminal cobalt atoms are coordinated by bridging ligands, then the SBUs assemble into a three-dimensional (3D) framework.

For example, the coordination environment in the SBU of 3D-$[Co_7(bdc)_6(nIm)_2(H_2O)_6]\cdot 3H_2O\cdot 3DMF$ (nIm = 2-nitroimidazole) is $Co_{sq\text{-}pyr}$–Co_{oct}–$Co_{sq\text{-}pyr}$ (sq-pyr = square-pyramidal, oct = octahedral) (Figure 1d).[16] Here one site of the terminal cobalt atoms is occupied with one N-donor atom from a bridging 2-nitroimidazole, which pillars the otherwise 2D-Co-bdc network to a 3D framework. The coordination of solvent molecules like DMF leads to the construction of 2D structures. The SBU of the 2D-$[Co_3(bdc)_3(DMF)_2(H_2O)_2]$ structure is built from trinuclear $Co_3(COO)_6$ clusters, where the terminal cobalt sites are occupied by one DMF oxygen atom and one water molecule to complete the vertices of an octahedron (Figure 1a).[15]

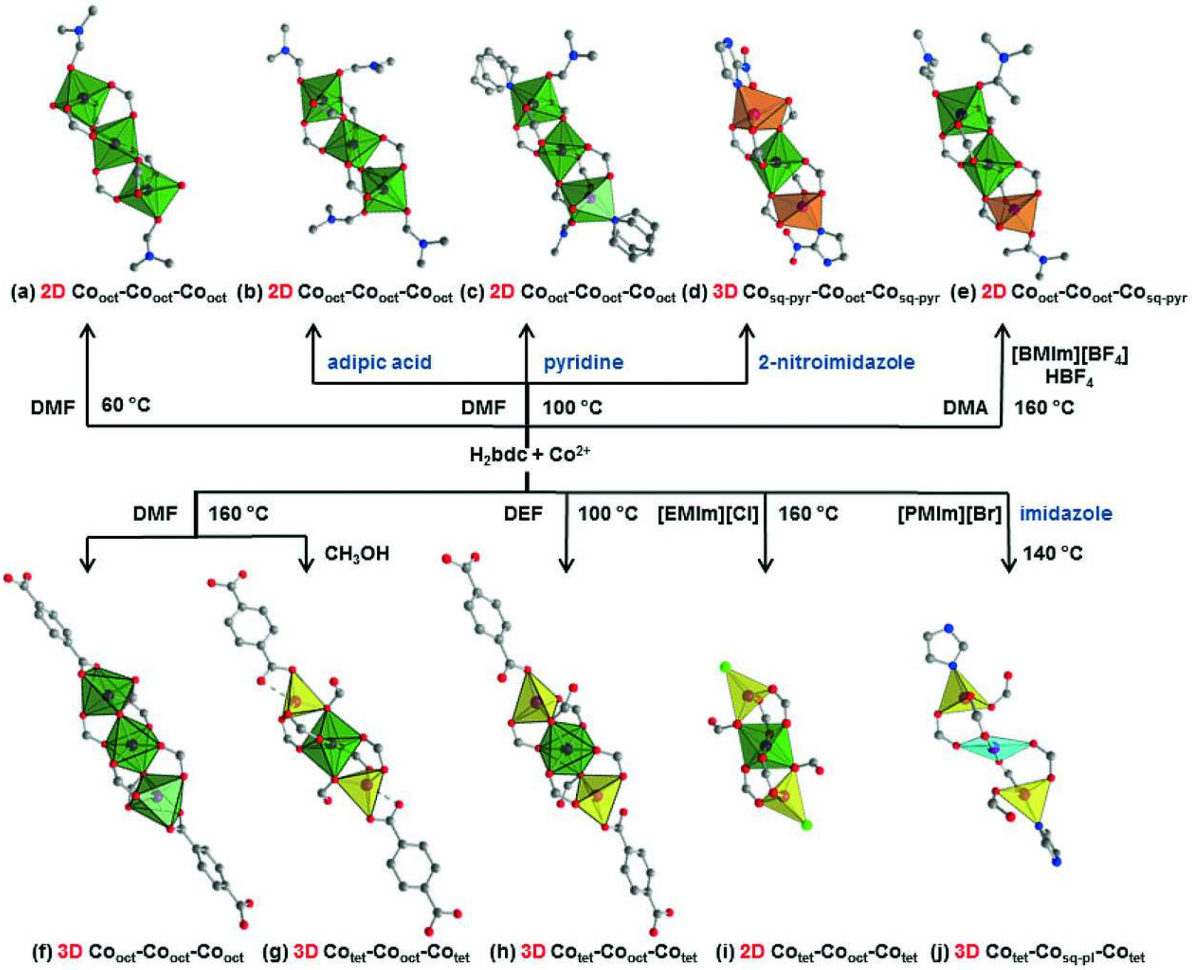

Figure 1. Polyhedral presentations and reaction conditions for the formation of ten types of SBUs built-up from trinuclear $Co_3(COO)_6$ clusters, with the Co coordination environment indicated as oct = octahedral, sq-pyr = square-pyramidal, sq-pl = square-planar, and tet = tetrahedral. (a) In 2D-$[Co_3(bdc)_3(DMF)_2(H_2O)_2]$ (DMF = dimethylformamide) (CSD-Refcode DUCQUP);[15] (b) in 2D-$[Co_3(bdc)_3(DMF)_4]_n$ (CSD-Refcode LOMQIP);[21] (c) in 2D-$[Co_3(bdc)_3(DMF)_2(py)_2]$ (py = pyridine) (CSD-Refcode NAJDUA);[17] (d) in 3D-$[Co_7(bdc)_6(nIm)_2(H_2O)_6]\cdot 3H_2O\cdot 3DMF$ (nIm = 2-nitroimidazole) (CSD-Refcode LACBID);[16] (e) in 2D-$[Co_3(bdc)_3(DMA)_3]\cdot DMA$ this work; (f) in 3D-$[Me_2NH_2]_2[Co_3(bdc)_4]\cdot 4DMF$ (CSD-Refcode VAKREG);[18] (g) in 3D-$[Me_2NH_2]_2[Co_3(bdc)_4]\cdot 2DMF$ (CSD-Refcode MOXDIN);[20] (h) in 3D-$[C_4H_{12}N]_2[Co_3(bdc)_4]_2\cdot 3C_5H_{11}NO$ (CSD-Refcode VEGMIE);[19] (i) in 2D-$[EMIm]_2[Co_3(bdc)_3Cl_2]$ (CSD-Refcode TACHUD);[22] (j) in 3D-$[Co_3(bdc)_3(Im)_2]_n$ (Im = imidazole) (CSD-Refcode XAPSOY).[23]

Various strategies have been used in the literature to synthesize MOFs (solvothermal, mechanochemical, sonochemical, dry-gel conversion).[24–26] One promising procedure is the use of ionic liquids (ILs) as solvents or additives to synthesize MOFs.[27–35] When they are incorporated into the framework, they often induce anionic networks.[36,37]

On the other hand, they can exert a structure-directing effect (*e.g.* templating) on the crystallization process of MOFs.[38–41] The ionothermal synthesis of 2D-$[R\mathrm{MIm}]_2[M_3(\mathrm{bdc})_3X_2]$ networks ($[R\mathrm{MIm}]X$ (R = ethyl, propyl, butyl, amyl; MIm = methylimidazolium; M = Zn, Co, Mn; $X = \mathrm{Cl}^-, \mathrm{I}^-$), was previously investigated for the influence of the $R\mathrm{Im}^+$ cation, which acts as a template and the halide anion with the function as a monodentate terminal ligand determining the 2D structural fashion of the network.[22,42–44] Herein, we report the synthesis and crystal structure of a 2D cobalt network with the formula $[Co_3(bdc)_3(DMA)_3]\cdot DMA$ *via* an ionic liquid (IL)-assisted solvothermal reaction.

Results and Discussion

Single crystals of $[Co_3(bdc)_3(DMA)_3]\cdot DMA$ could be obtained by the reaction of $Co(BF_4)_2\cdot 6H_2O$ and H_2bdc in a mixture of the ionic liquid [BMIm][BF_4] with DMA as the solvent at 160 °C (see Experimental Section for details). Additionally, tetrafluoroboric acid, HBF_4, as a modulator was added to insure a slow crystallization due to the protonation of the bdc^{2-} ligand.[45,46] As only the proton through its pH adjustment was intended as modulator, we chose HBF_4, which has the same weakly-coordinating anion as the IL in order to perturb the system as little as possible. Therefore, no other modulator such as often-used acetic acid was tested.

The representative nature of the single crystal for the bulk as-synthesized sample was verified by comparison of the experimental with the simulated powder X-ray diffractogram (PXRD) from the single crystal structure data (Figure 2).

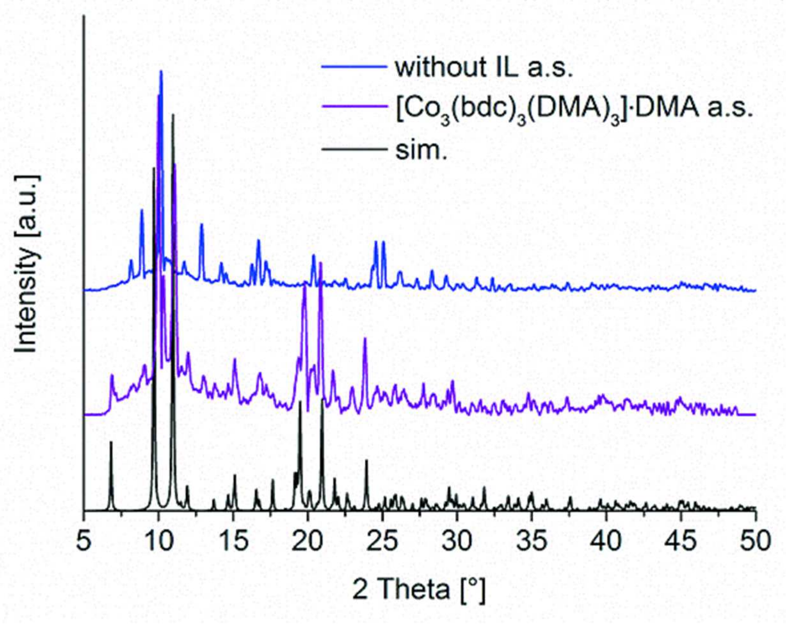

Figure 2. PXRD pattern of $[Co_3(bdc)_3(DMA)_3]\cdot DMA$ [simulated (black) and as-synthesized (purple)] and the PXRD pattern of the undefined phase obtained without the addition of the ionic liquid (blue).

The comparison between the experimental diffraction pattern of these phase with the simulated PXRD of $[Co_3(bdc)_3(DMA)_3]\cdot DMA$ confirmed the identity of the major crystalline part of the sample. However, it is also evident that a minor contribution of another still undefined crystalline phase was obtained (Figure 2). Without the addition of the IL under otherwise same reaction conditions, this yet undefined phase is formed in very small and unidentifiable crystals, which did not have sufficient quality for single crystal data analysis (Figure S2, Supporting Information). At the same time, this reaction shows the influence of the IL on the product formation. The IL is important for the controlled crystallization growth and functions as a structure-directing agent.

$[Co_3(bdc)_3(DMA)_3]\cdot DMA$ crystallizes in the monoclinic crystal system with the space group P_n. The asymmetric unit consists of three Co^{II} ions, three bdc^{2-} ligands, three coordinated DMA molecules, and one non-coordinated DMA molecule (Figure 3).

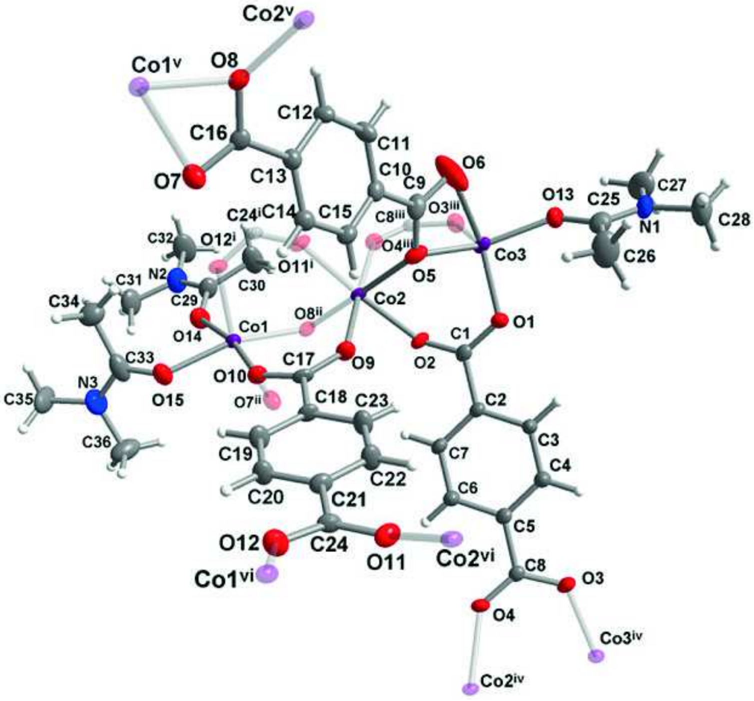

Figure 3. Thermal ellipsoid plot (50%) of the extended asymmetric unit in $[Co_3(bdc)_3(DMA)_3]\cdot DMA$ to show the complete coordination sphere for each Co atom and the bridging action of each ligand. Symmetry transformations: (i) 1/2 + x, 2 –y, 1/2 + z; (ii) –1/2 + x, – y, –1/2 + z; (iii) x, –1/2 + x,1–y, –1/2 + z, (iv) x, –1 + y, z; (v) 1/2 + x, 1 –y, 1/2 + z; (vi) 1/2 + x, 1 – y, 1/2 + z, (vii) x, 1 + y, z; (viii) 1/2 + x, – y, 1/2 + z; (ix) –1/2 + x, 2–y, –1/2 + z. The non-coordinated DMA solvent molecule of crystallization is omitted for clarity.

The three Co atoms form an hourglass-like trinuclear SBU, where the terminal cobalt atoms have an octahedral and square-pyramidal coordination environment Co_{oct}–Co_{oct}–$Co_{sq\text{-}pyr}$, respectively (Figure 4a, b).

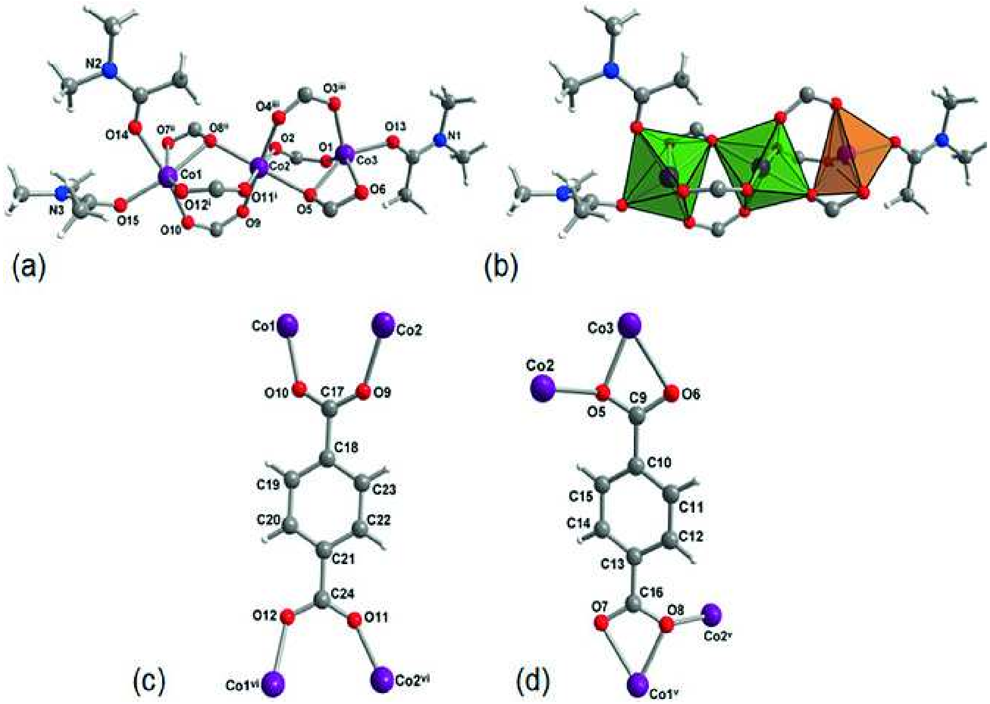

Figure 4. (a) Ball and stick presentation and (b) polyhedral view of the trinuclear hourglass-like SBU with Co_{oct}–Co_{oct}–$Co_{sq\text{-}pyr}$ cobalt coordination environments. The two different coordination modes of the bdc^{2-} ligand (c) bridging bidentate ($\mu_4 = \kappa^1\kappa^1\kappa^1\kappa^1$) and (d) chelating/ bridging bidentate ($\mu_4 = \kappa^1\kappa^2\kappa^1\kappa^2$).

The SBU $\{Co_3(COO)_6(DMA)_3\}$ possesses three crystallographic different Co^{II} ions, six carboxylate groups from six bridging bdc^{2-} ligands, and three terminal coordinated DMA molecules (Figure 4a). As shown in Figure 4 the bridging carboxylate ligands show different coordination modes. Two of the three crystallographically different ligands are bridging bidentate *via* a μ_4-($\kappa^1\kappa^1\kappa^1\kappa^1$) mode (Figure 4c) and the third linker is chelating/bridging bidentate in a μ_4-($\kappa^1\kappa^2\kappa^1\kappa^2$) mode (Figure 4d).

Co1 adopts an octahedral arrangement, surrounded by two oxygen atoms from two bdc^{2-} bidentate bridging ligands, two oxygen atoms from one chelating bridging carboxylate group, and two oxygen atoms from two coordinated DMA molecules. The lengths of the $Co1_{oct}$–O bonds are in the range of 2.02(4)– 2.27(4) Å. The central Co2 atom is surrounded by four oxygen atoms from different bdc^{2-} bridging ligands in the equatorial position and two oxygen atoms from two other bdc^{2-} ligands in the axial plane completing the octahedral coordination environment. The lengths of the $Co2_{oct}$–O bonds are in the range of 2.02(4)–2.17(5) Å. The coordination sphere on Co3 consists of two oxygen atoms of a bidentate bridging and two oxygen atoms from one chelating bridging carboxylate group. The fivefold coordination of Co3 is completed by a coordinated oxygen atom from a DMA molecule to a square-pyramidal coordination. The tau parameter (τ) defined by Addison *et al.* of τ = 0.3 indicates a closer to square-pyramidal (ideally τ = 0) coordination environment of Co3.[47] The lengths of the $Co3_{sq\text{-}pyr}$–O bonds are in the range of 1.97(4)–2.33(6) Å.

Each $\{Co_3(COO)_6(DMA)_3\}$ SBU acts as a 6-c-node and is linked by six bridging bdc^{2-} ligands (Figure 5a).

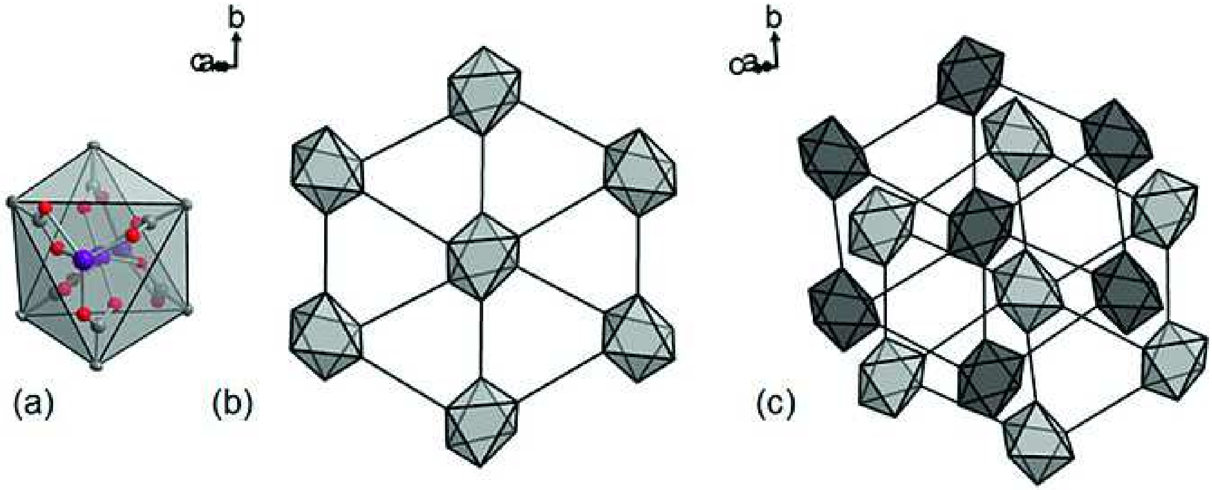

Figure 5. (a) Trinuclear hourglass-like SBU as 6-c-node by considering the carboxylate-carbon atoms as the point-of-extension and Co2 as central point. (b) 2D **hxl** topology with the short Schläfli symbol $3^6 \cdot 4^6 \cdot 5^3$ including triangular channels. (c) AB-stacking of two adjacent 2D nets. Non-coordinated DMA is omitted for clarity in all images.

The overall structure is a 2D-network of **hxl** topology with the short Schläfli symbol $3^6 \cdot 4^6 \cdot 5^3$ comprising triangular channels. The **hxl** sheets stack in an AB fashion (Figure 5b and c).[48,49] A 6-connected **hxl** topology is also known in the 2D manganese network $[Mn_{1.5}(bdc)_{1.5}(DMA)_2]$, which is built from trinuclear $\{Mn_3(COO)_6\}$ SBUs.[50]

Further, $[Co_3(bdc)_3(DMA)_3] \cdot DMA$ was characterized by IR spectroscopy (Figure S4, Supporting Information). The characteristic absorption bands for the coordinated ligands at 1585 cm^{-1} correspond to the asymmetric stretching vibration (vas) and the band at 1385 cm^{-1} to the symmetric stretching vibration (vs) of the carboxylate group. The frequency gap (Δv) between these bands $\Delta v = v_{as}(COO^-) - v_s(COO^-)$ of 200 cm^{-1} reveals that the carboxylate ligation is in the bidentate bridging mode ($\mu_{1,3}$- or $\eta^1:\eta^1:\mu_2$-).[51,52] The band at 1169 cm^{-1} can be assigned to the C–N stretching vibration and the band at 1019 cm^{-1} is compatible to the $C{-}CH_3$ rocking vibration from DMA.

Previously, the ionothermal synthesis of Co-bdc structures based on similar trinuclear $\{Co_3(COO)_6X_2\}$ SBUs (X = Cl^-, Br^-, I^-) in the IL [RMIm][*X*] (*R* = ethyl, *n*-propyl, *n*-butyl, and amyl; *X* = Cl^-, Br^-, I^-) as solvent was investigated for the effect of the $[RMIm]^+$ cation by varying the length of the *N*-alkyl chain and/or by changing the halide anion *X*.

Although in the compound presented in this work neither the IL cation nor the anion is incorporated into the network structure, the $[BMIm]^+$ cation could favor the formation of the 2D network. Otherwise the use of an IL with a larger N-alkyl chain could potentially lead to an expansion of the structure in the third direction. Such an influence of $[RMIm]^+$ cation size on the final structures was shown in the ionothermal reaction of $Co(NO_3)_2 \cdot 6H_2O$ with H_2bdc in a series of ILs, such as [EMIm][Br] (E = ethyl), [PMIm][Br] (P = propyl), [BMIm][Br] (B = butyl) and [AMIm][Br] (A = amyl). It was observed that the synthesis in ILs with smaller cations led to similar 2D-$[RMIm]_2[Co_3(bdc)_3Br_2]$ structures, where the IL cation and Br^- anion are incorporated in the structure.[44] These compounds are built from similar trinuclear $\{Co_3(COO)_6Br_2\}$ SBUs, where the terminal cobalt atoms have a distorted tetrahedral coordination sphere surrounded by three oxygen atoms from bdc^{2-} ligands and one monodentate Br^- ligand (akin to Figure 1i). Whereas with the larger N-alkyl chain in the $[AMIm]^+$ cation under otherwise same reaction conditions a 3D-$[AMIm]_2[Co_3(bdc)_4]$ framework was obtained. It consists of similar trinuclear $\{Co_3(COO)_8\}$ building units except in the place of the terminal Br^- ligand, two carboxylate groups from one bdc^{2-} ligand pillar the 2D layers into a 3D framework (akin to Figure 1g and h). In this case the $[RMIm]^+$ cation acts as template and through its size has a structure directing effect. An example, where the IL is not incorporated into the framework was presented in the synthesis of a neutral framework with the chemical formula 3D-$[CO_3(bdc)_3(Im)_2]_n$ from the reaction of $Co(NO_3)_2 \cdot 6H_2O$ with H_2bdc in [EMIm][Br] with the addition of imidazole (Figure 1j).[23] This compound possesses $\{Co_3(COO)_6Im_2\}$ SBUs, where the central cobalt atom adopts a square-planar coordination environment surrounded by four oxygen atoms from four different bdc^{2-} ligands and the terminal cobalt atoms adopt a tetrahedral coordination sphere by the coordination to three oxygen atoms from three bdc^{2-} and one nitrogen atom from the terminal imidazole ligand.

In contrast to the syntheses described above, where only the IL was used as solvent, in this work the formation of $[Co_3(bdc)_3(DMA)_3] \cdot DMA$ was achieved in a mixture of $[BMIm][BF_4]$ with DMA. The addition of DMA has a pivotal role in the construction of the 2D structure confirmed through the coordination by the DMA oxygen atom on terminal cobalt atoms of the trinuclear SBU. The structural environments of the Co_3 hourglass compounds shown in Figure 1 are determined by the synthesis temperature, the solvent or the addition of (terminating) co-ligands. Solvothermal reactions of Co^{2+} salts with H_2bdc in *N,N*-dimethylformamide (DMF) show a temperature dependent transition from 2D- to 3D-Co-bdc-networks. At lower temperatures (60–100 °C) DMF solvent molecules potentially coordinate as mono-dentate terminal ligands on the peripheral sites of the Co_3-SBU, whereas at higher temperatures about 160 °C the carboxylate group of the bdc^{2-} ligand has a stronger ability to coordinate on these terminal sites The reaction of $CoCl_2 \cdot 6H_2O$ with H_2bdc in DMF at 60 °C leads to the formation of 2D-$[Co_3(bdc)_3(DMF)_2(H_2O)_2]$ built-up from trinuclear $Co_3(COO)_6$ clusters with the Co sequence Co_{oct}–Co_{oct}–Co_{oct} (Figure 1a).[15] A similar Co_{oct}–Co_{oct}–Co_{oct} environment was achieved for 2D-[$Co_3(bdc)_3(DMF)_4$] in the reaction with $Co(NO_3)_2 \cdot 6H_2O$ instead of $CoCl_2 \cdot 6H_2O$ and with the addition of adipic acid at 100 °C (Figure 1b).[21] Without the addition of adipic acid but at an elevated temperature of 160 °C 3D-[Me_2NH_2]$_2$[$Co_3(bdc)_4$]·4DMF was formed (Figure 1f).[18] The octahedral environment of the terminal cobalt atoms in 3D- [Me_2NH_2]$_2$[$Co_3(bdc)_4$]·4DMF is completed by the coordination from two oxygen atoms from two bridging carboxylate groups and two oxygen atoms from one chelate carboxylate group. One bdc^{2-} ligand acts as a pillar to form a 3D coordination framework. The formation of 2D-[$Co_3(bdc)_3(DMA)_3$]·DMA presented in this work at also 160 °C could be due the modulator effect of HBF_4, which slows and modulates the deprotonation of H_2bdc. In similar reactions, N-donor additives like pyridine, nitroimidazole or imidazole coordinate preferably on the terminal cobalt sites of the Co_3-SBU (Figure 1c, d, and j). 2D networks are formed with the addition of mono-dentate N-donor coligands such as pyridine in [$Co_3(bdc)_3(DMF)_2(py)_2$], where each terminal Co^{2+} atom is saturated by one O-donor atom from DMF and one N-donor atom from pyridine to an octahedral coordination environment (Figure 1c).[17] 3D networks can be achieved with the use of bidentate co-ligands like imidazole or 2-nitroimodazole, which pillar the adjacent layers in the third direction. (Figure 1 d and j).[16,23]

Conclusions

The 2D-[$Co_3(bdc)_3(DMA)_3$]·DMA framework with hxl topology was successfully synthesized *via* an IL-containing solvothermal reaction. The obtained structure consists of {$Co_3(COO)_6(DMA)_3$} secondary building units with an hourglass shape. In comparison to other previously reported Co-bdc hourglass SBUs a new coordination sequence of Co_{oct}–Co_{oct}–$Co_{sq\text{-}pyr}$ was achieved. Thereby, the presence of IL was important to obtain well-shaped and large enough crystals, whereas in the absence of IL under otherwise identical conditions only very small, unidentifiable crystals could be obtained. Further, the IL in the solvent mixture seemed to induce the noted SBU modification to known structure types and allowed to obtain a new Co_3 hourglass configuration. Also, DMA played a pivotal role in the construction of the 2D structure through the coordination to the terminal cobalt atoms of the trinuclear SBU.

Experimental Section

The chemicals used were obtained from commercial sources. No further purification has been carried out. CHN analysis was performed with a Perkin–Elmer CHN 2400 (Perkin–Elmer, Waltham, MA, USA). IR spectra were recorded with a Bruker Tensor 37 IR spectrometer (Bruker Optics, Ettlingen, Germany) equipped with KBr unit. The intensity of adsorption is indicated as strong (s), medium (m), weak (w) and broad (br). The powder X-ray diffraction pattern (PXRD) was obtained with a Bruker D2 Phaser powder diffractometer with a flat silicon, low background sample holder, at 30 kV, 10 mA for Cu-Kα radiation (λ = 1.5418 Å).

Single Crystal X-ray Structure, Data Collection: Under a polarizing microscope suitable crystals were carefully selected and placed in protective oil. A crystal of sufficient quality was measured with a Bruker Kappa APEX2 CCD diffractometer with microfocus tube using Mo-Kα radiation (λ = 0.71073 Å). For data collection APEX2,[53] for cell refinement SAINT,[53] and for experimental absorption correction SADABS was used.[54] The structure was solved with SHELXT by intrinsic phasing and refined with SHELXL-2017 by full-matrix leastsquares on F2.[55,56] All hydrogen atoms were positioned geometrically (with C–H = 0.95 Å for aromatic CH and 0.98 Å for CH_3) and refined using riding models (AFIX 43 and 137) with $U_{iso}(H) = 1.2\ U_{eq}$ (CH) and 1.5 U_{eq} (CH_3). Crystallographic data and structure refinement results are summarized in Table 1. Selected bond lengths and bond angles are listed in Table 2.

Table 1. Crystallographic data for $[Co_3(bdc)_3(DMA)_3]\cdot$DMA.

	$[Co_3(bdc)_3(DMA)_3]\cdot$DMA
Empirical formula	$C_{36}H_{39}Co_3N_3O_{15}\cdot C_4H_9NO$
M/g mol^{-1}	1017.61
Crystal dimensions/mm	0.30 × 0.10 × 0.05
T/K	140
Crystal system	Monoclinic
Space group	P_n (no. 7)
a/Å	15.716(2)
b/Å	9.5722(13)
c/Å	15.868(2)
β/°	109.658(6)°
V/Å³	2248.0(6)
Z	2
D_{calc} /g cm^{-3}	1.503
(Mo Kα)/mm^{-1}	1.17
F(000)	1050
T_{max}, T_{min}	1.000, 0.755
$\Delta\rho_{max}$, $\Delta\rho_{min}$ [e Å^{-3}] a)	1.08, -0.63
R_1, wR_2 [I>2σ(I)] b)	0.0395, 0.1018
R_1, wR_2 [all data] b)	0.0448/0.1062
Goodness-of-fit an F^2 c)	1.015

a) Largest difference peak and hole. b) $R_1 = [\Sigma(|F_o|-|F_c|)/\Sigma|F_o|]$; $wR_2 = [\Sigma [w(F_o^2 - F_c^2)^2] / \Sigma[w(F_o^2)^2]]^{1/2}$. c) Goodness-of-fit $S = [\Sigma [w(F_o^2 - F_c^2)^2] / (n-p)]^{1/2}$.

Table 2. Selected bond length /Å and angles /° for $[Co_3(bdc)_3(DMA)_3]$ DMA.

Bond lengths (Å)			
Co1—O15	2.017 (4)	Co2—O2	2.087 (4)
Co1—O12^{i}	2.033 (4)	Co2—O8^{ii}	2.110 (4)
Co1—O10	2.041 (4)	Co2—O5	2.171 (5)
Co1—O8^{ii}	2.116 (4)	Co3—O3^{iii}	1.969 (4)
Co1—O14	2.186 (4)	Co3—O1	1.970 (4)
Co1—O7^{ii}	2.271 (4)	Co3—O13	1.987 (5)
Co2—O9	2.022 (4)	Co3—O5	2.068 (4)
Co2—O11^{i}	2.041 (4)	Co3—O6	2.328 (6)
Co2—O4^{iii}	2.076 (4)		
Bond angles (°)			
O15—Co1—O12^{i}	99.88 (18)	O4^{iii}—Co2—O2	92.59 (17)
O15—Co1—O10	85.70 (17)	O9—Co2—O8^{ii}	91.76 (17)
O12^{i}—Co1—O10	100.06 (18)	O11^{i}—Co2—O8^{ii}	89.46 (16)
O15—Co1—O8^{ii}	162.03 (18)	O4^{iii}—Co2—O8^{ii}	89.30 (16)
O12^{i}—Co1—O8^{ii}	97.72 (16)	O2—Co2—O8^{ii}	94.43 (15)
O10—Co1—O8^{ii}	94.84 (16)	O9—Co2—O5	88.67 (17)
O15—Co1—O14	85.12 (16)	O11^{i}—Co2—O5	89.90 (16)
O12^{i}—Co1—O14	85.29 (17)	O4^{iii}—Co2—O5	90.30 (17)
O10—Co1—O14	170.05 (17)	O2—Co2—O5	86.20 (16)
O8^{ii}—Co1—O14	92.72 (15)	O8^{ii}—Co2—O5	179.27 (18)
O15—Co1—O7^{ii}	102.08 (18)	O3^{iii}—Co3—O1	115.64 (19)
O12^{i}—Co1—O7^{ii}	155.41 (17)	O3^{iii}—Co3—O13	96.24 (19)
O10—Co1—O7^{ii}	92.52 (17)	O1—Co3—O13	97.79 (17)
O8^{ii}—Co1—O7^{ii}	59.94 (15)	O3^{iii}—Co3—O5	107.57 (18)
O14—Co1—O7^{ii}	85.67 (17)	O1—Co3—O5	91.83 (17)
O9—Co2—O11^{i}	96.21 (17)	O13—Co3—O5	147.3 (2)
O9—Co2—O4^{iii}	177.6 (2)	O3^{iii}—Co3—O6	99.5 (3)
O11^{i}—Co2—O4^{iii}	85.97 (18)	O1—Co3—O6	140.3 (2)
O9—Co2—O2	85.16 (17)	O13—Co3—O6	96.0 (2)
O11^{i}—Co2—O2	175.84 (19)	O5—Co3—O6	58.78 (19)

Symmetry codes: (i) x+1/2, –y+1, z+1/2; (ii) x, y+1, z; (iii) x+1/2, –y+2, z+1/2.

Crystallographic data (excluding structure factors) for the structure in this paper have been deposited with the Cambridge Crystallographic Data Centre, CCDC, 12 Union Road, Cambridge CB21EZ, UK. Copies of the data can be obtained free of charge on quoting the depository number CCDC-1857764 for $[Co_3(bdc)_3(DMA)_3]\cdot DMA$ (Fax: +44-1223-336-033; E-Mail: deposit@ccdc.cam.ac.uk, http://www.ccdc.cam.ac.uk).

$[Co_3(bdc)_3(DMA)_3]\cdot DMA$: $Co(BF_4)_2\cdot 6H_2O$ (26 mg, 0.11 mmol) and H_2bdc (22 mg, 0.12 mmol) were dissolved separately in a mixture of N,N-dimethylacetamide (4.5 mL) and $[BMIm][BF_4]$ (0.5 mL) with tetrafluoroboric acid HBF_4 (0.2 mL) as modulator. Both solutions were mixed, transferred in a Pyrex tube and heated to 160 °C for 40 h in a programmable oven and held at this temperature for 40 h, then cooled to room temperature over 30 h. Subsequently, single crystals of $[Co_3(bdc)_3(DMA)_3]\cdot DMA$ were obtained. Yield: 16.8 mg (25%). $C_{40}H_{48}Co_3N_4O_{16}$: calcd. C 47.21; H 4.75; N 5.51%; found: C 48.04; H 4.88; N 5.49%. IR (KBr): $\tilde{v}$ = 3600 (w), 3431 (br), 3147 (w), 3106 (w), 2961 (w), 2934 (w), 2871 (w), 1585 (m), 1504 (w), 1385 (s), 1169 (w), 1136 (w), 1019 (w), 1017 (w), 887 (w), 822 (w), 749 (w), 653 (w), 623 (w), 546 (w), 445 (w) cm^{-1}.

1 G. Maurin, C. Serre, A. Cooper, G. Férey, *Chem. Soc. Rev*. **2017**, *46*, 3104–3107.

2 H. Furukawa, K. E. Cordova, M. O’Keeffe, O. M. Yaghi, *Science* **2013**, 341, 1230444.

3 T. R. Cook, Y.-R. Zheng, P. J. Stang, *Chem. Rev*. **2013**, *113*, 734–777.

4 H. Li, M. Eddaoudi, M. O’Keeffe, O. M. Yaghi, *Nature* **1999**, *402*, 276–279.

5 C. Serre, F. Millange, C. Thouvenot, M. Noguès, G. Marsolier, D. Louër, G. Férey, *J. Am. Chem. Soc*. **2002**, *124*, 13519–13526.

6 F. Millange, N. Guillou, R. I. Walton, J.-M. Grenèche, I. Margiolaki, G. Férey, *Chem. Commun*. **2008**, 4732–4734.

7 L. Alaerts, M. Maes, L. Giebeler, P. A. Jacobs, J. A. Martens, J. F. M. Denayer, C. E. A. Kirschhock, D. E. De Vos, *J. Am. Chem. Soc*. **2008**, *130*, 14170–14178.

8 G. Férey, C. Mellot-Draznieks, C. Serre, F. Millange, J. Dutour, S. Surblé, I. Margiolaki, *Science* **2005**, *309*, 2040–2042.

9 S. Hausdorf, F. Baitalow, T. Böhle, D. Rafaja, F. O. R. L. Mertens, *J. Am. Chem. Soc*. **2010**, *132*, 10978–10981.

10 L. Du, Z. Lu, M. Ma, F. Su, L. Xu, *RSC Adv*. **2015**, *5*, 29505–29508.

11 J. Zhao, Q. Wang, C. Sun, T. Zheng, L. Yan, M. Li, K. Shao, X. Wang, Z. Su, J. *Mater. Chem. A* **2017**, *5*, 12498–12505.

12 A. R. Millward, O. M. Yaghi, *J. Am. Chem. So*c. **2005**, *127*, 17998–17999.

13 D. O. Miles, D. Jiang, A. D. Burrows, J. E. Halls, F. Marken, *Electrochem. Commun*. **2013**, *27*, 9–13.

14 N. L. Rosi, J. Kim, M. Eddaoudi, B. Chen, M. O’Keeffe, O. M. Yaghi, *J. Am. Chem. Soc*. **2005**, *127*, 1504–1518.

15 M. Bagherzadeh, F. Ashouri, M. Đaković, *J. Solid State Chem*. **2015**, *223*, 32–37.

16 X.-Q. Guo, M. Wang, Y.-F. Tang, F. Meng, G.-Q. Jiang, J.-L. Zhu, *CrystEngComm* **2016**, *18*, 1768–1774.

17 X.-F. Wang, H. Wang, S. Wang, J. Li, S. Li, K.-C. Zheng, X. Han, *RSC Adv*. **2016**, *6*, 14522–14530.

18 X.-F. Wang, Y.-B. Zhang, W. Xue, X.-L. Qi, X.-M. Chen, *CrystEngComm* **2010**, *12*, 3834–3839.

19 R. D. Poulsen, A. Bentien, M. Christensen, B. B. Iversen, *Acta Crystallogr., Sect. B* **2006**, *62*, 245–254.

20 F. Luo, Y.-X. Che, J.-M. Zheng, *Cryst. Growth Des*. **2009**, *9*, 1066–1071.

21 K. J. Lee, T.-H. Kim, T. K. Kim, J. H. Lee, H.-K. Song, H. R. Moon, *J. Mater. Chem. A* **2014**, *2*, 14393–14400.

22 Z.-H. Zhang, L. Xu, H. Jiao, *J. Solid State Chem*. **2016**, *238*, 217– 222.

23 Y.-L. Wang, N. Zhang, Q.-Y. Liu, X. Yang, H. Bai, L.-Y. Duan, H.-Y. Liu, *Inorg. Chem. Commun*. **2011**, *14*, 380–383.

24 N. Stock, S. Biswas, *Chem. Rev*. **2012**, *112*, 933–969.

25 N. Tannert, S. Gökpinar, E. Hastürk, S. Nießing, C. Janiak, *Dalton Trans*. **2018**, *47*, 9850–9860.

26 N. Abdollahi, M. Y. Masoomi, A. Morsali, P. C. Junk, J. Wang, *Ultrason. Sonochem*. **2018**, 45, 50–56.

27 M. Fischer, J. Schwegler, C. Paula, P. S. Schulz, M. Hartmann, *Dalton Trans*. **2016**, *45*, 18443.

28 M. Hovestadt, J. Schwegler, P. S. Schulz, M. Hartmann, *J. Chem. Phys*. **2018**, *148*, 193837.

29 S. Chen, J. Zhang, X. Bu, Inorg. Chem. **2008**, *47*, 5567–5569.

30 L. Xu, E.-Y. Choi, Y.-U. Kwon, *Inorg. Chem*. **2008**, *47*, 1907– 1909.

31 G. A. V. Martins, P. J. Byrne, P. Allan, S. J. Teat, A. M. Z. Slawin, Y. Li, R. E. Morris, *Dalton Trans*. **2010**, *39*, 1758–1762.

32 B. Tan, Z.-L. Xie, M.-L. Feng, B. Hu, Z.-F. Wu, X.-Y. Huang, *Dalton Trans*. **2012**, *41*, 10576.

33 W.-J. Ji, Q.-G. Zhai, S.-N. Li, Y.-C. Jiang, M.-C. Hu, *Chem. Commun*. **2011**, *47*, 3834.

34 W.-X. Chen, L. Tan, Q.-P. Liu, G.-R. Qiang, G.-L. Zhuang, *Dalton Trans*. **2014**, *43*, 16515–16521.

35 J. Liu, F. Zhang, X. Zou, G. Yu, N. Zhao, S. Fan, G. Zhu, Chem. Commun. **2013**, *49*, 7430.

36 J.-H. Liao, W.-C. Huang, *Inorg. Chem. Commun*. **2006**, *9*, 1227–1231.

37 W.-J. Ji, Q.-G. Zhai, M.-C. Hu, S.-N. Li, Y.-C. Jiang, Y. Wang, *Inorg. Chem. Commun*. **2008**, 11, 1455–1458.

38 H. M. Yang, X. L. Song, T. L. Yang, Z. H. Liang, C. M. Fan, X. G. Hao, *RSC Adv*. **2014**, 4, 15720.

39 Z. Lin, D. S. Wragg, J. E. Warren, R. E. Morris, *J. Am. Chem*. Soc. **2007**, *129*, 10334–10335.

40 L. Xu, S. Yan, E.-Y. Choi, J. Y. Lee, Y.-U. Kwon, *Chem. Commun*. **2009**, 3431–3433.

41 T. P. Vaid, S. P. Kelley, R. D. Rogers, *IUCrJ*. **2017**, *4*, 380–392.

42 Z.-H. Zhang, B. Liu, L. Xu, H. Jiao, *Dalton Trans*. **2015**, *44*, 17980.

43 Z. Wei, Z.-H. Zhang, M.-M. Wang, L. Xu, B. Liu, H. Jiao, C*rystEngComm* **2017**, *19*, 5402.

44 L. Xu, B. Liu, S.-X. Liu, H. Jiao, B. de Castroc, L. Cunha-Silva, *CrystEngComm* **2014**, *16*, 10649–10657.

45 F. Vermoortele, B. Bueken, G. Le Bars, B. Van de Voorde, M. Vandichel, K. Houthoofd, A. Vimont, M. Daturi, M. Waroquier, V. Van Speybroeck, C. Kirschhock, D. E. De Vos, *J. Am. Chem. Soc*. **2013**, *135*, 1146511468.

46 M. Taddei, *Coord. Chem. Rev*. **2017**, *343*, 1–24.

47 A. W. Addison, T. N. Rao, J. Reedijk, J. van Rijn, G. C. Verschoor, *J. Chem. Soc., Dalton Trans*. **1984**, 1349–1356.

48 V. A. Blatov, A. P. Shevchenko, D. M. Proserpio, *Cryst. Growth Des*. 2014, 14, 35763586.

49 T. G. Mitina, V. A. Blatov, *Cryst. Growth Des*. **2013**, *13*, 16551664.

50 Z.-Q. Jiang, Z. Zhao, G.-Y. Jiang, D.-C. Hou, Y. Kang, *Inorg. Chem. Commun*. **2011**, *14*, 1975–1977.

51 K. Nakamoto, *Infrared and Raman Spectra of Inorganic and Coordination Compounds*, 3rd ed., Wiley-Interscience, New York, **1978**.

52 G. B. Deacon, R. J. Phillips, *Coord. Chem. Rev*. 1**980**, *33*, 227–250.

53 Apex2, Data Collection Program for the CCD Area-Detector System; SAINT, Data Reduction, Frame Integration Program for the CCD Area-Detector System; Bruker Analytical X-ray Systems: Madison, WI, USA 19972012.

54 G. Sheldrick, Program for Empirical Absorption Correction of Area Detector Data, University of Göttingen, Germany, **1996**.

55 G. M. Sheldrick, *Acta Crystallogr., Sect. A* **2008**, *64*, 112–122.

56 G. M. Sheldrick, *Acta Crystallogr., Sect. C* **2015**, *71*, 3-8.

The article is reproduced from Ref. 117 with permission from WILEY-VCH Verlag GmbH & Co. KGaA, Weinheim 2018.

Supporting Information

Two-dimensional cobalt-carboxylate framework with hourglass trinuclear $Co_3(RCOO)_6(DMA)_3$ secondary building unit

Anna Goldman, Katharina Nardin, Simon-Patrick Höfert, Simon Millan, Christoph Janiak*

Institut für Anorganische Chemie und Strukturchemie, Heinrich-Heine-Universität Düsseldorf, Universitätsstraße 1, 40225 Düsseldorf, Germany. E-mail: janiak@uni-duesseldorf.de

* Corresponding author:
C. Janiak Tel.: +49 211 81 12286; fax: +49 211 81 12287.

E-mail addresses: anna.goldman@hhu.de, kanar100@gmx.de, Hoefert@hhu.de, Simon.Millan@hhu.de.

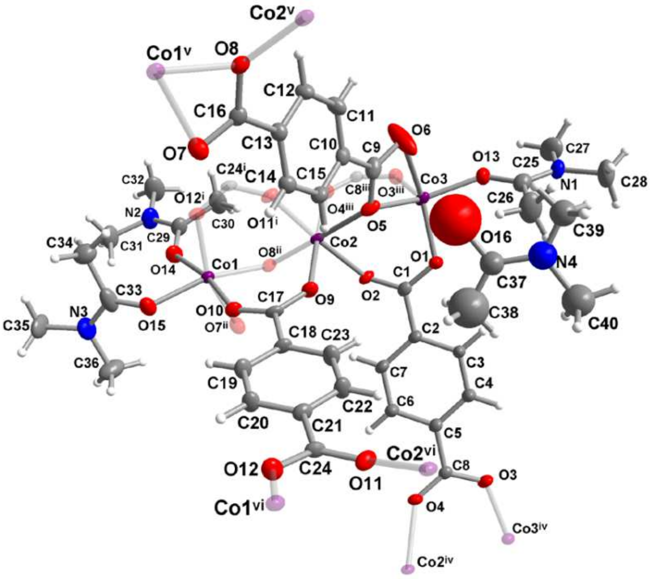

Figure S1. Thermal ellipsoid plot (50%) of the extended asymmetric unit in $[Co_3(bdc)_3(DMA)_3]\cdot DMA$ to show the complete coordination sphere for each Co atom and the bridging action of each ligand. Symmetry transformations: (i) ½ + x, 2 – y, ½ + z; (ii) - 1/2 + x, - y, -1/2 + z; (iii) x, -1/2 + x, 1 – y, -1/2 + z, (iv) x, -1 + y, z; (v) ½ + x, 1 – y, ½ + z; (vi) ½ + x, 1 - y, ½ + z, (vii) x, 1 + y, z; (viii) ½ + x, - y, ½ + z; (ix) -1/2 + x, 2 – y, -½ + z.

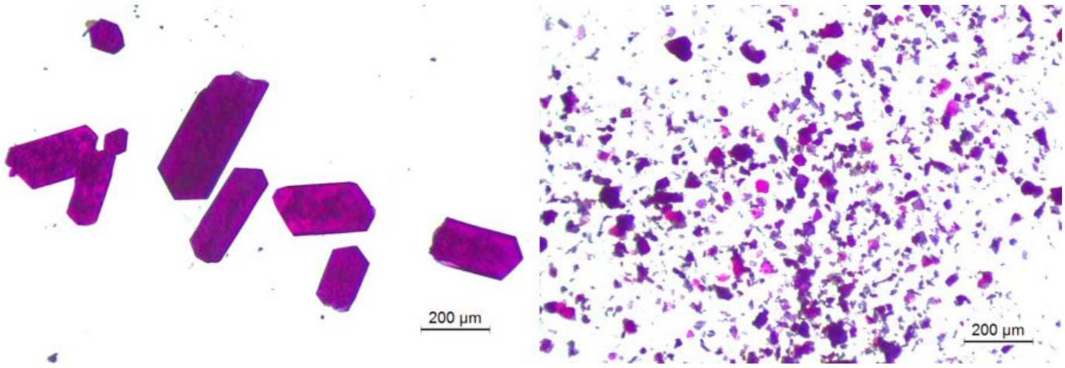

Figure S2. Single crystals of $[Co_3(bdc)_3(DMA)_3]\cdot DMA$ obtained by the reaction of $Co(BF_4)_2\cdot 6H_2O$ and H_2bdc in a mixture of the ionic liquid $[BMIm][BF_4]$ with DMA as solvent and tetrafluoroboric acid, HBF_4 at 160 °C (left). Single crystals of the undefined phase obtained by the reaction of $Co(BF_4)_2\cdot 6H_2O$ and H_2bdc in DMA and tetrafluoroboric acid, HBF_4 at 160 °C (that is, with no ionic liquid present) (right).

4 Zusammenfassung und Ausblick

In dieser Dissertation haben sich drei Themengebiete ergeben, die den Rahmen der vorliegenden Arbeit definieren. Der vorrangige Forschungsschwerpunkt dieser Arbeit liegt in der Entwicklung von kristallinen Netzwerkstrukturen auf Basis von bifunktionellen Monoalkylphosphonat-Carboxylat Liganden. Es wurden zwei neue isostrukturelle Metall-organische Gerüstverbindungen $[M_2(EtBCP)_2(DABCO)_{0.5}]\cdot 2DMA$ (M = Zn, Co) mit dem Ligand *O*-Ethyl-P-(4-carboxyphenyl)phosphonsäure (H_2EtBCP) synthetisiert. Durch die Anwesenheit der Ethylgruppe in der Phosphonat-Einheit konnte eine bidentate Koordination an das Metall erzielt und die Ausbildung des für Metallphosphonate typischen Schichtstrukturmotivs unterbunden werden. Die Verbindungen basieren auf einem **pcu**-Netz, das ein sehr einfaches und effizientes strukturelles Organisationsprinzip ist, welches sich beispielsweise in der IRMOF-Serie wiederfindet.[41] Es wird deutlich, dass der Strukturtyp selbst als Beispiel einer möglichen isoretikulären Reihe betrachtet werden kann, bei der eine Dimensionsskalierung linearer bifunktioneller Liganden erlaubt ist. Die Hypothese der synergistischen Kombination mit der Carboxylatfunktion in einem Liganden konnte bestätigt werden. Es wird gezeigt, dass die $\{[M_2(PO_2(OEt))_2]_2\}$ Monoalkylphosphonat-Einheit der Länge der $\{M_2(RCOO)_2(DABCO)\}$ paddle-wheel-Einheit entspricht, was einen Zugang zu weiteren gemischt-funktionellen MOFs eröffnet. Die aktivierten Verbindungen zeigen bei niedrigem Druck (195 K) eine zweistufige CO_2-Adsorptionsisotherme des Typs F-I und bei hohem Druck (298 K) ein analoges Verhalten mit einem Wendepunkt der Isotherme. Der stufenförmige Verlauf kann mit einer Porenöffnung von einer kleineren zu einer größeren Pore assoziiert werden. Dieses Verhalten resultiert aus der strukturellen Organisation der Verbindungen, die eine Netzwerkflexibilität aufgrund der Rotation des Phosphonats und der Carboxylateinheiten um die Achse der 1D-kettenförmigen SBUs ermöglicht. Des Weiteren kann die Funktionalisierung des Liganden mit zusätzlichen flexiblen organischen Gruppen das flexible Verhalten der Struktur begünstigen, indem sie wie ein „Hebel“ bei der Gasaufnahme wirken. Der zweite Teil dieser Arbeit fasst die in der Fachliteratur dargestellten Synthesen, Eigenschaften sowie Entwicklungen von MOFs mit offenen Metallstellen zusammen. Bei der Synthese von MOFs können Lösungsmittelmoleküle die Koordinationsumgebung der Metallionen in den Clustern vervollständigen. Offene Metallstellen in MOFs können durch die Entfernung von koordinierten labilen Lösungsmittelligandmolekülen erzeugt werden. Das Verfahren zur OMS-Erzeugung erfolgt normalerweise durch Lösungsmittelaustausch und anschließender Entfernung koordinierter Lösungsmittelmoleküle, was allgemein als "Aktivierung" bezeichnet wird. Die Aktivierung kann je nach Metallart und Flüchtigkeit des Lösungsmittels auf thermischen, chemischen oder photothermischen Wegen erfolgen.[118,119,120] Im Folgenden werden die drei Synthesestrategien von offenen Metallstellen kurz

zusammengefasst: Ein gängiges Verfahren koordinierte Lösungsmittelmoleküle zu entfernen erfolgt durch einen Lösungsmittelaustausch mit anschließender thermischer Aktivierung. Hier wird zunächst ein weniger flüchtiger (höher siedender) Lösungsmittelligand mit einem flüchtigeren (niedriger siedenden) Lösungsmittel ausgetauscht. Auf dieses Lösungsmittelaustauschverfahren folgt die thermische Aktivierung (Anwendung von Wärme, Energie und/oder (Hoch-)Vakuum). Dieses Verfahren hat sich zur Generierung von offenen Metallstellen in zahlreichen MOFs (u.a. Cu^{2+}-paddle-wheel MOFs (HKUST-1, NOTT-X (X = 100 – 107,) PCN-X (X = 10 – 14) etc.), M-MOF-74 (M = Mg^{2+}, Fe^{2+}, Co^{2+}, Ni^{2+}, Cu^{2+}, Zn^{2+}), MIL-101(M) (M = V^{3+}, Cr^{3+}, Fe^{3+}), MIL-100(M) (M = Sc^{3+}, V^{3+}, Cr^{3+}, Fe^{3+}), M-btt (M = Cr^{2+}, Mn^{2+}, Fe^{2+}, Cu^{2+}) sowie UIO-66 (Zr^{4+})) bewährt.[116,121,122,123,124,125,126,127,128,129,130,131,132,133,134,135,136,137]
Ein weiteres Verfahren ist die chemische Aktivierung.[124,138,139] Hier wird ein weniger flüchtiges Lösungsmittel wie Methanol, Ethanol oder Acetonitril durch eine (Wasch-)Behandlung mit einem leicht flüchtigen und nur sehr schwach koordinierenden halogenierten Lösungsmittel wie Dichlormethan ausgetauscht. Anders als bei der thermischen Aktivierung erfolgt die endgültige Entfernung des halogenierten Lösungsmittels bei Raumtemperatur ohne zusätzliche Wärmeenergie. Dieses Verfahren wurde zur Synthese von offenen Cu^{2+}-Stellen in HKUST-1 und MOF-2 sowie von offenen Cu^{2+} und offenen Ni^{2+}-Stellen in M-MOF-74 angewandt.[109,110,111] Im Vergleich zu den oben genannten Methoden des Lösungsmittelaustauschs und der Lösungsmittelentfernung durch thermische oder chemische Aktivierung, die unter Verwendung von Lösungsmittel und/oder Wärmeenergie durchgeführt werden, erfolgt die photothermische Aktivierung nur durch Bestrahlung der festen MOF-Probe mit (UV-Vis) Licht.[120] Anhand dieser Strategie wird in der Literatur die Synthese von offenen Cu^{2+}-Stellen in HKUST-1, offenen Mg^{2+}, Ni^{2+} und Zn^{2+}-Stellen in M-MOF-74 sowie offenen Zr^{4+}-Stellen in UIO-66 berichtet.[120]

Nach dem Aktivierungsprotokoll muss die Veränderung der Koordinationsumgebung des Metalls in der SBU, die Integrität des Netzwerks sicherstellen. Wichtig ist, dass die MOF-Struktur nicht kollabiert und ihre Kristallinität und Porosität erhalten bleiben, d.h. ein labiler terminaler Ligand sollte ohne Beschädigung des Netzwerks entfernt werden. Die Integrität des Netzwerks wird üblicherweise mit PXRD überprüft.

Das Vorhandensein von OMS kann durch die Verwendung geeigneter analytischer Methoden wie NMR (Nuclear magnetic resonance), TGA (Thermogravimetric analysis) und FT-IR (Fourier-Transform-Infrared) im Zusammenhang mit Gassorptionsstudien bestätigt werden. Zur Quantifizierung der relativen Menge (Prozentsatz) von Lewis-Säure-Stellen oder OMS in MOFs werden Techniken wie IR-Spektroskopie und temperaturprogrammierte Desorption (TPD) im Zusammenhang mit Gas- oder Dampfadsorptionsstudien verwendet[140,141,142,143]

Es hat sich gezeigt, dass sich bisher nur wenige Studien mit dem Thema OMS-Quantifizierung befasst haben und weitere Studien erforderlich sind.

Der Fokus der MOF-Synthesen liegt auf dem Design von MOFs mit Bindungsstellen, die auf die Adsorption eines bevorzugten Gastmoleküls abgestimmt sind. Im Vergleich zu MOFs, bei denen die Metallstellen vollständig besetzt sind, enthalten OMS-MOFs Bindungsstellen, die zu einer verstärkten Interaktion mit verschiedenen Sorbatmolekülen führen. Es hat sich gezeigt, dass OMS-Sorbat Wechselwirkungen nicht einfach aus Experimenten abgeleitet werden können. In solchen Fällen bilden Computerstudien eine Hauptgrundlage für das Studium und die Vorhersage der Sorptions- und Trenneigenschaften von MOFs. Sie verhelfen zum Verständnis, wie OMS mit den Gastmolekülen interagieren. Für die rechnerische Beschreibung der Interaktionen von MOFs mit Gastmolekülen gibt es verschiedene Ansätze, die sich in der Genauigkeit unterscheiden. Kraftfeldmethoden bilden eine Möglichkeit, die strukturellen Eigenschaften periodischer MOFs zu reproduzieren und erlauben abhängig von ihrer Parametrisierung eine ziemlich genaue Vorhersage von Geometrieparametern. Es wurde jedoch festgestellt, dass Standardkraftfelder ohne zusätzliche Parametrisierung kaum in der Lage sind, genaue thermodynamische Daten zu liefern. Genauere Werte für Bindungsenthalpien werden durch quantenmechanische Potentialberechnung der Energieoberflächen vorzugsweise unter Verwendung periodischer Begrenzung erhalten. Bei Verwendung des DFT-Levels ist die Einbeziehung von Van-der-Waals-Wechselwirkungen entscheidend. Der genaueste Ansatz beinhaltet eine Kombination von dispersionskorrigierten DFT- und high-level *ab-initio* Methoden, wie z.B. das DFT-D- und Coupled Cluster (CC) Verfahren. Im Allgemeinen eröffnen theoretische Berechnungen einen Zugang zu neuen Materialien, die auf eine gewünschte Eigenschaft zugeschnitten werden können und sind für die Ausführung des Experiments entscheidend. Die Synthese von OMS in MOFs ist die Basis für erhöhte (supramolekulare) Wechselwirkungen mit Gastmolekülen und eine vielversprechende Strategie, die MOF-Leistung für potentielle Anwendungen in den Bereichen der Gassorption und -trennung, Katalyse und Sensorik zu erreichen. Experimentelle Ergebnisse zeigten, dass OMS primäre Adsorptionsstellen für H_2, CO_2, CO, NO und C_2H_2 sind, was aus den hohen Adsorptionswärmen (Q_{st}) resultiert. Es hat sich auch gezeigt, dass MOFs mit OMS zu den vielversprechendsten festen Adsorbenzien zur selektiven Entfernung von CO_2 aus trockenen Gasgemischen gehören und ebenfalls hochaktive Lewis-Säure-Katalysatoren darstellen.

Der dritte Schwerpunkt dieser Arbeit befasst sich mit der Optimierung der MOF-Synthese durch die Verwendung von ionischen Flüssigkeiten (ILs). Aufgrund der weitreichenden Koordinationschemie von Cobaltkomplexen mit Carboxylat-Liganden und des Potentials von polynuklearen Cobaltcarboxylaten zur Ausbildung neuartiger Koordinationsfeststoffe mit interessanten Netzwerkstrukturen, wurde die Synthese von cobalthaltigen Netzwerkstrukturen verfolgt. Über eine IL-unterstützte Solvothermalreaktion wurde das 2D-Cobaltnetzwerk mit der Formel $[Co_3(bdc)_3(DMA)_3]\cdot DMA$ synthetisiert. Die erhaltene Struktur basiert auf einer trinuclearen $\{Co_3(COO)_6(DMA)_3\}$ „Sanduhr“-SBU. Jede $\{Co_3(COO)_6(DMA)_3\}$ SBU fungiert als 6-c-Knoten und ist über sechs verbrückende bdc^{2-}-Liganden verbunden. Die Struktur bildet ein 2D-Netzwerk der **hxl**-Topologie mit dreieckigen Kanälen. Im Vergleich zu anderen zuvor berichteten Co-bdc „Sanduhr“-SBUs, wurde eine neue Koordinationssequenz der Folge Co_{oct}-Co_{oct}-$Co_{sq\text{-}pyr}$ erhalten. Durch die Anwesenheit der IL konnte der Kristallisationsprozess optimiert werden. Ohne die Zugabe der IL unter sonst gleichen Reaktionsbedingungen, wurden kleine und nicht identifizierbare Kristalle erhalten, die nicht genügend Qualität für die Aufnahme von Einkristallstrukturdaten aufweisen. Die Verwendung von ILs als Lösungsmittel oder Additive zur Synthese von MOFs ist ein vielversprechendes Verfahren, denn ILs können einen strukturdirigierenden Effekt auf das Netzwerk ausüben und zu einem kontrollierten Kristallisationsprozess von MOFs beitragen.

5 Literaturverzeichnis

1 O. M. Yaghi and H. Li, *J. Am. Chem. Soc.*, 1995, **117**, 10401−10402.

2 S. R. Batten, N. R. Champness, X. M. Chen, J. Garcia-Martinez, S. Kitagawa, L. Ohrstrom, M. O'Keeffe, M. P. Suh and J. Reedijk, *Pure Appl. Chem.,* 2013**, 85**, 1715−1724.

3 R. A. Fischer and I. Schwedler, *Angew. Chem.,* 2014**, 126,** 7209−7214.

4 A. Werner, *Z. Anorg. Allg. Chem*., 1893, **3**, 267−330.

5 S. A. Allison, R. M. Barrer, *J. Chem. Soc. A*, 1969, **0**, 1717−1723.

6 H. J. Buser, D. Schwarzenbach, W. Petter and A. Ludi, *Inorg. Chem*., 1977, **16**, 2704−2710.

7 K. A. Hofmann and F. Küspert, *Z. Anorg. Allg. Chem*., 1897, **15**, 204−207

8 H. M. Powell and J. H. Rayner, *Nature*, 1949, **163**, 566−567.

9 B. Rungtaweevoranit, C. S. Diercks, M. J. Kalmutzki and O.r M. Yaghi, *Faraday Discuss.*, 2017, **201**, 9−45.

10 J. Rayner, and H. M. Powell, *J. Chem. Soc*., 1952, **67**, 319−328.

11 T. Iwamoto, T. Miyoshi, T. Miyamoto, Y. Sasaki and S. Fujiwara, *Bull. Chem. Soc. Jpn*., 1967, **40**, 1174−1178

12 S.-I. Nishikiori, T. Iwamoto, *Chem. Lett*., 1984, **13**, 319−322.

13 T. Hasegawa, S.-I. Nishikiori, and T. Iwamoto, *Chem. Lett*., 1985, **14**,1659−1662.

14 Y. Kinoshita, I. Matsubara and Y. Saito, *Bull. Chem. Soc. Jpn*., 1959, **32**, 741−747.

15 Y. Kinoshita, I. Matsubara and Y. Saito, *Bull. Chem. Soc. Jpn.*, 1959, **32**,1216−1221.

16 Y. Kinoshita, I. Matsubara, T. Higuchi and Y. *Saito, Bull. Chem. Soc. Jpn*., 1959, **32**, 1221−1226.

17 O. M. Yaghi, M. J. Kalmutzki and C. S. Diercks, *Introduction to Reticular Chemistry: Metal-Organic Frameworks and Covalent Organic Frameworks*, Wiley-VCH Verlag GmbH & Co. KGaA, Weinheim, 2019.

18 A. F. Wells, *Acta Crystallogr*., **1954**, *7*, 535−544.

19 A. F. Wells, in Structural Inorganic Chemistry, Oxford University Press, London, 5th ed., **1984**.

20 J. J. Perry IV, J. A. Perman and M. J. Zaworotko, *Chem. Soc. Rev*., 2009, **38**, 1400−1417.

21 M. O’Keeffe, M. A. Peskov, S. J. Ramsden and O. M. Yaghi, *Acc. Chem. Res*., 2008, **41**, 12, 1782–1789.

22 B. F. Hoskins and R. Robson, *J. Am. Chem. Soc*., 1989, ***111***, 5962−5964.

23 B. F. Hoskins and R. Robson, *J. Am. Chem. Soc*., 1990, ***112***, 1546−1554.

24 B. F. Abrahams, B. F. Hoskins, J. Liu and R. Robson, *J. Am. Chem. Soc*., 1991, **113**, 3045−3051.

25 S. Kitagawa, S. Matsuyama, M. Munakata and T. Emori, *J. Chem. Soc., Dalton Trans*., 1991, 2869−2874

26 S. Kitagawa, S. Kawata, Y. Nozaka and M. Munakata, J. *Chem. Soc., Dalton Trans*., 1993, 1399−1404.

27 M. Fujita, Y.J. Kwon, S. Washizu, and K. Ogura, *J. Am. Chem. Soc*., 1994, **116**, 1151–1152.

28 S. Subramanian, and M.J. Zaworotko, *Angew. Chem. Int. Ed*.,1995, **34**, 2127–2129.

29 O.M. Yaghi, M. O'Keeffe, N.W. Ockwig, H. K. Chae, M Eddaoudi and J. Kim, *Nature*, 2003, **423**, 705−714.

30 N.W. Ockwig, O. Delgado-Friedrichs, M. O'Keeffe, and O.M. Yaghi, *Acc. Chem. Res*., 2005, **38**, 176−182.

31 O.M. Yaghi, M. J. Kalmutzki and C. S. Diercks, Introduction to Reticular Chemistry: Metal-Organic Frameworks and Covalent Organic Frameworks, 2019, Wiley-VCH Verlag GmbH & Co. KGaA.

32 M. Eddaoudi, D. B. Moler, H. L. Li, B. L. Chen, T. M. Reineke, M. O'Keeffe, O. M. Yaghi, *Acc. Chem. Res*., 2001, **34**, 319−330.

33 M. O'Keeffe, M. Eddaoudi, H. L. Li, T. M. Reineke, O. M. Yaghi, *J. Solid State Chem*., 2000, **152**, 3−20.

34 O. M. Yaghi, M. O'Keeffe, N. W. Ockwig, H. K. Chae, M. Eddaoudi, J. Kim, *Nature*, 2003, **423**, 705−714.

35 V. Guillerm, D. Kim, J. F. Eubank, R. Luebke, X. Liu, K. Adil, M. Soo Lah, M. Eddaoudi, *Chem. Soc. Rev.,* 2014, **43**, 6141−6172.

36 A. Schoedel and S. Rajeh, *Top. Curr. Chem.*, 2020, **378**, 19.

37 H. Li, M. Eddaoudi, T. L. Groy and O. M Yaghi, *J. Am. Chem. Soc*., 1998, **120**, 8571−8572.

38 B. Chen, M. Eddaoudi, T. M. Reineke, J. W. Kampf, M. O'Keefe and O. M. Yaghi, *J. Am. Chem. Soc*., 2000, **122**, 11559−11560.

39 M. Eddaoudi, J. Kim, N. Rosi, D. Vodak, J. Wachter, M. O'Keefe, O. M. Yaghi, *Science*, 2002, **295**, 469−472.

40 H. Deng, C. J. Doonan, H. Furukawa, R. B. Ferreira, J. Towne, C. B. Knobler, B. Wang, O. M. Yaghi, *Science*, 2010, **327**, 846−850.

41 Z. Mai and D. Liu*, Cryst. Growth Des*., 2019, **19**, 7439−7462.

42 A. G. Wong-Foy, A. J. Matzger and O. M. Yaghi, *J. Am. Chem. Soc*., 2006, **128**, 3494−3495.

43 G. Férey, *Chem. Soc. Rev*., 2008, ***37***, 191−214.

44 W. Lu, Z. Wei, Z.-Y. Gu, T.-F. Liu, J. Park, J. Park, J. Tian, M. Zhang, Q. Zhang, T.Gentle III, M. Boscha and H.-C. Zhou, *Chem. Soc. Rev.*, 2014, **43**, 5561−5593.

45 Y. He, B. Li, M. O'Keeffe and B. Chen, *Chem. Soc. Rev.*, 2014, **43**, 5618−5656.

46 I. Spanopoulos, C. Tsangarakis, E. Klontzas, E. Tylianakis, G. Froudakis, K. Adil, Y. Belmabkhout, M. Eddaoudi and P. N. Trikalitis, *J. Am. Chem. Soc.*, 2016, **138**, 1568−1574.

47 T. M. McDonald, J. A. Mason, X. Kong, E. D. Bloch, D. Gygi, A. Dani, V. Crocellà, F. Giordanino, S. O. Odoh, W. S. Drisdell, B. Vlaisavljevich, A. L. Dzubak, R. Poloni, S. K. Schnell, N. Planas, K. Lee, T. Pascal, L. F. Wan, D. Prendergast, J. B. Neaton, B. Smit, J. B. Kortright, L. Gagliardi, S. Bordiga, J. A. Reimer and J. R. Long, *Nature*, 2015, **519**, 303−308.

48 E. M. Miner, T. Fukushima, D. Sheberla, L. Sun, Y. Surendranath and M. Dincă, *Nat. Commun.*, 2016, **7**, 10942.

49 A. Henschel, K. Gedrich, R. Kraehnert and S. Kaskel, *Chem. Commun.*, 2008, 4192−4194.

50 S. Horike, M. Dinca˘, K. Tamaki and J. R. Long, *J. Am. Chem. Soc.*, 2008, **130**, 5854−5855.

51 S. Wang, L. Bromberg, H. Schreuder-Gibson and T. A. Hatton, *ACS Appl. Mater. Interfaces*, 2013, **5**, 1269−1278.

52 L. Alaerts, E. Ségiun, H. Poelman, F. Thibault-Starzyk, P. A. Jacobs and D. E. De Vos, *Chem. – Eur. J.*, 2006, **12**, 7353−7363.

53 M. K. Bhunia, J. T. Hughes, J. C. Fettinger and A. Navrotsky, *Langmuir*, 2013, **29**, 8140−8145.

54 S. Kitagawa, R. Kitaura and S.-I. Noro, *Angew. Chem. Int. Ed.*, 2004, **43**, 2334-2375.

55 S. Kitagawa, and M. Kondo, *Bull. Chem. Soc. Jpn*, 1998, **71**, 1739−1753.

56 O. K. Farha, I.; Eryazici, N. C. Jeong, B. G. Hauser, C. E. Wilmer, A. A. Sarjeant, R. Q. Snurr, S. T. Nguyen, A. Ö. Yazaydın and J. T. Hupp, *J. Am. Chem. Soc.,* 2012**, 134**, 15016−15021.

57 K. Barthelet, J. Marrot, D. Riou and G. Férey, *Ange. Chem. Int. Ed.*, 2002, **41**, 281−284.

58 K. Uemura, S. Kitagawa, M. Kondo, K. Fukui, R. Kitaura, H. C. Chang and T. Mizutani, *Chem. – Eur. J.*, 2002, **8**, 3586−3600.

59 J. H. Lee, S. Jeoung, Y. G. Chung and H. R. Moon, *Coord. Chem. Rev.*, 2019, **389**, 161−188.

60 T. D. Bennett, A. K. Cheetham, A. H. Fuchs and F.-X. Coudert, *Nature Chem.*, 2017, **9,** 11−16.

61 S. Horike, S. Shimomura and S. Kitagawa, *Nature Chem.*, 2009, **1**, 695−704.

62 A. Schneemann, V. Bon, I. Schwedler, I. Senkovska, S. Kaskel and R. A. Fischer, *Chem. Soc. Rev.*, 2014, **43**, 6062−6096.

63 Z. Chang, D.-H. Yang, J. Xu, T.-L. Hu, X.-H. Bu, *Adv. Mater.*, 2015, **27**, 5432–5441.

64 P. L. Llewellyn, S. Bourrelly, C. Serre, Y. Filinchuk and G. Férey, *Angew. Chem. Int. Ed.*, 2006, **45**, 7751−7754.

65 K. Uemura, R. Matsudab, S. Kitagawa, *J. Solid State Chem.*, 2005, **178**, 2420−2429

66 C. Serre, F. Millange, C. Thouvenot, M. Noguès, G. Marsolier, D. Louër, G. Férey, *J. Am. Chem. Soc.*, 2002, **124**, 13519−13526.

67 T. Loiseau, C. Serre, C. Huguenard, G. Fink, F. Taulelle, M. Henry, T. Bataille, G. Férey, Chem. – *Eur. J.*, 2004, **10**, 1373−1382.

68 E. V. Anokhina, M. Vougo-Zanda, X. Wang, A. J. Jacobson, *J. Am. Chem. Soc.*, 2005, **127**, 15000–15001.

69 T. R. Whitfield, X. Wang, L. Liu, A. J. Jacobson, *Solid State Sci.*, 2005, **7**, 1096−1103.

70 M. Vougo-Zanda, J. Huang, E. Anokhina, X. Wang, A. J. Jacobson, *Inorg. Chem.*, 2008, **47**, 11535−11542.

71 J. P. S. Mowat, V. R. Seymour, J. M. Griffin, S.P. Thompson, A. M. Z. Slawin, D. Fairen-Jimenez, T. Duren, S. E. Ashbrook, P. A. Wright, *Dalton Trans.*, 2012, **41**, 3937−3941.

72 C. Serre, S. Bourrelly, A. Vimont, N. A. Ramsahye, G. Maurin, P. L. Llewellyn, M. Daturi, Y. Filinchuk, O. Leynaud, P. Barnes, G. Férey, *Adv. Mater.*, 2007, **19**, 2246−2251.

73 Y. Zhang, B. E. G. Lucier, V. V. Terskikh, R. Zheng and Y. Huang, *Solid State Nucl. Magn. Reson.*, 2017, **84**, 118−131.

74 D. N. Dybtsev, H. Chun and K. Kim, *Angew. Chem. Int. Ed.*, 2004, **43**, 5033−5036.

75 M. R. Ryzhikov and S. G. Kozlova, *Phys. Chem. Chem. Phys.*, 2019, **21**, 11977−11982.

76 W. Chen, S. Horike, D. Umeyama, N. Ogiwara, T. Itakura, C. Tassel, Y. Goto, H. Kageyama and S. Kitagawa, *Angew. Chem. Int. Ed.*, 2016, **55**, 5195−5200.

77 Y. Kim, R. Haldar, H. Kim, J. Koo and K. Kim, *Dalton Trans.*, 2016, **45**, 4187−4192.

78 A. Schneemann, P. Vervoorts, I. Hante, M. Tu, S. Wannapaiboon, C. Sternemann, M. Paulus, D. C. F. Wieland, S. Henke and R. A. Fischer, *Chem. Mater.*, 2018, **30**, 1667−1676.

79 M. Thommes, K. Kaneko, Al. V. Neimark, J. P. Olivier, F. Rodriguez-Reinoso, J. Rouquerol and K. S. W. Sing, *Pure Appl. Chem.*, 2015, **87**, 1051−1069

80 Q.-Y. Yang, P. Lama, S. Sen, M. Lusi, K.-J. Chen, W.-Y. Gao, M. Shivanna, T. Pham, N. Hosono, S. Kusaka, J. J. Perry Iv, S. Ma, B. Space, L. J. Barbour, S. Kitagawa and M. J. Zaworotko, *Angew. Chem. Int. Ed.*, 2018, **57**, 5684−5689.

81 S. Millan, B. Gil-Hernández, E. Milles, S. Gökpinar, G. Makhloufi, A. Schmitz, C. Schlüsener and C. Janiak, *Dalton Trans.*, 2019, **48**, 8057−8067.

82 T. M. McDonald, J. A. Mason, X. Kong, E. D. Bloch, D. Gygi, A. Dani, V. Crocellà, F. Giordanino, S. O. Odoh, W. S. Drisdell, B. Vlaisavljevich, A. L. Dzubak, R. Poloni, S. K. Schnell, N. Planas, K. Lee, T. Pascal, L. F. Wan, D. Prendergast, J. B. Neaton, B. Smit,

J. B. Kortright, L. Gagliardi, S. Bordiga, J. A. Reimer and J. R. Long, *Nature*, 2015, **519**, 303−308.

83 T. Zheng, Z. Yang, D. Gui, Z. Liu, X. Wang, X. Dai, S. Liu, L. Zhang, Y. Gao, L. Chen, D. Sheng, Y. Wang, J. Diwu, J. Wang, R. Zhou, Z. Chai, T. E. Albrecht-Schmitt and S. Wang, *Nat. Commun.*, 2017, **8**, 15369.

84 M. Taddei, F. Costantino and R. Vivani, *Eur. J. Inorg. Chem.*, 2016, 4300−4309.

85 M. Taddei and F. Costantino, *Crystals*, 2019, ***9***, 454.

86 G. Alberti, U. Constantino, S. Allulli and N. Tomassini, *J. Inorg. Nucl. Chem.,* 1978, **40**, 1113−1117.

87 A. Clearfield and G. D. Smith, *Inorg. Chem.*, 1969, **8**, 431−436.

88 D. Lanari, F. Montanari, F. Marmottini, O. Piermatti, M. Orrù, L. Vaccaro, *J. Catal.*, 2011, **277**, 80−87.

89 G. Alberti, M. Casciola, U. Costantino and R. Vivani, *Adv, Mater.*, 1996, **8**, 291-303.

90 G. Alberti, U. Costantino, M. Casciola, R. Vivani and A. Peraio, *Solid State Ionics*, 1991, **46**, 61−68.

91 M. Casciola, U. Costantino, A. Peraio and T. Rega, *Solid State Ionics*, 1995, **77**, 229−233.

92 M. B. Dines, P. M. Digiacomo, K. P. Callahan, P. C. Griffith, R. H. Lane and R. E. Cooksey, *ACS Symp. Ser.*, 1982, **13**, 223–240.

93 D. Cunningham, P. J. D. Hennelly and T. Deeney, *Inorg. Chim. Acta*, 1979, **37**, 95−102.

94 G. Cao, H. Lee, V. M. Lynch and T. E. Mallouk, *Solid State Ionics*, 1988, **26**, 63−69.

95 G. Cao, H. Lee, V. M. Lynch and T. E. Mallouk, *Inorg. Chem.*, 1988, **27**, 2781−2785.

96 Y. Ortiz-Avila, P. R. Rudolf and A. Clearfield, *Inorg. Chem*., 1989, **28**, 2137−2141.

97 G. Cao, V. M. Lynch, J. S. Swinnea, T. E. Mallouk, *Inorg. Chem.,* 1990, **29**, 2112−2117.

98 J. Le Bideau, C. Payen, P. Palvadeau and B. Bujoli, *Inorg. Chem.*, 1994, **33**, 488−4890.

99 S. Drumel, P. Janvier, D. Deniaud, B. Bujoli, *J. Chem. Soc. Chem. Commun.*, 1995, 1051−1052.

100 K. Maeda, J. Akimoto, Y. Kiyozumi and F. Mizukami, *Angew. Chem. Int. Ed.,* 1995, **34**, 1199−1201.

101 K. Maeda, Y. Kiyozumi and F. Mizukami, *Angew. Chem. Int. Ed.*, 1994, **33**, 2335-2337.

102 C. Serre, J. A. Groves, P. Lightfoot, A. M. Z. Slawin, P. A. Wright, N. Stock, T. Bein, M. Haouas, F. Taulelle and G. Férey, *Chem. Mater.*, 2006, **18**, 1451−1457.

103 M. T. Wharmby, G. M. Pearce, J. P. S. Mowat, J. M. Griffin, S. E. Ashbrook, P. A. Wright, L.-H. Schilling, A. Lieb, N. Stock, S. Chavan, S. Bordiga, E. Garcia, G. D. Pirngruber, M. Vreeke and L. Gora, *Microporous Mesoporous Mater.*, 2012, **157**, 3−17.

104 J. A. Groves, S. R. Miller, S. J. Warrender, C. Mellot-Draznieks, P. Lightfoot and P. A. Wright, *Chem. Commun.*, 2006, 3305−3307.

105 M. T. Wharmby, J. P. S. Mowat, S. P. Thompson and P. A. Wright, *J. Am. Chem. Soc.*, 2011, **133**, 1266−1269.

106 A. Schoedel, M. Li, D. Li, M. O’Keeffe and O. M. Yaghi, *Chem. Rev.*, 2016, **116**, 12466−12535

107 B. Gelfand, R. P. S. Huynh, S. Collins, T. Woo and G. K. H. Shimizu, *Chem. Mate.*, 2017, **29**, 10469−10477.

108 O. R. Evans, D. R. Manke and W. Lin, *Chem. Mater.*, 2002, **14**, 3866-3874.

109 S. S. Iremonger, J. Liang, R. Vaidhyanathan and George K. H. Shimizu, *Chem. Commun.*, 2011, **47**, 4430−4432.

110 S. S. Iremonger, J. Liang, R. Vaidhyanathan, I. Martens, G. K. H. Shimizu, T. D. Daff, M. Z. Aghaji, S. Yeganegi and T. K. Woo, *J. Am. Chem. Soc.*, 2011, **133**, 20048−20051.

111 B. Gelfand, J.-B. Lin and G. K. H. Shimizu, *Inorg. Chem.*, 2015, **54**, 1185−1187.

112 J.-W. Zhang, C.-C. Zhao, Y.-P. Zhao, H.-Q. Xu, Z.-Y. Du and H.-L. Jiang, *CrystEngComm*, 2014, **16**, 6635−6644.

113 B. Gelfand, J. Taylor and G. K. H. Shimizu, *CrystEngComm*, 2017, **19**, 3727−3736.

114 B. S. Gelfand, R. P. S. Huynh, R. K. Mah and G. K. H. Shimizu, *Angew. Chem. Int. Ed.*, 2016, **55**, 14614−14617.

115 A. Goldman, B. Gil-Hernández, S. Millan, S. Gökpinar, C. Heering, I. Boldog and C. Janiak, *CrystEngComm*, 2020, **22**, 2933−2944.

116 Ü. Kökçam-Demir, A. Goldman, L. Esrafili, M. Gharib, A. Morsali, O. Weingartc and C. Janiak‡*a, *Chem. Soc. Rev.*, 2020, *Chem. Soc. Rev.*, 2020, **49**, 2751−2798.

117 A. Goldman, K. Nardin, S.-P. Höfert, S. Millan and C. Janiak, *Z. Anorg. Allg. Chem.*, 2018, **644**, 1387−1392.

118 J.-C. Wang, F.-W. Ding, J.-P. Ma, Q.-K. Liu, J.-Y. Cheng and Y.-B. Dong, *Inorg. Chem.*, 2015, **54**, 10865−10872.

119 J. Bae, E. J. Lee and N. C. Jeong, *Chem. Commun.*, 2018, **54**, 6458–6471.

120 J. Espín, L. Garzón-Tovar, A. Carné-Sánchez, I. Imaz and D. Maspoch, *ACS Appl. Mater. Interfaces*, 2018, **10**, 9555−9562.

121 X.-S. Wang, S. Ma, K. Rauch, J. M. Simmons, D. Yuan, X. Wang, T. Yildirim, W. C. Cole, J. J. López, A. de Meijere and H.-C. Zhou, *Chem. Mater.*, 2008, **20**, 3145−3152.

122 F. Nouar, J. F. Eubank, T. Bousquet, L. Wojtas, M. J. Zaworotko and M. Eddaoudi, *J. Am. Chem. Soc.*, 2008, **130**, 1833−1835.

123 W. L. Queen, M. R. Hudson, E. D. Bloch, J. A. Mason, M. I. Gonzalez, J. S. Lee, D. Gygi, J. D. Howe, K. Lee, T. A. Darwish, M. James, V. K. Peterson, S. J. Teat, B. Smit, J. B. Neaton, J. R. Long and C. M. Brown, *Chem. Sci.*, 2014, **5**, 4569−4581.

124 H. K. Kim, W. S. Yun, M.-B. Kim, J. Y. Kim, Y.-Y. Bae, J. Lee and N. C. Jeong, *J. Am. Chem. Soc.*, 2015, **137**, 10009−10015.

125 J. Chen, X. Chen, Z. Zhang, Z. Bao, H. Xing, Q. Yang and Q. Ren, *Mol. Catal.*, 2018, **445**, 163−169.

126 X.-S. Wang, S. Ma, P. M. Forster, D. Yuan, J. Eckert, J. J. López, B. J. Murphy, J. B. Parise and H.-C. Zhou, *Angew. Chem., Int. Ed.*, 2008, **47**, 7263−7266.

127 A. A. Talin, A. Centrone, A. C. Ford, M. E. Forster, V. Stavila, P. Haney, R. A. Kinney, V. Szalai, F. El Gabaly, H. P. Yoon, F. Léonard and M. D. Allendorf, Science, 2014, 342, 66−69.

128 C. Prestipino, L. Regli, J. G. Vitillo, F. Bonino, A. Damin, C. Lamberti, A. Zecchina, P. L. Solari, K. O. Kongshaug and S. Bordiga, *Chem. Mater.*, 2006, **18**, 1337−1346.

129 C. P. Cabello, P. Rumori and G. T. Palomino, *Microporous Mesoporous Mater.*, 2014, **190**, 234−239.

130 M. Banerjee, S. Das, M. Yoon, H. J. Choi, M. H. Hyun, S. M. Park, G. Seo and K. Kim, *J. Am. Chem. Soc.*, 2009, **131**, 7524−7525.

131 K. Sumida, S. Horike, S. S. Kaye, Z. R. Herm, W. L. Queen, C. M. Brown, F. Grandjean, G. J. Long, A. Dailly and J. R. Long, *Chem. Sci.*, 2010, **1**, 184−191.

132 M. Dincă, W. S. Han, Y. Liu, A. Dailly, C. M. Brown and J. R. Long, *Angew. Chem., Int. Ed.*, 2007, **46**, 1419−1422.

133 E. D. Bloch, W. L. Queen, M. R. Hudson, J. A. Mason, D. J. Xiao, L. J. Murray, R. Flacau, C. M. Brown and J. R. Long, *Angew. Chem., Int. Ed.*, 2016, **55**, 8605−8609.

134 M. Dincă, A. Dailly, Y. Liu, C. M. Brown, D. A. Neumann and J. R. Long, *J. Am. Chem. Soc.*, 2006, **128**, 16876−16883.

135 E. D. Bloch, L. J. Murray, W. L. Queen, S. Chavan, S. N. Maximoff, J. P. Bigi, R. Krishna, V. K. Peterson, F. Grandjean, O. Gary, J. Long, B. Smit, S. Bordiga, C. M. Brown and J. R. Long, *J. Am. Chem. Soc.*, 2011, **133**, 14814−14822.

136 H.-H. Wang, L. Hou, Y.-Z. Li, C.-Y. Jiang, Y.-Y. Wang and Z. Zhu, *ACS Appl. Mater. Interfaces*, 2017, **9**, 17969−17976.

137 F.-G. Xi, Y. Yang, H. Liu, H.-F. Yao and E.-Q. Gao, *RSC Adv.*, 2015, **5**, 79216–79223.

138 J. Bae, J. S. Choi, S. Hwang, W. S. Yun, D. Song, J. Lee and N. C. Jeong, *ACS Appl. Mater. Interfaces*, 2017, **9**, 24743−24752.

139 J. S. Choi, J. Bae, E. J. Lee and N. C. Jeong, *Inorg. Chem.*, 2018, **57**, 5225−5231.

140 E. Haldoupis, J. Borycz, H. Shi, K. D. Vogiatzis, P. Bai, W. L. Queen, L. Gagliardi and J. I. Siepmann, J. Phys. Chem. C, 2015, **119**, 16058−16071.

141 M. Fischer, F. Hoffmann and M. Fröba, *ChemPhysChem*, 2010, **11**, 2220–2229.

142 T. Pham, K. A. Forrest, D. M. Franz, Z. Guo, B. Chen and B. Space, *Phys. Chem. Chem. Phys.*, 2017, **19**, 18587–18602.

143 J. Borycz, L.-C. Lin, E. D. Bloch, J. Kim, A. L. Dzubak, R. Maurice, D. Semrouni, K. Lee, B. Smit and L. Gagliardi, *J. Phys. Chem. C*, 2014, **118**, 12230−12240.